UCLouvain
Institut de recherche
en mathématique et physique

Search for Lepton Number and Flavor violations in K decays at the NA62 experiment

Doctoral dissertation presented by

Elisa Minucci

in fulfilment of the requirements for the degree of Doctor in Sciences

Jury de thèse

Prof. G. Bruno (President)	UCLouvain, Belgium
Prof. E. Cortina Gil (Supervisor)	UCLouvain, Belgium
Prof. J.M. Gérard	UCLouvain, Belgium
Prof. C. Lazzeroni	University of Birmingham, UK
Dr. T. Spadaro	LNF-INFN, Italy

November, 2018

This work has been partially supported by the *Fonds de la Recherche Scientifique (FNRS)* through a *Fonds pour la formation la Recherche dans l'Industrie et dans l'Agriculture (FRIA)* fellowship.

"Above all, don't fear difficult moments. The best comes from them."

Rita Levi-Montalcini (1909-2012)

Acknowledgments

The experience of the Ph.D. is arrived at the end and every single moment in the last four years and a half has contributed to make me grow as a physicist and as a person. Now is time to thank everyone which helped me and supported me during this amazing experience.

Thanks to my supervisor Prof. Eduardo Cortina for having given me the opportunity to start the Ph.D. Thanks for your support, for your help when things were not clear and thanks for the good ideas always came out from our meetings that inspired me.

Thanks to my colleague Plamen. We started our collaboration quite slow, but after a while we found a perfect equilibrium. Thanks for your help solving technical problems, for your advice and our discussions on physics questions. Thanks for you kindness and your support also after you left CP3.

Thanks to Prof. Giacomo Bruno, Prof. Jean-Marc Gerard, Prof. Cristina Lazzeroni and Dr. Tommaso Spadaro for having reviewed my thesis and for all your comments and suggestions which helped me to improve the final text. Thanks for having made the private defense a nice moment, I never felt under pressure and I learn a lot from the discussion we had.

Thanks to Jerome for having saved the data on my laptop. Thanks to Michele for having clarified some theoretical aspect of my search.

Thanks to all new people I met. Thanks to Ginette and Carinne for your kindness and for the chats in the cafeteria. Thanks to Alessia, Alina, Ambresh, Arthur, Bob, Claudio, Luca, Ken, Mathieu, Pieter, Pietro and Roberta for having shared nice and funny moment at the University and outside and for your help specially in the last months.

Thanks to Chiara and Alessandro. Thanks for being so friendly since the first time we met and for your constant support. Thanks for the dinners, the weekends around Belgium and for all moments we spent together.

Thanks to Chiara, my best friend. We have so many things in common: the physics, the love for Rome, the photography and many others. We can talk of everything, we support each other also if we are in two different countries. I'm grateful I met you. Thanks for everything.

Thanks to my friends Ambra, Davide, Stefano I., Cecilia, Stefano P., Martina, Agnese, Valentino, Isabella, Daniele, Stefano O., Claudia. We have not seen each other much in the last years, but I always had your affection.

Grazie ai miei cugini per le nostre cene ogni volta che torno in Italia.

Grazie ai miei nonni e ai miei zii che con affetto mi avete accompagnato durante questa esperienza.

Grazie alla mia famiglia: mamma, papà e Riccardo per comprendere i miei silenzi e le mie decisioni e per credere in me anche quando io sono la prima a non farlo. Grazie perchè so che, nonostante i pareri a volte discordanti, voi sarete sempre il mio punto di riferimento.

Grazie a Matteo. Grazie per la tua pazienza. Grazie per avermi fatto vivere con serenità questa esperienza e per avermi fatto rialzare quanto tutto mi sembrava andare storto.

Contents

Introduction

The elementary particles and their interactions find their better description in the Standard Model. Even though the SM has been verified with a high level of accuracy over a wide range of energies, and the last missing main block of the model, the Higgs boson has been discovered at the LHC experiments, there are open theoretical issues and experimental evidences which don't find an explanation within the SM. The fine tuning of some parameters of the SM; the evidence of neutrino oscillation which can happen only if neutrinos are massive, the evidence of matter-antimatter asymmetry in the Universe are only some of the reasons which lead the idea that the SM is not a fundamental theory, but only an effective description of particles at a low energy scale.

Nowadays experiments are mainly focused on searches of New Physics, which can be performed in two ways: studying transitions at higher and higher energy as is done at the experiments at LHC at CERN, or studying deviations from SM predictions with higher and higher sensitivities, in experiments aiming at isolating the effects of beyond SM theories in rare decays, as the NA62 experiment at CERN SPS.

Kaon physics has played a key role during the construction of the SM: kaons provided evidence of the necessary insights as the 'strangeness' to explain its long lifetime, the GIM mechanism to explain its small mixing. Also the discovery of CP violation effects within the weak interaction comes form kaon physics. Still now, kaons represent a unique environment where test the SM and search for new physics. Process as the Flavor Changing Neutral Current $K^+ \rightarrow \pi^+\nu\bar{\nu}$ has an exquisite sensitivity to new physics. Its branching ratio is rather precisely predicted from theory to be $\mathrm{Br}(K \rightarrow \pi\nu\bar{\nu}) = (8.4 \pm 1.0) \times 10^{-11}$, however,the existing measurement of this branching ratio is based on only few events, and the experimental precision is not sufficient to challenge the theory prediction and exclude New Physics contributions.

The work presented in this thesis has been carried out using the data collected at the NA62 experiment at CERN, which main goal is to measure the FCNC decay, $K^+ \to \pi^+\nu\bar{\nu}$, with an accuracy of same level of the theoretical prediction (10%) in order to test the SM and search for NP at the same time. The experiment uses a decay in flight technique and it has been designed to reach a background rejection at the level of 10^{12}.

Thanks to the high-intensity setup, the trigger system flexibility, and detector performance (high-frequency tracking of beam particles, redundant particle identification system and hermetic photon vetoes), NA62 is suitable for searching new physics effect from different scenarios. The analysis presented in this thesis is right in this context: search for Lepton Number and Flavor violations in charged kaon decays into three charged particles: $K^+ \to \pi^+\mu^+e^-$, $K^+ \to \pi^+\mu^-e^+$, $K^+ \to \pi^-\mu^+e^+$.

The results presented in this thesis have been obtained analyzed two data samples: one from the 2016 data-taking, called 2016A, collected from 16^{th} of September to 3^{rd} of November, after the installation of all station of the beam tracker (GigaTracker) and the other collected during 2017, called 2017A, between the 21^{st} of September and the end of October, after the installation of an absorber in the last magnet of the beam achromat, in order to absorb particles coming from kaon upstream decays (before the decay volume), which represents one of the main background source for the $K^+ \to \pi^+\nu\bar{\nu}$ analysis. The 2016A sample represents the full statistics available for this analysis from 2016, while, due to the data processing time, it was not possible to analyze the full 2017 data set.

The analysis presented in this work has been performed blinding the signal region, defined as a region between [480,505] MeV/c^2, around the K^+ mass, in the invariant mass spectrum of the selected tracks. The strategy for the analysis of the $K \to \pi\mu e$ decays has been developed: it consists of kinematic requests, used to select three track decays, particle identification criteria in order to distinguish between $\pi/\mu/e$ and on the reconstruction of the invariant mass at the reconstructed decay vertex position, used to distinguish between signal and background.

The estimation of the signal selection acceptance has been done using MC sample for each decay mode under study and it has been measured to be around 5%.

The data analyzed translates in a number of kaons of $N_K = (6.74 \pm 0.41)\ 10^{10}$ for 2016A sample and of $N_K = (10.31 \pm 0.13)\ 10^{10}$ for 2017A sample, computed taking into account all triggers available for the $K \to \pi\mu e$ analysis and the corresponding trigger efficiency.

The preliminary results shown in this work have been obtained studying the background from kaon decays, using the available MC statistics. Due to the lack of statistics for some of the main background sources, it is not possible to have a clear under-

standing of the level of background both in the defined control region and in the signal region. For this reason the upper limits for the $K \to \pi\mu e$ branching ratios have been obtained with the signal region still blind, using the Rolke-Lopetz method with the present level of precision on the background estimation and assuming that the number of observed events in the signal region is zero or one.

The results, even though the rough background estimation, are promising, showing already an improvement in the $K^+ \to \pi^+\mu^- e^+$ and $K^+ \to \pi^-\mu^+ e^+$ channel.

The work is organized in 6 chapters. In the first chapter a short overview of the Standard Model, mainly focused on the flavor physics and then a more detailed description of New Physics contributions to LN and LF violation are given. In the second chapter the NA62 experiment and the performances for each detector, obtained with the data collected during the 2015 commissioning run are presented. The third chapter is on the NA62 trigger: the first part of the chapter is dedicated to the description of the NA62 trigger system, while in the second part the trigger efficiency study performed on the triggers used in the analysis is reported. The fourth chapter describes the tool implemented by me within the NA62 framework for the reconstruction of decay vertex, which leads improvements with respect to the standard method used in NA62, specially if used in multi-tracks events. The fifth chapter is dedicated to the study of the particle identification procedure used in the analysis. In the final chapter all the steps for the selection of the signal, the study of the background sources and the results are reported.

Chapter 1

Theoretical framework

The main idea beyond the searches presented in this thesis is that the Standard Model (SM), the current model able to describe all the elementary matter constituents and their interactions, is not the fundamental theory of Nature. There are both theoretical and experimental reasons for which the SM can be interpreted as a manifestation at low energy of a more general theory. A theoretical argument is the necessity of fine-tuning. In some circumstances, one needs to adjust the parameters of the SM model very precisely in order to match with observations. The evidence of dark matter in the Universe suggested by cosmological data, constitutes one of the experimental arguments, since it cannot stem from SM. No SM particles possess all of the required properties to account for the amount of DM in the Universe. The evidence of matter-antimatter asymmetry in the Universe constitutes an additional argument with no plausible explanation from the Standard Model: three conditions are necessary for the formation of a matter-dominated universe a) C and CP violation, b) baryon number violation (BNV), and c) the absence of thermal equilibrium [1]. Although the existence of C and CP violation has been established experimentally, the amount of CP violation present in the Standard Model (SM) is known to be insufficient to generate the matter-antimatter asymmetry observed in the universe and numerous searches are dedicated to find sources of CP violation beyond the SM. The SM predicts BNV to occur at quantum level [5], the quantum number B-L is respected by the SM but not B and L separately[1]. Numerous searches are performed to search of BNV. An example is the search on baryon-antibaryon oscillations in the Ξ_b^0 system by the LHCb collaboration. This is a first search in the heavy flavor sector and it is of particular interest since Ξ_b^0 baryons may couple directly to flavor-diagonal six-fermion operators

[1] B stands for Baryon Number and L stands for Lepton Number

that violate baryon number. So far no evidence of BNV have been found, but a limit on the oscillation angular frequency of the Ξ_b^0 have been set [2].

However, despite some theoretical and experimental unsolved issues the SM is a successful model, verified over a huge range of energies [3, 4].

The concepts of symmetry and conservation laws are the basis of the SM. The invariance of a system with respect to a given transformation is very useful to determine the interaction structure; at the same time violation of some symmetry of the system can give important information about the underlying process. Discrete symmetry such as parity, i.e. $x \rightarrow x^{'} = -x$ (P), charge conjugation i.e. the interchange of particle and antiparticle (C) and time reversal, i.e. $t \rightarrow t^{'} = -t$ (T) have played an important role in shaping the interactions within the Standard Model. The study of such symmetries in flavor physics and in particular in the kaon sector was essential to redefine the structure of the weak interaction.

As for the Baryon Number, also the Lepton Number (LN) and Lepton Flavor (LF) are approximately conserved within the SM; their conservation is not imposed by any local gauge symmetry (Noether's theorem). Indeed the LF is not conserved in neutrino sector and the LN is violated at quantum level within the SM. While LF violations have been observed in neutrino oscillation, evidences of LN violation has not been observed yet.
To date one of the most interesting experimental result is the so called "*flavor anomaly*": lepton flavor non-universality in B-physics have been pointed out by the Belle, BaBar and LHCb experiments, measuring the R($D^{(*)}$) [9, 10, 11, 12, 13] and R($K^{(*)}$) [14] ratios and showing deviations from the SM predictions. These anomalies have led new ideas in building beyond the SM theories, which can have implication also in lepton flavor violation processes involving charged leptons.

In this sense, searches of LN and LF violations in charged kaon decays can play a crucial role in shaping new physics models, ruling out some of the proposed models and constraining parameters as couplings and masses of new particles.

In this chapter a short review of the SM is given, introducing the main components, the basic building blocks of matter and the fundamental interactions. Then a more detailed description of flavor physics within the SM is presented focusing on the phenomenology of LN and LF conservations in the SM and of LN and LF violations in physics beyond the Standard Model.

1.1 Introduction to the Standard Model

In the SM there are two types of particles, the basic building blocks of matter and the particles that mediate the interactions (Figure 1.1). The firsts are fermions with spin s=$\frac{1}{2}$ and are divided in two categories, quarks and leptons while the others are bosons with spin s=0,1. Quarks and leptons are organized into three generations:

$$1^{\text{st}}\text{generation} \quad e, \nu_e, u, d \tag{1.1}$$

$$2^{\text{nd}}\text{generation} \quad \mu, \nu_\mu, c, s \tag{1.2}$$

$$3^{\text{rd}}\text{generation} \quad \tau, \nu_\tau, t, b \tag{1.3}$$

Among the leptons, electrons, muons and taus are electrically charged and massive, while neutrinos are electrically neutral and assumed with zero mass by the theory. Quarks are all massive and electrically charged. Additionally they carry also the color charged, which exists in three states: "red"(R), "blue"(B) and "green"(G). In Nature only neutral color states are present, called hadrons distinguished between mesons and baryons. The first are made of one quark and one anti-quark as $\pi^+(u\bar{d})$ and $K^+(d\bar{s})$. The latter are made of three quarks as the proton p(uud). In total there are three interactions between all fermions mediated by twelve bosons: the photon,γ, mediates the electromagnetic interaction among all fermions but neutrinos. Eight gluons,g, mediate the strong interaction between all quarks. The gauge bosons $W^\pm$ and Z^0 mediate the electroweak interaction among all fermions.

The Standard Model is built within the quantum field theory (QFT) and it is based on symmetry principles. The SM Lagrangian is locally invariant under the gauge symmetry:

$$G_{SM} = SU(3)_C \times SU(2)_L \times U(1)_Y \tag{1.4}$$

The $SU(3)_c$ group responds to the symmetry under local color transformations and rules the strong interaction. The strong interaction mediators, associated to the $SU(3)_c$ generators are 8 gauge fields, called gluons, which carry themselves the color charge. Strong interactions conserve quark flavor; quarks cannot change flavor within strong processes.

The $SU(2)_L \times U(1)_Y$ is the symmetry group governing the electroweak interactions. The $SU(2)_L$ group describes the weak-isospin symmetry and the $U(1)_Y$ describes the weak hypercharged symmetry. The group describing the electromagnetic interactions, $U(1)_{em} \subset SU(2)_L \times U(1)_Y$ responds to the Quantum Electrodynamics (QED). The

$SU(2)_L \times U(1)_Y$ group includes left-handed quarks and leptons that form the weak-isospin doublets as well as the right-handed quarks and leptons which form weak-isospin singlets

$$\begin{pmatrix}\nu_e\\ e^-\end{pmatrix}_L \quad \begin{pmatrix}\nu_\mu\\ \mu^-\end{pmatrix}_L \quad \begin{pmatrix}\nu_\tau\\ \tau^-\end{pmatrix}_L \tag{1.5}$$

$$\begin{pmatrix}u\\ d\end{pmatrix}_L \quad \begin{pmatrix}c\\ s\end{pmatrix}_L \quad \begin{pmatrix}t\\ b\end{pmatrix}_L \tag{1.6}$$

$$e_R^- \quad \mu_R^- \quad \tau_R^- \tag{1.7}$$

$$u_R, d_R, \quad c_R, s_R, \quad t_R, b_R \tag{1.8}$$

The weak interactions only act on left-handed particles(and right-handed anti-particles) and thus violate parity. Electric charge (Q), weak isospin (T) and hypercharge (Y) are related by the equation: Q=T+Y/2. In order to maintain the gauge invariance of the SM Lagrangian under local symmetries, mass terms in the Lagrangian are forbidden. Introduction of mass terms for massive fermions and the $W^{\pm}$, Z^0 gauge bosons destroys the gauge invariance of the Lagrangian. If one ignores this symmetry-breaking effect, one encounters unrenormalizable divergences which make the theory meaningless. The mass terms for the weak gauge bosons ($W^{\pm}$, Z^0) and all fermions have to be generated in an invariant way. The problem is solved by the application of the principle of spontaneous symmetry breaking, the Brout-Englert-Higgs (BEH) mechanism. The cornerstone in the BEH mechanism is the assumption of a new field, the Higgs field, whose non-zero vacuum expectation value breaks the electroweak gauge symmetry of the Lagrangian. The introduction of the Higgs field generates new contributions in the Lagrangian: the Yukawa interaction, describing the interaction between the fermion fields and the Higgs scalar field, the fermion mass terms and the Higgs potential [3, 4].

1.2 Flavor Physics

The term *flavor physics* refers to the study of interactions which distinguish between flavors. Flavor physics is restricted to the weak and Yukawa interactions, since the strong gauge interactions, related to unbroken symmetries, do not distinguish among the flavors [16]. In Flavor Changing Charged Current (FCCC) processes, both up-type

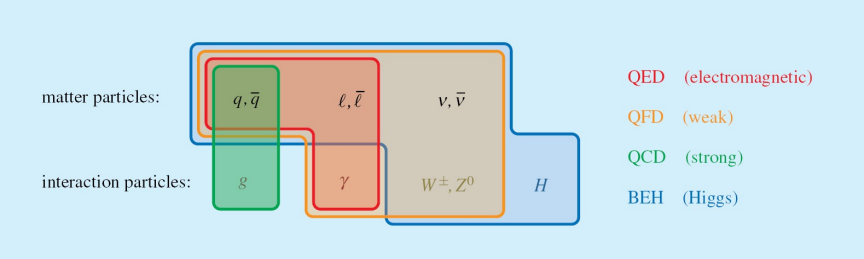

Figure 1.1: Schematic description of all fundamental particles and interaction in the SM [15].

and down-type flavors, and both charged lepton and neutrino flavors are involved. Within the Standard Model, these processes are mediated by the W-bosons and can occur at tree level. In Flavor Changing Neutral Current (FCNC) processes, either up-type or down-type flavors but not both, and either charged lepton or neutrino flavors but not both, are involved. Within the Standard Model, these processes do not occur at tree level, and are therefore suppressed. An example of FCNC process is the $K^+ \to \pi^+ \nu\bar{\nu}$, which is the main decay studied at NA62 [17, 18].

Flavor physics has played a key role in the shaping of the SM. The experimental evidence of differences in the branching ratio of decays with $\Delta S = 0$ (1.10) and $\Delta S = 1$ (1.11), where S is the strangeness number, spotted the possibility of different coupling between flavors.

$$\frac{\Gamma(K^+ \to \mu^+ \nu)}{\Gamma(\pi^+ \to \mu^+ \nu)} \sim \frac{1}{20} \tag{1.9}$$

$$Br(D^+ \to \pi^+ \pi^0) = (1.24 \pm 0.06) \times 10^{-3} \tag{1.10}$$

$$Br(D^+ \to K^+ \pi^0) = (1.89 \pm 0.25) \times 10^{-4} \tag{1.11}$$

This behavior refers to the non-universality of the weak interaction. The different coupling between flavors can be described if quark mass eigenstates and quark weak-interaction eigenstates do not coincide. In particular, assuming u′ and d′ being the

weak eigenstates and u, d, s the mass eigenstates, Cabibbo postulated the following relation:

$$d' = d\,cos\theta + s\,sin\theta,\;\; u' = u \tag{1.12}$$

where $\theta = 0.26$ rad is called Cabibbo angle [3, 19]. It was measured comparing the rate of $K^+ \to \mu^+\nu$ and $\pi^+ \to \mu^+\nu$ (1.9). From the relations (1.12) follows that the weak interaction mixed quarks belonging to the first and second generation, in particular $d \to u$ transitions are favored over $s \to u$ transitions.

The concept of rotation from the weak basis to the mass basis was extended by Glashow-Iliopoulus-Maiani (GIM mechanism) [3, 20], introducing a fourth quark,*c*, to answer to the experimental evidence of non FCNC decay at tree level:

$$\begin{pmatrix} d' \\ s' \end{pmatrix} = \begin{pmatrix} cos\theta & sin\theta \\ -sin\theta & cos\theta \end{pmatrix} \begin{pmatrix} d \\ s \end{pmatrix}, \begin{pmatrix} u' \\ c' \end{pmatrix} = \begin{pmatrix} u \\ c \end{pmatrix} \tag{1.13}$$

And indeed, the existence of the charm quark was suggested by $K_0 - \bar{K_0}$ mixing and confirmed in 1974 with the observation of the J/Ψ resonance [21, 22].

1.2.1 The CKM matrix

In 1964 it was observed that K^0 particle produced in strong interactions had different lifetimes. It decayed in different final states:

$$\tau(K_1 \to 2\pi) = 0.9 \times 10^{-10} sec. \tag{1.14}$$

$$\tau(K_2 \to 3\pi) = 0.5 \times 10^{-7} sec. \tag{1.15}$$

and the same was observed for the $\bar{K^0}$. These observations mean that K^0 and $\bar{K^0}$ particles produced in strong interaction, with their distinct strangeness content, are not the eigenstates that act in weak interactions and weak interactions do not conserved strangeness. The 2π and 3π final states are eigenstates of CP with eigenvalues +1 and -1 respectively, bringing to the conclusion that the neutral kaon CP eigenstates were not identified with $K^0(\bar{K^0})$ but with two other particles called K_1 and K_2. To connect the two sets of eigenstates, a quite natural idea is that the weak interaction eigenstates can be written as a mixtures of strong eigenstates:

$$|K_1\rangle = \frac{1}{\sqrt{2}}(\left|K^0\right\rangle + \left|\bar{K^0}\right\rangle) \tag{1.16}$$

$$|K_2\rangle = \frac{1}{\sqrt{2}}(\left|K^0\right\rangle - \left|\bar{K^0}\right\rangle) \tag{1.17}$$

where K_1 and K_2 have well defined lifetime:

$$|K_1(t)\rangle = e^{-im_1 t - \Gamma_1 t/2} |K_1\rangle \tag{1.18}$$
$$|K_2(t)\rangle = e^{-im_2 t - \Gamma_2 t/2} |K_2\rangle \tag{1.19}$$

In the same way the K^0 and $\bar{K^0}$ states can be written as:

$$\left|K^0\right\rangle = \frac{1}{\sqrt{2}}(|K_1\rangle + |K_2\rangle) \tag{1.20}$$
$$\left|\bar{K^0}\right\rangle = \frac{1}{\sqrt{2}}(|K_1\rangle - |K_2\rangle) \tag{1.21}$$

but the time evolution of this state brings to a final state with a number of $\bar{K_0}$; which means that the K^0 state will not only decay but will also oscillate into $\bar{K_0}$ and back with a oscillation frequency given by the mass difference between the two weak eigenstates ($\Delta m = m_2 - m_1$).

Moreover it was observed that K_2 (CP=-1) can decay in $K_2 \to \pi^+\pi^-$ (CP=+1) with a branching ratio of 10^{-3} [4, 26, 27], giving the first evidence of CP violation. The results obtained by Christenson, Cronin, Fitch and Turlay in 1964 pointed out that the K_1 and K_2 are not eigenstates of the weak interaction, they are slightly different and they usually refer to K_S^0 and K_L^0 for short and long lived one respectively.

$$\left|K_S^0\right\rangle = \frac{1}{\sqrt{1+|\epsilon^2|}}(|K_1\rangle - \epsilon\,|K_2\rangle) \tag{1.22}$$
$$\left|K_L^0\right\rangle = \frac{1}{\sqrt{1+|\epsilon^2|}}(|K_2\rangle + \epsilon\,|K_1\rangle) \tag{1.23}$$

where ϵ is related to the size of CP violation.

The phenomenon of mixing of meson refers to the indirect CP violation.
Direct CP violation can be spotted comparing the decay probability of the process $P \to f$ with its CP conjugate $\bar{P} \to \bar{f}$, where P can be a meson decaying into a final state f. Indirect and direct CP violation are usually quantified by two complex number ϵ and $\epsilon^{'}$ and a value different from zero of the ratio $\epsilon^{'}/\epsilon$ is an evidence of the presence of direct CP violation [24, 28]. A first hint of direct CP violation was pointed out by the NA31 experiment [32], measuring the quantity in (1.24). A better precision was needed to claim the discovery and the same measurement was performed subsequently by the NA48 experiment at CERN [33] and KTeV at Fermilab [34], confirming the observation of direct CP violation effects.

$$R = \frac{\Gamma(K_L \to \pi^0\pi^0)\Gamma(K_S \to \pi^+\pi^-)}{\Gamma(K_S \to \pi^0\pi^0)\Gamma(K_L \to \pi^+\pi^-)} = 1 - 6Re\left(\frac{\epsilon^{'}}{\epsilon}\right) \tag{1.24}$$

The present $\epsilon^{'}/\epsilon$ experimental value is [24, 29, 30, 31]:

$$\frac{\epsilon^{'}}{\epsilon} = (16.6 \pm 2.3) \times 10^{-4} \tag{1.25}$$

Recently analyses on the $\epsilon^{'}/\epsilon$ anatomy within the SM, presented in [35, 36], show that $\epsilon^{'}/\epsilon$ in the SM could turn out to be significantly lower than its experimental value as triggered by a first result on $\epsilon^{'}/\epsilon$ calculation using lattice QCD [37]. The $\epsilon^{'}/\epsilon$ ratio is also very sensitive to NP contributions [38] and correlation between $\epsilon^{'}/\epsilon$ and the branching ratio of $K^+ \to \pi^+\nu\bar{\nu}$ and $K_L \to \pi^0\nu\bar{\nu}$ are present: in particular models $\epsilon^{'}/\epsilon$, Br($K^+ \to \pi^+\nu\bar{\nu}$) and Br($K_L \to \pi^0\nu\bar{\nu}$) can be enhanced simultaneously over their SM values [18].

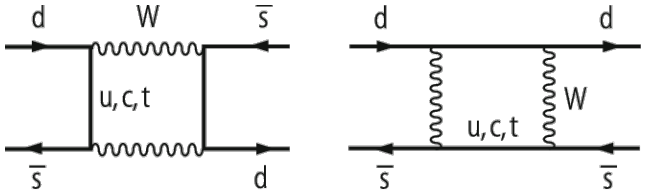

Figure 1.2: The box diagrams describing the ΔS= 2 transition, responsible of the $K^0 - \bar{K^0}$ mixing.

Considering only two generations of quarks, the quark mixing is described by a single real parameter, the Cabibbo angle θ (1.13) and CP violation in weak interaction is excluded. To include CP violation effect in the SM, Kobayashi and Maskawa predicted the existence of a third generation of quarks [23, 24], such that:

$$\begin{pmatrix} d' \\ s' \\ b' \end{pmatrix} = V_{CKM} \begin{pmatrix} d \\ s \\ b \end{pmatrix} \tag{1.26}$$

where V_{CKM} is the Cabibbo-Kobayashi-Maskawa (CKM) matrix. For the total probability conservation the V_{CKM} matrix has to be unitary. The V_{CKM} matrix can be parametrized by three angles (Cabibbo-like), θ_{12}, θ_{13}, θ_{23} describing the coupling between different generations and one phase factor $e^{i\delta_{KM}}$ which represents the only source of CP violation.

$$V_{CKM} = \begin{pmatrix} V_{ud} & V_{us} & V_{ub} \\ V_{cd} & V_{cs} & V_{cb} \\ V_{td} & V_{ts} & V_{tb} \end{pmatrix} \tag{1.27}$$

$$V_{CKM} \cong \begin{pmatrix} c_{12}c_{13} & s_{12}c_{13} & s_{13}e^{-i\delta_{KM}} \\ -s_{12}c_{23} - c_{12}s_{23}e^{i\delta_{KM}} & c_{12}c_{23} - s_{12}s_{23}s_{13}e^{i\delta_{KM}} & s_{23}c_{13} \\ s_{12}c_{23} - c_{12}c_{23}e^{i\delta_{KM}} & -c_{12}s_{23} - s_{12}c_{23}s_{13}e^{i\delta_{KM}} & c_{23}c_{13} \end{pmatrix} \tag{1.28}$$

where $c_{ij} = cos\theta_{ij}$ and $s_{ij} = sin\theta_{ij}$ (i,j=1,2,3).

Form the unitary condition follows the relation:

$$V_{ud}V_{ub}^{*} + V_{cd}V_{cb}^{*} + V_{td}V_{tb}^{*} = 0 \tag{1.29}$$

and other five similar relations can be constructed; they all correspond to a triangle in a complex plane, called unitary triangle (see Figure 1.3 and Figure 1.4).

The CKM matrix can be written in different parametrizations. One useful parametrization, the Wolfenstein parametrization [25], is inspired by the smallness of the Cabibbo angle and is the following:

$$V_{CKM} = \begin{pmatrix} 1 - \lambda^2/2 & \lambda & A\lambda^3(\rho - i\eta) \\ -\lambda & 1 - \lambda^2/2 & A\lambda^2 \\ A\lambda^3(1 - \rho - i\eta) & -A\lambda^2 & 1 \end{pmatrix} \tag{1.30}$$

where $\lambda = sin\theta_{12}$, $A\lambda^2 = sin\theta_{23}$, $A\lambda^3(\rho - i\eta) = sin\theta_{13}e^{i\delta_{KM}}$. In this representation, the violation of the CP symmetry is represented by the term proportional to the imaginary part of the δ_{KM} phase term. Since $\rho/\eta \sim$ O(1), CP violation is not intrinsically small.

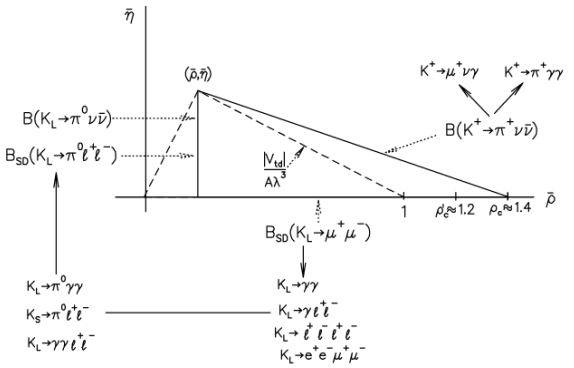

Figure 1.3: Role of rare kaon decays in determining the unitary triangle. The solid arrows point to auxiliary modes needed to interpret the main results, or potential backgrounds to them [24].

The determination of the various CKM matrix elements stems from a plethora of decays and studies. The main modes used to measure each CKM element are listed in Table 1.1 and the present status for the moduli of the CKM matrix are shown in (1.31). For the phase parameter constraints come from many measurements of the CP violating observables as the ϵ and $\epsilon^{'}$.

Matrix element	Experimental information
V_{ud}	β-decay (nuclear, neutron and pion decay)
V_{us}	$K \to \pi e \nu$, semileptonic kaon decays
V_{ub}	$b \to u e^- \bar{\nu_e}$ (but suffers of large $b \to c e^- \bar{\nu_e}$ background)
V_{cd}	semileptonic charm decay: $D \to K l \nu$ and $D \to \pi l \nu$
V_{cs}	semileptonic D and leptonic D_s decays
V_{cb}	exclusive/inclusive semileptonic decays of B mesons to charm
V_{td}	K and B oscillations mediated by box diagrams
V_{ts}	K and B oscillations mediated by box diagrams
V_{tb}	direct determination from top decays into bottom

Table 1.1: Summary of the methods use to measure the various CKM matrix elements.

$$V_{CKM} = \begin{pmatrix} 0.97434^{+0.00011}_{-0.00012} & 0.22506 \pm 0.00050 & 0.00357 \pm 0.00015 \\ 0.22492 \pm 0.00050 & 0.97351 \pm 0.00013 & 0.0411 \pm 0.0013 \\ 0.00875^{+0.00032}_{-0.00033} & 0.0403 \pm 0.0013 & 0.99915 \pm 0.00005 \end{pmatrix} \quad (1.31)$$

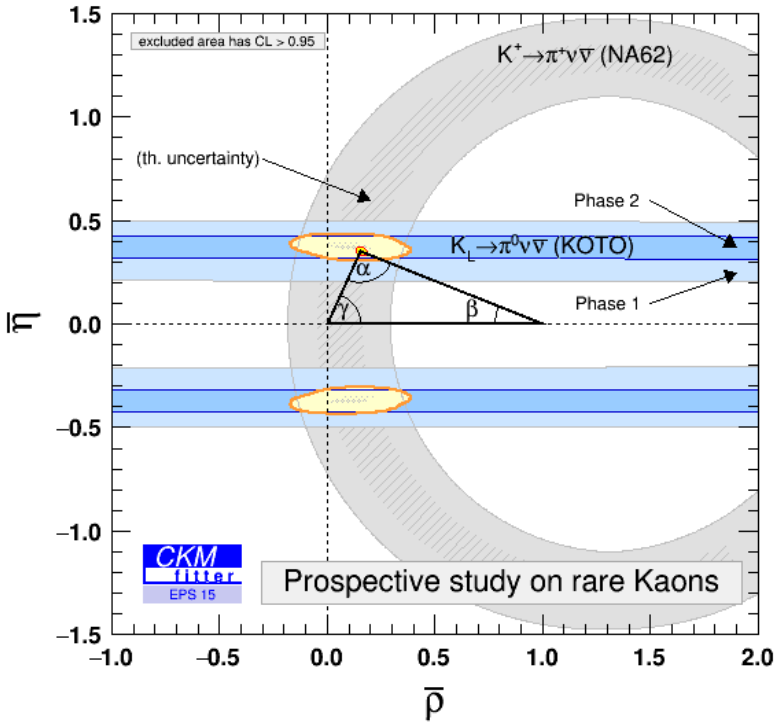

Figure 1.4: 95 % CL constraints on the $\bar{\rho}, \bar{\eta}$ complex plane, from $K \to \pi\nu\bar{\nu}$ physics experiments [24].

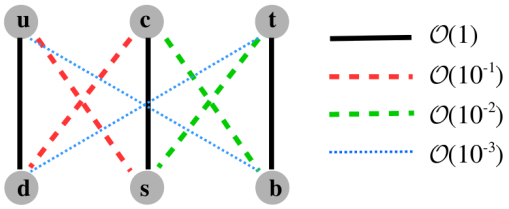

Figure 1.5: Representation of the possible transitions between the quark generations with the corresponding order of magnitude.

In conclusion, since the V_{CKM} matrix is not diagonal, FCCC tree-level interactions can occur. On the contrary, γ and Z interactions are flavor diagonal, so there are no FCNCs at tree-level. FCNC processes are extremely sensitive to new physics and can

be used to extract CKM parameters only if the SM is assumed. Within the kaon sector the amplitude of the $K^+ \to \pi^+\nu\bar{\nu}$, CP conserving, and the $K^0 \to \pi^0\nu\bar{\nu}$, pure CP-violated, are strongly related to some parameters of the CKM matrix (Figure 1.4) and at the same time are quite sensitive to physics beyond the SM. If new physics manifests in these decays, the CKM parameters extracted from them may differ from the same parameters obtained from other decays. Effects of new physics at the TeV scale may give greater than percent-level effects in the CKM parameter, thus CP asymmetries, mixing, semileptonic and rare decay in the B, K and D meson sectors should be measured with high precision.

1.3 Lepton number and Lepton flavor in SM and beyond

The lepton number L is defined as a quantum number with value +1 for leptons, -1 for anti-leptons and 0 for all other particles. In addition, leptonic flavor quantum numbers are defined, each associated to the individual lepton family. These flavor quantum numbers, denoted as $\mathrm{L}_f,\ f = e, \mu, \tau$, determine the total lepton number , which is the sum of three lepton flavor numbers L_{tot}=L_e+L_μ+L_τ [2].
Lepton Number (LN) and Lepton Flavor (LF) are accidentally conserved quantities within the SM since their conservation is not imposed by any local gauge symmetry (Noether's theorem). Decays such as:

$$\mu \to e\gamma \tag{1.32}$$
$$K^+ \to \pi^-\mu^+\mu^+ \tag{1.33}$$
$$K^+ \to \pi^+\mu^+e^- \tag{1.34}$$

are totally forbidden.

Search for LN and LF violations are performed in several experiments:

- MEG: $\mu \to e\gamma$
- LHCb, CMS, ATLAS, Belle: B mesons and τ decays
- NA62 in K sector

[2] In comparison quarks carry a different quantum number, the baryonic number B=1/3 (and B= 1/3 for anti-quarks). Mesons, composed of a quark and an anti-quark, together with leptons and gauge bosons, have B=0. While all baryons (anti-baryons), which are composed of three quarks (anti-quarks), are characterized by B=1 (B=-1), respectively.

The absence within the SM of right-handed neutrinos means that for the lepton family there are no Yukawa interaction. As a consequence, there is an exact lepton flavor conservation. Nevertheless, observations of neutrino oscillations prove that the neutrinos are massive particles, and flavor changing transitions are also possible in the lepton sector.

Different new physics models for non-zero neutrino masses predict the neutrinos to be either Dirac or Majorana fermions[3]. If neutrinos are Dirac particles they can contribute to the lepton flavor violation processes but not to lepton number violation. While if neutrinos are Majorana particles they can contribute to both lepton flavor and number violations processes and only by investigating the validity of lepton-number conservation we will be able to asses if neutrinos are Dirac or Majorana particles.
The inclusion of massive neutrinos in extensions of SM is not the only way to induce LN and LF violation processes. Other new physics models in which LN and LF violation can occur are presented in this section.

There are different type of LN and LF processes, they may be sensitive to different mechanisms and thus yield complementary information about the LN and LF origin:

- Pure leptonic LFV processes: $\mu \to e\gamma$, $\mu \to 3e$, $\tau \to \mu\gamma$, etc.
- Quark-lepton LFV processes of the type $d \to d\mu e$ as the neutrino-less conversion $\mu + (A, Z) \to e + (A, Z)$
- Quark-lepton LFV processes of the type $s \to d\mu e$ as the kaon decays: $K_L^0 \to \mu e$, $K^+ \to \pi^+ \mu e$
- Lepton number violating decays as the neutrino-less 2β-decay or $K^+ \to \pi^- l^+ l^+$ kaon decays.

For example, the observation of charged lepton flavor violation can be possible only beyond the SM. They are all GIM suppressed, except for the neutrino-less 2β-decay, which can probe LF violation ($\Delta L_e = 2$) via massive Dirac neutrinos. Also the first class of decays involves only leptons, while the other processes involve both quarks and leptons, thus can give complementary information on LF and LN violation, constraining different regions of the phase space (new particle mass and coupling) for

[3] Dirac particles are fermions described by fields ψ which satisfy the Dirac equation

$$(i\partial_\mu \gamma^\mu - m)\psi = 0 \tag{1.35}$$

Majorana particles are fermions described by fields χ which satisfy the condition

$$C\bar{\chi}^T = e^{i\xi}\chi, \;\; |e^{i\xi}|^2 = 1 \tag{1.36}$$

where C is the charge conjugation operator and $e^{i\xi}$ is and arbitrary phase. Thus Majorana fermions are eigenstates of the C operator, i.e. they are their own antiparticles.

each model taken into account.
In the following the description will focus on kaon decays.

1.3.1 Massive Neutrinos

After propagating a finite distance neutrino beams of a given flavor (electron, muon, tau) contain no longer only neutrinos of the initial flavor. That phenomenon has been established in "disappearance" experiments with atmospheric and accelerator neutrinos ($\nu_\mu \not\to \nu_\mu$, $\bar{\nu_\mu} \not\to \bar{\nu_\mu}$) [39, 40], solar neutrinos ($\nu_e \not\to \nu_e$) [41] and reactor neutrinos ($\bar{\nu_e} \not\to \bar{\nu_e}$) [42] and in "appearance" experiments with solar neutrinos ($\nu_e \to \nu_{\mu,\tau}$) [41]. The only consistent explanation of all of these phenomena is (i) neutrino masses are nonzero and distinct, (ii) the weakly interacting flavor neutrinos ν_e , ν_μ and ν_τ are nontrivial superpositions of the so called mass eigenstate neutrinos ν_1, ν_2, ν_3 with masses m_1, m_2, m_3, respectively. These superpositions are described, as for the quark sector, by a 3×3 unitary mixing matrix, the PMNS matrix (1.37) [44]. This idea was suggested for the first time by Pontecorvo in 1957 [43] for two lepton families and subsequently extended to three families by Maki, Nakagawa and Sakata [44], in a similar way as the CKM.

$$U_{PMNS} = \begin{pmatrix} c_{12}c_{13} & s_{12}c_{13} & s_{13}e^{-\delta} \\ -s_{12}c_{23} - c_{12}s_{23}e^{i\delta} & c_{12}c_{23} - s_{12}s_{23}s_{13}e^{i\delta} & s_{23}c_{13} \\ s_{12}c_{23} - c_{12}c_{23}e^{i\delta} & -c_{12}s_{23} - s_{12}c_{23}s_{13}e^{i\delta} & c_{23}c_{13} \end{pmatrix} \begin{pmatrix} 1 & 0 & 0 \\ 0 & e^{i\lambda_{21}} & 0 \\ 0 & 0 & e^{i\lambda_{31}} \end{pmatrix} \tag{1.37}$$

where $c_{ij} = cos\theta_{ij}$,$s_{ij} = sin\theta_{ij}$, θ_{12}, θ_{13}, θ_{23} are the three mixing angle, δ is the CP violation Dirac phase and λ_{21}, λ_{31} are the two CP violation Majorana phase ($\Delta L = 2$ processes).

The neutrino field can be written as:

$$\nu_{\alpha L} = \sum\nolimits_k U_{\alpha k}\nu_{kL} \tag{1.38}$$

and the oscillation probability to change flavor from ν_α to ν_β after traversing a length S is

$$P_{\nu_\alpha \to \nu_\beta}(S) = |\langle \nu_\beta | |\nu(S)\rangle| \sum\nolimits_{kj} U_{\beta k}U^*_{\alpha k}U^*_{\beta j}U_{\alpha j}e^{-i\frac{\Delta m^2_{ik}S}{2E}} \tag{1.39}$$

which depends on the U_{PMNS} matrix elements and the neutrino mass differences.
The values of all three mixing angles θ_{12}, θ_{13}, θ_{23} and the two independent mass-squared differences Δm^2_{21} and $\Delta m^2_{31} \sim \Delta m^2_{32}$ are all known with good accuracy,

while the potential CP-violating parameters, along with the so-called neutrino mass hierarchy, remain virtually unconstrained.

Also the neutrino nature is still unconstrained and the scenario could change significantly if neutrinos are Dirac or Majorana particles.

Dirac case. If neutrinos are Dirac particles, they can be treated as all the other massive fermions. In a minimally extended SM, three neutrino right-handed singlets ν_{lR} (l=e, mu, τ) are introduced in the SM Lagrangian and the Dirac mass terms is [45, 46]:

$$\mathcal{L}^D(x) = -\sum\nolimits_{l,l'} \bar{\nu_{l'}}_R(x) M^D_{l,l'} \nu_{lL}(x) + h.c. \tag{1.40}$$

derived by the Yukawa coupling Y^ν of the left-handed lepton doublets $\Psi_L = (l_L, \nu_L)$, the Higgs doublet Φ and the right handed singlet ν_R after the spontaneous symmetry breaking. The M^D is a 3 $\times$ 3 complex matrix, that can be represented in the form:

$$M^D = VmU^\dagger \tag{1.41}$$

where V and U are unitary mixing matrices and m is a diagonal matrix. From (1.40) and (1.41):

$$L^D(x) = -\sum_{i=1}^{3} m_i \bar{\nu_i}(x) \nu_i(x) \tag{1.42}$$

where ν_i are the mass eigenstates. The flavor eigenstates ν_{lL} and the mass eigenstates ν_{iL} are connected by the mixing matrix U_{PNMS}((1.37)):

$$\nu_{lL} = \sum_{i=1}^{3} U_{il} \nu_{iL}(x) \tag{1.43}$$

In this scenario the total lepton number is conserved.

Majorana case. If neutrinos are Majorana particles by definition they are their own antiparticles, $\nu_{lR} = (\nu_{lL})^c = C\bar{\nu^T_{lL}}$. In this case the corresponding Lagrangian mass term is [45, 46]:

$$L^L(x) = -\frac{1}{2} \sum\nolimits_{l,l'} \bar{\nu_{l'}}_L(x) M^L_{l,l'} (\nu_{lL})^c(x) + h.c. \tag{1.44}$$

where M^L is a complex symmetrical 3$\times$3 matrix that can be represented in the form:

$$M^L = UmU^T \tag{1.45}$$

with U unitary matrix and $m_{ik} = m_i\delta_{ik}$ ($m_i > 0$). As for the Dirac case the flavor eigenstates ν_{lL} and the mass eigenstates ν_{iL} are connected by the mixing matrix U_{PNMS}((1.43)). In this scenario the Lagrangian in not invariant under the global gauge transformation $\nu_{lL}^{'}(x) = e^{i\alpha}\nu_{lL}(x)$. Therefore it is foreseen to add right-handed sterile neutrinos.

Seesaw mechanism

Several mechanisms have been proposed to generate neutrino mass terms [47]. One of them is the so called "type I see-saw mechanism"[48]. In this particular model, n_s right-handed sterile Majorana neutrinos N_m (m = 4,. . ., n_s+3) are introduced, which interact with the SM lepton doublets ψ_l ($l = e, \mu, \tau$) and the Higgs doublet Φ via Yukawa coupling Y^N and also possess a Majorana mass term M^R.

$$\begin{aligned} L_{Y,M}(x) &= L_Y(x) + L_M^N(x) \\ &= -Y_{lm}^N(x)\bar{\psi_{lL}}(x)\Phi(x)N_{mR}(x) - \frac{1}{2}M_{Rm'm}\bar{N_{m'L}^c}(x)N_{mR}(x) + h.c. \end{aligned} \tag{1.46}$$

A Dirac mass term is generated after spontaneous symmetry breaking:

$$L_D^\nu(x) = -\bar{\nu_{lL}}(x)m_{Dlm}N_{mR}(x) + h.c. \tag{1.47}$$

and the total mass term $L_{D,M} = L_D^\nu + L_M^N$ is:

$$L_{D,M}(x) = -\frac{1}{2}(\bar{\nu_L}, \bar{N_L^c}) \begin{pmatrix} 0 & M_D \\ M_D^T & M_R \end{pmatrix} \begin{pmatrix} \nu_R^c \\ N_R \end{pmatrix} + h.c. \tag{1.48}$$

where $\nu_L = (\nu_e, \nu_\mu, \nu_\tau)_L$ is a 3-component vector formed of SM neutrinos and $N_R = (N_4, ..., N_{n_s+3})$ is a n_s-component vector formed of the right-handed singlets N_m. $M_D = vY^N$ is a 3×n_s matrix while M_R is a $n_s \times n_s$ matrix. The mixing between the electroweak and mass eigenstates is described by the relation

$$\nu_{lL} = \sum_{i=1}^{3} U_{li}\nu_{iL}^M + \sum_{m=4}^{n_s+3} \mathcal{U}_{lm}N_{ml}^{Mc},\ UU^\dagger + \mathcal{U}\mathcal{U}^\dagger = \mathbb{I} \tag{1.49}$$

where U is a 3×3 matrix determining the SM neutrino mixing and $\mathcal{U}$ is a 3×n_s matrix describing the mixing between sterile and SM neutrinos. A crucial aspect of the type I see-saw mechanism described above is that a non-zero $\mathcal{U}$ matrix implies the existence

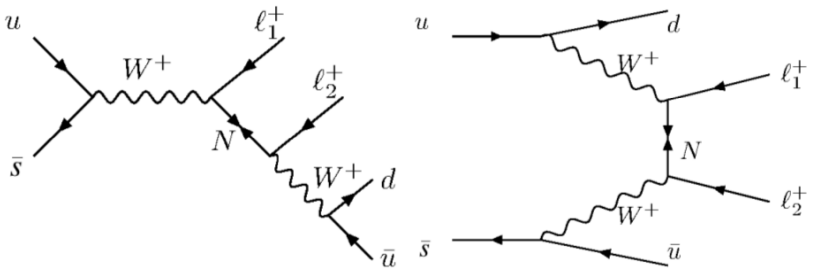

Figure 1.6: Feynman diagrams describing the massive Majorana neutrinos contributions to the ΔL = 2 process $K^{\pm} \to \pi^{\mp} l_1^+ l_2^+$

of interaction terms between sterile neutrinos and $W^{\pm}, Z^0$ bosons. In this scenario the contributions to the $K^{\pm} \to \pi^{\mp} l_1^+ l_2^+$ decay amplitude come from the Feynman diagrams in Figure 1.6 [50].

In the limit of light sterile neutrinos ($m_N << m_K$) the estimated branching ratio is([51])

$$\begin{aligned} Br(K^{\pm} \to \pi^{\mp} l_1^{\pm} l_2^{\pm}) &= \tau_K \frac{G_F^4 m_K^3}{16\pi^3} f_K^2 f_\pi^2 |V_{us} V_{ud}|^2 \phi^L_{l_1 l_2} < m_{l_1 l_2} >^2 \\ &\sim 1.7 \times 10^{-18} MeV^{-2} \phi^L_{l_1 l_2} < m_{l_1 l_2} >^2 \end{aligned} \tag{1.50}$$

where τ_K is the kaon lifetime, $\phi^L_{l_1 l_2}$ is the reduced phase space integral and $< m_{l_1 l_2} >$ is the effective Majorana mass.

In the limit of heavy sterile neutrinos ($m_N >> m_K$) the estimated branching ratio is [51]

$$\begin{aligned} Br(K^{\pm} \to \pi^{\mp} l_1^{\pm} l_2^{\pm}) &= \tau_K \frac{G_F^4 m_K^3}{128\pi^3} f_K^2 f_\pi^2 |V_{us} V_{ud}|^2 \phi^H_{l_1 l_2} < m^{-1}_{l_1 l_2} >^2 \\ &\sim 2.3 \times 10^{-8} MeV^{-2} \phi^H_{l_1 l_2} < m^{-1}_{l_1 l_2} >^2 \end{aligned} \tag{1.51}$$

where τ_K is the kaon lifetime, $\phi^H_{l_1 l_2}$ is the reduced phase space integral and $< m^{-1}_{l_1 l_2} >$ is the effective inverse Majorana mass.

In both limits the theoretical expectations for the $Br(K^{\pm} \to \pi^{\mp} l_1^{\pm} l_2^{\pm})$ branching ratios are far from the current experimental sensitivity $O(10^{-12})$. Even in the scenario with $m_{N_m} \sim m_K$ the $Br(K^{\pm} \to \pi^{\mp} l_1^{\pm} l_2^{\pm}) \sim 10^{-14}$ is barely covered with actual experimental sensistivity.

In the scenario with of a fourth neutrino N with a large Majorana mass the observation of LN violation provides both information on the mass of the fourth neutrino and

on the coupling strength. In Figure 1.7a, Figure 1.7b and Figure 1.7c constraints on charged lepton coupling $|V_{l4}|$ to the fourth neutrino as a function of its mass are shown for the electron and muon case [52].

1.3.2 Leptoquark

Lepton flavor violation process can be produced if leptoquark couples with fermions of more than one family. Leptoquarks are scalar or vector particles that carry both baryon and lepton number. In this scenario (Pati-Salam model [57]) leptons can be seen as a fourth color in a $SU(4)_c$ group. At a scale above the electroweak scale, gauge symmetry breaks into the $SU(3)_c$, leptoquarks acquire mass and de-couple in lepton and quarks.

As an example the branching ratio for $K^+ \to \pi^+\mu^+e^-$ (Figure 1.8), computed with respect to the $K^+ \to e^+\pi^0\nu$ is given by:

$$\frac{Br(K^+ \to \pi^+\mu^+e^-)}{Br(K^+ \to e^+\pi^0\nu)} = \frac{1}{8sin^2\theta_c}\left(\frac{g_{LQ}}{g}\right)^4\left(\frac{M_w}{M_{LQ}}\right)^4 \tag{1.52}$$

where g_{LQ} is the leptoquark coupling constant and M_{LQ} is the leptoquark mass. Then:

$$M_{LQ} \sim 500TeV\left[\frac{10^{-12}}{Br(K^+ \to \pi^+\mu^+e^-)}\right]^{1/4} \tag{1.53}$$

Assuming $g_{LQ} \sim g_{W,Z}$ and $Br(K^+ \to \pi^+\mu^+e^-) \sim 1.3 \times 10^{-11}$, which is the present limit, the leptoquark mass results $\sim$ 260 TeV.

The recent "anomalies" in B physics, i.e. the observation of a non-universal behavior of different lepton species in the specific in $b \to c, s$ semi-leptonic processes, need beyond SM constructions. Within the proposed New Physics models to solve the " anomalies" in B physics, the Pati-Salam model predicts a massive vector Leptoquark with the correct quantum numbers to fit the anomalies. The problem of the "orig-ina" model proposed by Pati-Salam are the strong bounds on the LQ couplings to the first and second generations, leading to $M_{LQ} > 200$ TeV from $K_L \to \mu e$. To solve this problem different variations of the original Pati-Salam model (PS) have been pro-posed as the one in [58], called PS^3. This model provides a consistent description for the hints of lepton-flavor non-universality observed in B decays and predicts a well-defined pattern of non-standard effects in low-energy observables, in particular it implies large LFV effects. For example in Figure 1.9 the correlation between the

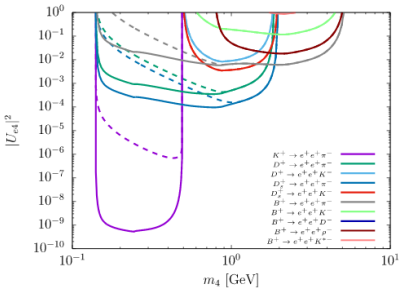

(a) Excluded regions above the curves for $|U_{e4}|^2$ versus m_4 from $M_1^+ \to e^+e^+M_2^-$ searches.

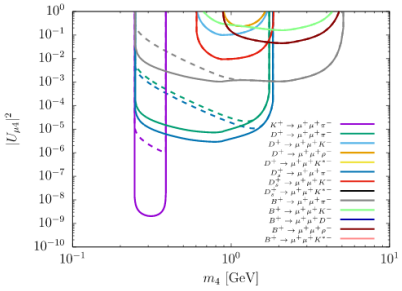

(b) Excluded regions above the curves for $|U_{\mu 4}|^2$ versus m_4 from $M_1^+ \to \mu^+\mu^+M_2^-$ searches.

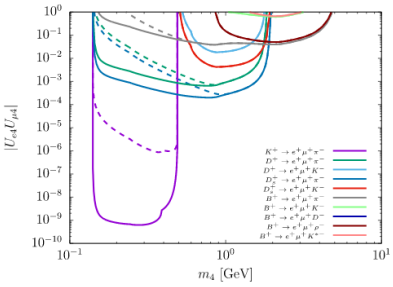

(c) Excluded regions above the curves for $|U_{e4}U_{\mu 4}|$ versus m_4 from $M_1^+ \to \mu^+e^+M_2^-$ searches.

Figure 1.7: Excluded region for the leptonic mixing matrix elements $|U_{e4}|^2$, $|U_{\mu 4}|^2$ and $|U_{e4}U_{\mu 4}|$ as a function of the heavy sterile neutrino mass m_4. Dashed lines denote the bounds derived taking into account the requirement of having the heavy neutrino decaying within a finite detector, i.e. imposing that its length of flight does not exceed a nominal value $L_{\nu 4}^{flight} = 10\ m$ [52]

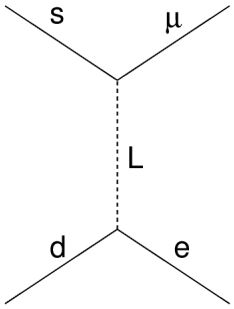

Figure 1.8: Feynman diagram for the $K^+ \to \pi^+\mu e$ LF violation decay mediated by Leptoquark

branching ratio of $B^+ \to K^+\tau^+\mu^-$ and $\tau \to \mu\gamma$ expected in PS^3 model is shown, having direct connection to the NP enhancement in R(D$^{(*)}$) and $b \to sll$. An other interesting result in the PS^3 model is the expected decay rate Br($K_L \to \mu e$)$\sim 10^{-12}$ which is not too far from the sensitivity of present experiments. In the same model, the branching ratio for $K \to \pi\mu e$ is expected to be smaller than the Br($K_L \to \mu e$) due to the small available phase space.

1.3.3 New Heavy Bosons

Lepton flavor violation processes can occur in extensions of the standard model with an additional U(1)$^{'}$ gauge symmetry and an associated Z$^{'}$ boson [53]. In case of Z$^{'}$ bosons with family non-universal coupling, quark and lepton flavor mixing process have contributions from tree-level Z$^{'}$ flavor violating exchanges. In the case of $K_L^0 \to e\mu$ only axial and pseudo-scalar hadron current can contribute to the $< 0|H_w|K_L^0 >$ decay amplitude, while scalar, vector and tensor hadron currents can contribute to the $< \pi|H_w|K >$ decay amplitude of $K^+ \to \pi^+\mu e$ [54, 55, 56]. The contribution to the $K_L^0 \to e\mu$ branching ratio due to the axial only interaction can be written as:

$$Br = \left[\frac{16}{sin\theta_c g^2}\right]^2 \left(\frac{h^{'}}{h^{''}}\right)^2 \left[\frac{h^{''}}{M_{Z'}} M_W\right]^4 \tag{1.54}$$

It is proportional to the couplings of the new boson with the d-s ($h^{''}$) quarks and $e^{\mp}$-$\mu^{\pm}$ ($h^{'}$) pair and the mass of the heavy new boson. Models with s-channels exchange

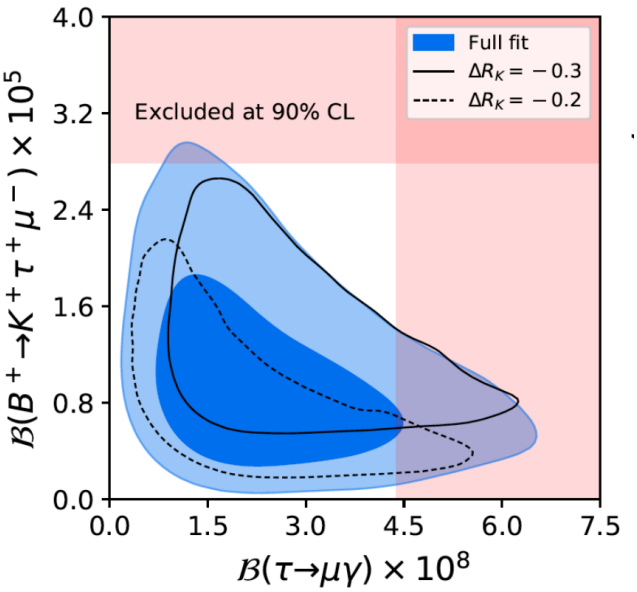

Figure 1.9: 68% (dark blue) and 95% (light blue) posterior probabilities of B($B^+ \to K^+\tau^+\mu^-$) and B($\tau \to \mu\gamma$) from the global fit. The black lines denote the 95% posterior probabilities fixing the R_K NP shift, $\Delta R_K = -0.3$ (solid) and $\Delta R_K = -0.2$ (dashed). The red bands show the 90% CL exclusion limits for these observables [59]

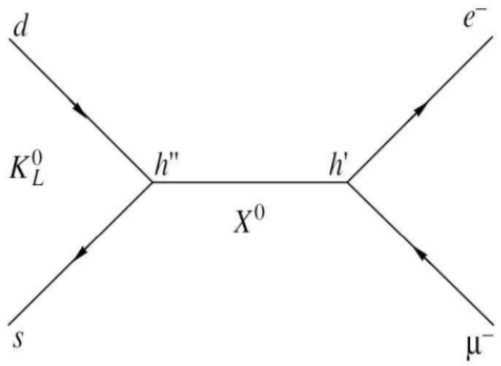

Figure 1.10: Feynman diagram for the $K_L^0 \to e\mu$ LF violation decay due to an s-channel exchange of a heavy new boson X_0 [56]

of Z$'$ bosons are strongly constrained as they would results in a significant mass split

between the K_S^0 and K_L^0 due to the process:

$$K^0 \leftrightarrow Z^{'} \leftrightarrow \bar{K^0} \tag{1.55}$$

The resulting mass difference is given by:

$$\Delta m_K^{'} \approx \frac{8}{3} m_K f_K^2 \left(\frac{h^{''}}{M_{Z'}} \right)^2 \tag{1.56}$$

and under the extreme assumption that the s-channels exchange of Z$^{'}$ is the only contribution to the mass splitting, i.e $\Delta m_K^{'} = \Delta m_K = 3.49 \times 10^{-12} MeV/c^2$, then

$$\left(\frac{h^{''}}{M_{Z'}} \right)^2 = \frac{\Delta m_K}{m_K} \frac{3}{8} \frac{1}{f_K^2} = 2.8 \times 10^{-7} TeV^{-2} \tag{1.57}$$

where m_K is the K^0 mass and $f_K = 160 MeV$ is the kaon decay constant. Under this assumption the upper limit of the $K^+ \to \pi^+ \mu e$ branching ratios are $Br(K^+ \to \pi^+ \mu e) < 2 \times 10^{-16}$. However one would expect $\Delta m_K^{'} < \Delta m_K$, due to the fact that SM weak interactions alone can account for a significant fraction of Δm_K.
Different limit for $Br(K^+ \to \pi^+ \mu e)$ are expected under the hypothesis of $g_{Z'} \sim g_{W,Z}$. In this scenario, the branching ratios of the $K_L^0 \to e\mu$ and $K^+ \to \pi^+ \mu e$ decays as a function of the new boson mass parameter are shown in Figure 1.11. Considering the present upper limits the mass parameter, derived from (1.54) is already above 100 TeV, confirming that LFV decays may be sensitive to large energy scale, not even accessible at the future generation of colliders. The results shown in 1.11 are extremely interesting as they point out values of the branching ratio between $10^{-10} - 10^{-13}$, which are not far from the sensitivities reachable at present or near future experiments. In particular NA62 will reach sensitivities up to 10^{-12} and would give a strong impact in the $K^+ \to \pi^+ \mu e$ decays under the last scenario.

1.4 Present status of LN and LF violation in charged kaon decays

Searches of LN and LF violation in the charged kaon decays have been done in the past. The present PDG limits are listed in Table 1.2. The results on $K^+ \to \pi^- \mu^+ \mu^+$ was set by the NA48/2 experiment at CERN [74], while the results on $K^+ \to \pi^- e^+ e^+$

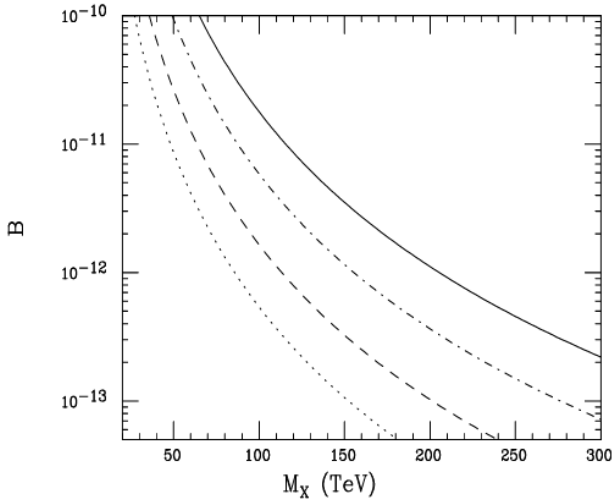

Figure 1.11: Branching fractions for $K_L^0 \to e\mu$ and $K^+ \to \pi^+\mu e$ as a function of M_X, the mass of the new boson, assuming the coupling $g_{Z'} \sim g_{W,Z}$. The K_L mode is represented by the solid(S) and dashed(V) curves while the K^+ mode is represented by the dash-dotted(S) and dotted(V) curves. Here S,V stands for scalar and vector interactions [55].

Decay	Mode	Upper limit (90% C.L)
$K^+ \to \pi^-\mu^+\mu^+$	LNV+LFV	8.6×10^{-11} [60]
$K^+ \to \pi^-e^+e^+$	LNV+LFV	6.4×10^{-10} [62]
$K^+ \to \pi^-\mu^+e^+$	LFV+LNV	5.0×10^{-10} [62]
$K^+ \to \pi^+\mu^+e^-$	LFV	1.3×10^{-11} [61]
$K^+ \to \pi^+\mu^-e^+$	LFV	5.2×10^{-10} [62]

Table 1.2: Current experimental upper limits on LN and LF violation charged kaon decays.

and all three $K \to \pi\mu e$ decays were set by the E865 experiments at Brookhaven Alternating Gradient Synchrotron (AGS) [63].

The E865 experiment was primarily designed to search for $K^+ \to \pi^+\mu^+e^-$, but it has been exploited to search for other three tracks kaon decays as $K^+ \to \pi^+e^+e^-$, $K^+ \to \pi^+\mu^-e^+$ and $K^+ \to \pi^-\mu^+e^+$ decays. As NA62 the E865 experiment used a not-separated beam at 6 GeV/C, produced by a proton beam of 25.5 GeV/c impinging a copper target, and a decay in flight technique, with $\sim$6% of kaons decaying within

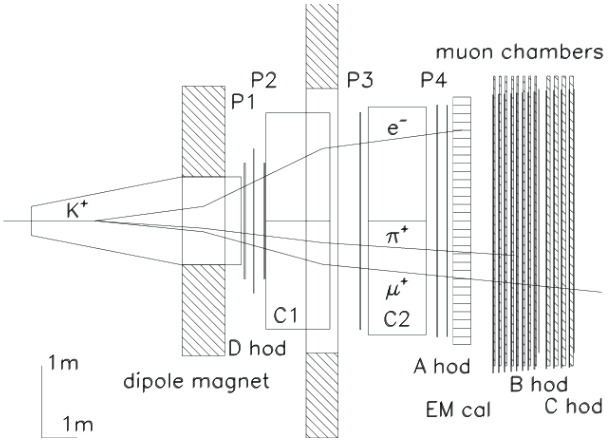

Figure 1.12: Overview of the E865 detector with a simulated $K^+ \to \pi^+\mu^+e^-$ event. C1 and C2 are the gas Cerenkov counters; P1, P2, P3, P4 are proportional chambers. A detailed description of the apparatus is in [63]

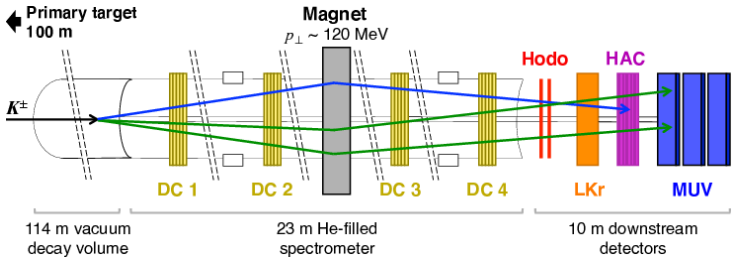

Figure 1.13: Schematic diagram of the NA48/2 experiment, showing drift chambers (DC1–4), trigger hodoscope (Hodo), NA48 liquid-krypton electromagnetic calorimeter (LKr), hadronic calorimeter (HAC), and muon vetoes (MUV). In the picture is visible a $K^+ \to \pi^-\mu^+\mu^+$ event. A detailed description of the apparatus is in [74]

the decay volume. The detector layout is shown in Figure 1.12, where is also visible a simulated $K^+ \to \pi^+\mu^+e^-$ decay.

The background sources are of two types: kaon decays and accidentals combinations of π,μ,e originating from separated kaon decays. Considering the first type of background the $K^+ \to \pi^+\pi^+\pi^-$ and $K^+ \to \pi^+\pi^0_D$ decays are the main source of background for all three $K \to \pi\mu e$ channels. In addition to them the $K^+ \to \mu^+\pi^0_D\nu$ is a source of background for the $K^+ \to \pi^+\mu^+e^-$ channel, while the $K^+ \to \pi^+\pi^-e^+\nu$ is possible background for the $K^+ \to \pi^-\mu^+e^+$ and $K^+ \to \pi^+\mu^-e^+$ channels.

NA48/2 was design to search for direct CPV from precise measurement of the charge asymmetry in the three body decay the decays $K^+ \to \pi^+\pi^{0,\pm}\pi^{0,\mp}$ and their charge

conjugates. The NA48/2 experiment operated with high-intensity, unseparated, simultaneous, highly-collimated, 60-GeV momentum $K^{\pm}$ beams. The detector layout is shown in Figure 1.13. The $K^+ \to \pi^-\mu^+\mu^+$ analysis is a direct product of the corresponding allowed rare decay $K^+ \to \pi^+\mu^+\mu^-$. In Figure 1.14 the invariant mass plots are shown for the two searches. As shown in the plot the only source of background is the $K^+ \to \pi^+\pi^+\pi^-$ decay.

Thanks to a better mass resolution($\sigma_{\pi ll} \sim 1.5 MeV/c^2$), higher intensity and a better background rejection, improvements in $K^+ \to \pi^{\pm} l_1^{\mp} l_2^{+}$, where $l_1, l_2 = (\mu, e)$ are expected at NA62.
In particular sensitivities of $\mathcal{O}10^{-12}$ are expected for all LN and LF violation decays.

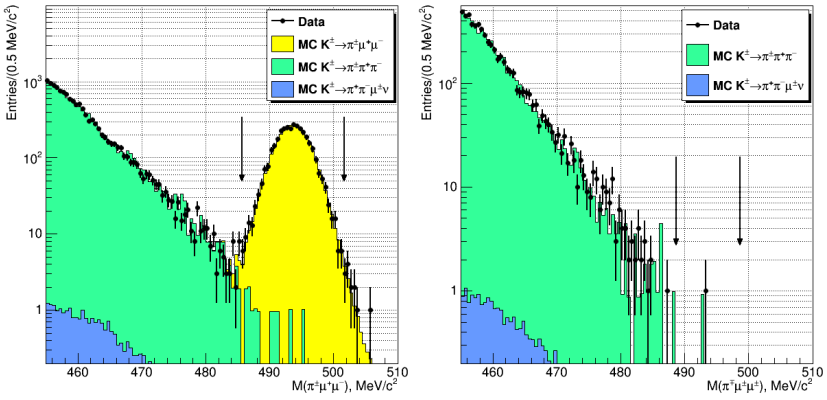

Figure 1.14: Three-track invariant mass from $K^{\pm} \to \pi^{\pm}\mu^+\mu^-$ (left-panel) and $K^{\pm} \to \pi^{\mp}\mu^+\mu^+$ (right panel) samples.

1.5 Conclusion

In the Standard Model (SM), the lepton L and baryon B numbers are conserved, only at classical level, due to the accidental $U(1)_L \times U(1)_B$ symmetry. The L and B non-conservation is a generic feature of various extensions of the SM. That is why lepton-number violating processes are sensitive tools for testing theories beyond the SM.
Discovery of neutrino oscillations has clearly demonstrated the LF violation; this implies that neutrinos are massive and mixed particles and requires extension of the SM (New Physics). Instead no LF violation within charged leptons have been observed. Indeed in the minimal extension of the SM with three massive standard neutrinos, evidence of LF violation in charged leptons are expect to be at a non observable level, e.g $Br(\mu \to e\gamma) \sim 10^{-54}$ [64].

Some extensions of the SM built to explain experimental evidence as the neutrino oscillations or the flavor anomaly in B-physics, can introduce LN and LF violation NP effects. In this chapter some of all available models have been presented.

The see-saw mechanism proposed to generate neutrino mass terms adding right-handed sterile neutrinos, can be a source of LN violation ($\Delta L = 2$) through the exchange of Majorana neutrinos. In this scenario the decay branching ratios depend on the sterile neutrinos masses and they are expected to be of the order of $10^{-24} - 10^{-34}$ (Table 1.3), still far from the actual reachable values.

Decay	Upper limit (90% C.L)	Indirect bound on Br (heavy neutrinos)	Indirect bound on Br (light neutrinos)
$K^+ \to \pi^- \mu^+ \mu^+$	8.6×10^{-11} [60]	5.9×10^{-32}	2.3×10^{-33}
$K^+ \to \pi^- e^+ e^+$	6.4×10^{-10} [62]	1.1×10^{-24}	6.2×10^{-34}
$K^+ \to \pi^- \mu^+ e^+$	5.0×10^{-10} [62]	5.1×10^{-24}	2.0×10^{-34}

Table 1.3: Indirect upper bound on the the branching ratio of the rare kaon decays with $\Delta L = 2$ (LN violation) [49].

LN and LF violations appear also in models which include leptoquarks (Pati-Salam model), scalar or vector particles carrying both L and B numbers; considering the present upper limit of decays such as the $K^+ \to \pi^+ \mu^+ e^-$ the leptoquark mass is expected to be around 250 TeV. A variation of the original Pati-Salam model built to explain the discrepancy with respect to the SM observed in R($D^{(*)}$) and R($K^{(*)}$) can have implication in pure leptonic, B-meson and K-meson LF violation processes. In this model particular interesting are Br($K_L \to \mu e$) and Br($\mu \to 3e$) expected to be around 10^{-12} and 10^{-14}, respectively.

An other possible beyond the SM construction is the extension of the SM with an additional U(1) gauge symmetry and an associated new heavy boson, which can be source of LF violation. It has been showed that the branching ratios of LF violating decays depend on the new boson ($Z^{'}$) mass: for $Z^{'}$ mass of the order of 200 TeV and assuming $g_{Z'} \sim g_{W,Z}$ the expected Br($K \rightarrow \pi\mu e$) may be of the order of 10^{-13}, value that can be experimentally reachable in the near future. In particular NA62, where the expected sensitivity is $\sim 10^{-12}$, can have a strong impact in constraining the parameters of this $Z^{'}$ model.

Another example is represented by the work presented in [71], where an EFT is built to explain the observed flavor anomaly in B-sector. In this work a relation between the recent result on R($K^{(*)}$) and LF violation in K-sector, in particular in $K^+ \rightarrow \pi^+\mu e$ have been found, showing that for EFT cutoffs between 5-15 TeV, compatible with the discrepancies in $B \rightarrow K^* ll$, Br($K^+ \rightarrow \pi^+\mu e$)$\sim 10^{-12} - 10^{-13}$ are expected. This result is extremely interesting as it can be probed at NA62 in the near future.

The scenarios presented in this section are not exhaustive, there are many other models such as Supersymmetry [66], technicolor [65], Little Higgs model [67, 68], axion-like particles [69, 70], in which LN and LF violation can occur.
All scenarios show that LN and LF violating decays in kaon sector can be a powerful probe to test high energy scale $\mathcal{O}$(100 TeV). In some of the models presented the expected branching ratio for $K \rightarrow \pi\mu e$ are not too far from the present experimental sensitivity and NA62 can give a strong contribution in these kind of searches.

NA62 is expected to improve the present limits on charged kaon LN and LF violating decays of one or two order of magnitude with respect to the present experimental limits, reaching branching ratios of the order of 10^{-12} as shown in Table 1.4.

Decay	Mode	Upper limit (90% C.L)	NA62 prospects
$K^+ \rightarrow \pi^-\mu^+\mu^+$	LNV+LFV	8.6×10^{-11} [60]	$\sim 10^{-12}$
$K^+ \rightarrow \pi^-e^+e^+$	LNV+LFV	6.4×10^{-10} [62]	$\sim 10^{-12}$
$K^+ \rightarrow \pi^-\mu^+e^+$	LNV+LFV	5.0×10^{-10} [62]	$\sim 10^{-12}$
$K^+ \rightarrow \pi^+\mu^+e^-$	LFV	1.3×10^{-11} [61]	$\sim 10^{-12}$
$K^+ \rightarrow \pi^+\mu^-e^+$	LFV	5.2×10^{-10} [62]	$\sim 10^{-12}$

Table 1.4: NA62 prospective for LN and LF violation K^+ decays and corresponding current upper limits.

Chapter 2

The NA62 experiment

The NA62 experiment is a fixed target experiment placed at CERN Super-Proton-Synchrotron (SPS). In 2016-2018 run NA62 aims to collect $\sim$ 20 $K^+ \to \pi^+\nu\bar{\nu}$ events [17, 18] in about two years of data taking increasing the present precision on its branching ratio [72].[1] Assuming the nominal beam intensity, in two years of data taking O(10^{13}) kaon decays can be collected. Considering a 4% signal acceptance, a $K^+ \to \pi^+\nu\bar{\nu}$ branching ratio of the order of 10^{10} and requiring a signal/background ratio of 10, a rejection factor of the order of 10^{12} is needed.

The NA62 experimental strategy and the detector layout has been designed to reach the main goal of the experiment, but the high statistics and the detector performances allow to do many other analyses on kaon decays. Several complementary analyses have been started in NA62 to measure the branching ratio of rare decays (Br $\sim 10^{-8}$) and to search for forbidden decays in the SM, as the Lepton Number(LN) and Lepton Flavor(LV) violating kaon decays which are the topic of this PhD thesis.

The experimental technique, the beam line, the detector layout and performances, with dedicated descriptions for each sub-detectors are presented in Sec.2.1, Sec.2.2 and Sec.2.3, respectively.

[1] The number of events expected in two years of data taking is computed assuming a beam intensity of $\sim$ 60% of the nominal value, 33 $\times 10^{11}$ proton on target (POT) and a signal acceptance of $\sim$ 4%

2.1 Experimental technique

The main goal of the experiment and most of the complementary searches involve rare, ultra-rare and forbidden K^+ decays. To perform a successful search for rare and forbidden decays the experiment has to collect a huge amount of kaon decays and must be able to detect signal and reject background, mainly coming from the most abundant kaon decays as $K^+ \to \mu^+\nu$, $K^+ \to \pi^+\pi^0$and $K^+ \to \pi^+\pi^+\pi^-$.

The experimental technique adopted in NA62 consists of: a high-momentum kaons decaying in flight, kinematics variables to separate signal from background, detectors with high time resolution and particle identification detector with high detection efficiency.

The NA62 kaon beam is produced by the interaction of the proton beam at 400 GeV/c extracted from the SPS with an upstream beryllium target. The charged secondary beam, containing kaons is selected in momentum (75 GeV/c) using collimators and then directed through the detector. The advantage of a high-momentum beam is that the background rejection against events with photons in the final state improves with the energy, in particular the higher energy of the decay products increases detection efficiency of π^0 coming from the $K^+ \to \pi^+\pi^0$, the $K^+ \to \pi^+\pi^0\pi^0$ and $K^+ \to \pi^0 l^+\nu$ decays (l=e,μ), while the decay in flight technique allows for having an integrated flux of O(10^{13}) in few years of data taking. On the other hand using a high-momentum beam, the charged particles in the beam cannot be efficiently separated and the beam contains kaons, together with pions and protons.

Despite what happens at collider experiments, at fixed target experiments the beam particles last for a few seconds long spill (or burst). During the SPS spill of 3 s effective duration, the particle rate in the NA62 positive secondary hadron beam is 750 MHz, of which about 6% is from K^+, leading to 5 MHz of K^+ decays in the 65 m long decay region. Pion and protons represent the most popular particles in the beam, $\sim$70% and $\sim$23% respectively, as a consequence the detectors upstream of the decay region are exposed to a particles flux $\sim$16 times greater than the kaon flux (Table 2.2). This is not the case for all the other detectors; downstream detectors are not illuminated by undecayed particles in the beam, which remain inside the beam pipe nor by the muons from pion decays. Note that 75% of the kaons do not decay before hitting the beam dump at the end of the beam line .

As mention before, the detector layout has been optimized for the $K^+ \to \pi^+\nu\bar{\nu}$ measurement. The $K^+ \to \pi^+\nu\bar{\nu}$ signature consists of a single π^+ track emerging from a K^+ track and of the absence of any other detected particles.
The squared missing mass variable, defined as the squared of the difference between

	π^+	p	K^+	$\mu^+ + e^+$	Tot.
$\Phi(MHz)$	525	173	45	6.6+0.3	750
Φ/Φ_{tot}	70 %	23 %	6 %	0.9 % + 0.04 %	100 %
Φ/Φ_K	11.6	3.8	1	0.14+0.007	16.66

Table 2.1: Secondary beam composition at the last Gigatracker station, 102.4 m downstream the production target [76].

the K^+ track quadri-momentum (P_K) and the π^+ track quadri-momentum (P_π)

$$m^2_{miss} = (P_K - P_\pi)^2 \tag{2.1}$$

is the kinematic variable used to discriminate the signal from the main background kaon decays. The definition of two mass regions allows the rejection of more than 90% of the main K^+ decays and a kinematic rejection factor of O(10^4-10^5) is expected. This factor can be obtained reaching an high-resolution reconstruction of the time of the order of 100 ps, space, and emission angles of beam and daughter particles. The only kinematic rejection factor is not sufficient to obtain an overall rejection of 10^{12}, for this reason the capability of vetoing events with additional photons in the final state with extremely high efficiency (O(10^8)) and an additional charged particle identification, to better identify charged particles, of order O(10^7) are paramount to meet the goal of the experiment.
All aspects introduced above for the main goal of the experiment are fundamental for any measurement of rare kaon decays and search of forbidden kaon decays at NA62.
In particular the analysis presented in this thesis involves a three body decay with only charged particles in the final state: pion, muon and electron. In this specific configuration the particle identification system to distinguish between π/μ/e, the muon detector and the photon detectors play an important role. Timing is also extremely important to well associate reconstructed tracks in the same event and reject possible accidentals. The main kinematic variables to distinguish between signal and background are the total momentum Eq. 2.2 and the invariant mass Eq. 2.3 of the three particles in the final state, at the vertex position:

$$\vec{P_{tot}} = (\vec{P_\pi} + \vec{P_\mu} + \vec{P_e}) \tag{2.2}$$

$$m_{inv} = \sqrt{(P_\pi + P_\mu + P_e)^2} \tag{2.3}$$

where P_π, P_μ, P_e are the four-momentum of the three tracks in the final state, measured with the magnetic spectrometer, assuming the pion, muon and electron mass hypothesis, respectively.

2.2 The NA62 beam

The NA62 beam is produced using a primary proton beam at 400 GeV/c extracted from the CERN SPS and directed via the P42 beam line to a beryllium target, called T10 (400 mm long, 2 mm diameter). The beam line dedicated to the NA62 experiment is a "straight line", connecting the T10 target to the center of the liquid Krypton calorimeter. It is installed along the existing K12 beam line used for the NA48 and NA48/2 [73] [74] experiments in the ECN3 cavern.

The beam line can be divided in five different regions: the target region, the upstream region, where beam particles are identified and tracked, the fiducial decay region, the downstream region, where particles emerging from beam decays are tracked and identified and the end of the beam region.
The target region is the region where the T10 target, used to produce the secondary beam is located.
Between the target region and the upstream region the beam line is composed of several collimators and magnets to selected the right momentum and to focus the beam. After the T10 target the particles inside the secondary beam with an angle $>\sim 6$ mrad, before they can decay to muons, are absorbed by a collimator; then the produced beam is focused by three quadrupole magnets and bent vertically by the first of two front-end achromats (see Figure 2.1).

The first achromat performs the momentum selection. It consists of four, vertically-deflecting, dipole magnets: the firsts two produce a parallel downward displacement of the beam by 110 mm while the other two return the beam along the undeviated axis. In the middle of the first achromat the beam passes through a set of graduated holes of two motorized and water-cooled beam-dump units, called TAX1 and TAX2; a specific combination of vertical positions and permitted ranges, allow to select the wanted beam with a momentum around 75 GeV/c and a 0.8 GeV/c rms. Between TAX1 and TAX2 the beam passes through a tungsten radiator, 1.3 X_0 thick. Positrons passing through the radiator loose enough energy via bremsstrahlung radiation and are rejected after the seconds two dipole magnets (see Figure 2.1). At this point the beam is composted only of positively-charged particles and is cleaned from more than 99.6% of the initial positrons.
After the first front-end achromat, three quadrupole magnets refocus the beam. At this point the upstream region starts. A pair of quadrupole magnets make the beam more wide and parallel, to optimize the kaon identification in the KTAG, the photon detection system of CEDAR, the differential Cherenkov detector which aims to identify kaons (Section 2.12), and again it is refocused using another pair of quadrupoles. Before entering the decay region, the beam passes trough a region where there is the

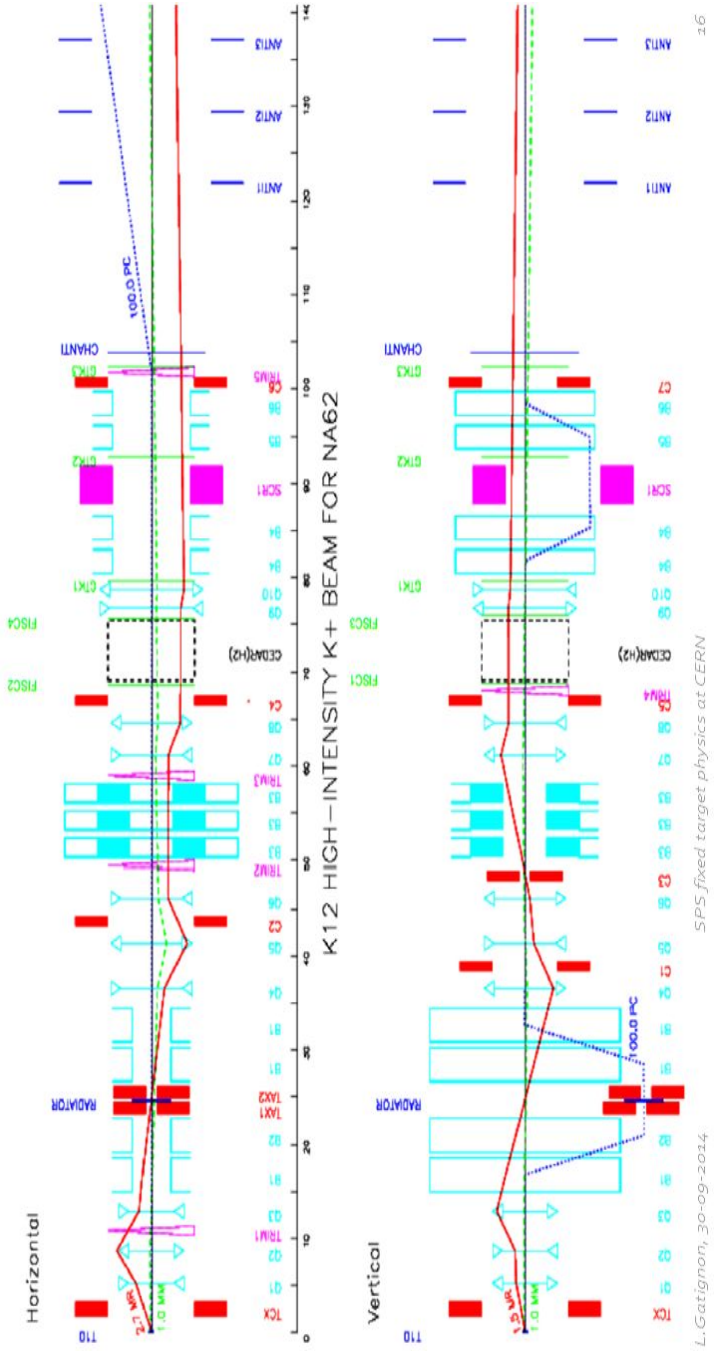

Figure 2.1: Detailed scheme of the beam line from the T10 target to the decay fiducial region. In the picture both the the horizontal and vertical views are shown.

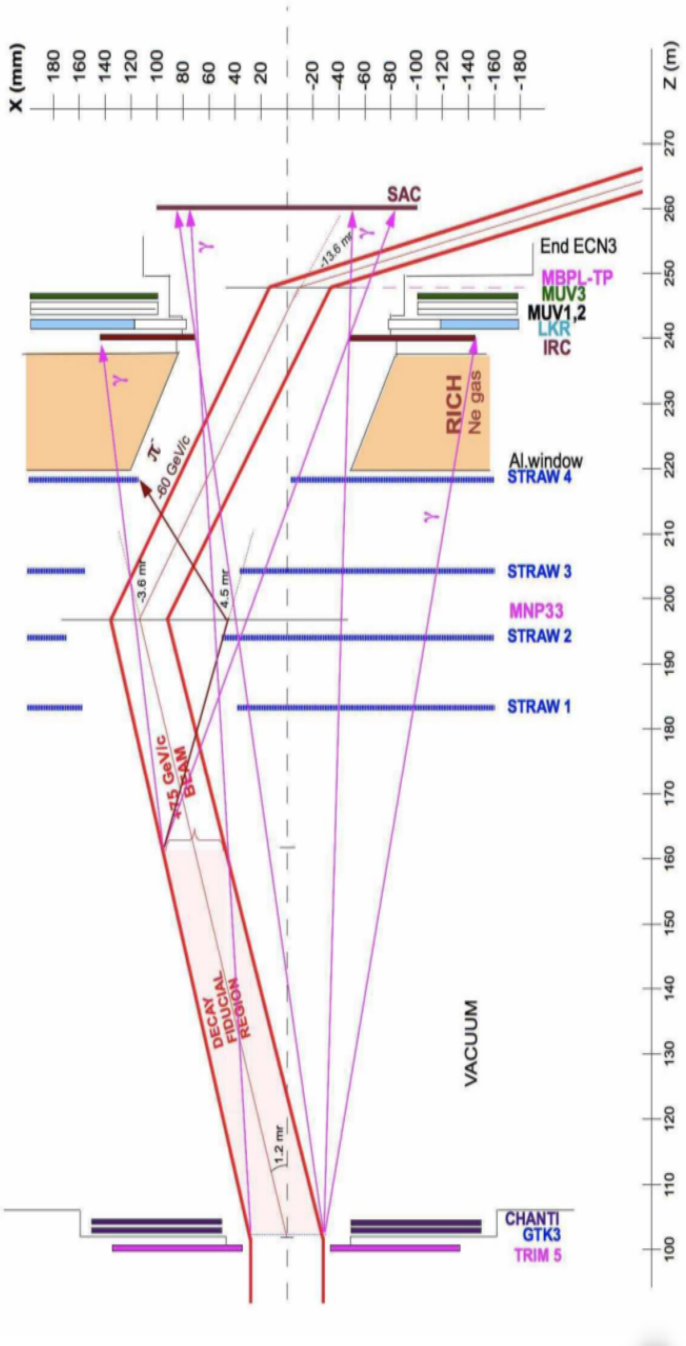

Figure 2.2: Schematic layout of the beam downstream the GigaTracker spectrometer. Shown is the angular deviation of the charged kaon beam and the 2σ width of the beam profile.

second achromat and the GigaTracker spectrometer, used to measure the beam momentum. The GigaTracker is composed of three stations of Silicon pixel detector, placed before, between and after two dipole magnets pairs. Just before the third station of the GigaTracker, the beam is bent of +1.2 mrad in the x-axis, to compensate the following bent of the MNP33 magnets of -3.6 mrad and to match the LKr calorimeter beam pipe hole (see Figure 2.2).

The region between the last station of the GigaTracker and the first station of the magnetic spectrometer define the decay volume. Almost 10% of kaons present in the beam decays inside this region.

The rest of the beam line is composed of the downstream part, mainly dedicated to detect the decay products. It goes from the first station of the magnetic spectrometer till the muon veto detector. Between the first two and the last two STRAW chambers a dipole magnet is installed to measure downstream charged particles momenta.
At the end of the experimental hall the beam is deflected by +21.6 mrad to avoid the small calorimeter(SAC) placed to detect photons emitted at low angle.

2.3 The detector layout

The NA62 experimental setup is shown in Figure 2.3. The setup can be divided in four different sub-systems: the tracking system, the particle identification system, the photon veto system and the muon veto system. The experiment needs tracking detectors for both K^+ and downstream particles, a calorimeter system to detect photons and to identify positrons,pions and muons and a particle identification system to identify the incident kaons and to distinguish between the different type of downstream particles, mainly pions, muons and positrons. To reduce the fraction of particles escaping detection the detectors have a cylindrical geometry around the beam axis, while to reduce possible effects due to multiple scattering in trackers, detectors with low material budget have been designed. Following breaks in the vacuum to accommodate some of the beam line elements, the beam spectrometer GTK and all detectors surrounding the decay region as well as the spectrometer detecting the final-state particles are placed in vacuum to avoid interactions and scattering of the beam, that can mimic the $K^+ \to \pi^+\nu\bar{\nu}$ and rare decays signals.

To match the incoming K^+ crossing the GTK with a rate of $\sim$ 750 MHz to the daughter particles, an excellent timing performance of the detectors dedicated to the K^+ identification (KTAG) and tracking (GTK) and to the π^+ identification (RICH) and tracking (STRAW), at the level of 100-150 ps, is needed. Without this precise timing, an accidental beam particle can be mistaken for the decaying kaon and wrongly asso-

ciated to the decay products. With the quoted time resolution the wrong association is kept at 1% level and the required background rejection level is satisfied.

The tracking system is composed of two detectors: the GigaTracker spectrometer(GTK), to track beam particles and the STRAW spectrometer to track downstream particles. The spatial matching between the K^+ track, extrapolated to the fiducial region and the downstream tracks, extrapolated backward, allows rejection of events with a badly measured daughter particle direction as a consequence of a possible large angle scattering in the first straw chamber. The GTK and STRAW detectors are described in detail in Section 2.3.1.

The particle identification system is composed of a Cherenkov threshold detector (KTAG), operated to be blind to all particles but kaons of appropriated momentum and direction and a Ring Imaging Cherenkov (RICH) detector. In NA62, the positive identification of the K^+ is important because about 94% of the beam particles are not kaons. The KTAG is located upstream the GTK. With a time resolution of about 100 ps, it can flag the kaon time window accurately and hence reject pion or proton beam-gas interactions, which could be misinterpreted as signal events. The KTAG will also improve the rejection of candidates originating from beam particles interactions in the last GTK station. The RICH is located after the last station of the STRAW spectrometer and it aims to distinguish between π, μ and e. The RICH has a remarkable timing properties: its time resolution is better than 100 ps and makes this detector ideal to measure the arrival time of downstream particles and to match them to the parent particle measured by the GTK. The particle identification system is described in Section 2.3.2

The photon-veto system is composed of three sub-detectors, covering a range of emission angles from 0 to 50 mrad with respect to the beam line. The sub-detectors involved are: a system of 12 Large Angle Veto (LAV) calorimeters covering an angle interval from 8.5 to 50 mrad, an electromagnetic calorimeter for the detection of photons, pions and leptons (μ, e) between 1 and 8.5 mrad (LKr), and two small-angle forward calorimeters covering the region below 1 mrad (IRC and SAC). The photon veto system requires an overall inefficiency of about 10^{-8} for the detection of at least one of the π^0 decay products. Given the detector design, only about 0.2% of the $K^+ \to \pi^+\pi^0$events have one photon from the π^0 going undetected. LAV, LKr, IRC and SAC are described in Section 2.3.3.

The muon veto system will be fundamental for guaranteeing background rejection of all kaon decays with muons in the final state, as the $K^+ \to \mu^+\nu_\mu$ decay, one of the main background source for the goal of the experiment, or to asses the presence of muons in the final state, as used in the analysis presented in this thesis. The system is composed of three stations, named MUV1, MUV2, and MUV3. The last station is

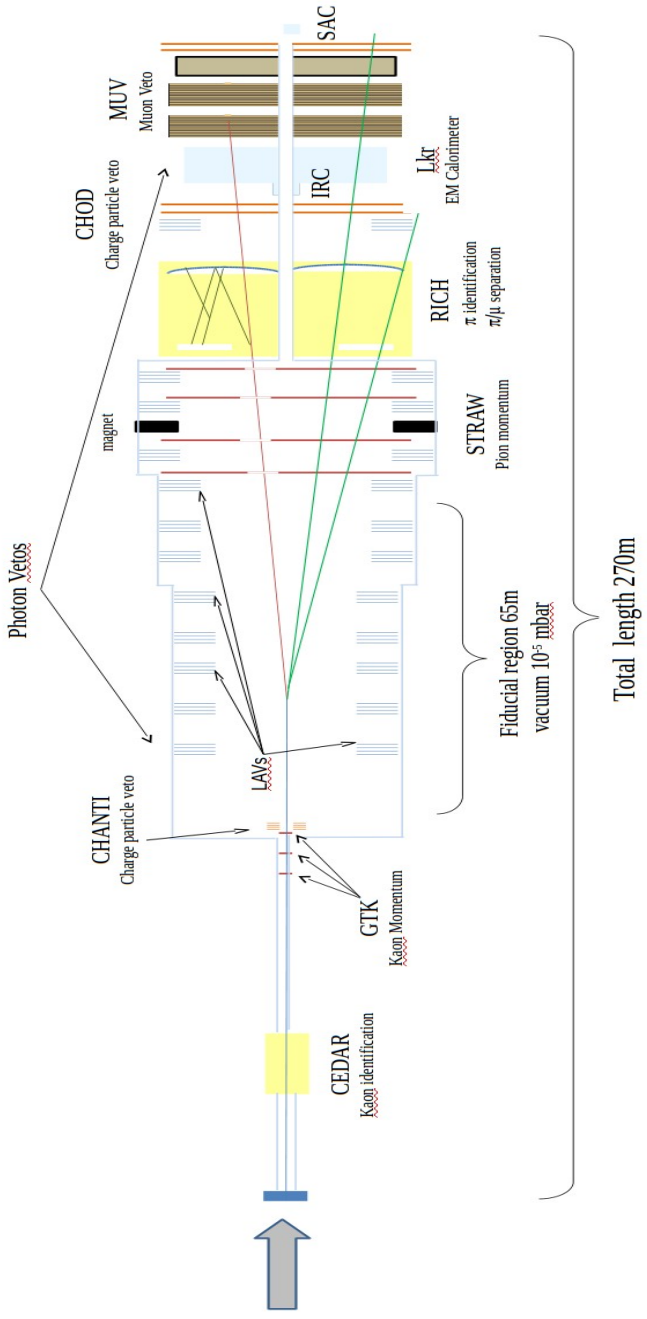

Figure 2.3: Schematic layout of the experiment setup.

used as a muon veto, while the first two are used as a hadronic calorimeter to measure the energy released by hadrons. The MUV system is described in Section 2.3.4.

Finally, two auxiliary detectors are present: a Charged HODoscope (CHOD) and a Charged ANTIcounter (CHANTI), described in Section 2.4.
The first is aimed at revealing the passage of charged particles. Since the 2016 two charged hodoscopes are present along the detector line: the NA48-CHOD and the CHOD. The two detectors are used in the trigger logic, in particular to provide a fast determination of the time and point of impact of charged particles. These information are useful to reject or to select events with more than one charged track at the first level of the trigger logic.
A charge particle veto, the CHANTI, will veto events with charged particles produced by beam particle inelastic interactions with the last GigaTracker station, muon halo close to the beam or events with additional charged particles in the final state produced upstream the fiducial volume. All these types of events might introduce a background to the $K^+ \to \pi^+ \nu\bar{\nu}$ signal.

The detectors are operated and interconnected by a high performance trigger and data acquisition system, described in Chapter 3.

2.3.1 The tracking system

The GigaTracker spectrometer

The beam spectrometer provides accurate measurements of momentum, time and direction of the incoming particles. It is placed in vacuum before the fiducial decay region and it is composed of three identical Silicon pixels stations installed around four dipole magnets arranged as an achromat as shown in Figure 2.4. This configuration allows to characterize the beam particles, in particular the vertical displacement of 60 mm of the central station is used to measure the momentum. It fits with the central value of the beam momentum and with the field strength of the magnets.

Assuming the veto inefficiency on π^0 to be of the order of 10^{-8} and the muon veto inefficiency at the level of 10^{-7}, the required level of background rejection (S/B$\geq$10 with a $K^+ \to \pi^+ \nu\bar{\nu}$ signal acceptance at the level of few %) can be achieved with a squared missing mass resolution of $(\Delta m)^2 \sim 8 \cdot 10^{-3} GeV^2/c^4$. The required squared missing mass resolution can be obtained if the GigaTracker provides a 0.2% rms momentum resolution and an angular resolution at the exit of the achromat of 16 μrad, to be combined with good performances of the downstream particles tracker (Section 2.9). In addition, to avoid the combinatorial background a hit time resolution of 200 ps is requested.

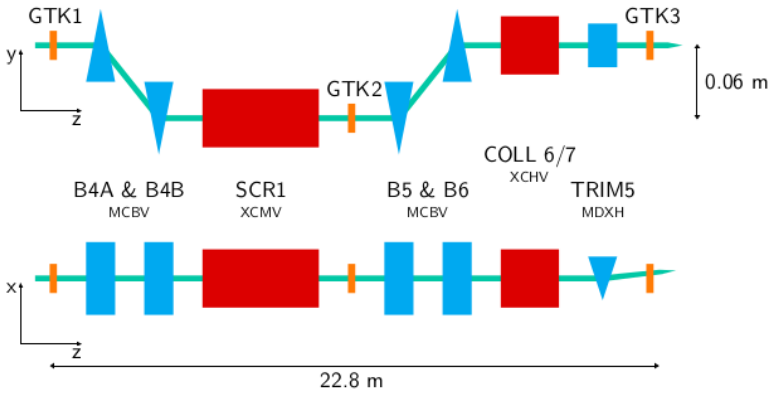

Figure 2.4: Layout of the GigaTracker detector within the achromat in the vertical(Y) and horizontal(X) views.The magnets B4A,B4B, B5 and B6 are standard dipoles. The SCR1 (scraper) is a toroidally-magnetized motorized collimator which, together with the the return yokes of the last two magnets(B5,B6) of the achromat, defocus μ^+ having a momentum <55 GeV/c, dispersed out of the 75 GeV/c parent π^+, K^+ beam. Moreover, the upper jaw of SRC1 blocks the undeviated muons, as the neutral (neutrons, K_L^0) or negatively-charged (π^-,K^-) tracks, ensuring that they are not transmitted to the end of the beam. The COLL6/7 is a 1 m long four-jaw motorized collimator. The TRIM5 is short dipole magnet that provides the final kick of 1.2 mrad in the x direction.

Each station is made of 18000 pixels of 300×300 μm^2 size arranged in a matrix of 200×90 pixels, corresponding to a total area of 62.8×27 mm^2. The matrix is read out by application-specific integrated circuits (ASIC) arranged in two rows of five chips each (Figure 2.5); each chip is composed of 40×45 pixels.

The most challenge aspects in building the GigaTracker were: the reduction of material budget, the improvement of time resolution and the radiation damage. The angular and momentum resolutions depend on pixel size, distance between stations and multiple Coulomb scattering (Eq. 4.1 and Eq. 4.4 respectively). For this reason a limit on the material budged for each station of 0.5 X_0 was chosen, corresponding to a maximum detector thickness in the active area of 500μm and a pixel size of 300μm was considered appropriated.

The sensors have been made from 200 μm thick wafers of $\geq$ 3 kΩcm resistivity silicon. The most probable signal yield is approximately 15000 electron-hole pairs (equivalent to 2.4 fC) for a 75 GeV/c beam particle crossing the silicon, which is sufficient to

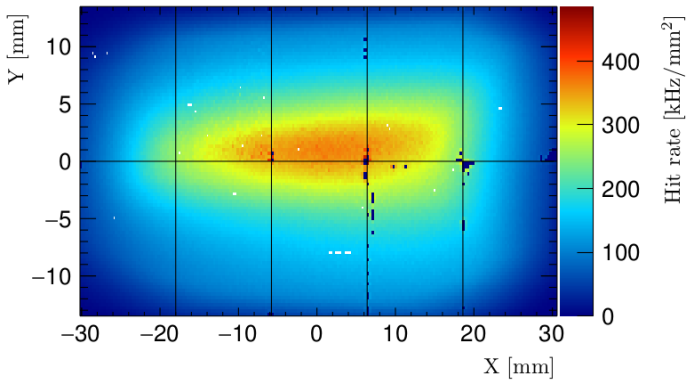

Figure 2.5: Illumination of one of the three GTK station operated in the beam at 35% of nominal intensity during the 2015 data taking. The two rows of five chips are well visible in the plot.

discriminate the physical signal from electronics noise, which is of the order of 0.04 fC [77]. Read-out chips (ROC) were thinned to 100 μm before bonding them to the sensors with SnAg bumps 10-15 μm high. A initial planar matrix of p-in-n pixel diodes has been chosen as the base configuration, although the front-end amplifier is bi-polar and n-in-p structures can also be handled.

$$\Delta x, \Delta y(\text{r.m.s.})(\text{mrad}) = [2(\sigma/22.8)^2 + \delta^2 + (13.2\delta/22.8)^2]^{1/2} =\sim 0.016 \text{ mrad} \tag{2.4}$$

$$\frac{\Delta p}{p}(\text{r.m.s.})(\%) =[\sigma^2 + (9.6\sigma/22.8)^2 + (13.2\sigma/22.8)^2 + (9.6 \times 13.2\delta/22.8)^2]^{1/2} \times 100/60 =\sim 0.22\% \tag{2.5}$$

$$\sigma(x, y) = \frac{0.3 \text{ mm}}{\sqrt{12}} \approx 0.087 \text{ mm} \tag{2.6}$$

where σ is the the spatial resolution of a single GTK station (2.6) and δ is the multiple scattering in a single GTK station. Considering that in case of nominal beam intensity

the detector is exposed to a beam rate of 750 MHz (see Table 2.1), a hit time resolution of 200 ps is mandatory to have a precise matching between kaon and downstream particles. Considerable effort has been invested to meet the design request [79].

Being exposed to a high particles rate, the radiation can damage the silicon sensor, introducing defects which can change the detector performance. Several precautions are taken in order to reduce the probability of radiation damages: cooling the detector, increasing the bias voltage and the replacement of damaged assemblies. The loosing of gain due to radiation damage is mitigated by using a cooling system which allows to operate at -15 °C (see Figure 2.6). A cooled fluid, single-phase C_6F_{14}, flows through 150 parallel micro-channels which act as heat exchangers [78]. Under these conditions and taking into account a nominal condition for the beam intensity, each station can be operated for more than 100 days without any significant degradation [2].

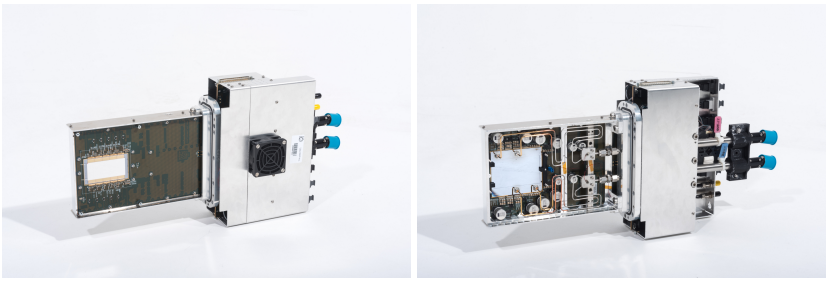

Figure 2.6: Photos of an assembled station seen from the sensor (right) and cooling side (left).

In 2015 the detectors installed were equipped with p-in-n sensor and the bias voltages were set and scanned in the range between 200 and 300 V [80], while since 2016 all sensor are n-in-p. In 2016 the bias voltages were set and scanned in the range between 100 and 300 V, while in 2017 were set and scanned between 100 and 200 V. The analysis of 2015 data showed a single pixel time resolution of 150 ps (Figure 2.7) in perfect agreement with the designed value; this is obtained applying two corrections to the raw time: a time offset correction and a time-walk correction [76] [79].

The impact of GTK performances on the analysis can be expressed by the improvement of the width (rms) of the $m^2_{miss} = (P_K - P_\pi)^2$ as a function of the pion mo-

[2]During the 2016 the beam intensity was $\sim$ 30% of the design value and the GTK was exposed to a particles rate of $\sim$225 MHz. In particular the sensor located in the third station was put in the place only for the last 60 days of the data taking, so it was possible to use it also during the 2017 data-taking, showing no degradation in terms of performance

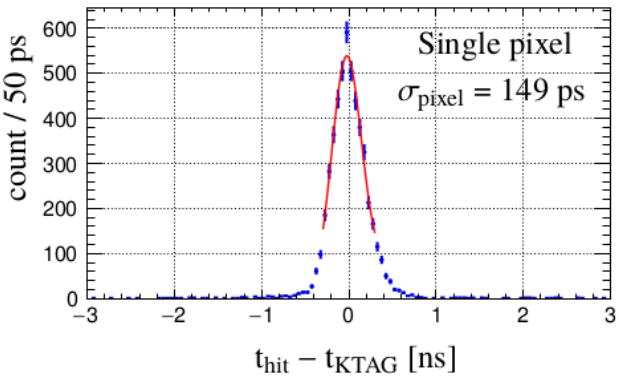

Figure 2.7: Time resolution of a single pixel. The time resolution is obtained by comparing the corrected hit time to the KTAG time, which has a resolution of 70 ps.

mentum for a selected $K^+ \to \pi^+\pi^0$ decays, where P_K is the kaon four momentum measured with the GigaTracker and P_π is the pion four momentum measured with the STRAW. As shown in Figure 2.8, using the measured kaon momentum instead of the nominal value, reduces the distribution width [76].

The STRAW spectrometer

The straw spectrometer provides measurements of momentum, time and direction of downstream particles emerging from K^+ decays. It is placed along $\sim$ 35 m after the fiducial decay region and consists of four chambers and a large aperture dipole magnet (MNP33). To minimize the probability of multiple scattering the detector has been made of ultra-light material, while it is installed in vacuum, to reduce particle interactions, which can affect the track momentum measurement and thus its resolution.

The magnet is installed after the first pair of chambers. It imposes a momentum kick of 270 MeV/c in the horizontal plane (x-z), corresponding to an integrated magnetic field of $\sim$0.36 Tm.
Each straw chamber is made of 1792 straw tubes arranged into two modules.
Each module contains two planes where the straw tubes have different orientation, called views. One module has the views measuring the X(0°) and Y(90°) coordinates and the other the U(45°) and V(-45°) (see Figure 2.9). Every view is composed of four layers of 112 straw tubes each, built as shown in Figure 2.10 and presents an empty region in the central part, allowing to have an hole in the final chamber of

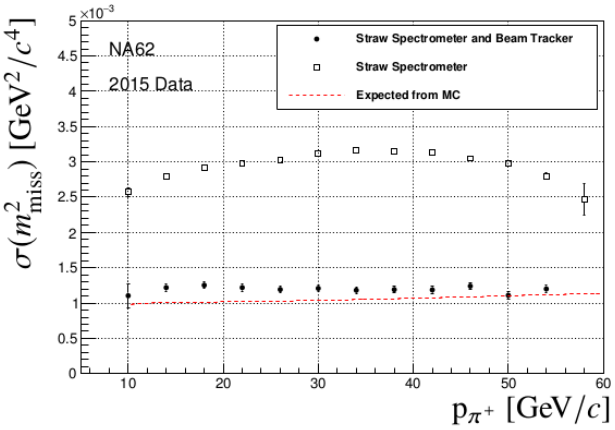

Figure 2.8: Standard deviation of m^2_{miss}, defined in (2.1) for a sample of $K^+ \to \pi^+\pi^0$ as a function of the pion mass. Dots correspond to the m^2_{miss} computed using the kaon momentum measured the the GTK. Squares correspond to the m^2_{miss} computed using the kaon nominal momentum and directions. The red dashed line corresponds to the expected m^2_{miss} resolution measured with a MC sample.

$\sim$12 cm for the beam passage. Such layout is needed for resolving reconstruction ambiguities [81]. The horizontal position of the hole in each chamber is defined by the nominal beam path. The active area of each chambers covers a diameter of $\sim$2.1 m.

For the physics performance required by the experiment, the STRAW detector has to satisfy the following specifications: a spatial resolution $\leq 130\mu$m; a material budget corresponding to $\leq 0.5\%$ of a radiation length for each station; a gas mixture of Argon (70%) + CO_2 (30%); For the straw tubes located close to the beam line, operation in a high rate environment (up to 40 kHz/cm, and up to 500 kHz/straw tube).
The calibration of the detector has been performed using reconstructed $K^+ \to \pi^+\pi^+\pi^-$. The reconstructed mass of three pions shown in Figure 2.11 is in agreement with the PDG kaon mass and the mass resolution is $\sim$ 0.9 MeV/c^2.

To achieve the requested level of background rejection using the m^2_{miss} kinematic variable, $\sim 10^4$, it follows that the track momentum resolution and angular resolution have to be better then 1% and $60\mu rad$, respectively. The evaluation of the performance of the straw chambers with the 2015 data is in agreement with the design specifications. The angular resolution decreases from 60 μrad for tracks at 10 GeV/c to 20 μrad for tracks at 20 GeV/c and the resulting track momentum resolution is consistent

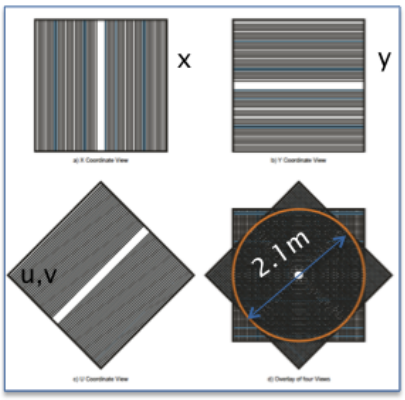

Figure 2.9: The drawing shows the views forming a straw chamber. Near the middle of each view a few straws are left out forming a free passage for the beam.

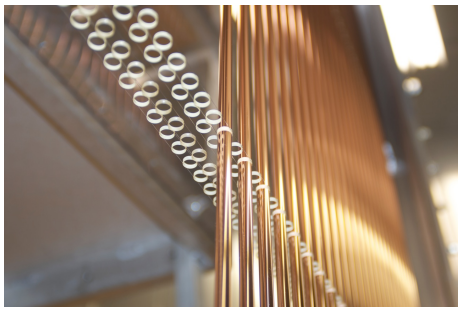

Figure 2.10: Straw tube layout in one of the four views.

with:

$$\frac{\sigma_P}{P} = 0.30\% \oplus 0.005\% \cdot P[GeV/c] \tag{2.7}$$

where the first term is due to effects of multiple scattering, while the second one is related to the spatial resolution [76].

2.3.2 Particle Identification system

The KTAG detector

The system devoted to tag kaons inside the beam is composed of two parts: the CEDAR and the KTAG. The CEDAR is a differential Cherenkov counter with achro-

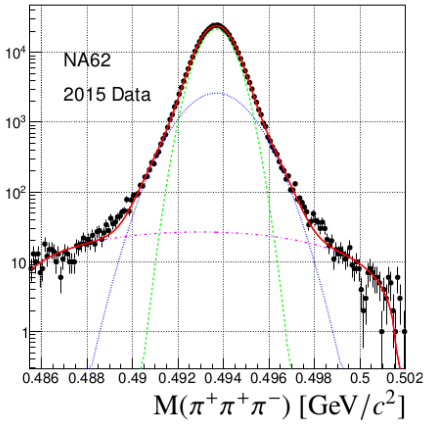

Figure 2.11: $K^+ \to \pi^+\pi^+\pi^-$ reconstructed invariant mass. The distribution is fitted by two Gaussian functions (dashed and dotted lines) describing the core and the tails and a polynomial (dash-dotted line) describing the combinatorial background.

matic ring focusing, filled with nitrogen gas (N_2). The sum of the gas in the CEDAR volume and the CEDAR window correspond to a total radiation length of $3.5\times10^{-2}X_0$. The detector has been build and used since many years to distinguish kaons, pions and protons in the unseparated beam provided by the CERN SPS. The CEDAR is built to be sensitive only to particles with fixed Cherenkov angle θ_c. Indeed only the light ring passing through a diaphragm of radius R=100 mm can be detected. According to the Eq. 2.8, the detector can be set to be sensitive to a specific particle type with mass m, in a monochromatic beam with momentum p, by tuning the pressure of the gas (thus the refractive index n)

$$cos\theta_c = \frac{1}{n\beta} = \frac{1}{n}\sqrt{1+\frac{m^2}{p^2}} \tag{2.8}$$

where β indicates the particle velocity in units of the speed of light c. It follows that, in order to maximize the kaon identification and being the center of the diaphragm fixed, the pressure operational value might be $\sim$1.75 bar at room temperature [3].

Due to the high kaon rate (45 MHz), to reach the required time resolution of $\sim$100ps, the CEDAR has been equipped with a new photon detector, called KTAG. The new light collector system is made of eight quartz windows located at the exit of the vessel, where the light is first focused; then the light is directed onto eight spherical mirrors. The mirrors reflect the light radially outwards into eight light boxes (referred to as

[3]The exact value of the gas pressure is set performing a pressure scan

sectors) as shown in Figure 2.12. Each sector is instrumented with 48 PMTs to collect the signal.

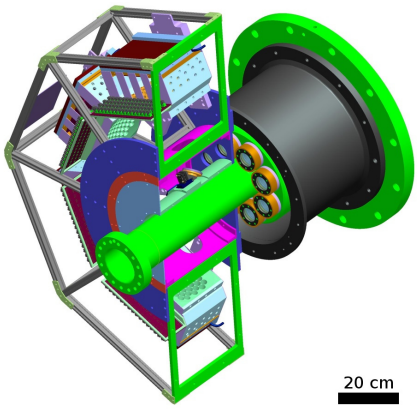

Figure 2.12: Drawing of the upstream part of the CEDAR and the KTAG.

The time resolution measured during the 2015 data taking was 300 ps for a single channel, while considering 20 PMTs signals detected on average per beam kaon, a time resolution of 70 ps is achieved. The KTAG kaon identification efficiency, requiring Cherenkov light in coincidence in at least 5 sectors, was estimated to be $>98\%$ (Figure 2.13) [76].

The RICH detector

The purpose of the RICH detector is to improve the charged particle identification and to assign a precise time information to that particle. The detector is made of a vessel 17 m long and 3.8 m in diameter, filled with Neon gas at atmospheric pressure (see Figure 2.14) and located after the last straw chamber.

The optics is composed of 18 hexagonal shape and two semihexagonal shape spherical mirrors, used to build the ring associated to the Cherenkov cone, produced by a particle traversing the gas. To avoid absorption of reflected light of the beam pipe, the central mirror is divided into two spherical surface one with the center of curvature on the left and one on the right of the beam pipe. The two semihexagonal mirrors are place close to the center and have a circular opening to accommodate the beam pipe (157

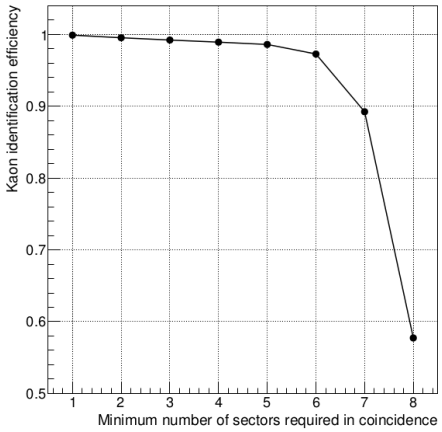

Figure 2.13: Kaon identification efficiency as a function of the minimum number of sectors required in coincidence.

mm in diameter). The two mirror surfaces are tilted at different angles respect to the vessel axis. This asymmetry is meant to improve light collection for positive charged particles, redirecting light into the central region of the PMT flanges.
The light produced is directed to two flanges located in the upstream part of the vessel. Each flange is composed of $\sim$1000 PMs, installed in an honeycomb structure with a photo sensor pitch of 18 mm. To improve light collection Winston cones have been machined in front of each PMTs. This granularity is a crucial parameter to optimize the angular resolution. By definition the radius produced at the PMT flanges is:

$$r = f tan\theta_c \tag{2.9}$$

where f = 17 m is the focal length of the mirrors and θ_c is the angle of the emitted Cherenkov cone. The angle θ_c depends on the particle mass, momentum and on the gas refractive index as shown by the relation in Eq. 2.10

$$cos\theta_c = \frac{1}{n\beta} = \frac{1}{n}\sqrt{1+\frac{m^2}{p^2}} \tag{2.10}$$

where β is the particle velocity in units of speed of light c. The detector is blind to particles with a momentum below the momentum threshold defined by the condition $cos\theta_c$=1. Since the Neon refraction index at atmospheric pressure is such that (n-1)$\sim$66$\times10^{-6}$, the momentum threshold for pions is $p^{\pi}_{th} = 12$ GeV/c. This limit the pion momentum to be p^{π} >15 GeV/c to have enough PMT to fit the ring. At fixed momentum the RICH response depends on the particle mass(Eq. 2.10), then considering that (n-1)$\ll$1 and m/p$\gg$1 the radius relation can be written in the following way:

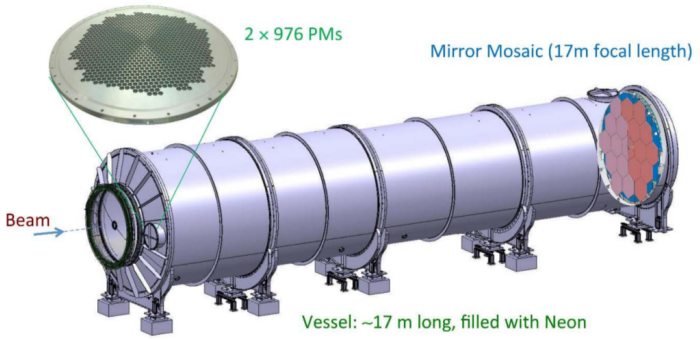

Figure 2.14: Sketch of the RICH detector. A zoom on one of the two disks accommodating the light collectors (PMTs) is visible in the left part, while the mirror mosaic is made visible in the neon vessel on the right part.

$$r = f tan\theta_c \sim f\theta_c \sim f\sqrt{2\left(1 - \frac{1}{n}\sqrt{1 + \frac{m^2}{p^2}}\right)} \tag{2.11}$$

From Eq. 4.6 a relation between the radius resolution and the mass resolution, as a function of momentum can be derived. This mean that exists an upper limit on the momentum for which the mass resolution is sufficient to well separate the particles.

$$\frac{\delta m}{m} \sim -\left[\frac{(n-1)p^2}{m^2} - \frac{1}{2}\right]\frac{\delta r}{r} \tag{2.12}$$

In particular in the NA62 RICH detector, given $\delta r/r \sim 2 - 3mm$, from (2.12), for p$\geq$35 GeV/c the probability of a μ being mis-identify as a π became higher than the maximum affordable value (10^{-2}), needed to match the desired sensitivity.

During the 2015 data taking the RICH time resolution was assessed to be 140 ps (Figure 2.15), in agreement with the request value by design (100-150 ps). Figure 2.16 shows the Cherenkov ring radius as a function of momentum with no selection on the particle type: electrons, muons, charged pions and scattered charged kaons can be clearly seen [76]. Using the data from the 2015 commissioning run, a muon rejection factor of 10^2, corresponding to a pion identification of 80% has been measured. The pion identification has been improved in 2016 and 2017, performing a mechanical mirror alignment.

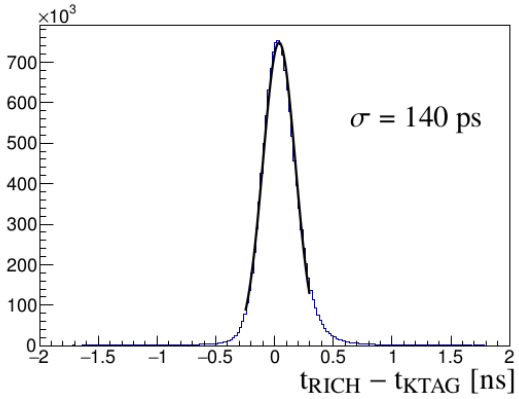

Figure 2.15: Time difference between the average time of a Cherenkov ring and the KTAG time. The width of the Gaussian fit is 140 ps, in agreement with the design request ($\sim$ 100 ps).

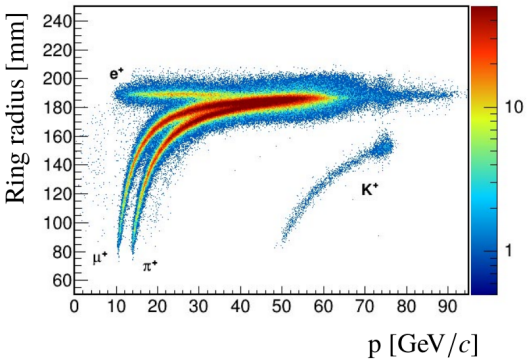

Figure 2.16: Cherenkov ring radius as a function of particle momentum; electrons, muons, charged pions and scattered beam kaons can be clearly seen. Particles with momentum higher than 75 GeV/c are due to halo muons.

2.3.3 Photon veto system

Large Angle Veto system

The Large Angle Veto (LAV) system is composed of 12 stations placed along the decay region. Each station operates in vacuum, but the last, which operates in air.
The stations are made of a circular crown of active material around the beam axis (see Figure 2.17) and are separated by a mutual distance varying between 6 and 12 meters, to obtain the required angular coverage, between 8 and 50 mrad for particles emitted in the fiducial volume. The LAV system mainly detects photons and electrons from kaon decays, pions through hadronic interaction in the material as well as muons in the beam halo. The system can operate with very low threshold, below or at the level of one minimum ionizing particle (MIP), in order to keep the detection efficiency for low energy photons as high as possible.

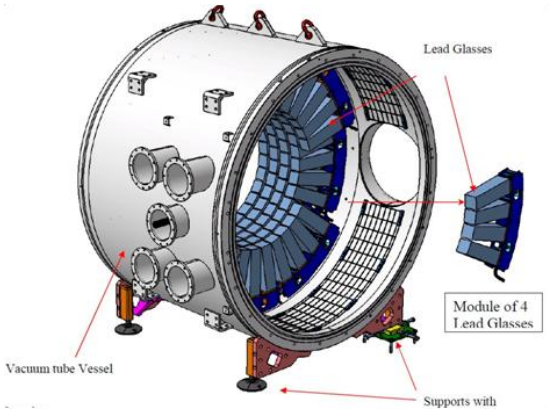

Figure 2.17: Sketch of a LAV station.

In particular, to provide the required background suppression against $K^+ \to \pi^+\pi^0$decays, the LAV system must provide:

- A photon inefficiency of 10^{-4} for photons with 50 MeV $\ll E_\gamma \ll$ 1GeV
- An energy resolution of 10% at 1GeV
- A time resolution of $\sim$1ns

Each LAV station is made of four or five rings of Cherenkov detector, formed by the lead glass counters recycled from the OPAL barrel calorimeter. In order to reach a

complete hermeticity and to ensure that at least three blocks are seen by a particle entering the LAV in the beam direction (corresponding to $\sim 20X_0$) the blocks in successive rings are staggered in azimuth and the number of rings in each station has been optimize. Each crystal has the shape of a truncated prism of lead glass, containing 74% of PbO, is covered by a Tyvek wrapping, and was already instrumented with PMT. At the major base, an optic light guide links the counter to the PMT, which converts the Cherenkov light produced by the passage of charged particles in an electric pulse. In general, a Cherenkov detectors makes use of the light produced when a charged particle passes through the material, but thanks to the high amount of lead, the lead glass blocks are able to efficiently detect photons. Since photons are neutral particles, the detection is done starting from the first e^+-e pair produced after the photon interaction in the counter and detects the charged component of the electromagnetic shower.

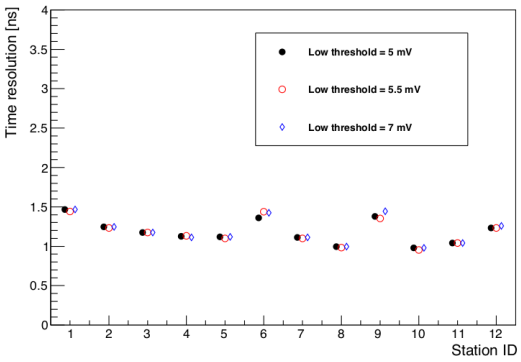

Figure 2.18: Time resolution for each LAV stations for a high threshold of 15 mV and three different values of the low threshold.

With 2015 data, and after the application of slewing corrections, time resolutions at the level of 1 ns are achieved for all LAV stations, as shown in Figure 2.18. Some difference from station to station is attributed to uncertainties in the determination of the channel-by-channel time offsets [76]. The measured time resolutions result in agreement with the design value.

Liquid Krypton Calorimeter

The Liquid Krypton calorimeter is a quasi-homogeneous calorimeter build for the NA48 experiment and reused in NA62 [82] [83]. The LKr is filled with liquid krypton kept at 121K $\pm 0.1\%$ by a cryogenic system. The energy response is linear within

0.2% in a the range 5-100 GeV, while the calorimeter length is 127 cm, corresponding to $27X_0$, so that showers up to 50-GeV are almost entirely contained in the detector. The cryostat has thickness of about $0.65X_0$ of passive material. As a result, $\sim$50 MeV are passively lost for the energy reconstruction of each particle. Photons of energy less than few hundreds MeV are reconstructed with significant inefficiency.
The sensitive area is divide in 13.248 cells with a cross section of 2×2 cm^2. The cells are formed by Cu-Be electrodes aligned along the longitudinal axis of the experiment, and have a zig-zag shape to avoid inefficiencies when a particle shower is very close to the anode (Figure 2.19).

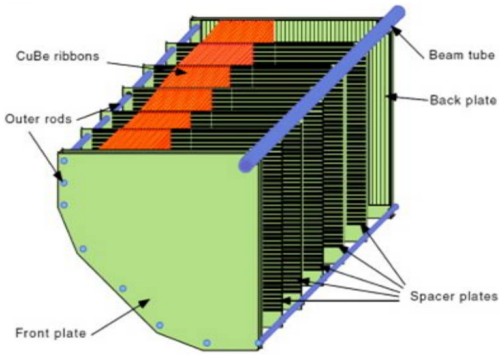

Figure 2.19: Section of LKr.

Thanks to the excellent uniformity of the medium and the fine granularity electrodes the detector has a good energy and position resolution. A first estimation of the energy resolution from simulated data is:

$$\frac{\sigma_E}{E} = \frac{4.8\%}{\sqrt{E}} \oplus \frac{11\%}{E} \oplus 0.9\% \tag{2.13}$$

where the energy is measured in GeV. The energy resolution is degraded respect to the NA48, due to the presence of non-linear energy response and due to additional material in the region upstream of the calorimeter. The expected time resolution is $\sim$ 500 ps; the one estimated using the 2015 data is 550 ps (Figure 2.20) in agreement with the expected value [76].

The LKr information can be use for electron and photon detection and contributes to pion and muon identification.

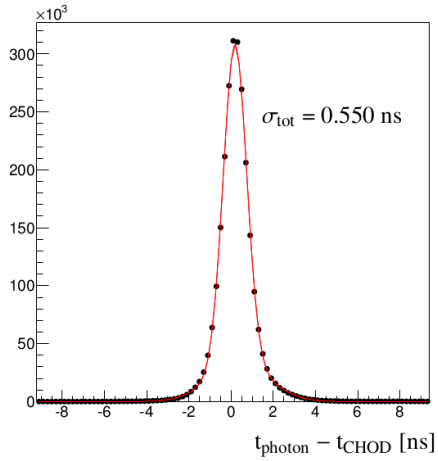

Figure 2.20: LKr time resolution, computed using a sample of $K^+ \to \pi^+\pi^0$. The plot shows the time difference between the closest photon time and the π^+ candidate time measured with the CHOD. The width of the distribution, from a Gaussian fit is 550 ps, in agreement with the expected value.

Small Angle Veto system

The small angle veto system is build to cover the small angle region near the beam pipe. The SAV is composed of two sub-detector: the Intermediate Ring Calorimeter (IRC) and the Small-Angle Calorimeter (SAC). Both detectors are aimed at detecting and vetoing photons with energies above 5 GeV, while being exposed to kaon products as well as to the muon beam halo and to neutral particles produced along the beam line. The two detector make use of the same technology; they are shashlyk calorimeters, with lead and plastic-scintillator plates traversed by wavelength shifting (WLS) fibers running along the beam direction. To guarantee a photon rejection inefficiency of the order of 10^{-4} the two detectors have a thickness $> 16\mathrm{X}_0$.
The IRC detector has a cylindrical shape and it is located around the beam pipe, just before the LKr. The outer radius of the IRC is centered at the Z-axis of the experiment while the inner radius is centered at the beam axis
The SAC operates in vacuum and is placed on a rail in an approximately 7-m long and 100-cm diameter vacuum tube. The detector is put at a small angle with respect to the X axis in order to avoid the possibility of a photon originating from the fiducial region to channel in a single fiber. Studies show that an angle of few mrads is enough to recover a high efficiency for photon detection.

2.3.4 Muon veto system

The muon veto system is composed of three sub-detectors called MUV1, MUV2 and MUV3 (see Figure 2.21). The MUV stations are placed at the end of the detector chain, being the muons the most penetrating particles; the firsts two work as hadronic calorimeters, while the MUV3, located after 80 cm thick iron wall, corresponding to 5 nuclear-interaction lengths, to ensure the passage of the only muons, is a fast muon veto used at the lowest trigger level as well as for offline muon identification.

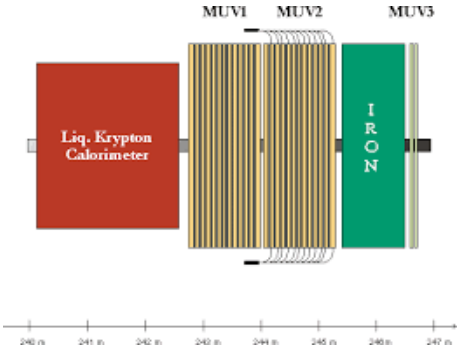

Figure 2.21: Scheme of the full calorimetric system, LKr, MUV1, MUv2 and MUV3.

The MUV1 and MUV2 detectors are sampling calorimeters, made from alternate layers of iron (25 for MUV1 and 23 for MUV2) and scintillators strips (24 for MUV1 and 22 for MUV2). In both modules the scintillator strips are alternately oriented in the horizontal and vertical directions.

With the 2015 data taking the time resolution for the two detectors, shown in Figure 2.22, has been measured to be $\sim$0.9 ns for muons, in agreement with what it was requested by design (1 ns) and the energy resolution was evaluated:

$$\frac{\sigma_E}{E} = 0.115 \oplus \frac{0.38}{\sqrt{E}} \oplus \frac{1.37}{E} \tag{2.14}$$

where E is in GeV (Figure 2.23) [76].

The MUV3 module consists of an array of 12$\times$12 scintillator tiles of 220$\times$220$\times$50 mm^3 size, installed over a surface of 2640$\times$2640 mm^2. Eight smaller tiles are mounted around the beam pipe.The PMTs used for the MUV3 readout are positioned about 20 cm downstream, in a light-tight box. This geometry reduces to below 250 ps the time

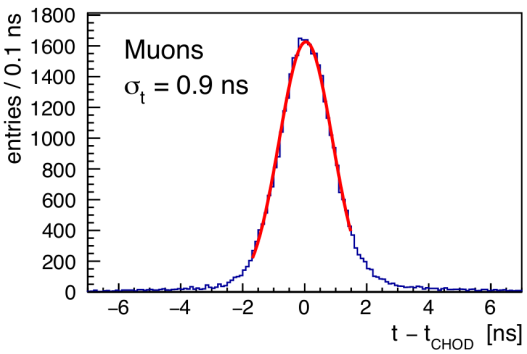

Figure 2.22: MUV1 and MUV2 time resolution for muons selected form $K^+ \to \mu^+\nu$ decays with respect to the CHOD reference time.

jitter caused by different paths of photons from particles hitting different parts of the scintillator tile. Each tile is read out by two PMTs and the coincidence of the two PMT signals is used for timing purposes.

The signal time resolution in individual channels measured with the 2015 data was in the 0.4-0.6ns range in agreement with the design value. MUV3 muon identification efficiency was measured in 2015 using a sample of beam halo muons to be >99.5% for muons with momenta above 15 GeV/c (Figure 2.24) [76].

2.4 Auxiliary detectors

2.4.1 Charged HODoscope

The Charge HODoscope (CHOD) aims at revealing the passage of charged particles at the entrance of the LKr. Since the 2016 two charged hodoscopes are present along the detector line: the NA48-CHOD and the CHOD. The two detectors are used in the trigger logic, in particular to provide a fast determination of the time and point of impact of charged particles. These information are useful to reject or to select events with more than one charged track at the first level of the trigger logic.

The NA48-CHOD, as its name suggests, is reused form the NA48 experiment and it is made of two planes of scintillator slabs, oriented along the horizontal and vertical direction, respectively. Each slab is read out at one end by a photomultiplier. Two independent time measurements are provided by the NA48-CHOD for each charged

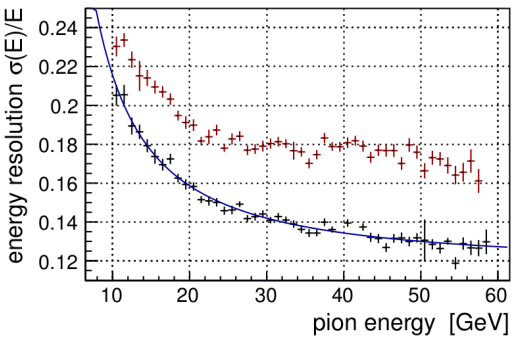

Figure 2.23: Energy resolution of MUV1 and MUV2 before correction (red crosses) and after correction (black crosses). The line represents the paramatrization of the energy resolution given in Eq. 2.14.

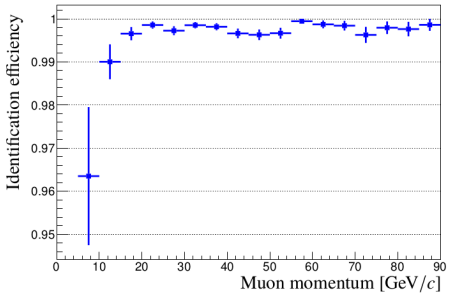

Figure 2.24: MUV3 muon identification efficiency, measured from beam halo muons as a function of momentum.

particle crossing a vertical and a horizontal slab, which reduces the possible tails in the event time distribution due to out-of-time accidental activity, interactions in the upstream material and back-scattering from the LKr calorimeter.
The NA48-CHOD track signal is defined as the coincidence of hits in one vertical and one horizontal counter within a predefined time window. The signal time is the mean time of two hits. The analysis of the data collected in 2015 showed a time resolution of 210 ps, in agreement with the performance measured in the NA48 experiment and with the NA62 requirements.

The CHOD is a new detector made of 152 plastic scintillator tiles. The scintillation light is collected and transmitted by wavelength shifting fibers, and is detected by silicon photomultipliers (SiPMs). The CHOD time resolution is of $\mathcal{O}(1ns)$ and the

detection efficiency, measured with a muon sample from the $K^+ \to \mu^+\nu$ is above 99%. In particular the time resolution measured in 2017, when the new constant fraction discriminators (CFDs) have been installed, improved with respect to the 2016 situation, passing from 1.1ns to 0.76 ns.

2.4.2 CHarged ANTIcounter

As already mentioned, the CHarged Anticounter, CHANTI, will veto events with charged particles produced by beam particle inelastic interactions with the last GigaTracker station, muon halo close to the beam or events with additional charged particles in the final state produced upstream the fiducial volume. All these types of events might introduce a background to the signal identification.

It is composed of six square hodoscope stations 300×300 mm^2 in cross section with a 95×65 mm^2 hole in the centre to leave room for the beam. Each station is separated from the next one in such a way that the the angular region between ∼50 mrad and ∼1.35 rad is covered hermetically for particles generated on GTK3. The stations are made of scintillator bars of triangular cross section readout with fast wavelength-shifting (WLS) fibers coupled to silicon photomultipliers (SiPMs).

During the 2015 commissioning run the CHANTI detection efficiency has been measured, using a muon beam, showing an uniform efficiency above 99% in all stations. The time resolution has also been measured being 830 ps, adequate to keep the random veto probability to an acceptable level of a few percent.

2.5 Conclusion

The NA62 experiment has been built to measure the $K^+ \to \pi^+\nu\bar{\nu}$ branching ratio with 10% precision thus it is optimized to detect K^+ decays with a single positive charged track in the final state. Nevertheless all other kaon decay measurements and searches take advantage of the detectors performances (time resolution, detection efficiency) and of the high statistics that NA62 can achieve. The excellent time resolution is fundamental to match the kaon beam with downstream particles while the high detection efficiency of the particle identification system ($\mathcal{O}(10^{-7})$) and of the photons veto system ($\mathcal{O}(10^{-8})$ for single photon detection) are essential to select the proper event and control the background.

The analysis presented in this thesis exploits the information from most of the detectors: KTAG to be sure that a kaon is present in the event, STRAW to measure tracks

momenta, LKr and MUV and RICH, for particle identification. Due to a close kinematic of the decay the identification of the three particles allows fully reconstruction of the event at the vertex position: momentum and mass of the parent particle. For this reason the use of the GTK is not mandatory but could help to improve the background rejection, for example it can be use to improve the resolution of the vertex position, as described in Chapter 4 , or it can be use to reduced possible wrong downstream tracks association to the event, checking that each downstream track is within a defined time window with respect to the selected GigaTracker track.

Chapter 3

The NA62 trigger scheme

The task of a trigger system is to select rare events and to suppress background and non-interesting events as efficiently as possible. As any other selection, trigger systems introduce a bias, i.e. select or reject more efficiently certain classes of events with respect to other competitive processes. The best condition for an experiment being completely flexible in term of analysis program and unbiased, is to use a trigger-less acquisition system, which means taking all data. In real life this choice is not feasible because high energy particle experiments are exposed to high particle rates which don't match the limited bandwidth allowed by the data acquisition system and the storage system. Also, in general, not all events are of interest. The trigger purpose is to make possible the data acquisition of interesting events, defining the trigger acceptance or rejection on the basis of event topology (multiplicity, direction of particles), particle type, energy deposition, decay point (vertex), etc. [85].

HEP experiments rely on complex multilevel trigger systems: the lower level trigger systems is typically built in custom hardware using fast and non processed information coming directly from different detectors. The higher trigger levels consist of software performing partial or complete event reconstruction which allows the application of decision algorithms. Within each level the trigger signals produced by various detectors are combined into logical expressions, using Boolean algebra (AND,OR,NOT) and the resulting outputs from several levels are combined into a trigger chain, called *mask* at NA62.

At NA62 an *event* is a decay of a beam particle within the fiducial volume of the detector and it is accepted if it fulfills at least one mask.

The filtering done at the trigger level is not always enough to reduce the rate of events at an acceptable level, in these cases the mask can be scaled down by a *downscaling factor* D, such that on average only every D-th selected event is kept by the system [86].

The first part of this chapter is focused on the description of the NA62 trigger scheme. NA62 is exposed to a particle flux of 750 MHz in the upstream region and an event rate in the downstream region of $\sim$12 MHz, due to beam particles decays, mainly K^+ and π^+ [1], while the maximum output trigger rate is 10KHz, dictated by costs, technology, performance issues and available bandwidth for data-storage to disk. During the 2016 and 2017 data taking several masks where setup in order to cover a wide physics program.

The second part of this chapter is dedicated to the study of the trigger efficiency. The knowledge of the trigger efficiency is essential for the $K \to \pi\mu e$ analysis since it impacts the final result on the branching ratios. Indeed the computation of the branching ratio is strongly related to the data sample size, i.e. the number of kaons (N_K) collected and this number is affected by the trigger efficiency. For example N_K can be written as:

$$N_K = \frac{N_X}{Br(X) \cdot A_X \cdot \epsilon} \tag{3.1}$$

where $Br(X)$ is the branching ratio of the kaon decay X, used to compute the kaon flux, A_X is the corresponding selection acceptance, N_X is the number of events passing the selection and ϵ is the trigger efficiency.

In the analysis presented in this work, data collected with three trigger masks aiming to select events with multiple tracks in the final state have been used. The study of the trigger efficiency of those trigger masks has been performed offline. It is quite challenging: it cannot be performed with MC samples, as the primitive and algorithm conditions cannot be perfectly reproduced and at the same time there are no kaon decays that can be selected in data fully compatible with the signal channels and with a branching ratio such that there is enough statistics to measure the trigger efficiency. Nevertheless, thanks to the similar kinematics to $K \to \pi\mu e$, the K3π decay is a good way to study the trigger efficiency for most of the primitives and algorithms used to built the three masks. All the details of the study are presented in the second part of this chapter.

[1] These values refer to a data taking at the nominal beam intensity. In the specific $\sim$5 MHz are due to kaons decays and $\sim$7 MHz are due to pions decays

3.1 Logic levels and requirements of the trigger scheme

The NA62 experiment has adopted a trigger made of three logic levels, whose purpose is to reduce the rate of events from ∼10 MHz to 10 KHz, with a reduction factor of ten at each step [75].
The lowest-level trigger is a hardware trigger called Level 0 (L0). It is based on the output of few sub-detectors, those with a fast signal response and a good time resolution: RICH, NA48-CHOD, CHOD and MUV3. If a positive L0 is issued, then data is read-out from the front-end electronics buffers of each detector in a specific time window and sent to dedicated PCs, where a Level 1 trigger (L1) is implemented in software. At this level only the information from some detectors are checked. If the event passes the L1 request then the event is sent to event-builder PCs where a software-based Level 2 trigger (L2) is implemented. It handles the information coming from all detectors to make additional cuts [75, 87]. Events passing the final selection are stored on the Central Data Recorder (CDR).The overall trigger scheme of NA62 and the relevant trigger rates and connections are shown in Figure 3.1

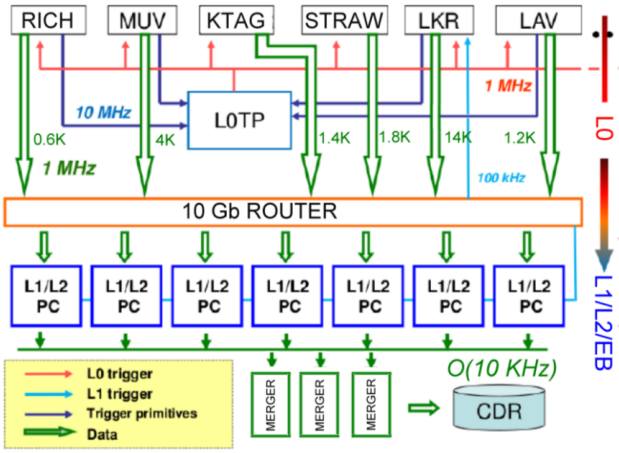

Figure 3.1: Overall trigger scheme of NA62 the relevant trigger rates and connections. For simplicity only few detectors are displayed [75].

During 2016 and 2017 data taking the beam intensity was lower with respect to the nominal intensity: it was 30% - 40% of the nominal intensity in 2016 and around 60% in 2017. In these conditions the average output rate at L0 was ∼2M triggers per burst

and the average L1 output rate was ∼240k triggers per burst. As described in Section 2, the NA62 beam is carried in bursts (also called spills) which have an effective length of ∼3.3 s. Then the trigger rates mentioned above translante in ∼600kHz at L0 and ∼70kHz at L1, being well below the maximum allowed rate (1 MHz for the L0 and 100 kHz for the L1).

The rates are mainly dominated by the mask dedicated to $K^+ \to \pi^+\nu\bar{\nu}$ analysis, as can be seen in Table 3.1 and Table 3.2, where all implemented masks are listed with the corresponding L0 conditions and downscaling factor.

For the L2 trigger, during the 2016 and 2017 data taking it simply builds the event merging the information from all detectors after L0 and L1 trigger selections. Indeed since the beam intensity was not the nominal one the L1 output trigger rate was at a reasonable level, allowing not to use the L2 trigger and avoiding the injection of additional biases and inefficiencies.

The trigger masks called *Multi-Track*, *Muon Multi-Track* and *Electron Multi-Track* reported in Table 3.1 and Table 3.2 have been used to collect data for the $K \to \pi\mu e$ analysis. An other important trigger mask is the *Control*, used to performed the study on the L0 trigger efficiency.

3.1.1 Timing and trigger distribution

The clock reference for time measurements is generated by a high-quality clock generator located in the experimental area, with a frequency of 40.079 MHz, free running and with high accuracy and stability. Despite what happens in colliders, at fixed target experiments the beam particles last for a few seconds long *spill* (or *burst*).The duration of each spill is approximately 6 seconds, while the inter-burst period between two consecutive extractions is around 10 seconds. The burst is delimited by a Start of Burst (SOB) signal which is delivered by the SPS one second before the actual extraction of the beam, and by an End Of Burst (EOB), delivered ∼0.5 seconds after the end of the particle extraction. A dedicated system is used for encoding and delivering both the clock and the trigger data to the read-out systems of the experiment. The fundamental unit of time is the inverse of the clock frequency: 24.950741 ns, namely *time-stamp*. The time information coming from any individual channel is given with this unit of time. The counting of time-stamp starts at each burst with the SOB, thus any event within a burst is uniquely identified by a time-stamp. The upper 24 bit of the time-stamp (Primitive timestamp high), corresponds to 6.4 μs which defined the time unit with which primitives are sent to the L0 trigger processor. For a better time resolution the first 8 bits of the primitive are dedicated to time information, corresponding to a time unit of 97.466 ps (*fine time*, *Timestamp low*).

Mask Name	L0 Condition	Triggers/Burst	Downscaling
Pinunu	RICH×Q1×!Qx×!M1×!LAV12×!E20	1.2M	1
Di-Muon	RICH×Qx×MO2	0.2M	1
Di-Muon exotics	RICH×Q2×!E20	0.3M	1
Electron Multi-Track	RICH×QX×E20	0.35M	2
Muon Multi-Track	RICH×QX×MO1	0.15M	5
Multi-Track	RICH×QX	0.05M	50
Muon exotics	RICH×Q2×MO1	0.15M	10
Non-Muon	RICH×Q1×!M1	0.02M	200
Control	CHOD	0.06M	400
Total		∼2.5M	

Table 3.1: L0 triggers and downscalings for each mask present during the 2016 data taking. The number of triggers/burst quoted in the second column is already divided by the corresponding downscaling factor. The definition of each primitive is in Table 3.3

Mask Name	L0 Condition	Triggers/Burst	Downscaling
Pinunu	RICH×Q1×!Qx×!M1×!LAV12×!E20	1.35M	1
Di-Muon	RICH×Qx×MO2	0.15M	2
Electron Multi-Track	RICH×QX×E20	0.18M	8
Muon Multi-Track	RICH×QX×MO1×E10	0.04M	10
Multi-Track	RICH×QX	0.35M	100
Muon exotics	RICH×Q2×MO1	0.13M	5
Neutrino	RICH×Q1×!Q2×MOQX	0.008M	20
Non-Muon	RICH×Q1×!M1	0.03M	200
Control	CHOD	0.09M	400
Total		∼2.2M	

Table 3.2: L0 triggers and downscalings for each mask present during the 2017 data taking. The number of triggers/burst quoted in the second column is already divided by the corresponding downscaling factor. The definition of each primitive is in Table 3.4

3.1.2 L0 hardware trigger

The L0 hardware trigger filters events based mainly on inputs coming from a small set of fast sub-detectors. The maximum output rate of the Level 0 trigger is 1 MHz with a maximum latency of 1 ms. Each sub-detector elaborates the data received and when a given set of conditions are met, 32-bit words, called primitives, are generated. A variable number of L0 Trigger Primitives are merged into a single Multi-Trigger Packet(MTP) sent to the L0 Trigger Processor (L0TP). The number of primitives in any MTP can vary between 1 and an agreed (programmable) maximum (MTP packing factor), can be different from one MTP to the next, and can also be different for different sub-detectors. The MTP format is represented in Figure 3.2. First 64 bits are

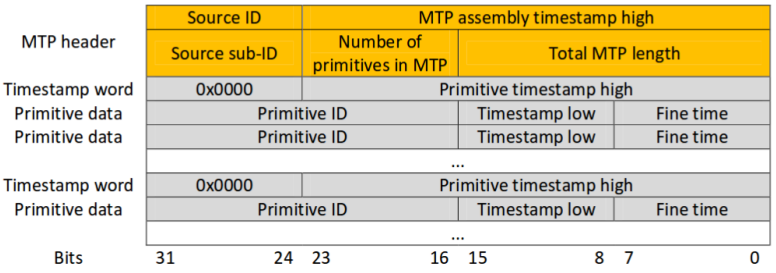

Figure 3.2: Multi-Trigger Packet format. [75].

the *MTP header*, where some general information are located. *Source ID* is a 8-bit identifier for the detector or sub-system which generates data. *MTP timestamp* is the detector time in unit of 25 ns, indicating when the packet has been delivered by the front-end TDAQ boards (TEL62 boards). It can be used for debug purpose, monitoring the delay between the generation of the primitive data and their delivering. *Source Sub ID* is an identifier of the individual DAQ board (or part of it) within a detector or sub-system generating the data. *Number of Primitives in MTP* is the number of primitives encapsulated in the packet. *Total MTP* length is the total length of the MTP in bytes, including the header. After the 64-bit header, data are divided in two parts. A first part consists of the *Primitive ID* which identifies the conditions satisfied by the event, and the *fine time* which represents a more precise measurement of the event time. Finally the field *Timestamp* contains the number of 40 MHz counts at which the present primitive occurred. MTP packets are sent periodically, even in case of zero primitives, the default period being 6.4 μs (*frame*).

Primitives are sent via Ethernet link to the level zero trigger processor (L0TP) responsible for the L0 trigger decision [88]. The L0TP has been designed to check if

primitives, generated asynchronously by detectors, are aligned in time. It compares the primitives to a defined series of trigger configurations (masks). If for a given timestamp the primitives match a mask, the trigger is validated and a trigger signal is sent to all detectors. Detectors contributing to the L0 trigger are: NA48-CHOD, CHOD, RICH, LKr, LAV, MUV3. The conditions used to make decisions are based on calorimetric energy (LKr) and number of cluster or hits in all mentioned detectors, eventually checking the geometric position of those clusters/hits. The definition of clusters or hits depends on the specific detector. In what follows, a simple description of the L0 trigger conditions are reviewed.

- **NA48-CHOD**. It allows the selection of events with at least one charged particle. A hit is defined by a pair of signals occurring in time and space coincidence between the horizontal and vertical planes. Hit multiplicity might be used to select or reject events with multiple charged particles.
- **CHOD**. As the NA48-CHOD it tags events with charged particle within the detector acceptance, based on hit multiplicity after time clustering. Several conditions can be implemented depending on clusters positions.
- **RICH**. It produces positive primitives for any charged track above Cerenkov threshold, based on hit multiplicity after time clustering. A cluster is defined as a group of hits belonging to the same Cerenkov ring, within a certain time window.
- **LAV12**. It tags events with photons mainly from $K^+ \to \pi^+\pi^0$or muon from the beam halo, checking if there are hits within a certain time window.
- **MUV3**. Its main purpose is to veto events with muons and the muon halo components from π and K decays upstream the final collimator. The conditions implemented are based on tiles coincidences. The MUV3 can produce also positive primitives to trigger events with muons in the final state, distinguishing also between events with one or more tiles crossed. The MUV3 trigger primitives can be built checking the following conditions:
  - tight: hit is produced when two signals arrive in the same tile within a certain time window;
  - loose: if two signals are further apart the coincidence window. Usually loose hits are due to inefficiency and/or noise;
  - inner: if the signal is in the 8 central tiles
  - outer: if the signal is not in the 8 central tiles.

  The implementation of the last condition is important for events with multiple muons, since muons not related to kaons decays hit mainly the inner part of the

detector. Almost half of the multi-muon event rate is due to accidental coincidences between unrelated muons. At the nominal beam intensity the expected multi-muon event rate is 1.1 MHz and $\sim$55% of that is due to accidental coincidences between unrelated muons. Considering only muons in the outer tiles reduces the event rate of a factor 2.

- **Calorimeter**. It retrieves energy information from the electromagnetic (LKr+IRC +SAC) and hadronic (MUV1+MUV2) calorimeters. It is used in positive mode for particles identification based on energy deposits. The calorimeter system can be used also as veto, providing primitives based on cluster multiplicity. Cluster search is performed in parallel for each of the sub-detectors.

Some available L0 primitives are summarized in Table 3.3 and Table 3.4 for 2016 and 2017 data taking respectively. The whole list can be found in [76].

Data from all sub-detectors are stored in front-end buffers during L0 trigger evaluation. Upon reception of a positive L0 trigger, most sub-detectors will send their data to dedicated PCs within an adequate time window (frame) around a L0 timestamp. As explained, the frame period is 6.4 μs. The type and amount of data it contains may be different for different trigger types; a data frame may even be empty or indicate an error. No sub-detector may ignore a L0 trigger. Exceptions are the GTK readout system and the CREAM system used for calorimeters [84]. Due to a large data fluxes the GTK and CREAM systems save data into local temporary buffers upon reception of a L0 trigger, but actual readout happens only after the reception of the L1 trigger at a lower rate.
An additional feature of the L0TP is the possible request of a downscaling factor for each mask. If the downscaling factor (D_s) is equal to 1 the L0TP sends the trigger signal every time the corresponding mask is validated, otherwise it sends the signal just one time out of D_s. The use of downscaling factors is driven by the presence of several trigger masks, set to differentiate as much as possible the physics program of the experiment, and at the same time by the limited available bandwidth and storage space.

3.1.3 L1 software trigger

The L1 trigger reduces the data rate by a factor of 10, from 1 MHz to 100 kHz, processing the data with simple algorithms, using the full data stream information from some sub-detectors to reconstruct complicated objects, as tracks. The following L1 trigger algorithms were deployed since 2016 and were applied one after the other depending on the specific trigger mask.

Detector	Name	Description
NA48 CHOD	CONTROL	at least one coincidence between the horizontal and vertical slabs
RICH	RICH	clusters of at least 3 hits in time
CHOD	Q_1	at least one cluster in any quadrants
	Q_2	at least two cluster in any quadrants
	Q_x	at least one cluster in two diagonally-opposite quadrants
LAV	LAV12	at least one hit in time in LAV12
LKr	E20	total energy above 20 GeV
MUV3	M1	at least one signal
	M2	at least two signals
	MO1	at least one signal in the outer tiles
	MO2	at least two signals in the outer tiles

Table 3.3: Summary of some L0 primitives available during 2016 data taking.

Detector	Name	Description
NA48 CHOD	CONTROL	at least one coincidence between the horizontal and vertical slabs
RICH	RICH	clusters of at least 3 hits in time
CHOD	Q_1	one or more cluster in any of the four quadrants
	Q_2	at least two clusters in any of the four quadrants
	Q_x	at least two clusters in two diagonally-opposite quadrants
LAV	LAV12	at least one hit in time in LAV12
LKr	E10	total energy above 10 GeV
LKr	E20	total energy above 20 GeV
MUV3	M1	at least one signal
	M2	at least two signals
	MO1	at least one signal in the outer tiles
	MO2	at least two signals in the outer tiles
	MOQX	coincidence of signals in outer tiles of at least one pair of opposing quadrants

Table 3.4: Summary of some L0 primitives available during 2017 data taking.

- **KTAG**. The KTAG L1 can be used in positive or negative mode. It uses the KTAG sector-multiplicity to positively identify a beam kaon. The algorithm requires minimum five sectors in coincidence and in time with the L0 trigger.

- **LAV**. The LAV L1 algorithm selects events with at least 3 hits in $\pm$ 10ns time window compared to the L0 trigger time. The algorithm is used as veto, to reduce the background due to $K^+ \to \pi^+\pi^0$.
  During the 2016 and 2017 data taking the algorithm was used in veto mode.

- **STRAW**: Two L1 algorithms exist:

  - Pinunu: select at least a reconstructed track with a momentum P_x <50 GeV/c and reconstruct the vertex using the CDA[2] method, asking a vertex position between -100 m and 180 m and a CDA<20cm with respect to the beam axis. It is used for the $K^+ \to \pi^+\nu\bar{\nu}$ trigger mask or for any single-track selection.
  - Exotics: select at least a reconstructed negative track and reconstruct the vertex, using the cda method, asking a vertex position between -100 m and 180 m and a cda<20cm with respect to the beam axis. All reconstructed tracks have a momentum P_x <50 GeV/c. It is used to filter multi-tracks events.

3.1.4 L2 software trigger

The L2 trigger reduces the L1 trigger rate to the allowed rate of 10 kHz. It is based on partially reconstructed events and combines information from different sub-detectors. A possible trigger condition would combine information from the GTK and from the STRAW spectrometer to allow cut on the vertex position. The L2 software trigger architecture was implemented in 2015, but no algorithms were implemented during the 2016 and 2017 data taking. Since the experiment runs at a beam intensity lower than the nominal one and the reduction factor applied by the L1 algorithms has been sufficient to take the total bandwidth at an affordable level.

[2]Clostest Distance of Approach(CDA) is the shortest distance between two tracks. In the case mentioned in this chapter it is the shortest distance between the nominal kaon direction and the selected downstream track, reconstructed in the STRAW.

3.2 Study of trigger efficiencies for the $K \to \pi\mu e$ analysis

The $K \to \pi\mu e$ analysis makes use of three trigger masks, whom definitions are in Table 3.5 and Table 3.6 for 2016 and 2017 data taking respectively [3].

MASK Name	L0 trigger	L1 trigger	Downscaling factor
Multi-track (MT)	RICH $\times$ Q_X	KTAG $\times$!LAV $\times$ STRAW$_{exo}$	50
Muon Multi-track (μMT)	RICH $\times$ Q_X $\times$ MO1	KTAG $\times$!LAV $\times$ STRAW$_{exo}$	5
Electron Multi-track (eMT)	RICH $\times$ Q_X $\times$ E20	KTAG $\times$!LAV $\times$ STRAW$_{exo}$	2

Table 3.5: Masks present in 2016 data taking and used for $K \to \pi\mu e$ analysis.

MASK Name	L0 trigger	L1 trigger	Downscaling factor
Multi-track (MT)	RICH $\times$ Q_X	KTAG $\times$ STRAW$_{exo}$	100
Muon Multi-track (μMT)	RICH $\times$ Q_X $\times$ MO1 $\times$ E10	KTAG $\times$ STRAW$_{exo}$	10
Electron Multi-track (eMT)	RICH $\times$ Q_X $\times$ E20	KTAG $\times$ STRAW$_{exo}$	8

Table 3.6: Masks present in 2017 data taking and used for $K \to \pi\mu e$ analysis.

For each mask a downscaling factor greater than one was used, in order to maintain the total data acquisition rate at the allowed level.
In 2017 removing the !LAV condition at L1 from the multi-track triggers was needed due to the low efficiency of that algorithm assessed with 2016 data selecting K3π events. As a consequence the L1 reduction factor for those trigger masks decreases respect to the 2016 configuration of a factor 3, thus the downscaling factors, applied at L0, increased accordingly ($\sim$ 2 times higher than 2016).

In what follows the results on the trigger efficiency studies, performed offline on data, for $K \to \pi\mu e$ and the normalization decay, the K3π decay mode, are presented. Thanks to the same number of tracks in the final state and a similar kinematic for most of the L0 conditions and L1 algorithms the trigger efficiency measured with K3π is assumed to be valid also for the $K \to \pi\mu e$ decays.

[3] The meaning of each primitive/algorithm has been already presented in previous sections.

Each primitive/algorithm efficiency is computed using a control sample as follows

$$\epsilon_{prim/algo} = \frac{\text{events selected for which the primitive/algorithm is on}}{\text{all events selected}} \tag{3.2}$$

In case of L0 primitive efficiency, the numerator in Eq. 3.2 is represented by all events selected in the control sample for which the primitive under study is present. The term *control sample* refers to events selected from a data sample collected with a minimum bias trigger called CONTROL (see Table 3.3 and Table 3.4).

The L1 algorithm efficiency is measured using as control sample a fraction of events built with autopass data[4] selecting events collected with multi-track trigger mask (Table 3.5, Table 3.6), for which a L1 trigger chain is implemented.

The section is organized as follows: first the K3π selection strategy is presented. The K3π events are also used for other studies in this work (vertex fitting, particle identification efficiency). Then the trigger efficiency measurement for each primitive/algorithm is described and the results for the 2016 and 2017 data-taking are presented. The trigger efficiency for each primitive/algorithm has been checked as a function of the most interesting variables: time (burst number), instantaneous intensity, vertex position, energy in the LKr, track momentum and track angle. Even though in some cases dependencies have been spotted they are not taken into account in the final results presented in this work, but they would be considered in the future. The trigger efficiency for each primitive/algorithm has been measured for each run and it has been obtained taking the output of the linear fit from the trigger efficiency curve as a function of the vertex position, since this variable takes into account the kinematics of the decay and at the same time is not related to any trigger condition.

3.2.1 K3π Selection

K3π events are selected from data requiring the following conditions in order to assure that the selected tracks are inside the detector acceptance and are well reconstructed (quality checks), are coming from the same event (timing checks) and are coming from a single K^+ decay.

- there are three good track reconstructed in the events;
- the selected event is in time with the trigger;
- the reconstructed vertex position is within the fiducial volume, defined between [105,180] m;

[4] Autopass data means that the L1 algorithms are not applied but the response to the algorithm is saved

- there is at least one beam particle identified as a kaon in the KTAG, within a time window of $\pm$3ns with respect to the event time;
- the reconstructed total momentum at the vertex is compatible with the beam momentum within $\pm 3\sigma_P$, where $\sigma_P \sim 0.85$ GeV/c;
- the reconstructed invariant mass at the vertex, under the 3-π hypothesis, is compatible with the kaon mass within $\pm 3\sigma_M$, where $\sigma_M \sim 0.9$ GeV/c^2;

In particular a good track is defined as a track which satisfies the conditions listed below:

- it is reconstructed with hits from at least three of the four chamber with a $\chi^2 < 30$;
- each track is well separated from the others in the first STRAW chamber: there are no reconstructed tracks in a radius of 4 cm around the selected track;
- its momentum is between [10,60] GeV;
- there is a candidate associated within a time window of $\pm$2ns in the NA48-CHOD or CHOD;
- it is in the LKr and MUV3 geometrical acceptance, but there are no candidates in the MUV3 in time with the track;
- there is not LAV, IRC and SAC activity in a time window of $\pm$3ns with respect to the trigger time.

The event time is defined as the mean time of the three tracks, where the track time is the time of the NA48-CHOD or CHOD candidate associated.

To check if the events selected are K3π events, the 2-d plot of the $\theta_{K-track}$ versus the track momentum is used, where $\theta_{K-track}$ is the angle between the selected track and the beam direction. The top-plot in Figure 3.3, done with minimum bias data from 2016 data-taking, shows the $\theta_{K-track}$ versus the track momentum distribution before any K3π selection. In the plot can be clearly visible events from $K\mu 2$, $K2\pi$ and $K3\pi$, which represent the most popular kaon decays and a beam component at $\sim$75GeV/c. After applying the $K3\pi$ selection criteria, the sample is cleaned from all contributions except K3π, as reported in the bottom plot in Figure 3.3.

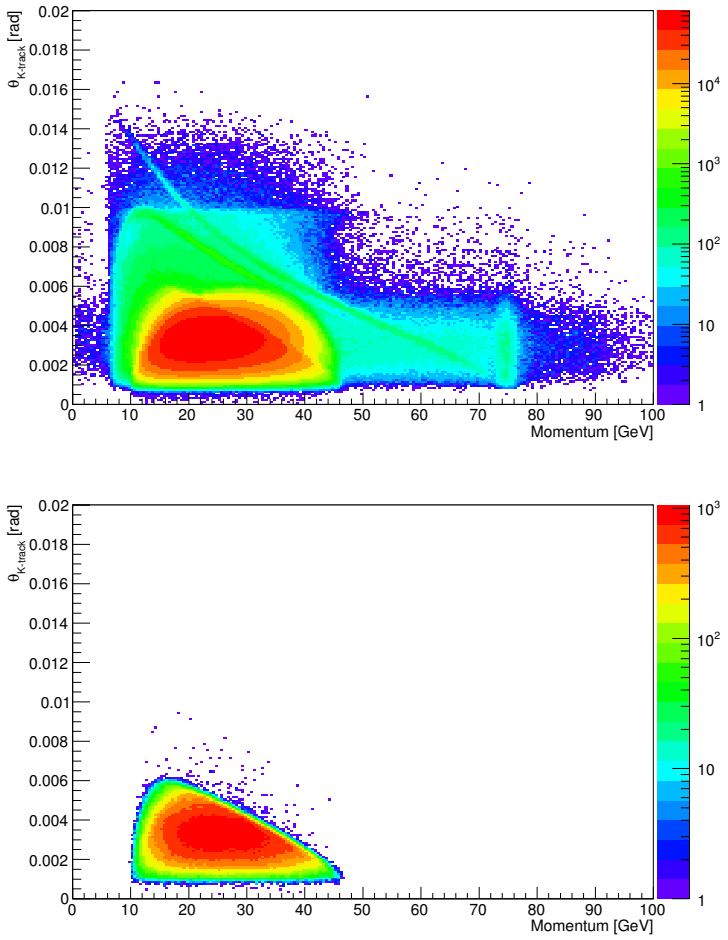

Figure 3.3: Distribution of the angle between each track and the nominal kaon direction versus the track momentum for a minimum bias data sample from 2016 run, before (top) and after(bottom) the $K^+ \to \pi^+\pi^+\pi^-$ event selection.

3.2.2 L0 trigger efficiency studies

RICH L0 trigger efficiency

At the L0 the RICH cannot be used to make decision based on the particle type, but only on the number of hits produces in the event; it can be mainly used to select or reject events with high multiplicity. The RICH primitive efficiency has been measured using K3π events for both signal and normalization decay. This assumption can be considered valid since the expected multiplicity for the two modes, assessed using MC samples, is compatible within the error, as shown in Table 3.7. The difference shown in the table between the K3π data and K3π MC samples is mostly related to pile-up events in the data: indeed while in the MC sample only K3π events are simulated, in the data the total number of hits is due to the selected event plus, for example, muons from the beam in time with the event. Nevertheless this contribution is the same for the K3π and the $K \rightarrow \pi\mu e$. Also small differences in the some reconstruction parameters, between MC samples and data samples could be present, e.g the photomultipliers efficiency.

Decay	RICH Multiplicity (number of hits-mean value $\pm$ std)
$K^+ \rightarrow \pi^+\mu^+e^-$ (MC)	42.3 $\pm$ 5.6
$K^+ \rightarrow \pi^+\mu^-e^+$ (MC)	42.6 $\pm$ 5.4
$K^+ \rightarrow \pi^-\mu^+e^+$ (MC)	43.4 $\pm$ 5.5
$K^+ \rightarrow \pi^+\pi^+\pi^-$ (MC)	45.0 $\pm$ 9.0
$K^+ \rightarrow \pi^+\pi^+\pi^-$ (data)	54.7$\pm$18.2

Table 3.7: Evaluated RICH multiplicity for $K \rightarrow \pi\mu e$ and $K^+ \rightarrow \pi^+\pi^+\pi^-$ decays with MC simulated events and $K^+ \rightarrow \pi^+\pi^+\pi^-$ decay data events.

The RICH primitive efficiency shows a constant behaviour with respect to all the interesting variables mentioned above as can be seen in the plots in Figure 3.6 and Figure 3.7 for a run from 2016 and 2017 data sample respectively.

2016 The RICH efficiency as a function of the run number for 2016 data sample is shown in Figure 3.4, showing a quite stable efficiency.

The global RICH efficiency results $\epsilon_{RICH} = (99.52 \pm 0.01)\%$

2017 The RICH efficiency as a function of the run number for 2017 data sample is shown in Figure 3.5.

It shows a stable efficiency around $\epsilon_{RICH} = (99.96 \pm 0.01)\%$

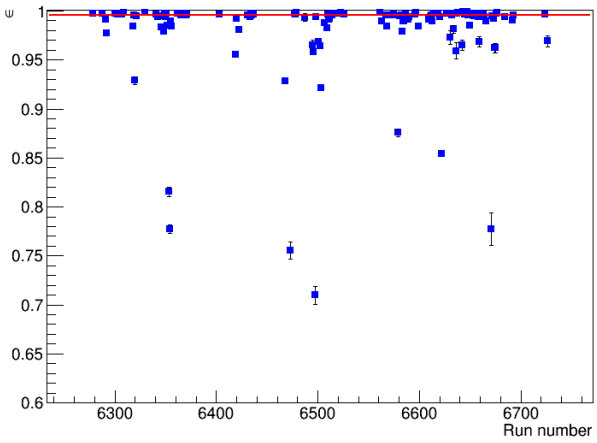

Figure 3.4: RICH primitive efficiency for each run of 2016 data sample taken at 30%-40% of the nominal beam intensity.

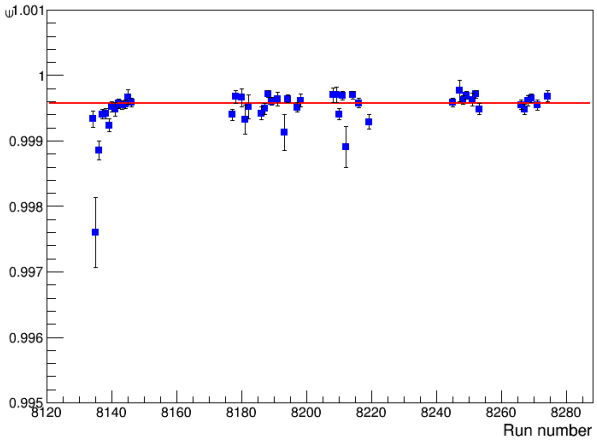

Figure 3.5: RICH primitive efficiency for each run of 2017 data sample taken at around 60% of the nominal beam intensity.

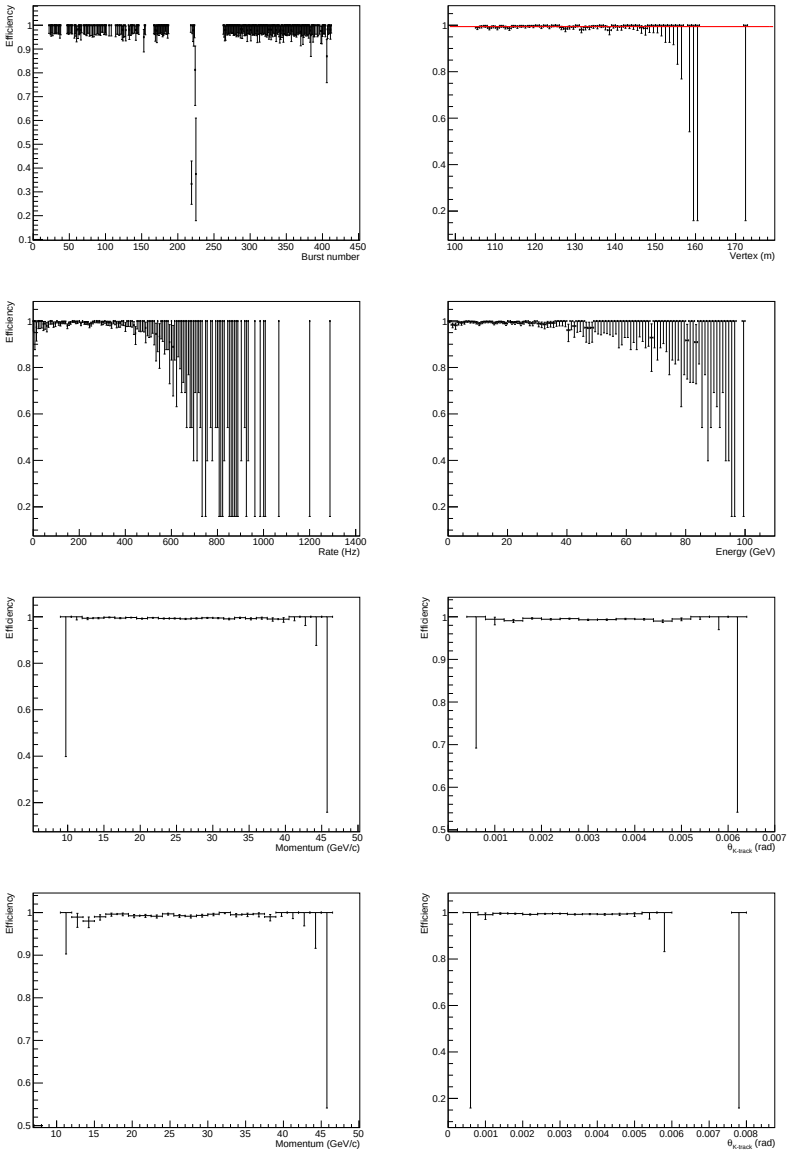

Figure 3.6: RICH primitive efficiency for Run 6346 of 2016 data as a function of the burst number, vertex position, instantaneous rate, energy in the LKr, negative track momentum and angle and positive track momentum and angle.

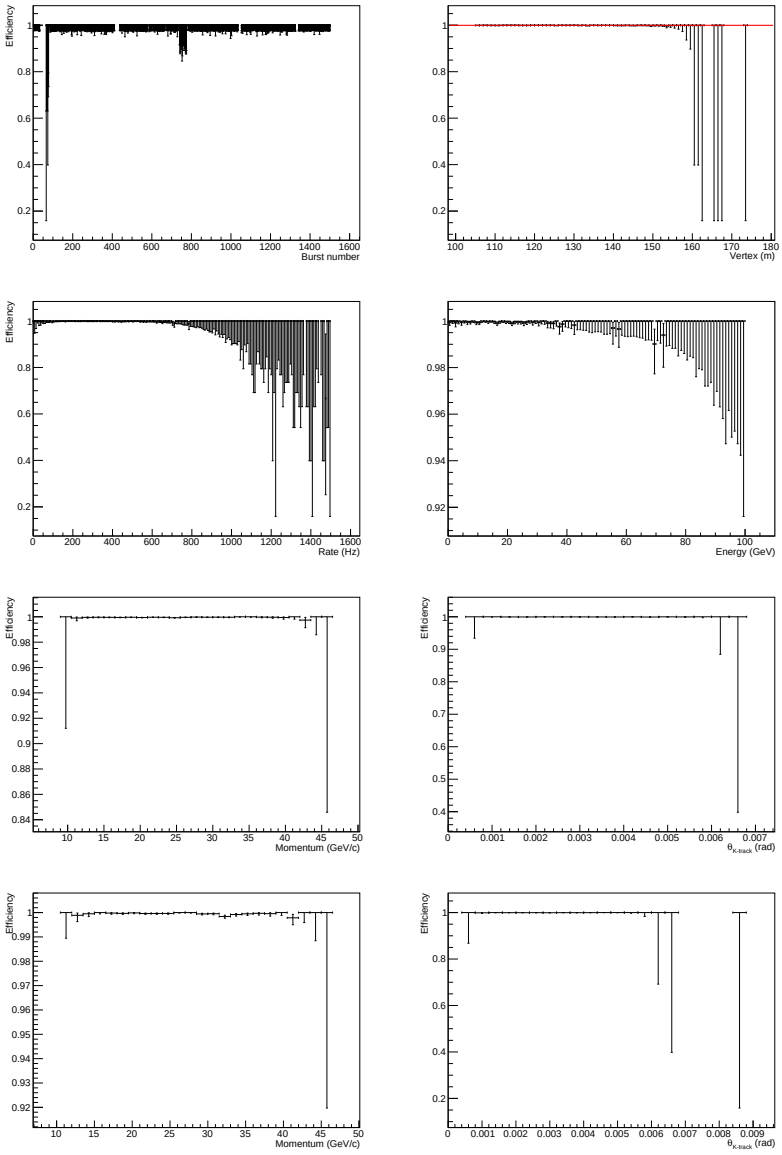

Figure 3.7: RICH primitive efficiency for Run 8146 of 2017 data as a function of the burst number, vertex position, instantaneous rate, energy in the LKr, positive track momentum and angle and negative track momentum and angle.

Qx L0 trigger efficiency

The Qx primitive efficiency has been measured using K3π events for both signal and normalization channel. The Qx trigger condition can be produced by the Jura-top and Saleve-bottom ($Q_{JT} - Q_{SB}$) or by the Saleve-top and Jura-bottom ($Q_{ST} - Q_{JB}$) quadrants in the CHOD, as pictured in Figure 3.8. In order to rely on the Qx trigger

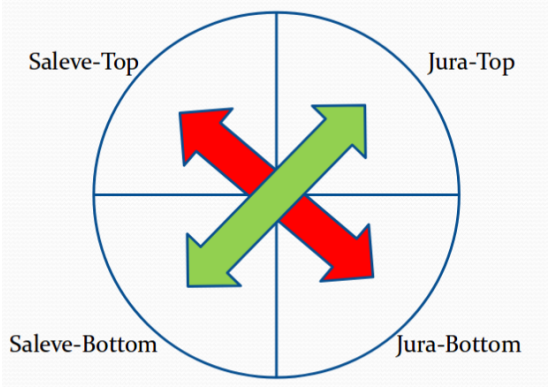

Figure 3.8: Sketch of the four quadrant in CHOD detector.

efficiency measured with the K3π also for the signal it is necessary to determine which is the expected probability for K3π and $K \to \pi\mu e$ to trigger the Qx condition. The values shown in Table 3.8 confirm that the two Qx illumination (Q_{JT}-Q_{SB} and Q_{ST}-Q_{JB}) are the same, within $\sim$1%, among the samples. The table shows also the Qx estimation for $K^+ \to \pi^+\pi^+\pi^-$ events from a data sample, being in agreement with the MC sample within $\sim$1%.

Decay	Q_{JT}-Q_{SB}	Q_{ST}-Q_{JB}
$K^+ \to \pi^+\mu^+e^-$ (MC)	49.8%±1.0%	49.4%±1.0%
$K^+ \to \pi^+\mu^-e^+$ (MC)	49.0%±1.0%	50.3%±1.0%
$K^+ \to \pi^-\mu^+e^+$ (MC)	49.4%±1.0%	49.8%±1.0%
$K^+ \to \pi^+\pi^+\pi^-$ (MC)	50.1%±1.0%	49.8%±1.0%
$K^+ \to \pi^+\pi^+\pi^-$ (data)	50.9%±0.5%	49.0%±0.5%

Table 3.8: Probability to have the Qx condition built with Q_{JT}-Q_{SB} or Q_{ST}-Q_{JB} for $K \to \pi\mu e$ and $K^+ \to \pi^+\pi^+\pi^-$ MC simulated events and $K^+ \to \pi^+\pi^+\pi^-$ data events

This study is particularly important for the measurement of Qx efficiency in 2016 data, since the primitive generation was affected by a bug in all quadrants but the

Q_{JT}, which cannot be cured offline. The fact that the probability to trigger the Q_{JT}-Q_{SB} or the Q_{ST}-Q_{JB} is the same in all samples means that the bug affects in the same way the K3π and the $K \to \pi\mu e$ decay channels. The bug was found in the clustering module: if a hit starts a cluster cell and the incoming hit merges that cluster cell or starts an earlier cluster cell, the clustering module behaves correctly, if the first hit starts a cluster cell and the incoming hit moves to the next cluster cell, on the contrary, the quadrant information of that hit is lost. Whether behaviour occurs depends on the order of the hits into the clustering module. Since the bug affects only three out of four quadrant the Qx primitive efficiency is different if built with two quadrant affected by the bug(Q_{ST}-Q_{JB}) or with only one (Q_{JT}-Q_{SB}).

2016 The Qx efficiency shows a quite stable behavior has a function of all observable taken in consideration except the instantaneous rate (Figure 3.11). The decrease of the Qx efficiency when the instantaneous intensity increases is somehow expected, since it is driven by the bug present in the firmware that is intensity-dependent. For the moment the Qx efficiency for each run is obtained from the linear fit of the efficiency curve as a function of the vertex position and the dependency with respect to the instantaneous rate is not take into account. In the future it should be corrected, studying the Q_X trigger efficiency in bins of instantaneous rate[5].

The Q_X trigger efficiency as a function of the run number for 2016 data sample is shown in Figure 3.9.

The global Qx efficiency results:

$$\epsilon_{Qx} = (88.21 \pm 0.02)\%$$

While the Q_{JT}-Q_{SB} and Q_{ST}-Q_{JB} trigger efficiencies result [6]:

$$\epsilon_{Q_{JT}-Q_{SB}} = (91.3 \pm 1.5)\%$$
$$\epsilon_{Q_{ST}-Q_{JB}} = (79.5 \pm 1.3)\%$$

showing a lower efficiency if the Qx primitive is built with two quadrants affected by the bug, respect to the other configuration. As the probability that Q_X is triggered by the Q_{JT}-Q_{SB} or the Q_{ST}-Q_{JB} condition is 50/50 (Table 3.8), the Q_X trigger efficiency for each run is exactly the mean value of the efficiency of the two configurations.

[5] In order to performed such study the bin size will be changed with respect to the plots presented in this work

[6] The results shown for the Q_{JT}-Q_{SB} and Q_{ST}-Q_{JB} efficiencies are obtained from a run of 2016 sample

2017 Also for the 2017 data the Qx efficiency shows a quite stable behaviour respect to the most significant variables, as can be seen in plots in Figure 3.12. The Qx efficiency as a function of the run number for 2017 data sample is shown in Figure 3.10. The result for each run has been obtained as for the 2016 data.

The global Qx efficiency results:

$$\epsilon_{Qx} = (97.81 \pm 0.01)\%$$

and the efficiency of the two possible configurations are the same. As can be seen the bug present in 2016 has been cured and the efficiency improved significantly.

MO1 L0 trigger efficiency

As already described the MO1 primitive excludes muons going in the inner part of MUV3, defined by the 8 tiles around the beam shown in Figure 3.17. The MO1 efficiency is measured using a sub-sample of $K^+ \to \pi^+\pi^+\pi^-$, with at least one pion decaying in flight. Also in this case no significant differences have been spotted between the three signal channels and the $K^+ \to \pi^+\pi^+\pi^-$ decay, as shown in Table 3.9, where the percentage of hits in the inner and outer region of MUV3 are reported. The measurement done with K3π events from data results quite higher compared to the K3π MC sample due to the presence of muon halo which is not taken into account in the simulation, but at the same time this is not a problem for the estimation of the trigger efficiency for the signal, using the K3π decay, since the muon halo effect will be the same for $K^+ \to \pi^+\pi^+\pi^-$ and $K \to \pi\mu e$.

Decay	Inner Tiles	Outer Tiles
$K^+ \to \pi^+\mu^+e^-$ (MC)	(6.4±2.9)%	(93.6 ± 1.2)%
$K^+ \to \pi^+\mu^-e^+$ (MC)	(5.5±2.2)%	(94.5 ±0.8)%
$K^+ \to \pi^-\mu^+e^+$ (MC)	(6.1±2.1)%	(93.9 ± 0.8)%
$K^+ \to \pi^+\pi^+\pi^-$ (MC)	(8.05±5.0)%	(92.0 ±2.0)%
$K^+ \to \pi^+\pi^+\pi^-$ (data)	(16.8±4.0)%	(83.2 ±2.5)%

Table 3.9: Event rate in the 8 inner tiles and in all other of MUV3 for $K^+ \to \pi^+\pi^+\pi^-$ and $K \to \pi\mu e$ MC simulated events and $K^+ \to \pi^+\pi^+\pi^-$ data events

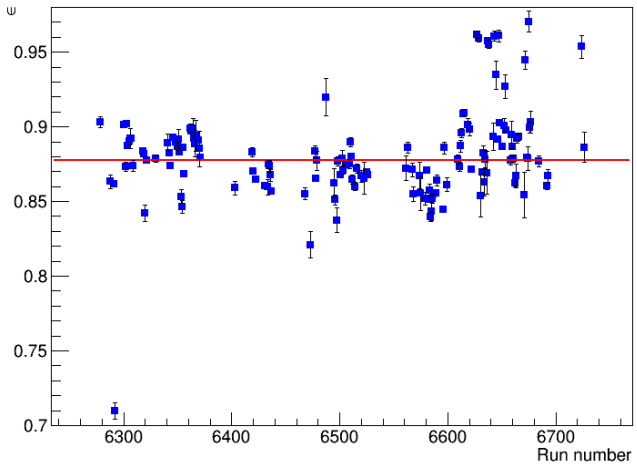

Figure 3.9: Qx primitive efficiency for each run of 2016 data sample taken at a beam intensity between 30% and 40% of the nominal value.

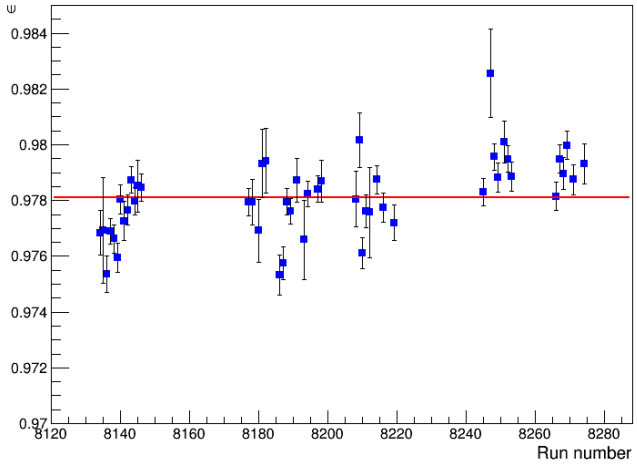

Figure 3.10: Qx primitive efficiency for each run of 2017 data sample taken at a beam intensity around 60% of the nominal value.

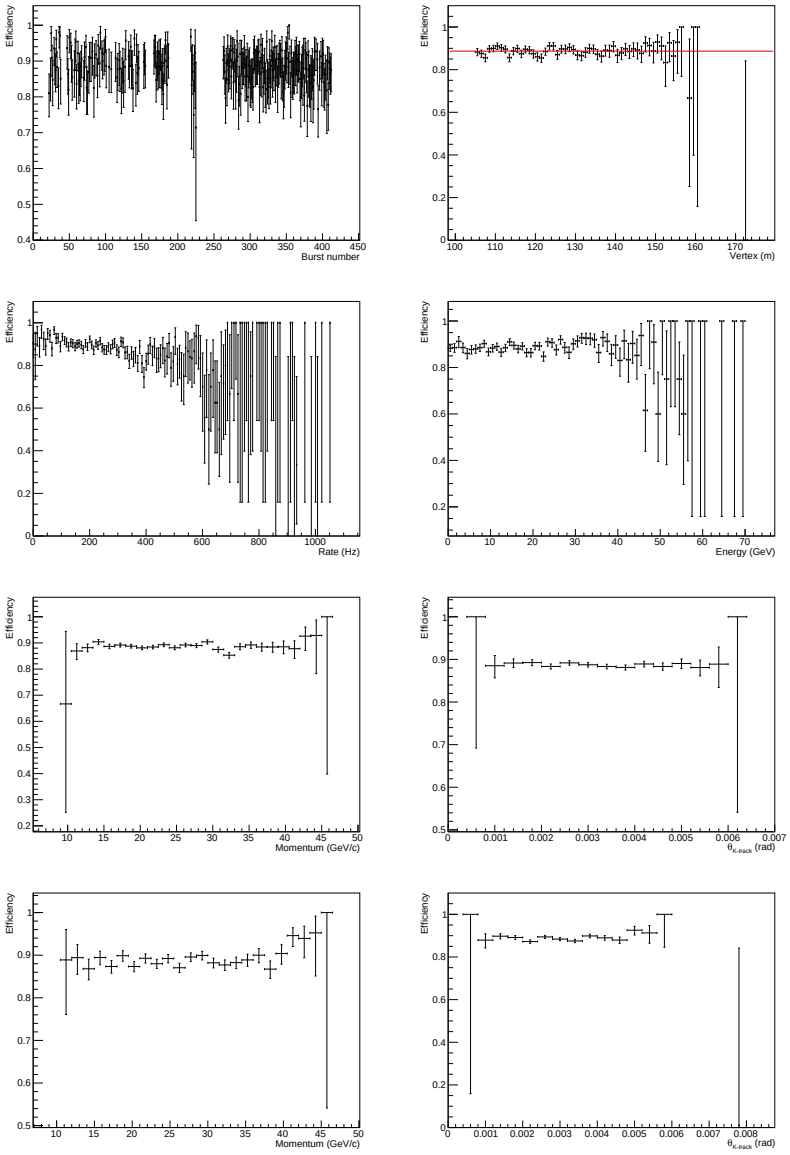

Figure 3.11: QX primitive efficiency for Run 6346 of 2016 data as a function of the burst number, vertex position, instantaneous rate, energy in the LKr, positive track momentum and angle and negative track momentum and angle.

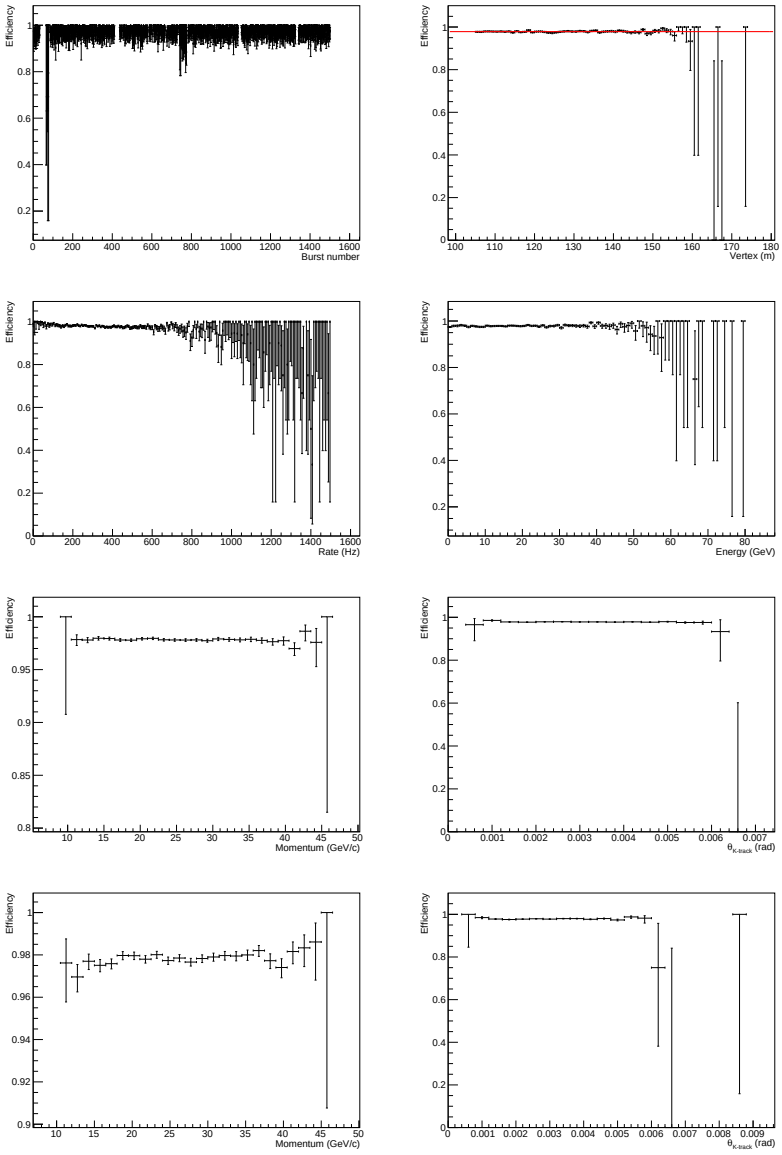

Figure 3.12: QX primitive efficiency for Run 8146 of 2017 data as a function of the burst number, vertex position, instantaneous rate, energy in the LKr, positive track momentum and angle and negative track momentum and angle.

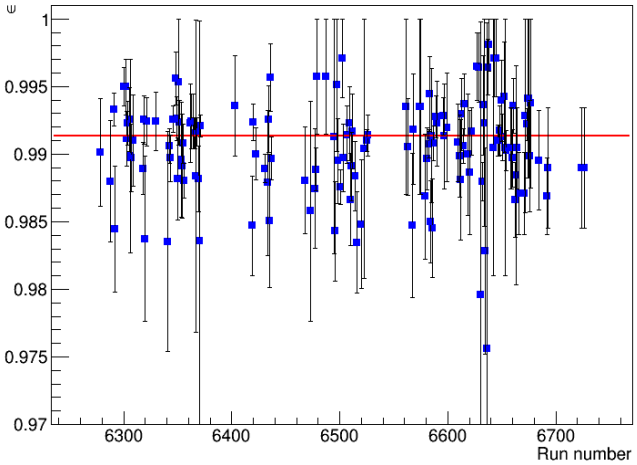

Figure 3.13: MO1 primitive efficiency for each run of 2016 data sample taken at a beam intensity between 30% and 40% of the nominal value.

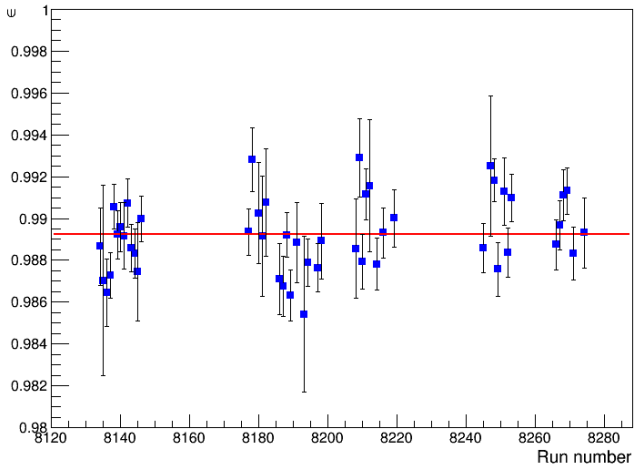

Figure 3.14: MO1 primitive efficiency for each run of 2017 data sample taken at a beam intensity at ∼60% of the nominal value.

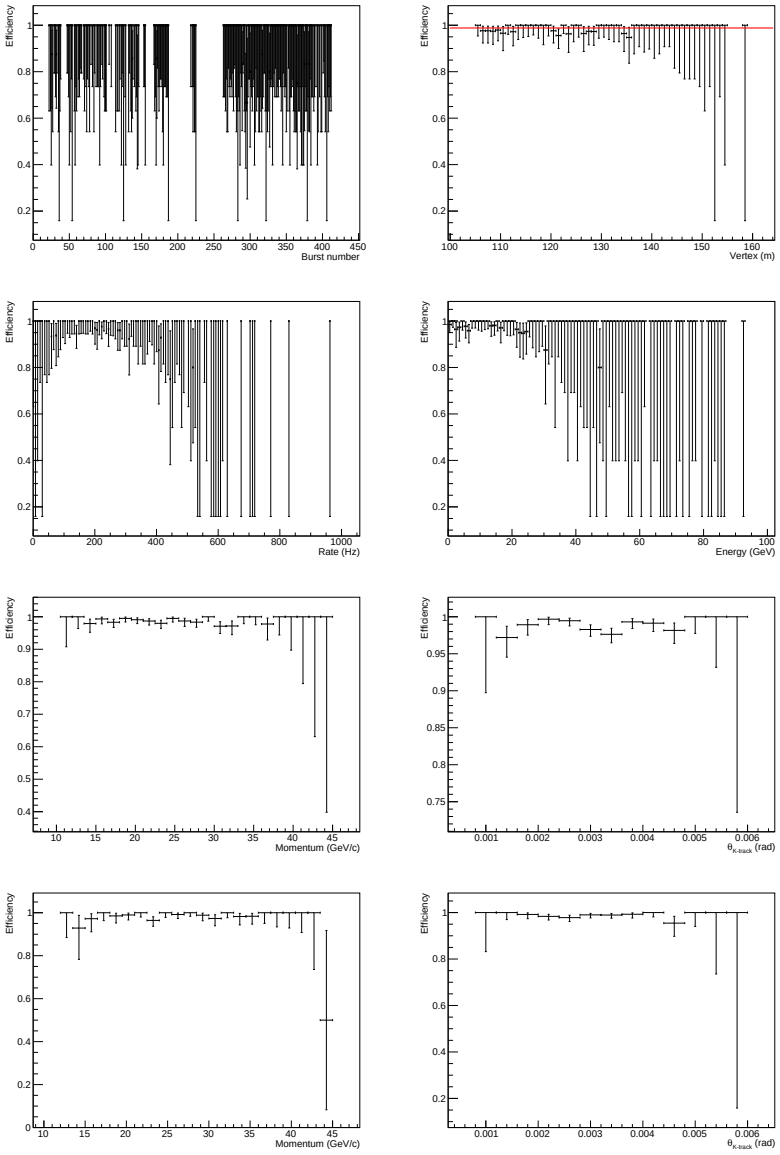

Figure 3.15: MO1 primitive efficiency for Run 6346 of 2016 data as a function of the burst number, vertex position, instantaneous rate, energy in the LKr, positive track momentum and angle and negative track momentum and angle.

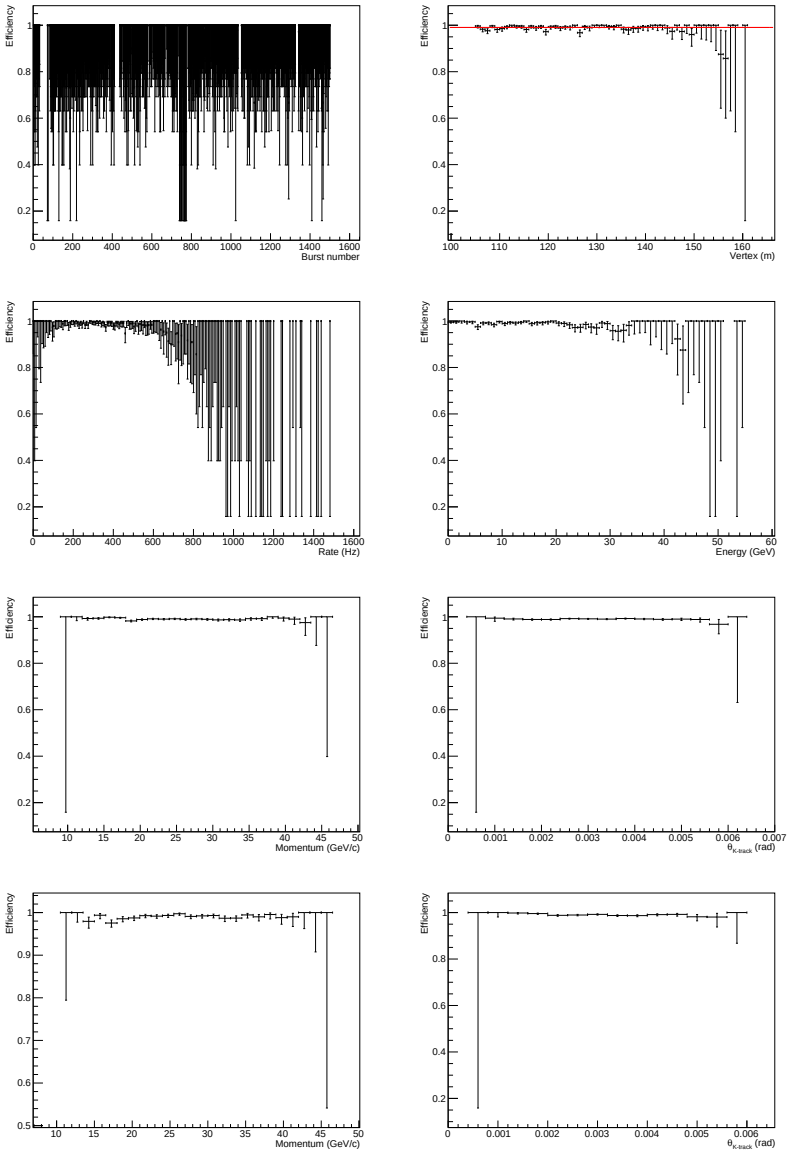

Figure 3.16: MO1 primitive efficiency for Run 8146 of 2017 data as a function of the burst number, vertex position, instantaneous rate, energy in the LKr, positive track momentum and angle and negative track momentum and angle.

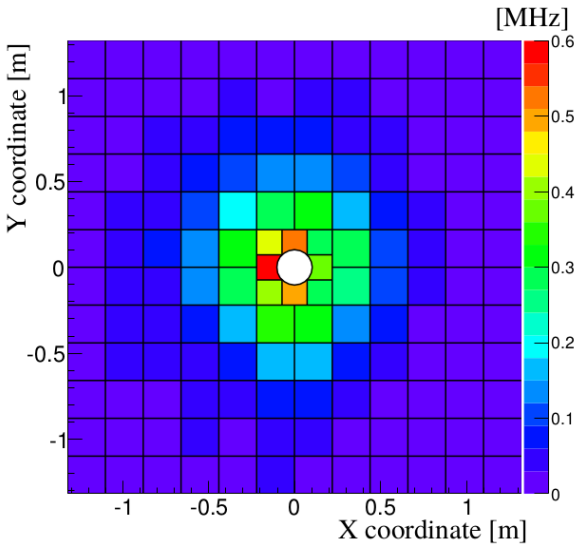

Figure 3.17: Monte Carlo MUV3 illumination plot assuming a nominal beam intensity. The 8 smaller tiles, around the beam hole are the inner tile excluded by the MO1 condition.

2016 The MO1 efficiency is quite stable respect to the most significant variables (Figure 3.15). The run-by-run MO1 efficiency is shown in Figure 3.13. The efficiency estimation for each run is taken from the linear fit of the efficiency curve as a function of the event vertex position as for the other primitives.

The corresponding global efficiency results:

$$\epsilon_{MO1} = (99.14 \pm 0.02)\%$$

2017 The MO1 efficiency as a function of the most interesting variable is quite stable (Figure 3.16). The efficiency for each analyzed run of 2017 data sample is shown in Figure 3.14.

The global MO1 efficiency results:

$$\epsilon_{MO1} = (98.92 \pm 0.02)\%$$

E10 and E20 trigger efficiency

The E10 and E20 trigger efficiencies have been measured for both signal and normalization decay. Unlike the RICH, Qx and MO1 primitives the K3π decay mode cannot be used to measure the E10 and E20 efficiencies for the signal. The final state composition is quite different in terms of particle type and the energy deposition in the LKr depends on the particle interaction with matter. As a consequence the total energy deposition for the two samples is significantly different (Figure 3.18).

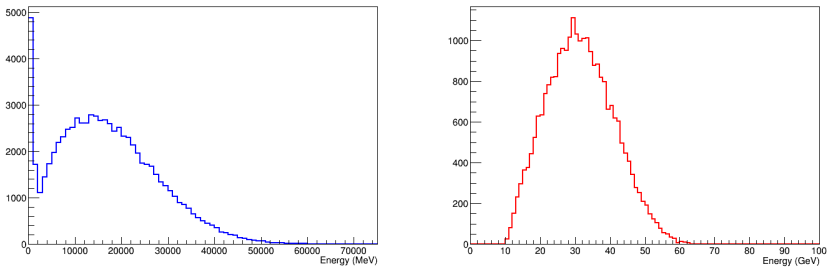

Figure 3.18: Expected $K^+ \to \pi^+\pi^+\pi^-$ (left) and $K \to \pi\mu e$ (right) energy deposition in the LKr obtained form MC samples.

While for the $K^+ \to \pi^+\pi^+\pi^-$ decay it is possible to derive the trigger efficiency directly from the data, for the signal it is not as simple. Indeed there are not kaon decays with a similar particles composition in the final state and with a branching ratio such that there is enough statistics to measure the trigger efficiency. For this reason a not fully data-driven technique has been used.

For the signal the E10 and E20 efficiency has been measured with a sample of $K^+ \to \pi^+\pi^0$selected from control triggers.
The $K^+ \to \pi^+\pi^0$, $\pi^0 \to \gamma\gamma$ decay is selected in such a way that one or two photons are in the LKr. Then the efficiency plot obtained from $K^+ \to \pi^+\pi^0$is weighted taking into account the MC $K \to \pi\mu e$ energy deposition distribution, defined as:

$$E_{tot}^{LKr} = E_{\pi}^{LKr} + E_{\mu}^{LKr} + E_{e}^{LKr}$$

As shown in Figure 3.19(top), the E_{π}^{LKr} is not simulated as well as we need within the NA62 MC. To correct this the π energy is corrected injecting the π energy deposition measured from data using K3π events. Figure 3.19 bottom shows that after correction

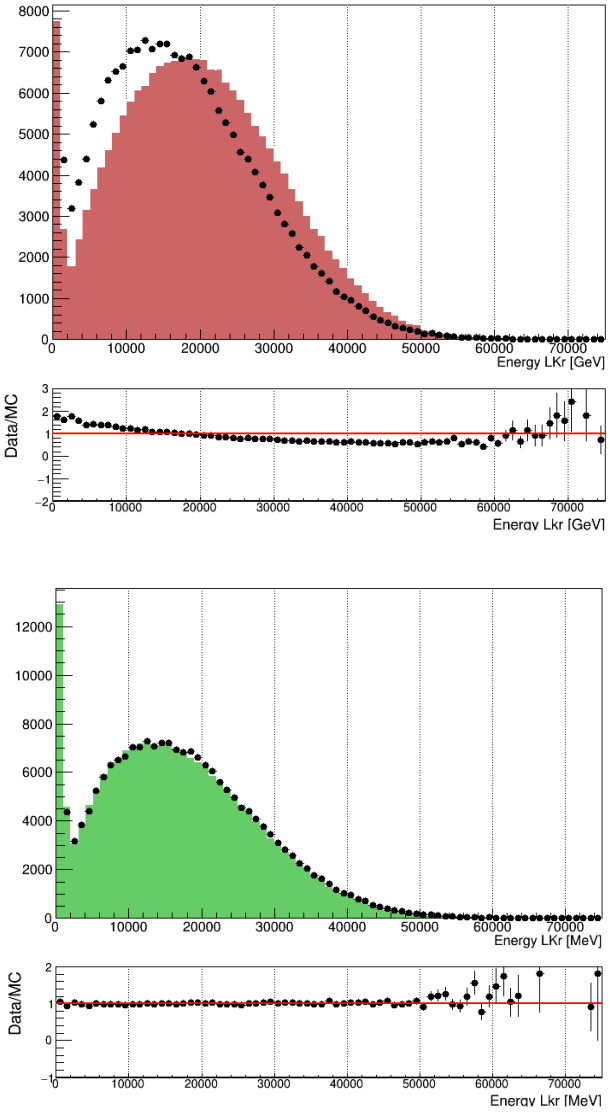

Figure 3.19: K3π energy distribution in the LKr. Top: data-MC comparison using the generated MC sample. Bottom: data-MC comparison after the pion energy deposition correction, injecting the true energy deposition, obtained from a data sample. The dots represent the data, while the colored area is the distribution from the MC sample.

the MC-data comparison of the K3π total energy distribution in the LKr improves and the agreement is good.

2016 In 2016 only the E20 primitive was present in the trigger masks used in the analysis (Table 3.5). In Figure 3.20 the E20 efficiency for a random run as a function of the energy in the LKr is shown. On the left the plot for the $K^+ \to \pi^+\pi^0$and on the right the same plot for the signal channels.
The curve shows a drop around 40 GeV which is not expected, since the implemented condition asked for E>20 GeV and the K2π and $K \to \pi\mu e$ energy deposition is peacked at $\sim$40Gev and $\sim$30Gev respectively.
This feature is present in all runs analyzed and is due to a bug in the time ordering of the bits within the LKr primitive, which has been cured for the 2017 data taking.

For the normalization channel the E20 efficiency is quite low, $\sim$35%, since the K3π energy deposition is mostly below $\sim$ 20GeV as shown in Figure 3.18 left.

2017 In 2017 the E10 and E20 conditions were present, the first implemented in the Muon multi-track mask and the latter in the electron multi-track mask as in 2016 (Table 3.6).
The E20 efficiency as a function of the total energy deposition is plotted in Figure 3.21 for one random run from the 2017 sample taken as an example. Despite the 2016 data, the efficiency is stable above 20 GeV, showing a rapid increase of the trigger efficiency at $\sim$ 20 GeV as expected. Above 25 GeV the efficiency results $\sim$98%.
The E10 efficiency as a function of the total energy deposition is shown in Figure 3.22 for one run from the 2017 data taking as an example. Above 15 GeV the efficiency is stable around $\sim$98%

For the normalization channel the efficiency evaluated for each run is reported in Figure 3.23 for E10 and in Figure 3.24 for E20, while the efficiency curves as a function of the most significant variables are shown in Figure 3.25 and Figure 3.26 for E10 and E20 primitive respectively. The E10 primitive efficiency is $\sim$73% while the E20 efficiency is $\sim$30%.

The dependency of the LKr (E20,E10) trigger efficiency versus the total energy in the LKr is not taken into account in the final results presented in Section 6, but it would be considered in the future. A study in bins of energy will be done in order to increase the precision on the kaon flux. This will have an impact specially for 2016 data sample, where a stronger dependency with respect to the LKr total energy has been spotted.

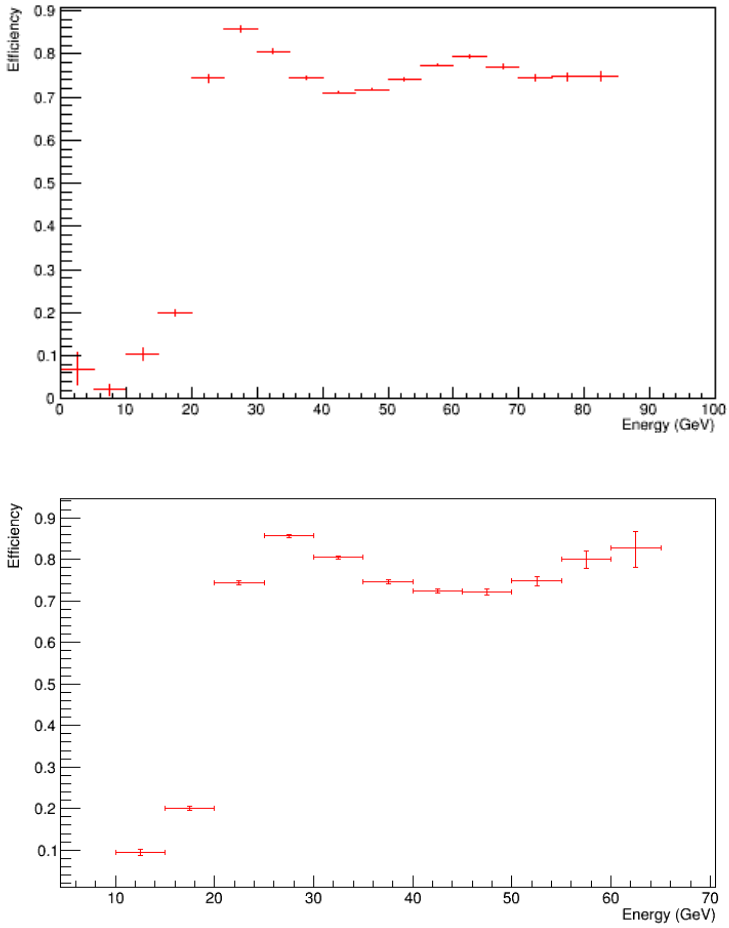

Figure 3.20: E20 primitive efficiency for Run 6501 of 2016 data as a function of the energy in the LKr. The top plot is for a sample of $K^+ \to \pi^+\pi^0$while the bottom plot is the efficiency curve weighted with the $K \to \pi\mu e$ MC energy distribution.

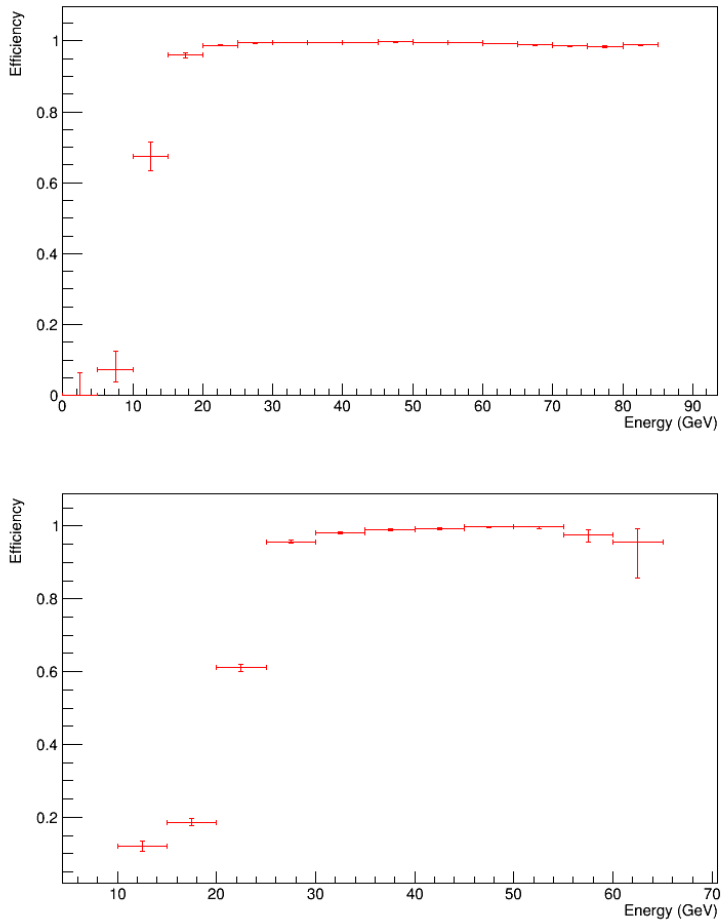

Figure 3.21: E20 primitive efficiency for Run 8134 of 2017 data as a function of the energy in the LKr. The top plot is for a sample of $K^+ \to \pi^+\pi^0$while the bottom plot is the efficiency curve weighted with the $K \to \pi\mu e$ MC energy distribution.

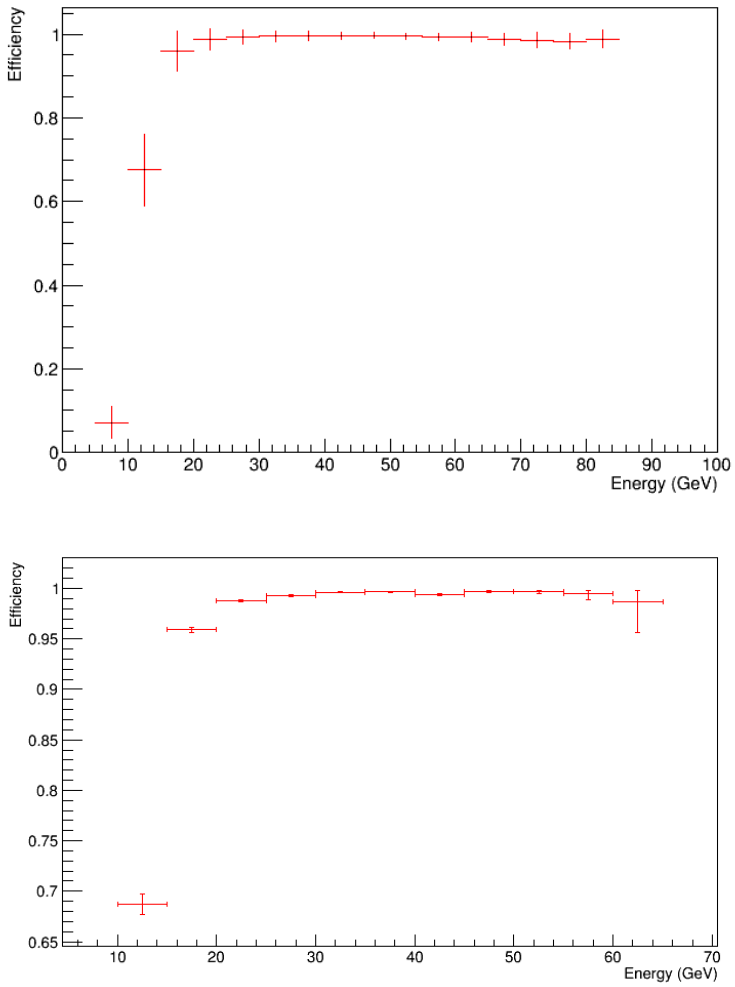

Figure 3.22: E10 primitive efficiency for Run 8134 of 2017 data as a function of the energy in the LKr. The top plot is for a sample of $K^+ \to \pi^+\pi^0$while the bottom plot is the efficiency curve weighted with the $K \to \pi\mu e$ MC energy distribution.

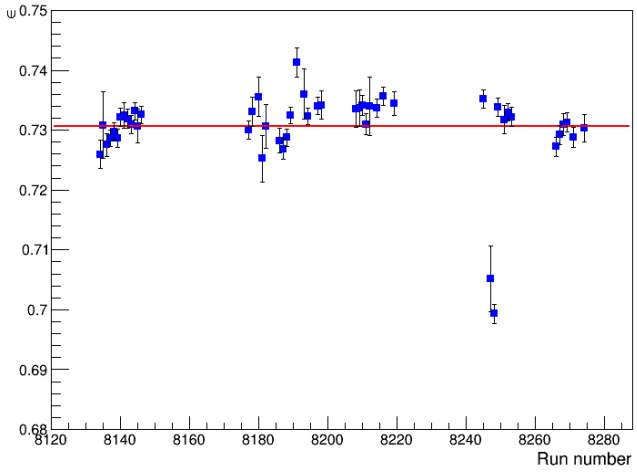

Figure 3.23: E10 primitive efficiency for each run of 2017 data sample taken at a beam intensity ∼60% of the nominal value.

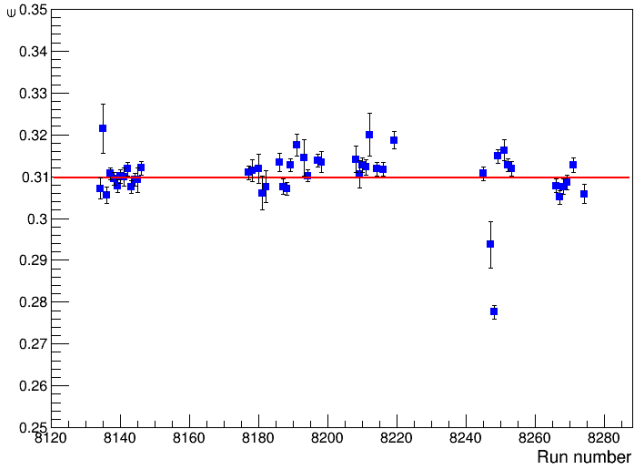

Figure 3.24: E20 primitive efficiency for each run of 2017 data sample taken at a beam intensity ∼60% of the nominal value.

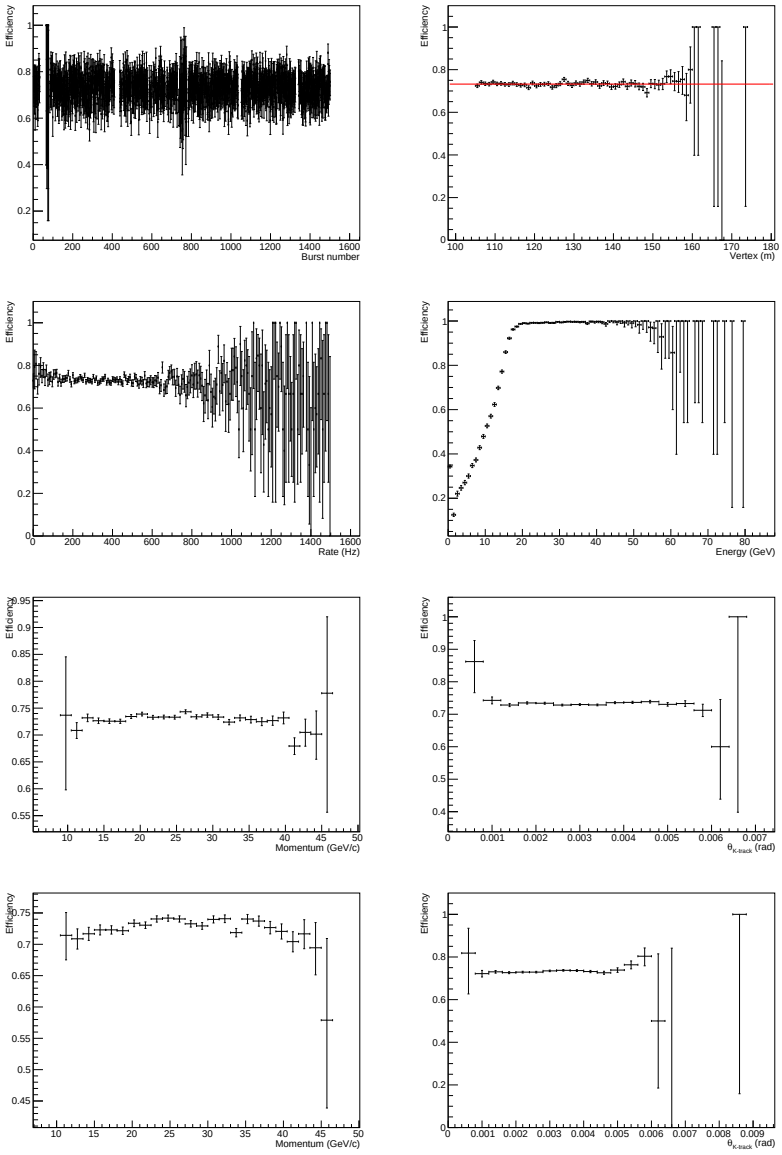

Figure 3.25: E10 primitive efficiency for Run 8146 of 2017 data as a function of the burst number, vertex position, instantaneous rate, energy in the LKr, positive track momentum and angle and negative track momentum and angle.

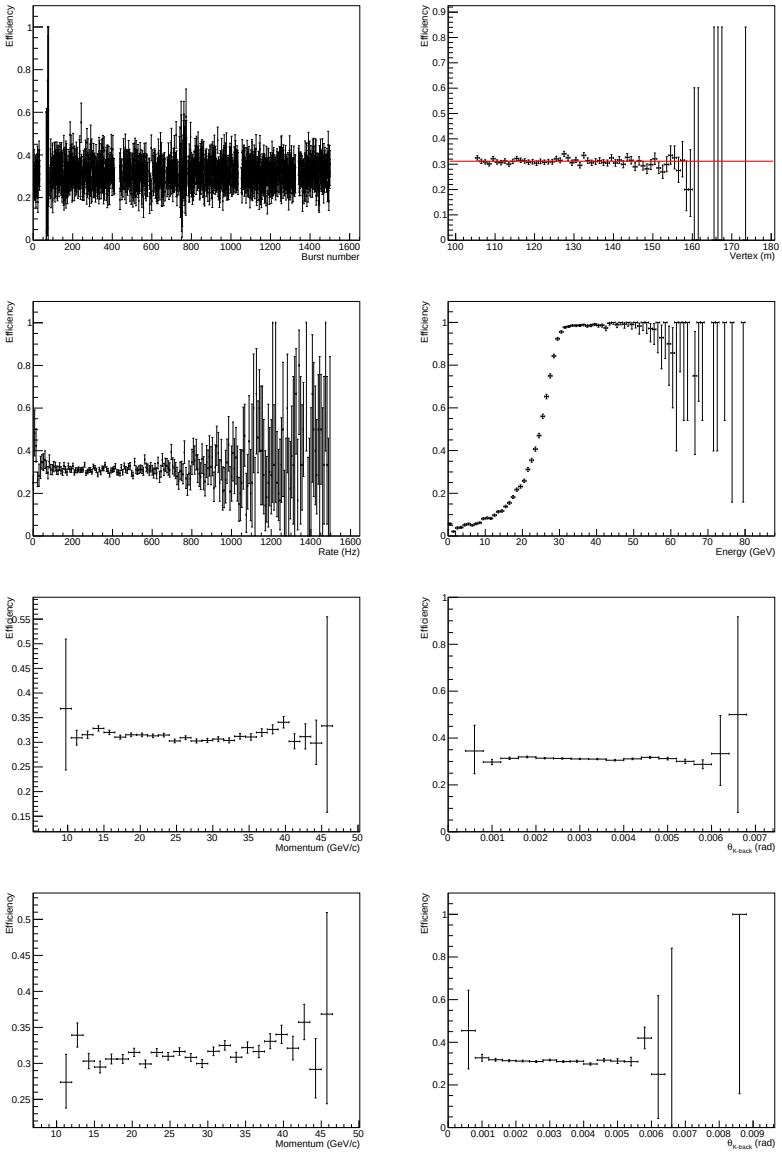

Figure 3.26: E20 primitive efficiency for Run 8146 of 2017 data as a function of the burst number, vertex position, instantaneous rate, energy in the LKr, positive track momentum and angle and negative track momentum and angle.

3.2.3 L1 trigger efficiency studies

In 2016 the L1 trigger for the masks used in the $K \to \pi\mu e$ analysis consisted of three algorithms applied one after the other: KTAG, !LAV and STRAW$_{exo}$, while in 2017 the !LAV condition has been removed. As for the RICH, Qx and MO1 primitives also for the KTAG and STRAW$_{exo}$ algorithms the efficiency for the signal channels can be estimated using the normalization decay, while for the !LAV algorithm a dedicated study has been performed.

KTAG algorithm

The KTAG algorithm efficiency can be measured with K3π or any other kaon decay for both signal and the normalization channel, since the algorithm action is just to select kaons without having any information about the decay type.

2016 The algorithm efficiency as a function of the most significant variables is shown in Figure 3.29, for a random run of the 2016 sample. The efficiency is flat with respect to all observables. The efficiency for each run, obtained taking the result of the linear fit of the efficiency curve as a function of the vertex position, is pictured in Figure 3.27.

The corresponding global value is $\epsilon_{KTAG} = (99.57 \pm 0.01)\%$ The decreasing of efficiency after Run 6560 it is due to an intervention in the KTAG at the data acquisition level; indeed one of the TEL62 board was excluded from the DAQ due to malfunctioning.

2017 The same procedure is followed to evaluate the KTAG efficiency for the 2017 sample. In Figure 3.30 the efficiency, from a single run, as a function of time, vertex position, instantaneous rate, LKr energy, tracks angle and momentum is reported, showing a flat distribution respect to all variables.

In Figure 3.28 the measured value for each run is shown, obtaining a global efficiency $\epsilon_{KTAG} = (99.85 \pm 0.01)\%$

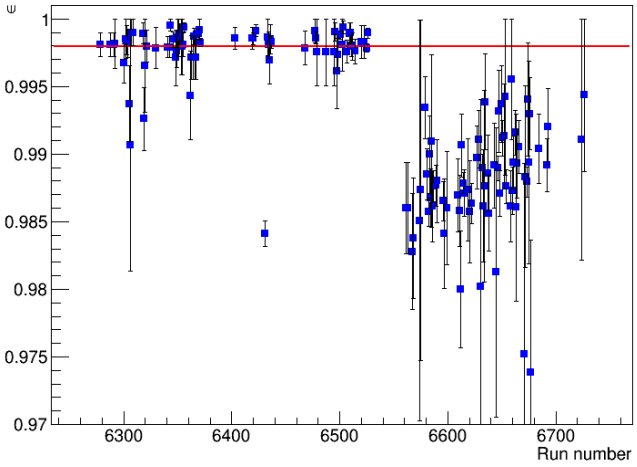

Figure 3.27: KTAG efficiency for each run of 2016 data sample taken at ∼40% of the nominal beam intensity.

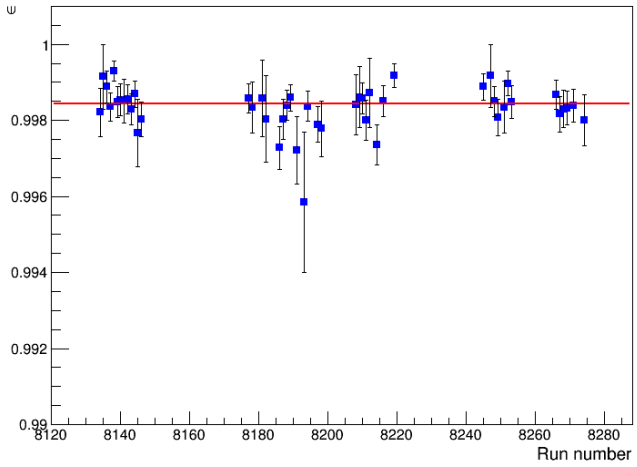

Figure 3.28: KTAG efficiency for each run of 2017 data sample taken at ∼60% of the nominal beam intensity.

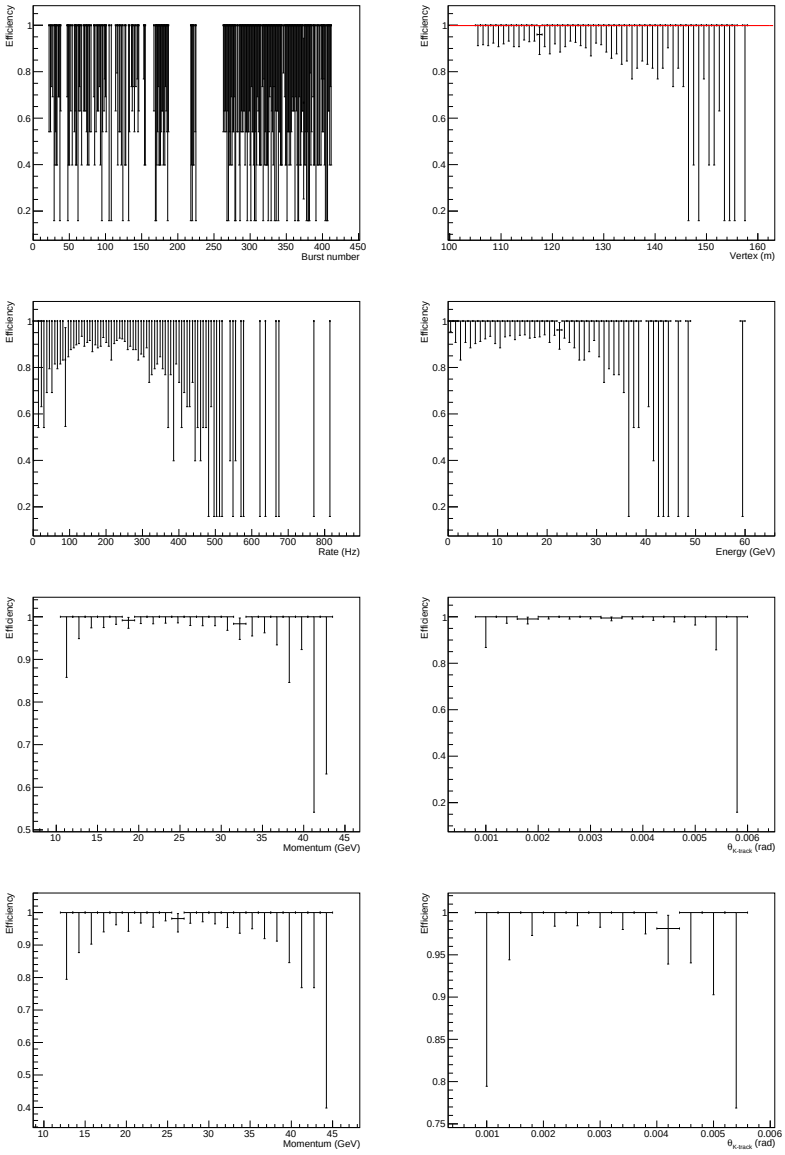

Figure 3.29: KTAG algorithm efficiency for Run 6346 of 2016 data as a function of the burst number, vertex position, instantaneous rate, energy in the LKr, positive track momentum and angle and negative track momentum and angle.

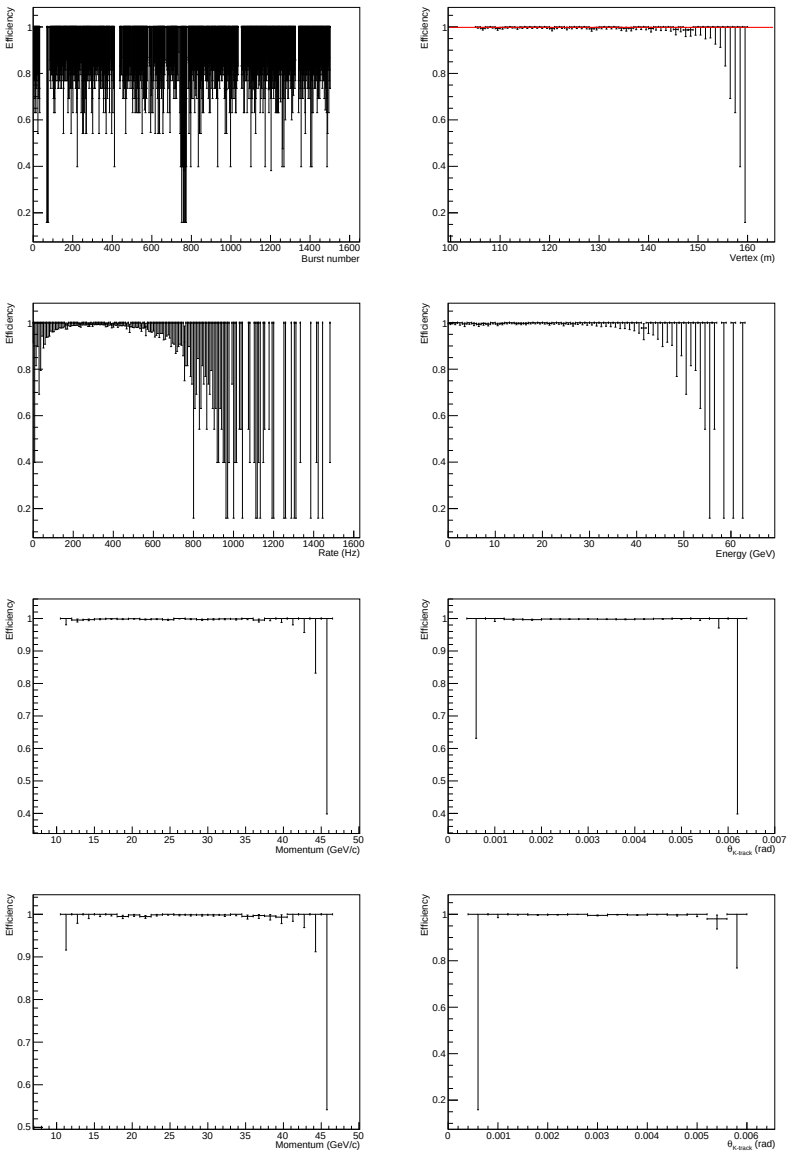

Figure 3.30: KTAG algorithm efficiency for Run 8146 of 2017 data as a function of the burst number, vertex position, instantaneous rate, energy in the LKr, positive track momentum and angle and negative track momentum and angle.

STRAW algorithm

The efficiency of the STRAW algorithm has been measured with $K^+ \to \pi^+\pi^+\pi^-$ events for the signal also, even if the STRAW reconstruction efficiency behave a bit differently if the track is a pion, a muon or an electron (Figure 3.31). Those differences will be include in the estimation of the systematic uncertainty. More precisely, the probability to fully reconstruct a $K^+ \to \pi^+\pi^+\pi^-$ or a $K \to \pi\mu e$ event, obtained with MC samples, is $\sim$89% and $\sim$92% respectively.

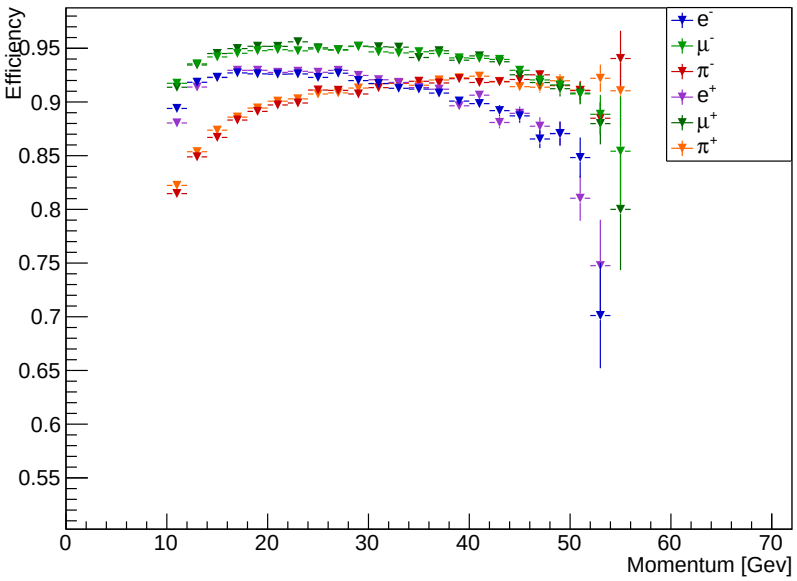

Figure 3.31: STRAW reconstruction efficiency for pions, muons, electrons, positive and negative, obtained using $K \to \pi\mu e$ MC samples, applying a good track selection using only the STRAW. The efficiency in this case is defined as the ratio between tracks passing the selection and all generated track within the fiducial decay volume

The STRAW algorithm efficiency has been studied as a function of the main variable (Figure 3.34 for 2016 data and Figure 3.35 for 2017 data) and the efficiency for each run has been evaluated taking the value obtained fitting the efficiency curve with respect to the vertex position. Since the STRAW algorithm asks for a negative track to be reconstructed, the corresponding efficiency shows a trend as a function of the negative track angle. This trend is not taken into account in the final STRAW efficiency

quoted in this work, but it would be considered in the future and a study in bins of track angle will be performed.

2016 The value for each run is pictured in Figure 3.32 and the average value results

$$\epsilon_{STRAW} = (96.28 \pm 0.03)\%$$

2017 The STRAW algorithm efficiency for each run is reported in Figure 3.33. The corresponding global value results

$$\epsilon_{STRAW} = (94.76 \pm 0.03)\%$$

LAV algorithm

The LAV L1 algorithm asks for events with at least 3 hits within a defined time window of $\pm$10 ns with respect to the L0 trigger time. The LAV condition is used in veto and was used in the trigger masks selected for the $K \to \pi\mu e$ analysis only in 2016 data-taking, because its efficiency, for those masks, was assessed to be quite low, $\sim$80% and then removed in 2017.

Activity in LAVs in time with the event can be due to pion nuclear interactions with some material along the NA62 detector, as for example the RICH mirror supports, and due to muons from the beam accidentally in time with the event. Therefore the trigger efficiency could depend on the number of pions in the event and since it is different in the signal channels and in the K3π, the latter cannot be used to measure the LAV trigger efficiency for $K \to \pi\mu e$.

The efficiency has been evaluated directly from data for both signal and normalization decay.

For the normalization channel, the K3π decay, the LAV efficiency has been measured selecting K3π events, using only autopass data (as done for KTAG and STRAW) or reproducing the algorithm condition directly in the analysis, asking for less than 3 hits in $\pm$10 ns with respect to the trigger time in all LAVs. The results, reported in the following, using the two methods are compatible showing a quite low efficiency as mentioned before:

$$\epsilon_{LAV} = (81.70 \pm 0.07)\%$$
$$\epsilon_{LAVEmulated} = (82.30 \pm 0.05)\%$$

If the LAV algorithm efficiency is measured after asking in the K3π selection no-LAV activity within $\pm$3ns with respect to the trigger, then the trigger efficiency improves, as expected, obtaining an efficiency of

$$\epsilon_{LAV} = (94.57 \pm 0.03)\%$$

as shown in Figure 3.36). The LAV trigger algorithm shows still $\sim$5% of inefficiency, because the time window used in the L1 algorithm to check the number of hits is larger, $\pm$10ns, than the one used in the analysis. In the following, for the normalization channel, the LAV efficiency assessed in the latter condition is used.

Despite most of the other trigger conditions, it is not possible to asses the LAV algorithm efficiency for the signal using the results from the K3π, since the number of pion in the final state is different, one instead of three. For this study the $K^+ \to \pi^+\pi^0\pi^0$ decay results reasonable, since it has only one charged pion in the final state and the pion angle-momentum spectrum is quite similar to the one from $K \to \pi\mu e$, thus it has a similar kinematic. On the other hand the low $K^+ \to \pi^+\pi^0\pi^0$ acceptance ($<$1%), mainly due to the request on the four photons from the two π^0 being within the LKr acceptance and the small fraction of control sample available (autopass events) do not allow to evaluate the LAV efficiency for each run, but only as a global value, using all available statistics.

The result, as a function of the pion angle, is shown in Figure 3.37

$$\epsilon_{LAV} = (95.1 \pm 0.3)\%$$

It is obtained asking in the event selection that there is no LAV activity in a time window of $\pm$3ns, as it is request in the $K \to \pi\mu e$ selection.

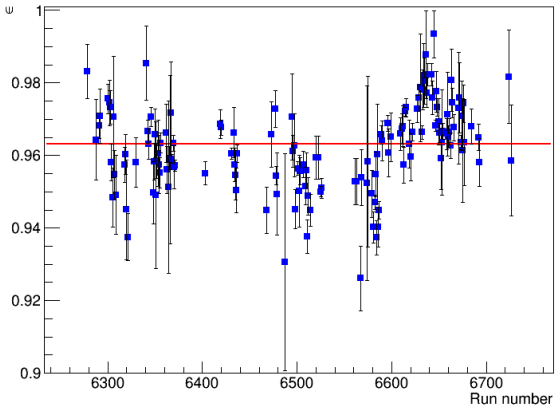

Figure 3.32: STRAW efficiency for each run of 2016 data sample taken at ∼40% of the nominal beam intensity.

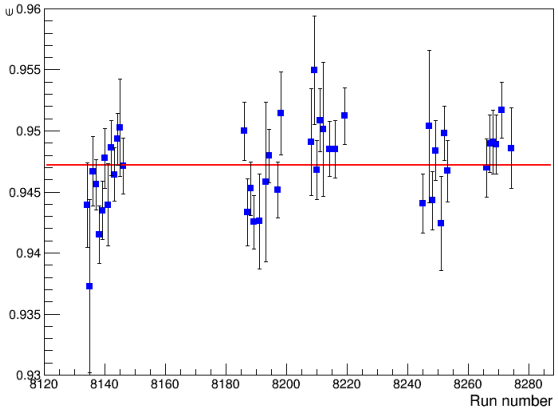

Figure 3.33: STRAW efficiency for each run of 2017 data sample taken at ∼60% of the nominal beam intensity.

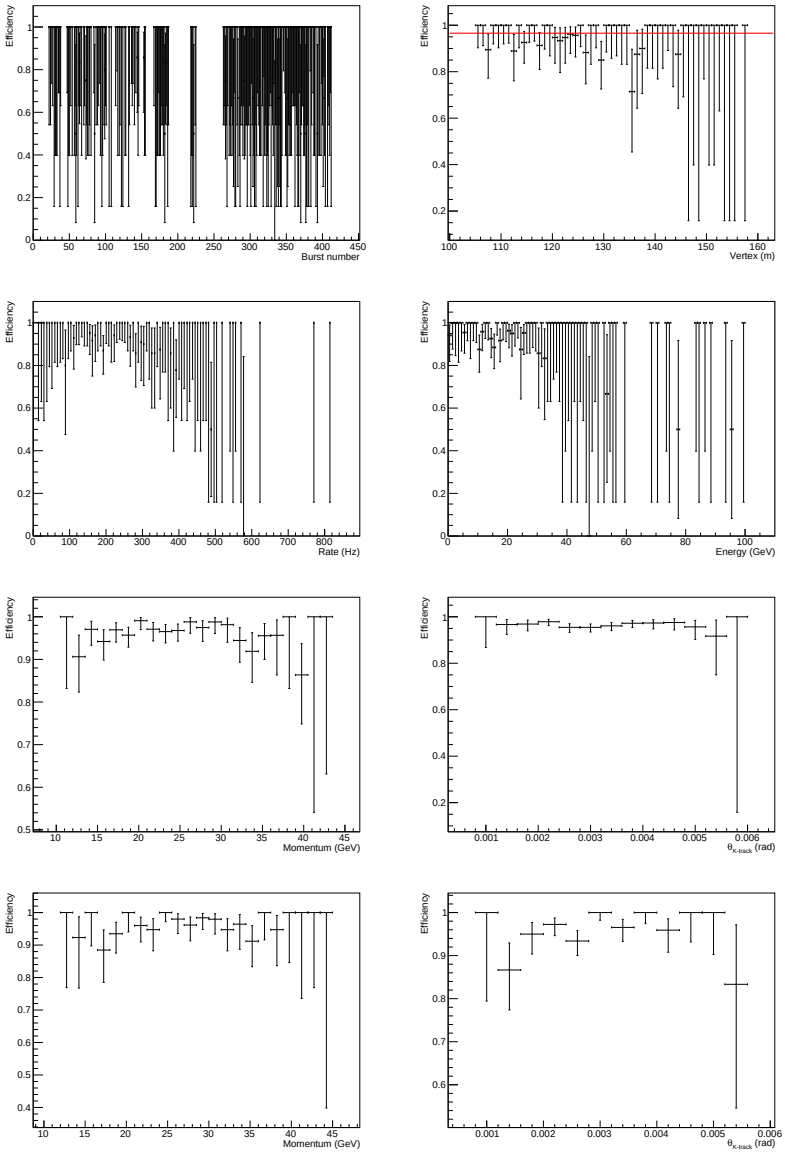

Figure 3.34: STRAW algorithm efficiency for Run 6346 of 2016 data as a function of the burst number, vertex position, instantaneous rate, energy in the LKr, positive track momentum and angle and negative track momentum and angle.

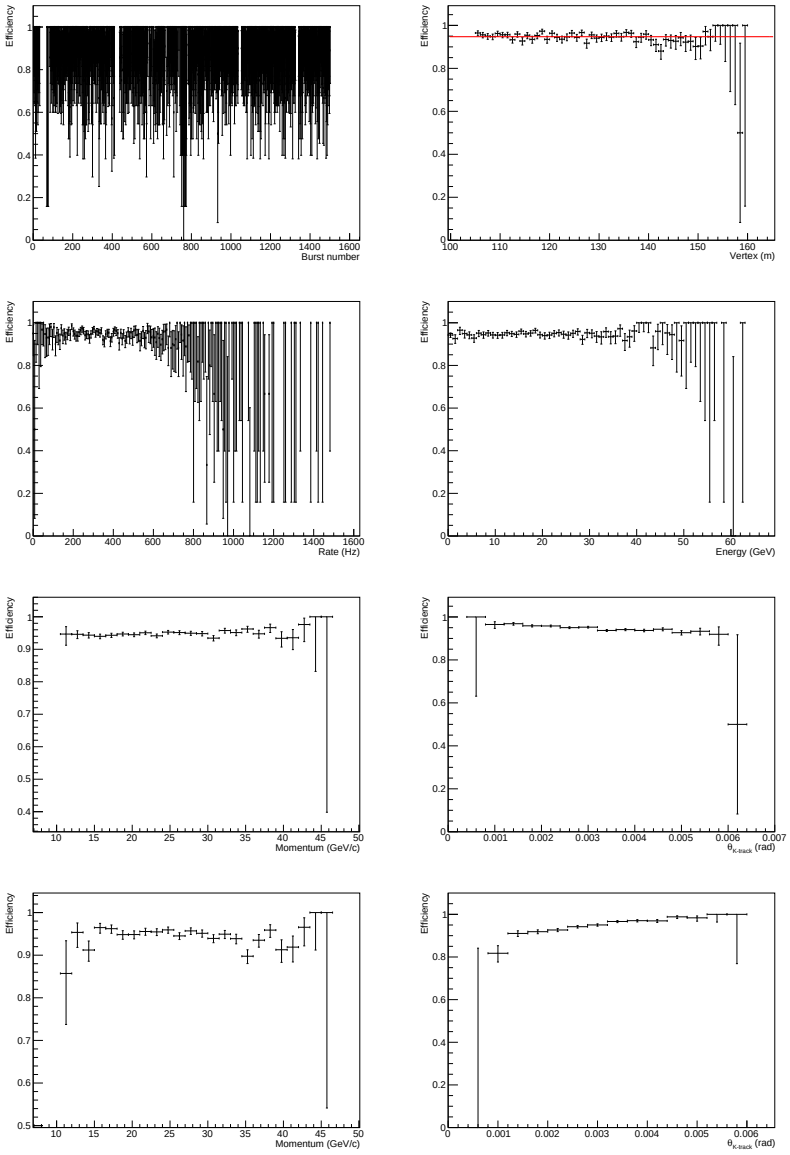

Figure 3.35: STRAW algorithm efficiency for Run 8146 of 2017 data as a function of the burst number, vertex position, instantaneous rate, energy in the LKr, positive track momentum and angle and negative track momentum and angle.

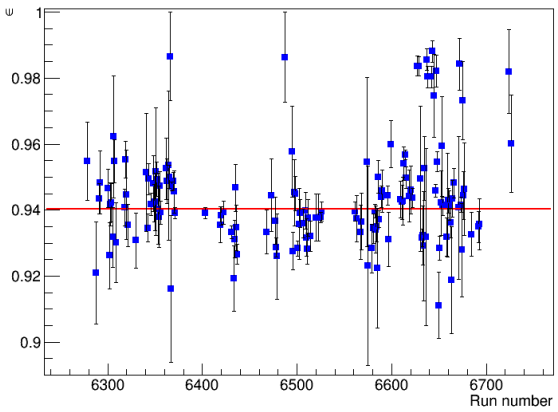

Figure 3.36: LAV efficiency for each run of 2016 data sample taken at ∼40% of the nominal beam intensity.

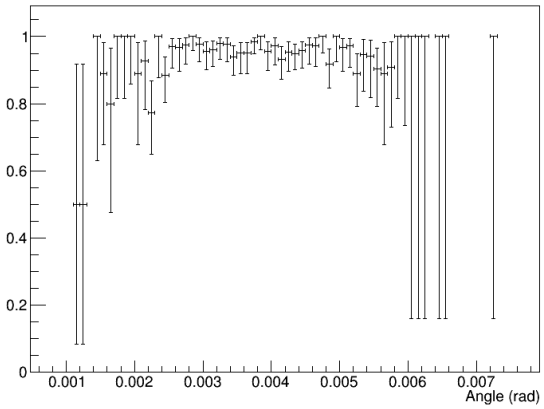

Figure 3.37: LAV efficiency as a function of the π^+ track momentum for 2016 data sample.

3.3 Conclusions

The study of the trigger efficiency is essential for the analysis presented in this thesis since the sample size depends strongly on how efficient is the trigger selection.

At the same time the trigger efficiency measurements present several difficulties. First of all the measurements cannot be done using MC sample: the L0 conditions are quite complex and cannot be fully simulated. Another difficulty is represented by the possible dependencies with respect to some of the observables taken into account: time, instantaneous rate, vertex position, total energy in the LKr, tracks angle and momentum. Possible trends are not taken into account in the results presented in this work, but they would be consider in the future. In addition due to changes in the triggers, meant to improve the trigger efficiency, separated studies for 2016 and 2017 are needed.

Another important argument is the fact that even if the normalization sample and the $K \to \pi\mu e$ channels have a similar kinematics they are different in the particles composition of the final state and this translates in a possible different trigger efficiency, mainly for those conditions in which the final state composition can play an important role. This is the case of the LKr triggers, E10 and E20 and of the LAV L1 algorithm for which a different strategy has been adopted in order to obtain a reasonable result for the $K \to \pi\mu e$ case. In particular for the E10 and E20 it was used a non fully data-driven technique, measuring the trigger efficiency from data, selecting a K2π sample and then weighting the efficiency distribution as obtained with the $K \to \pi\mu e$ MC total energy distribution in the LKr. While for the LAV the $K^+ \to \pi^+\pi^0\pi^0$ decay mode has been used.

The overall trigger efficiency for the masks used in the analysis, measured for the normalization channel is reported in Table 3.10 and Table 3.11 for the 2016A sample and 2017A sample, respectively. While the overall trigger efficiency measured for the signal channels is reported in Table 3.12 and Table 3.13 for the 2016A sample and 2017A sample, respectively.

The trigger efficiency studies presented in this chapter show that the NA62 trigger and DAQ system, despite few bugs and inefficiencies present during the 2016 data taking, improved during the 2017 data taking and consequently the data quality.

MASK Name	Trigger efficiency
Multi-track (MT)	$(79.59 \pm 0.31)\%$
Muon Multi-track (μMT)	$(78.90 \pm 0.31)\%$
Electron Multi-track (eMT)	$(24.45 \pm 0.40)\%$

Table 3.10: Multi-track,Muon Multi-track and Electron Multi-track overall trigger efficiency for 2016 data taking for the normalization channel.

MASK Name	Trigger efficiency
Multi-track (MT)	$(92.51 \pm 0.05)\%$
Muon Multi-track (μMT)	$(66.90 \pm 0.05)\%$
Electron Multi-track (eMT)	$(28.86 \pm 0.05)\%$

Table 3.11: Multi-track,Muon Multi-track and Electron Multi-track overall trigger efficiency for 2017 data taking for the normalization channel

MASK Name	Trigger efficiency
Multi-track (MT)	$(80.03 \pm 0.32)\%$
Muon Multi-track (μMT)	$(79.35 \pm 0.32)\%$
Electron Multi-track (eMT)	$(64.11 \pm 0.40)\%$

Table 3.12: Multi-track,Muon Multi-track and Electron Multi-track overall trigger efficiency for 2016 data taking.

MASK Name	Trigger efficiency
Multi-track (MT)	$(92.51 \pm 0.05)\%$
Muon Multi-track (μMT)	$(88.85 \pm 0.05)\%$
Electron Multi-track (eMT)	$(85.32 \pm 0.05)\%$

Table 3.13: Multi-track,Muon Multi-track and Electron Multi-track overall trigger efficiency for 2017 data taking. The efficiency for the μMT and eMT masks is computed considering an energy E>15GeV and E>25 GeV respectively.

Chapter 4

Vertex reconstruction

In this chapter a procedure for estimating the position of the kaon decay vertex based on the method of least-squares fitting, implemented within the NA62 analysis framework is discussed. The performance of the method in obtaining the vertex position is assessed with MC simulated events and data. [89].

4.1 The method

The goal of the method is to estimate the vertex position by combining the trajectories of a set of charged particles under the assumption that they originate (or in the case of the kaon track - end) in a common interaction point. The inputs to the vertex fit are the parameters and covariance matrices of the tracks provided by the STRAW and the GTK reconstructions.
The algorithm described here is based on the Billoir - Fruhwirth - Regler implementation [90] for vertex least-squares fitting (LS). The LS method is a global fit of the vertex position and track momenta which considers the combined vector of parameters of all, n, tracks in the event and the 5n$\times$5n matrix of their covariance elements. However, the NA62 experiment is interested in kaon decays where we expect up to three tracks (+ the kaon track) only. Moreover the fitted STRAW and GTK tracks are assumed to have no cross-track correlation. This allows us to decompose the covariance matrix into lower rank sub-matrices and hence reduce the number of operations involved in matrix inversions ($\sim$ O(N^3)) by a factor of 10.

Tracks can be locally parametrized by a 5-dimensional vector m_i , where *i* enumerates the track number. The NA62 uses the following parametrization at a reference plane

Z = const:

$$\theta_{X,i}, \theta_{Y,i}, X_i, Y_i, P_i \tag{4.1}$$

where the reference plane Z could be defined at the first STRAW chamber. These track parameters are viewed as virtual measurements within the vertex LS formalism which aims to find the best estimate of the vertex position $\vec{x}$ and the three-dimensional new track parameters $\vec{q_i}$ at the vertex position.

$$\vec{x}(x, y, z) \qquad \text{vertex coordinates,} \tag{4.2}$$

$$\vec{q_i}(\theta_{x,i}, \theta_{y,i}, P_i) \qquad \text{slopes and momentum of track } i, \tag{4.3}$$

$$\vec{m}_i(\theta_{X,i}, \theta_{Y,i}, X_i, Y_i, P_i) \qquad \text{parametrization of the measured track } i \tag{4.4}$$

If the true vertex position and momentum ($\vec{x}$,$\vec{q_i}$) of track *i* are known the $\vec{m_i}$ can be expressed as:

$$\vec{m_i} = h(\vec{x^t}, \vec{q_i^t}) + \vec{v_i} \tag{4.5}$$

where h is a function which maps the vector of parameters $\vec{q}$ into the vector of measurements $\vec{m}$ and $\vec{v_i}$ is the measurement noise. The solution of the vertex fit is the set of parameters q that minimize the χ^2 function:

$$\chi^2 = [\vec{m} - h(\vec{q})]^T W [\vec{m} - h(\vec{q})] \tag{4.6}$$

where W is the weight matrix, defined as the inverse of the combined covariance matrix of all measurements, as defined in Appendix A. In the LS the measurement model h must be linear in the unknown parameters q. If that is not the case, and indeed for the NA62 parametrization it is not, the model has to be linearised. Expanding around the current (or initial and best known) estimate of the vertex parameters ($x^{(0)}$,$q_i^{(0)}$), which, for NA62, is the vertex position estimated with the CDA method and the tracks momentum measured with STRAW. All details of the method can be found in Appendix A.

4.1.1 Momentum constraint

In cases like the $K \to \pi\mu e$ decay, in which the decay is fully reconstructed using the charged tracks in the final state, the additional information of the GTK on the measured kaon momentum can be used in the fit to constraint the sum of the momenta of the tracks. However, such a momentum constraining term in the vertex χ^2 Eq. 4.6

would have non-zero derivatives to all momentum vectors and it will be difficult to include in the presented LS formulation. Instead, the momentum constraint is applied by using the Kalman filter formula after the vertex LS fit has converged. Effects due to non-linearity can be ignored if the change in the total momentum is small.

4.1.2 Magnetic field in the decay volume

The residual magnetic field in the decay region, which is due to the geomagnetic field and the magnetization of the decay tank, has been measured in 2013 and the results are reported in [91, 92][1]. The residual magnetic field is an important issue for decay in flight experiments; for example from a kinematic point of view it gives rise to a polar angle dependence of the reconstructed invariant mass. A routine to propagate the charged particles in the field has been implemented within the NA62 framework. In addition to particle tracking the routine has been expanded to propagate trough the field also the covariance matrix of the track parameters. The magnetic field components have been measured in 39 z-planes in the range from z_0= 105.795 m to z_0 =177.845 m. The field is not homogeneous and the track propagation is done in steps. The dependence of the momentum kick in x and y on the field components B_x, B_y and B_z is parametrized with low-order polynomials which are recalculated at each z-plane. Although the effect of the field correction on the precision of the vertex LS fit is small, it has been demonstrated that it results in improved invariant mass and kaon z-position resolution (see Section 4.2).

4.2 Performance studies with MC and Data

The performance of the LS method is assessed with $K^+ \to \pi^+\pi^+\pi^-$ events using both MC simulated events and data events. The selection procedure is the same for MC and data samples except for small refining applied in the data sample to clean it from eventually pileup events.

Only events with three tracks reconstructed in the STRAW with hits in at least three chambers, with a χ^2 <20, a momentum P <60GeV and within the geometrical acceptance of the four STRAW chambers and of the CHOD have been considered.

The vertex seed position is determined by finding the CDA between each pair of tracks and then taking the mean of the centers of all CDA line segments.

[1] Numerically, the magnitude of the vertical component of the Earth field in Geneva is about 0.3 G, which provides a field integral of about 0.003 Tm and a momentum kick of 1 MeV/c to charged particles (|q|= 1) at 25 GeV on a path length of 100 m.

4.2.1 Study with Monte Carlo sample

The performance studies done on MC shows that a fast convergence of the LS fit ($\Delta\chi^2 << 0$) with three iterations being sufficient. The χ^2 distribution of the fit (Figure 4.1) shows a good agreement with the probability density function with three degrees of freedom (as it is in the case of 3 tracks with 5 degrees of freedom each, 3 fitted vertex coordinates and 3 momentum parameters per fitted track, without considering the kaon track).

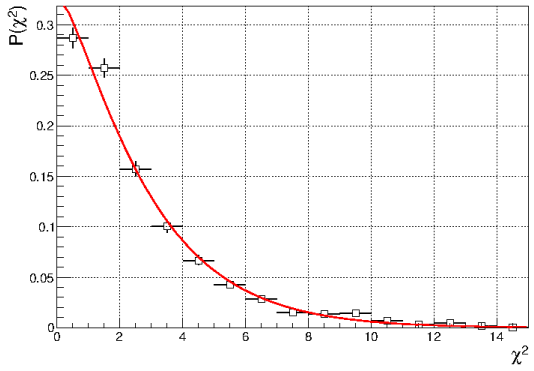

Figure 4.1: χ^2 distribution of the vertex parameters, obtained with the LSF method, fitted with the χ^2 probability density function with $k = 3$ degrees of freedom.

The performance of the LS method compared to the CDA-based method has been assessed with respect to the true value, using the MC sample. The effect of including in the vertex measurement the kaon track has evaluated.

The LSF improves the vertex position by $\sim$30% with respect to the CDA-based estimation (as reflected by the RMS in Table 4.1). The LSF improves also the track momentum (Table 4.2). It has a strong impact on the slopes (θ_x,θ_y) and almost negligible effect on the momentum magnitude P as expected since the momentum magnitude is not needed for the parametrization of the track trajectories and it changes during the LSF only because of the non-zero covariances with the other track parameters.

Including the kaon track in the fit leads to further improvement on the vertex position, having stronger effect on the x and y coordinates than the z (Figure 4.2). Similarly, the precision on the track slopes improves significantly while the momentum P remains almost unchanged (Figure 4.3). However, using the momentum of the kaon track to

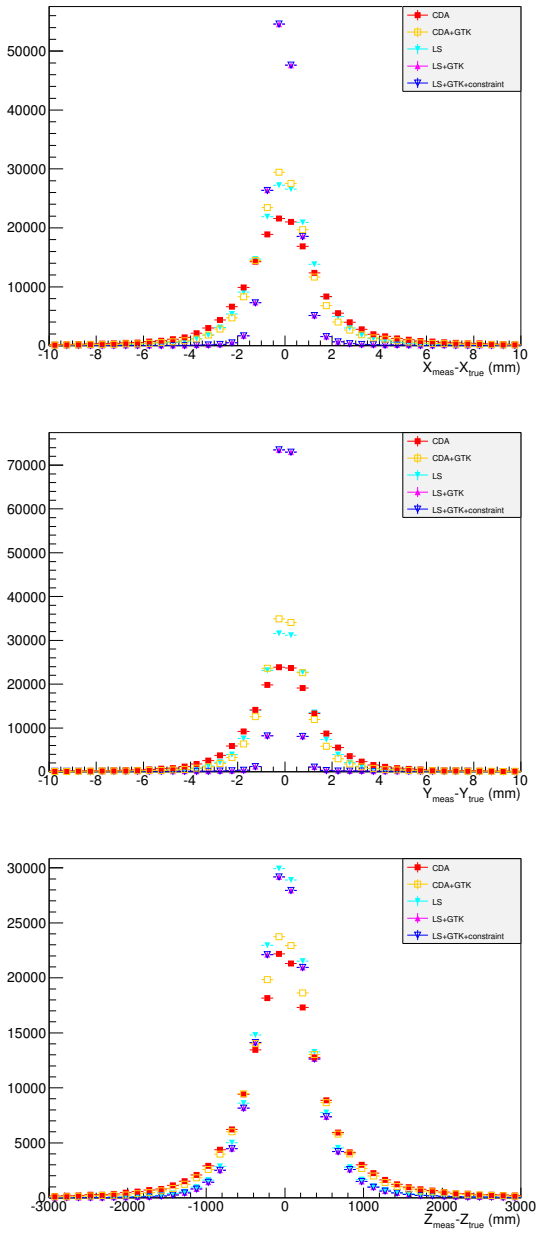

Figure 4.2: Distribution of the measured vertex x, y and z coordinates around the true vertex position, obtained using a K3π MC sample.

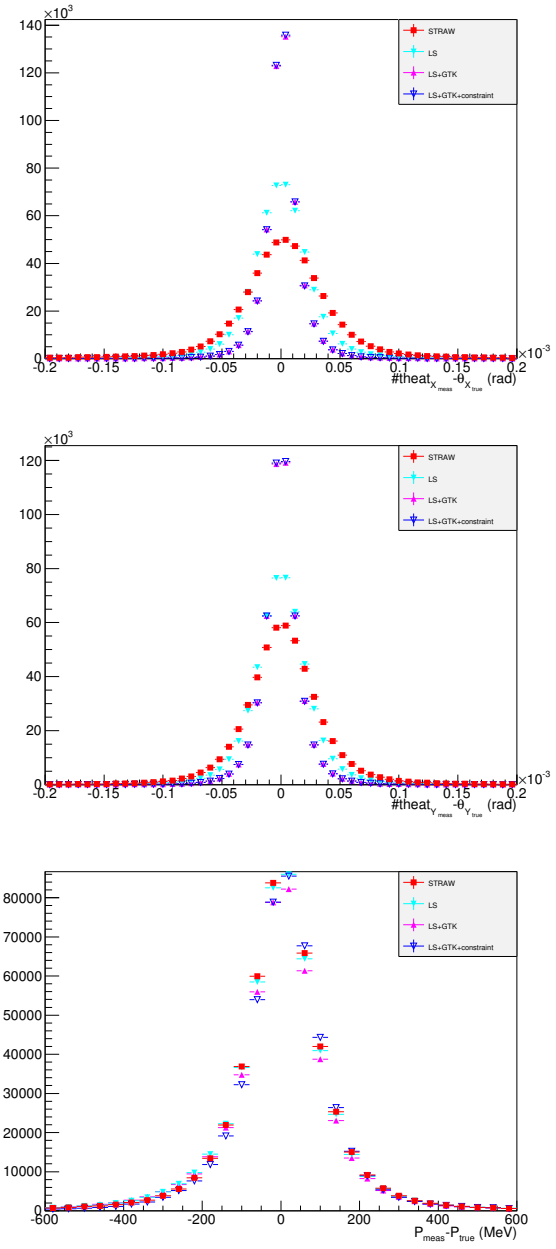

Figure 4.3: Distribution of the measured θ_x, θ_y and P track momentum parameters around their true values, obtained using a K3π MC sample.

apply a constraint on the sum of the pion track momenta gives a $\sim$20% improvement in P and as a consequence in the invariant mass (Figure 4.4).

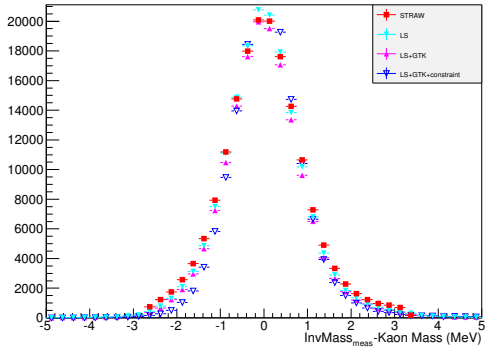

Figure 4.4: Distribution of the measured invariant mass respect to the kaon mass, obtained using a K3π MC sample.

	CDA	CDA + GTK	LSF	LSF + GTK	LSF + GTK + P_{tot} constraint
X RMS (mm)	2.32	1.68	1.49	0.49	0.49
Y RMS (mm)	1.61	1.03	1.18	0.08	0.08
Z RMS (mm)	624.83	593.68	423.45	412.87	412.85

Table 4.1: RMS of the vertex coordinates measured using the different methods and constraints obtained using a K3π MC sample.

	STRAW	LSF	LSF + GTK	LSF + GTK + P_{tot} constraint
θ_x RMS (μrad)	45.39	27.12	14.54	14.67
θ_y RMS (μrad)	35.10	23.94	14.44	14.45
P RMS (MeV/c)	149.68	139.49	135.19	115.97
M_{inv} RMS (MeV/c^2)	1.12	1.00	0.97	0.83

Table 4.2: RMS of the track momentum components measured using the different methods and constraints obtained using a K3π MC sample.

4.2.2 Study with Data

A study of the LS fit procedure is presented also based on data taken during the 2016 data taking. Plots shown in this section are done selecting $K^+ \to \pi^+\pi^+\pi^-$ events only on control triggers. The control trigger corresponds to a minimum bias condition, based on the NA48-CHOD. The implemented trigger condition asks for at least one coincidence of hits in the same quadrant of the horizontal and vertical planes of the detector. The $K^+ \to \pi^+\pi^+\pi^-$ event selection is as presented for the MC sample, except for additional requests meant to clean the sample from possible pileup tracks (detailed description of the $K^+ \to \pi^+\pi^+\pi^-$ selection has been presented in Section 3.2.1).

The distributions of the reconstructed vertex position and invariant mass of the three tracks at the vertex position computed using the LS method is shown in Figure 4.5(top). As expected most of the events populate the region around the kaon mass, covering a Z-vertex position form 95 m to 185 m, while the standard fiducial decay region is the [105,180]m region. A small percentage of events, $\sim$5% having a wrong invariant mass is concentrated between 90 m and 102 m. This behavior is due to the momentum kick given by the TRIM5. Indeed the momentum assigned to those tracks at the vertex position is wrong and it must be corrected for the effect of the TRIM5 Figure 4.5.

In Figure 4.6 the distribution of the difference between the Z-vertex position obtained wit the LS method and the CDA method is reported. It shows a peak around zero and a resolution $\sigma_{dVtx} = 160$mm. Assuming the results on the CDA and LS Z-vertex position resolutions obtained with MC and considering that the two quantities are fully correlated, the resolution $\sigma_{dVtx} = 160\text{mm}^2$ is in agreement with what obtained from the MC study. This means that there is, also in real data, an improvement on the Z-vetex position resolution.

[2] $\sigma^2_{dVtx} = \sigma^2_{cda} + \sigma^2_{LS} - 2\sigma_{cda}\sigma_{LS}$

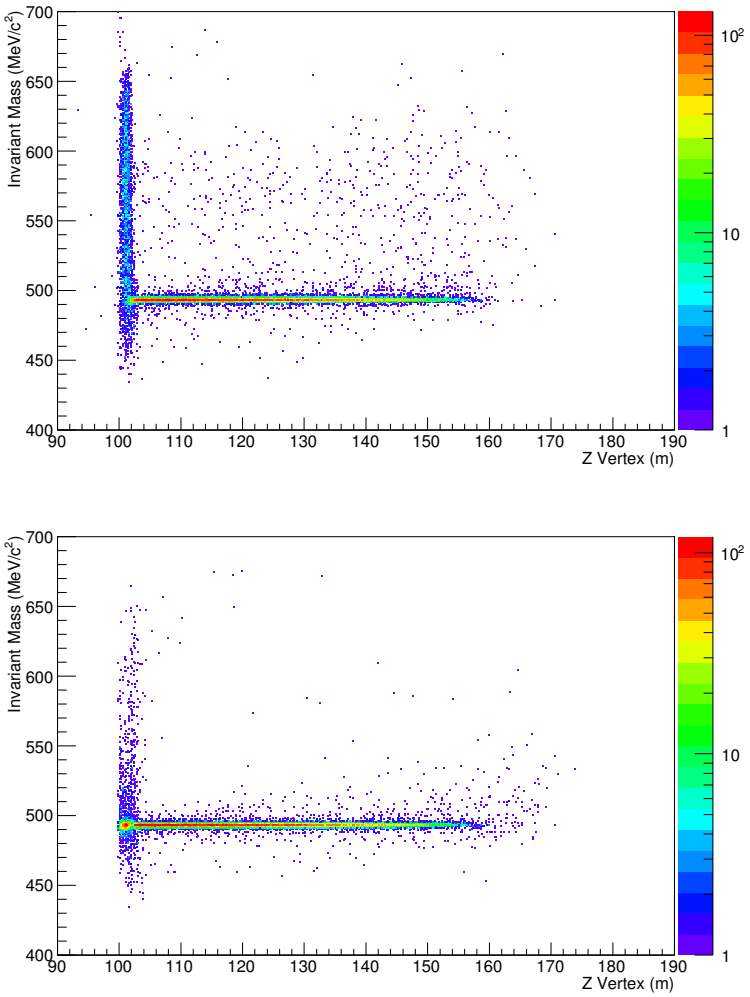

Figure 4.5: Distribution of the $K^+ \to \pi^+\pi^+\pi^-$ invariant mass as a function of the Z-vertex position using the LS method (top) from real data. The bottom plot shows the $K^+ \to \pi^+\pi^+\pi^-$ invariant mass as a function of the Z-vertex position distribution after the TRIM5 correction for those events with a vertex position below the third GTK station

4.3 Conclusions

The results, obtained with a MC sample, show an improved vertex position and track momenta as compared to using a simpler CDA based vertex estimator. Also, including the GTK track in the fit allows for further improvement on the track momenta and the kaon invariant mass resolution.

The data sample has been used mainly to prove the functioning of the LS method. Since there are no data samples in which the vertex position is known for sure, it is impossible to measure the resolution of the vertex position from data, but it has been proved that also in data there is an improvement on the Z-vetex position resolution, with respect to the CDA method.

The Least Squared method for the vertex fitting presented in this chapter has been implemented within the NA62 framework and it is an official method used also in other analyses to reconstruct the vertex position. In this work the vertex is reconstructed using LS method, without including the GTK track but adding the propagation in the residual magnetic field present in the decay volume. Although the effect of the field correction on the precision of the vertex LS fit is small, it results in improved tracks momenta and directions and thus improved invariant mass resolution of $\sim 3\%$ with respect to the LS method without the field correction.

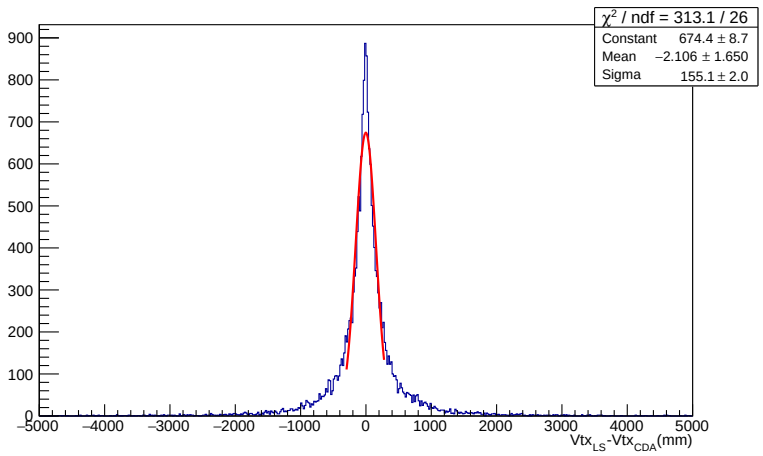

Figure 4.6: Distribution of the difference between the z-vertex position obtained with the LS method and the CDA method.

Chapter 5

Particle Identification

The NA62 detector has a particle identification (PID) system with high performance. It is composed by the KTAG, to identify kaons in the beam; the RICH to identify downstream tracks and mainly to separate pions, muons and electrons; the electromagnetic calorimeter(LKr) and the hadronic calorimeter(MUV1+MUV2) to distinguish downstream particles using the information on the energy deposition and the fast muon detector, MUV3, to identify muons. The detectors have been described in detail in Section 2.

In this section the PID strategy used in the $K \rightarrow \pi\mu e$ analysis is presented. It is based on RICH, LKr, and MUV3 information.The PID strategy has been tested with both MC and data samples, selecting both single-track and three-track kaon decays and pion, muon, electron identification efficiencies have been evaluated.

5.1 Detectors and variables used in PID

LKr

The LKr detector is used to distinguish between pions, muons and electrons, using the quantity E/P, which represents the ratio between the energy deposited by a particle in the electromagnetic calorimeter and its momentum measured with the STRAW detector. The E/P quantity helps to separate between electrons and all other particles. Electrons/positrons produce electromagnetic showers and all energy is released within the detector; thus the E/P ratio for e^+/e^- is close to 1 for each particle momentum.

On the contrary the LKr standalone cannot be used to distinguish between pions and muons. Muons are seen by the detector as a minimum ionizing particle (MIP) and the average energy deposited is of the order of few hundred MeV corresponding to a E/P close to zero.

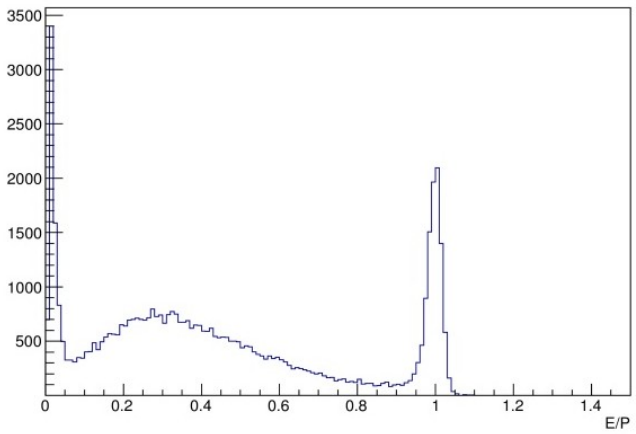

Figure 5.1: Combined LKr energy over momentum distribution for pions, muons and electrons extracted from data.

Pions on the other hand produce hadronic showers that cannot be fully contained in the LKr, subsequently the energy deposited is a fraction of the total energy, depending on the track momentum and the starting point of the shower within the LKr detector. The corresponding E/P distribution is a broad distribution covering a range form 0 to ~ 0.9. This means that, in some cases, pions can behave as a MIP and cannot be distinguished from muons. There is also a non zero probability that pions release all their energy in the LKr; in these cases pions can be confused as electrons.

The E/P distribution extracted from real data, for each kind of particle is shown Figure 5.1. The pion sample is obtained selecting $K^+ \to \pi^+\pi^0$decays, the muon sample selecting $K^+ \to \mu\nu$ and the electron sample selecting $K^+ \to \pi^0 e^+\nu$ (see Section 5.3).

MUV3

The MUV3 detector is a fast muon detector located after a iron wall of 80 cm; It produces a signal only if the track is a muon and it is used to select or reject muons.

RICH

The RICH is a Ring Imaging Cerenkov detector. Its setup is optimized to detect single positive charged particles, which means that the mirror plane is tilted in order to maximize the collection of light from positive charged particles, nevertheless it can be used to identify also negative charged particles.

The software reconstruction uses a likelihood fit to reconstruct rings. For each reconstructed track in the STRAW the algorithm computes the likelihood $\mathcal{L}_{hyp}$((5.1)) under several particle hypothesis: pion, muon, electron, kaon or background:

$$\mathcal{L}_{hyp} = \sum_{n}^{N_{Obs}} ln\left((\frac{\rho}{d_n} \times Gauss(R_{hyp}, \sigma_{res}, d_n) + \rho_{bkg} \right) \tag{5.1}$$

where N_{Obs} is the number of hits in the RICH in time with the track, R_{hyp} is the reconstructed ring radius, d_n is the distance of hits to the predicted ring center, obtained from the track extrapolation to the RICH, σ_{res} is the ring resolution extracted from the standard Single Ring Algorithm, ρ is the expected line density and ρ_{bkg} is the background hits area density.

The $\mathcal{L}_{hyp}$ obtained is normalized to be at maximum equal to one and the most likelihood hypothesis is defined as the hypothesis with the largest $\mathcal{L}_{hyp}$.

The likelihood value for each hypothesis itself, together with the most likely hypothesis are used to discriminate between pions, muons and electrons in the momentum range between 10 GeV and 35 GeV.

In particular to identify a particle as A-type respect to B-type and C-type a variable R_A, called likelihood ratio, is build as follows:

$$R_A = \frac{\mathcal{L}(A)}{\mathcal{L}(B) + \mathcal{L}(C)} \tag{5.2}$$

If a track is compatible with the A-hypothesis, then the likelihood value to be A-type is much bigger than the likelihood to be B-type and C-type and the corresponding

likelihood ratio is much bigger than 1. To positively identify a track as A-type, B-type or C-type, the corresponding likelihood ratio must satisfy the condition

$$R_i > 1.1 \text{ where } i = A, B, C \tag{5.3}$$

In the context of NA62 A-type, B-type and C-type refers to pion, muon and positron. The condition on $R_i > 1.1$ has been choosen in order to reject problematic events ($R_i = 1$) for which the same probability is associated to multiple hypothesis.

A representation of the likelihood ratio is shown in Figure 5.2. The plots show the inverse of the likelihood ratio, used here only to better represent the results. The plots refer to a sample of muon selected from data , following the Kμ2 selection criteria. As can be seen most of the selected tracks are compatible with the muon hypothesis ($1/R_\mu$ <0.9)(top plot), while <1% of the tracks are compatible with the pion hypothesis(bottom plot).

The R_i quantity is used to identify both positive and negative tracks, while the most likely hypothesis is checked only if the track is positively charged.

The three hypothesis are checked if a track has a momentum between [15,35] GeV, since the RICH Cerenkov threshold for pions is $\sim$ 12 GeV, for muons is $\sim$ 9 GeV and it is of few GeV for electrons. If a track has a momentum between [10,15] GeV only the electron and muon hypothesis are tested. In all other cases the PID relies on the LKr and MUV3 only.

5.2 PID Selection

Muon

Tracks are identified as muons if: a) there is a signal associated to the track in the MUV3 in a time window of $\pm$2 ns respect to the KTAG time, b) the E/P<0.2.
If the track momentum is between [10,35] GeV, the RICH is also used.
Positive track:

- Most likely hypothesis is to be a muon;
- $R_\mu = \frac{\mathcal{L}(\mu)}{\mathcal{L}(\pi)+\mathcal{L}(e)}$ >1.1 for P[15,35] GeV;
- $R_\mu = \frac{\mathcal{L}(\mu)}{\mathcal{L}(e)}$ >1.1 for P[10,15] GeV;

Negative track:

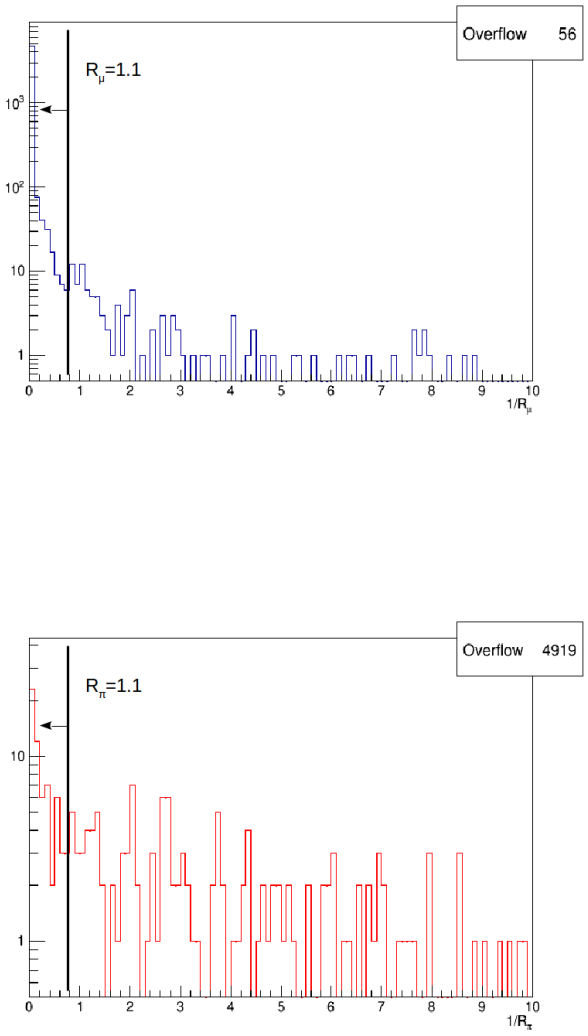

Figure 5.2: Output of the inverse of R_i for a sample of Kμ2 extracted from data without any PID selection. The top plot is the distribution of $1/R_i$ being a muon ($1/R_\mu$), while the bottom plot is the distribution of $1/R_i$ being a pion ($1/R_\pi$). In the plots also the threshold value used to identify particles ($R_i > 1.1$, $1/R_i < 0.9$) is reported.

- $R_\mu = \frac{\mathcal{L}(\mu)}{\mathcal{L}(\pi)+\mathcal{L}(e)} > 1.1$ for P[15,35] GeV;
- $R_\mu = \frac{\mathcal{L}(\mu)}{\mathcal{L}(e)} > 1.1$ for P[10,15] GeV;

Pion

Tracks are identified as pions if: a) there is no signal associated in the MUV3 and b) the E/P$<$0.95
If the track momentum is between [15,35] GeV, the RICH is also used:
Positive track:

- Most likely hypothesis is to be a pion;
- $R_\pi = \frac{\mathcal{L}(\pi)}{\mathcal{L}(\mu)+\mathcal{L}(e)} > 1.1$ for P[15,35] GeV;

Negative track:

- $R_\pi = \frac{\mathcal{L}(\pi)}{\mathcal{L}(\mu)+\mathcal{L}(e)} > 1.1$ for P[15,35] GeV;

Electron

Tracks are identified as positrons(electrons) if: a) if there is no signal associated to the track in the MUV3 and b) the 0.95$<$E/P$<$1.05.
If the track momentum is between [10,35] GeV, the RICH is also used:
Positive track:

- Most likely hypothesis is to be a positron;
- $R_\mu = \frac{\mathcal{L}(e)}{\mathcal{L}(\pi)+\mathcal{L}(\mu)} > 1.1$ for P[15,35] GeV;
- $R_\mu = \frac{\mathcal{L}(e)}{\mathcal{L}(\mu)} > 1.1$ for P[10,15] GeV;

Negative track:

- $R_\mu = \frac{L(e)}{\mathcal{L}(\pi)+\mathcal{L}(\mu)} > 1.1$ for P[15,35] GeV;
- $R_\mu = \frac{\mathcal{L}(e)}{\mathcal{L}(\mu)} > 1.1$ for P[10,15] GeV;

5.3 Kaon decays selection

The kaon decays selected to perform the PID efficiency study are: $K^+ \to \mu^+\nu$, $K^+ \to \pi^+\pi^0$, $K^+ \to \pi^0 e^+\nu$, $K^+ \to \pi^+\pi^0$Dalitz ($\pi^0 \to e^+e^-\gamma$) and $K^+ \to \pi^+\pi^+\pi^-$.
The event selection is done using only kinematics information as defined in the following sections to avoid any possible bias.
For each decay the selection acceptance (5.4) and the level of contamination from other decays are evaluated using MC samples.

$$A = \frac{n_{pass}}{N_{gen}} \tag{5.4}$$

where n_{pass} is the number of events passing the selection criteria, N_{gen} is the number of generated events. In the following the contamination level is express in terms of sample purity defined as:

$$P = \frac{1}{1 + \frac{Br_{bkg}}{R \times A \times Br_{sig}}} \tag{5.5}$$

where Br_{sig} and Br_{bkg} are the branching ratios of the signal and background channels respectively, A is the signal acceptance and R is the background rejection factor defined as the ratio between all generated background events and the number of background events passing the criteria to select the signal (R=$N^{bkg}_{gen}/n^{bkg}_{pass}$).

5.3.1 Single track selection

The selection of single-track events is performed asking for a single positive track well reconstructed by the STRAW detector ($\chi^2 < 40$) within the STRAW, LKr, CHOD and NA48-CHOD acceptance.

The selected track has to be associated, spatially and in time, to a CHOD and NA48-CHOD candidate and has to match a kaon candidate, reconstructed by the Gigatracker.

The vertex between the downstream track and the kaon, reconstructed with the Closest Distance Approach (CDA) method, is required to be within the standard fiducial decay region, [105,180]m.

Further checks are then performed: there must be a KTAG candidate in time with respect to the vertex time, the latter defined as the mean value of the CHOD candidate and NA48-CHOD candidate associated to the track. The selected track has to be in $\pm$ 3 ns with respect to the trigger and the best matching Gigatracker candidate.

The last check is that there is no LAV, IRC and SAC activity in $\pm$ 3ns with respect to the trigger time.

In Figure 5.3 the distribution of the squared missing mass built under the pion hypothesis with respect the track momentum, after the single track event selection, is shown. In the plot the main kaon single track decay can be distinguished.

Specific conditions are then verified in order to select the different single-track decay.

$K^+ \to \mu^+\nu$

To select $K^+ \to \mu^+\nu$ event is required that:

- the selected track is in the MUV3 acceptance and it has a MUV3 candidate associated in time and space;
- the track can have no cluster or one cluster associated in the LKr, within $\pm$ 5 ns;
- the squared missing mass variable: $M^2_{miss} = (P_\mu - P_K)^2 < 3\sigma^2_M$, where $\sigma_M \sim 60$ MeV is the $K^+ \to \mu^+\nu$ mass resolution.

The Kμ2 selection acceptance results to be (15.55$\pm$0.02)% and no events from K2π, Ke3, Kμ3 MC samples pass the Kμ2 selection criteria, so there is no contamination in the sample up to 10^6.

$K^+ \to \pi^+\pi^0$

To select $K^+ \to \pi^+\pi^0$event is requested that:

- the selected track is in the MUV3 acceptance but there are no MUV3 candidates associated to it;
- In the LKr there must be three well separated clusters of which one associated to the track. The other two clusters must have no candidates in time with the event and in the CHOD and NA48-CHOD within $\pm$ 20 mm with respect to extrapolated cluster position, in order to avoid possible photon conversion.

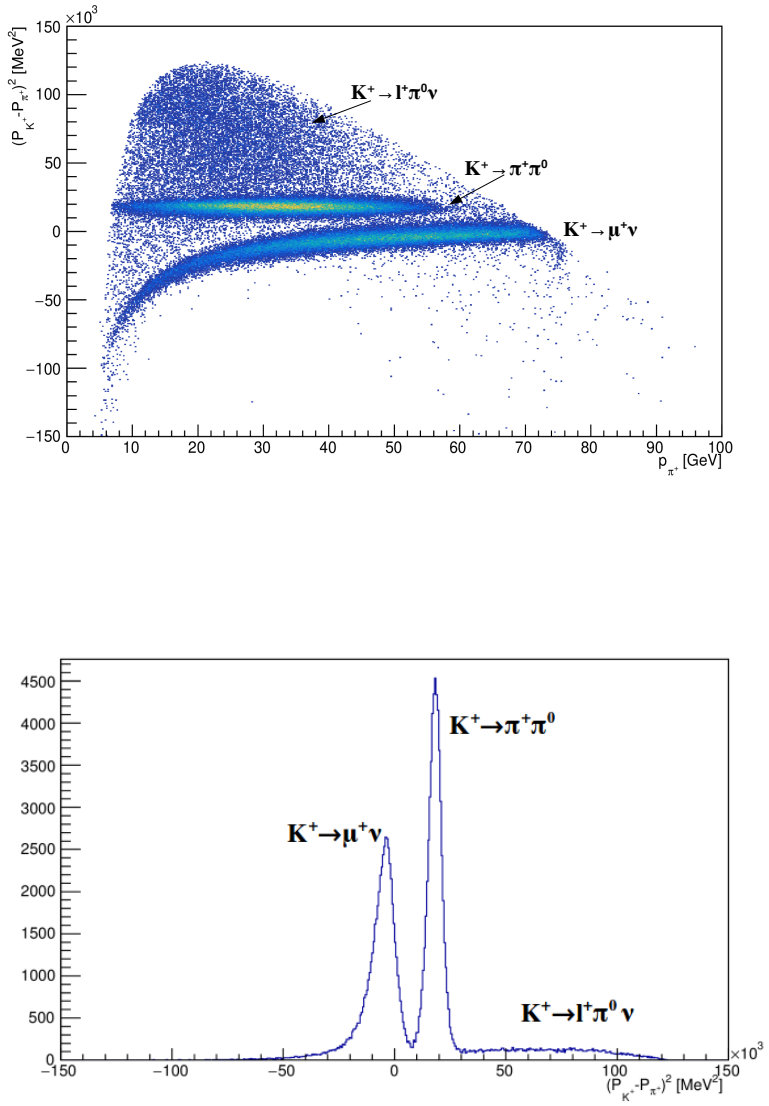

Figure 5.3: Output of the single track selection. The plot on top shows the distribution of the squared missing mass built under the pion hypothesis with respect to the track momentum. The $K^+ \to \pi^+\pi^0$, $K^+ \to \mu^+\nu$ squared missing mass distribution are well visible. Also the distribution due to $K^+ \to \pi^0 e^+\nu$and $K^+ \to \pi^0\mu^+\nu$ can be recognized. The plot on bottom is the projection of the plot on top in the squared missing mass.

- the reconstructed squared missing mass: $M^2_{miss} = (P_\pi - P_K)^2 < M^2_{\pi^0} \pm 3\sigma^2_{\pi^0}$, where $\sigma_{\pi^0} \sim 55$ MeV is the $K^+ \to \pi^+\pi^0$mass resolution.

The $K^+ \to \pi^+\pi^0$selection acceptance is (9.00±0.03)%; possible contamination come from $K^+ \to \pi^0 e^+\nu$and $K^+ \to \pi^0\mu^+\nu$. The sample purity assessed with 10^6 $K^+ \to \pi^0 e^+\nu$and 10^6 $K^+ \to \pi^0\mu^+\nu$ MC events, results to be ∼99.55%.

$K^+ \to \pi^0 e^+\nu$

To select $K^+ \to \pi^0 e^+\nu$event is requested that:

- the track is in the MUV3 acceptance but it has no MUV3 candidates associated in time;
- the number of LKr reconstructed clusters in time with respect to the trigger (± 5 ns) and well separated, has to be equal to three and one of the three clusters must be associated to a track;
- the squared missing mass $M^2_{miss} = (P_e - P_K)^2$ is greater than $M^2_{\pi^0} + (5\sigma^2_{\pi^0})$, which mean it is well outside the region occupied by K2pi;
- it is requested that the squared missing mass built under the muon hypothesis is well outside the $K^+ \to \mu^+\nu$ range;
- the squared missing mass built under the pion hypothesis is not compatible with the $K^+ \to \pi^+\pi^0$and $K^+ \to \pi^+\pi^+\pi^-$ region
- the missing mass squared built with the track and the two photons is compatible with the kaon mass hypothesis: $M^2_{miss} = (P_K - P_e - P_{\pi^0}) < 3\sigma_M$.

The $K^+ \to \pi^0 e^+\nu$selection acceptance results to be (3.24±0.02)% and the sample purity is ∼89.20%. The major contamination(∼ 10%) comes from the $K^+ \to \pi^0\mu^+\nu$. The purity level has been evaluated using ∼ 10^6 $K^+ \to \pi^0\mu^+\nu$ and ∼ 10^6 $K^+ \to \pi^+\pi^0$MC events.

5.3.2 Three track selection

To select three-track vertex events the following conditions are checked: there are three tracks reconstructed with the STRAW and well separated, of which two positive and one negative.

All tracks have to be in the CHOD and NA48-CHOD acceptance and a CHOD and/or a NA48-CHOD candidate has to be associated to each track.

Also each track must be in the LKr acceptance and MUV3 acceptance.

Then a three-track vertex is reconstructed and verified to be within [105,180] m range.

The selected event must be in time ($\pm$ 3 ns) with respect to a KTAG candidate, where the event time is the mean of the three tracks time. The last condition is the no LAV, IRC and SAC activity in a $\pm$ 3 ns time window, with respect to the trigger time.

$K^+ \to \pi^+\pi^+\pi^-$

After the common selection of a three-track vertex to select K3π the following kinematic cuts are applied:

- the three track total momentum $|P_{tot}| < P_K + 3\sigma_P$ where $\sigma_P \sim 1$ GeV/c is the total momentum resolution
- the invariant mass $|M_{inv}| < M_K + 3\sigma_M$; where $\sigma_M \sim 850$ MeV/c^2 is the mass resolution.

The $K^+ \to \pi^+\pi^+\pi^-$ selection acceptance is (10.70$\pm$0.03)%; it has been found that sources of contamination are the Ke4 and the Kμ4 decays. However the level of contamination is very low and the sample purity has been evaluated to be $\sim$ 99.99% (using sample of 10^6 Ke4 and Kμ4)

$K^+ \to \pi^+\pi^0$ Dalitz

The selection of $K^+ \to \pi^+\pi^0$Dalitz decay requires additional condition to be checked, with respect to the general three-track vertex selection.

- There must be four clusters in the LKr in time with the trigger in a $\pm$ 5 ns time window of which one have to be associate to the selected tracks.
- the reconstructed π^0 mass:$|M_{\pi^0}^{reco} - M_{\pi^0}| < 3\sigma_{\pi^0}$ where $\sigma_{\pi^0} = 12MeV$ is the π^0 mass resolution
- the reconstructed kaon mass:$|M_K^{reco} - M_K| < 3\sigma_K$ where $\sigma_K \sim 7MeV$ is the mass resolution.

Additional checks on the position of the photons from the reconstructed π^0 with respect to the selected ones and on the squared missing mass $M^2_{miss} = (P_K - P_\pi)^2$ are applied.

The $K^+ \to \pi^+\pi^0$Dalitz decay selection acceptance results to be (0.45±0.01)% and the main source of contamination are: Ke4, Kμ4. However the level of purity has been evaluated to be ∼99.99%, using 10^6 $K^+ \to \pi^+\pi^- e^+\nu$ and $K^+ \to \pi^+\pi^-\mu^+\nu$ events.

5.4 PID Efficiency Results

The PID selection efficiency, including LKr, MUV3 and RICH, as described at the beginning of this chapter, is reported here for pion, muon and positrons selected from single track events. Afterwards the results for positive and negative pion and for positron and electron selected from K3π and K2π_D events respectively, are presented.

A comparison between the PID efficiencies obtained with data samples and MC samples is also reported. Note that in all MC samples used for this study also daughter particles decays are simulated in particular: $\pi \to \mu\nu$ and $\mu \to e\nu$ can induce some fake inefficiency like in data, even though the kinematic variables used in the selection (total momentum, missing mass, invariant mass, etc...) cut most of these events, so the expected effect should be small (per-mille level).

The PID efficiency study shows some disagreement between data and MC: one of the reason could be due to the non well reproduced pion energy deposition in the LKr, with respect to data or it can be found in the ring fit algorithm of the RICH which works better for MC samples, as in the MC there are no pile-up events producing additional hits.

A comparison between the PID efficiency for single track events and multi-tracks events is reported, showing better results for single track events, as expected. Indeed the detector is optimized to fit the single track kinematics and also each detector can handle better single tracks events. For example in multi tracks kaon decays there could be cases where the two positive tracks are close; in these cases in the RICH it is not easy to reconstruct and separate the two ring associated and this can introduce some inefficiency with respect to single track events.

Since the PID efficiency study shows different performance for real data and MC samples, and as the final $K \to \pi\mu e$ selection acceptance is evaluated including the PID criteria and using MC, it is needed to take into account of those discrepancies in the final results as a systematic uncertainty.

What is missing in this study is the measurement of the PID efficiency for positive and negative muons from multi-tracks events. This can be performed using for example the $K^+ \to \pi^+\mu^+\mu^-$ rare decay, of which, on the other hand, the sample available considering the 2016A+2017A data is of only few thousand events. In addittion since the PID procedure presented here use also the RICH output, the statistics of the sample would be reduce further. For this reason at the moment for positive and negative muons from multi-tracks events the results obtained for positive and negative pions selected from K3π are used and included in the final results presented in this work. Also as the performance for muons and pions are not exactly the same, the above assumption would introduce an addittional systematic error in the final results.

5.5 Single Track Events

Positive Muons

The muon identification efficiency for positive muons is obtained selecting $K^+ \to \mu^+\nu$ events. In Figure 5.4 the efficiency to identify the track as a muon, as a function of the track momentum in bins of 5 GeV, from real data (top plot) and MC (bottom plot) is reported. In this plot the probability to mis-identify the track as a pion(red) or a positron(blue) is also reported. The same results are shown in Table 5.1 and Table 5.2 in the momentum range [10,65] GeV for data and MC respectively.

Positive Pions

The pion identification efficiency for positive pions is evaluated using a sample of $K^+ \to \pi^+\pi^0$. In Figure 5.5 the efficiency to identify the track as a pion, as a function of the track momentum in bins of 5 GeV, from data (top plot) and MC (bottom plot) is reported; the mis-identification of the track as a muon or a positron is also shown. The same results, in the momentum range [10,65] GeV, are listed in Table 5.3 and Table 5.4 for a data and MC sample, respectively.

Positron

The positron identification efficiency is evaluated using a sample of Ke3 decays. In Figure 5.6 the efficiency to identify the track as a positron, as a function of the track

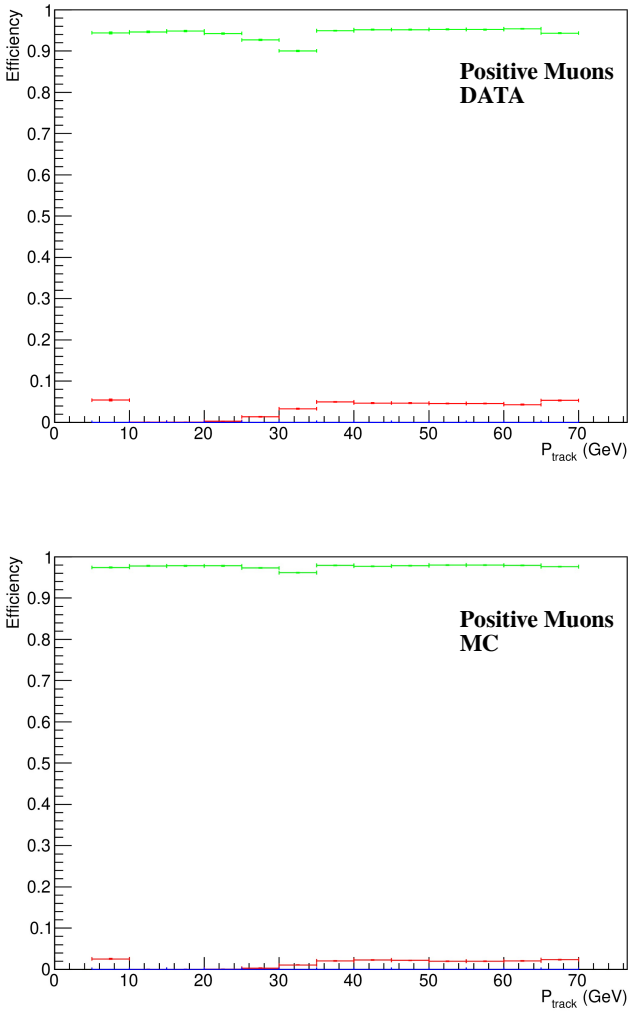

Figure 5.4: Muon identification efficiency as a function of the track momentum in bins of 5 GeV. In green is the probability to identify a muon-like track as a muon, in red the probability to be identified as a pion and in blue the probability to be identified as a positron. On the top plot are the identification probability obtained from data; while the bottom plot has been made with a $K^+ \to \mu^+\nu$ MC sample.

Momentum range (GeV)	μ^+ (10^{-2})	π^+ (10^{-2})	e^+ (10^{-2})
[10,15]	94.4±0.2	5.4±0.2	<0.02
[15,20]	94.7±0.2	0.01±0.03	<0.01
[20,25]	94.9±0.2	0.01±0.02	<0.01
[25,30]	94.2±0.2	0.3±0.04	<0.01
[30,35]	92.7±0.1	1.3±0.1	<0.007
[35,40]	90.1±0.2	3.3±0.1	<0.006
[40,45]	94.9±0.1	5.0±0.1	<0.005
[45,50]	95.2±0.1	4.7±0.1	<0.004
[50,55]	95.2±0.1	4.7±0.1	<0.004
[55,60]	95.4±0.1	4.5±0.1	<0.004
[60,65]	94.4±0.1	4.3±0.1	<0.004

Table 5.1: Particle Identification probability for a sample of positive muons (DATA), selected from $K^+ \to \mu^+\nu$ decays, to be identified as a muon, pion or positron, in each momentum bin. Since with the analyzed number of events ($\sim 5 \times 10^5$) no tracks have been identified as positrons a limit on the positron mis-identification at 90% C.L has been set.

Momentum range (GeV)	μ^+ (10^{-2})	π^+ (10^{-2})	e^+ (10^{-2})
[10,15]	97.7±0.1	0.02±0.1	<0.02
[15,20]	97.8±0.1	0.02±0.02	<0.01
[20,25]	97.8±0.1	0.01±0.01	<0.01
[25,30]	97.3±0.1	0.3 ±0.02	<0.01
[30,35]	96.1±0.1	1.1 ±0.03	<0.007
[35,40]	97.9±0.1	2.1 ±0.05	<0.006
[40,45]	97.9±0.1	2.3 ±0.1	<0.005
[45,50]	97.8±0.1	2.2 ±0.1	<0.004
[50,55]	98.0±0.1	2.0 ±0.1	<0.004
[55,60]	98.0±0.1	2.0 ±0.1	<0.004
[60,65]	98.0±0.1	2.1±0.1	<0.004

Table 5.2: Particle Identification probability for a sample of positive muons (MC), selected from $K^+ \to \mu^+\nu$ decays, to be identified as a muon, pion or positron, in each momentum bin. Since with the analyzed number of events ($\sim 5 \times 10^5$) no tracks have been identified as positrons a limit on the positron mis-identification at 90% C.L has been set.

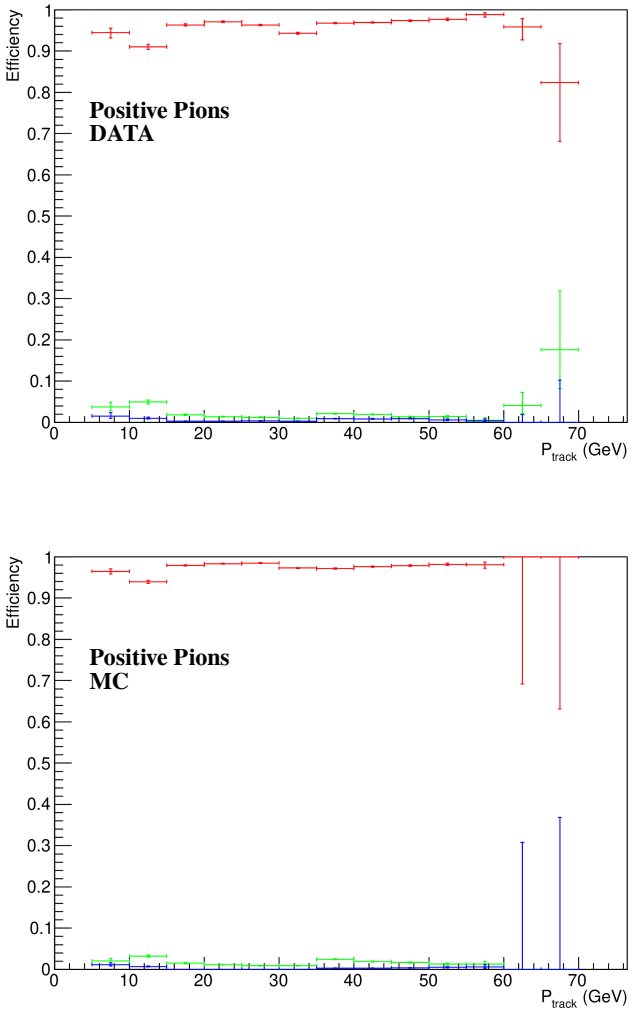

Figure 5.5: Pion identification efficiency as a function of the track momentum in bins of 5 GeV. In red is the probability to identify a pion-like track as a pion, in green the probability to be identified as a muon and in blue the probability to be identified as a positron. The top plot is obtained from a data sample collected in 2017; while in the bottom plot the identification efficiency obtained from a MC sample is shown.

Momentum range (GeV)	π^+ (10^{-2})	μ^+ (10^{-2})	e^+ (10^{-2})
[10,15]	91.1±1.1	4.9±1.1	1.0±0.8
[15,20]	96.3±0.6	1.8±0.5	0.3±0.2
[20,25]	97.1±0.3	1.4±0.2	0.3±0.1
[25,30]	96.3±0.2	1.3±0.1	0.4±0.1
[30,35]	94.3±0.2	0.9±0.1	0.3±0.1
[35,40]	96.8±0.2	2.1±0.1	0.9±0.1
[40,45]	96.9±0.2	1.9±0.1	0.9±0.1
[45,50]	97.4±0.2	1.3±0.1	0.9±0.1
[50,55]	97.7±0.2	1.4±0.2	0.6±0.1
[55,60]	98.9±0.3	0.5±0.3	0.3±0.2

Table 5.3: Particle Identification probability for a sample of positive pions (DATA), selected from $K^+ \to \pi^+\pi^0$decays, to be identified as a pion, muon or positron, in each momentum bin.

Momentum range (GeV)	π^+ (10^{-2})	μ^+ (10^{-2})	e^+ (10^{-2})
[10,15]	94.0±0.6	3.2±0.5	1.0±0.4
[15,20]	97.9±0.4	1.5±0.3	0.3±0.2
[20,25]	98.3±0.2	1.1±0.1	0.3±0.02
[25,30]	98.5±0.1	0.9±0.1	0.4±0.01
[30,35]	97.3±0.1	0.9±0.1	0.3±0.01
[35,40]	97.1±0.1	2.4±0.1	0.9±0.01
[40,45]	97.6±0.1	1.9±0.1	0.9±0.1
[45,50]	97.9±0.1	1.7±0.1	0.9±0.1
[50,55]	98.1±0.2	1.3±0.2	0.6±0.1
[55,60]	98.1±0.2	1.2±0.2	0.3±0.2

Table 5.4: Particle Identification probability for a sample of positive pions (MC), selected from $K^+ \to \pi^+\pi^0$decays, to be identified as a pion, muon or positron, in each momentum bin.

momentum in bins of 5 GeV, for real data (top plot) and MC (bottom plot) is reported. It is also reported the probability of mis-identify the track as a pion(red) or a muon(green). The same results are shown in Table 5.5 and Table 5.6 in the momentum range [10,55] GeV for a data sample and a MC sample, respectively.

As mentioned before the $K^+ \to \pi^0\mu^+\nu$ contaminates the sample at $\sim$10% level, as a consequence the data sample used to evaluated the positron PID efficiency is not enough clean. Indeed in Figure 5.6 (top) it is clear the effect of real muons, inducing an increase of the muon identification, which it is not present in the MC plot. For this reason, using the presented Ke3 selection, the positron PID efficiency cannot be extracted direcly from data.

5.6 Three Track Events

Three-track vertex events are used to evaluate the efficiency of the PID procedure for multi track events and for positive and negative tracks.

Pions

The K3π events have been used to extract the PID efficiency for positive and negative pions.

The results are shown in Figure 5.7 and reported in Table 5.7 and Table 5.8 for positive pion (data and MC sample respectively).
In Figure 5.8, Table 5.9 and Table 5.10 the particle identification efficiency for negative pion is reported.

A comparison between positive and negative pions is shown (Figure 5.9) as a function of the track momentum, showing a better performance for positive pions than negative. Also in Figure 5.14 the comparison between the positive poin efficiency obtained from MC sample for single track events and three tracks events is reported, pointing out a better performance of the PID procedure for single track events, as expected from the experiment design.

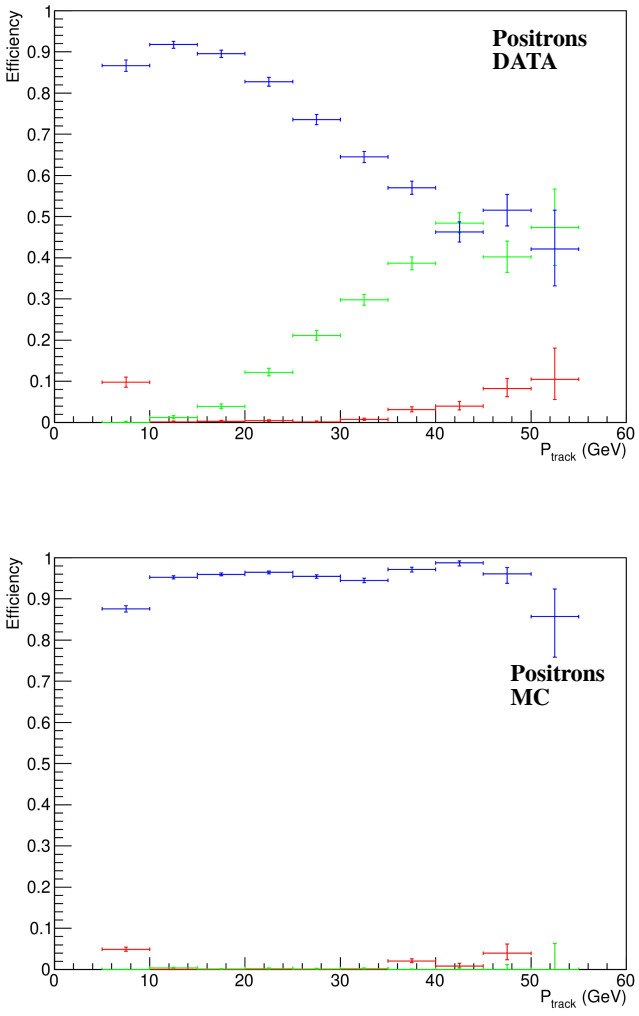

Figure 5.6: Positron identification efficiency as a function of the track momentum in bins of 5 GeV for a data sample (top) and a Ke3 MC sample (bottom). In blue is the probability to identify a positron-like track as a positron, in red the probability to be identified as a pion and in green the probability to be identified as a muon. In the plot on top, it is clear the effect of the Kμ3 contamination: the tracks tagged as muons in this case are mostly real muons and not due to particle mis-identification.

Momentum range (GeV)	e^+ (10^{-2})	π^+ (10^{-2})	μ^+ (10^{-2})
[10,15]	91.8±1.3	0.2±1.3	1.2±0.2
[15,20]	89.6±0.8	0.3±0.2	3.9±0.4
[20,25]	82.8±0.9	0.4±0.2	12.2±0.6
[25,30]	73.6±1.0	0.2±0.3	21.2±0.9
[30,35]	64.5±1.2	0.7±0.2	29.8±1.2
[35,40]	57.0±1.3	3.1±0.3	38.6±1.3
[40,45]	46.3±1.6	3.4±0.6	48.5±1.6
[45,50]	51.5±2.5	8.2±1.1	40.2±2.5
[50,55]	42.1±3.8	10.5±2.5	47.3±3.8

Table 5.5: Particle Identification probability for a sample of positrons (DATA), selected from $K^+ \to \pi^0 e^+ \nu$decays, to be identified as a positron, pion or muon in each momentum bin.

Momentum range (GeV)	e^+ (10^{-2})	π^+ (10^{-2})	μ^+ (10^{-2})
[10,15]	95.3±0.7	4.9±0.5	<0.1
[15,20]	95.3±0.4	<0.01	0.3±0.2
[20,25]	96.4±0.3	<0.01	0.1±0.1
[25,30]	95.5±0.3	<0.01	0.2±0.1
[30,35]	94.5±0.4	<0.01	0.1±0.1
[35,40]	97.1±0.5	<0.1	0.2±0.2
[40,45]	98.7±0.5	2.1±0.5	<0.2
[45,50]	96.1±0.5	0.8±0.7	<0.5
[50,55]	85.7±1.5	3.9±2.3	<1.1

Table 5.6: Particle Identification probability for a sample of positrons (MC), selected from $K^+ \to \pi^0 e^+ \nu$decays(MC), to be identified as a positron, pion or muon in each momentum bin. Upper limits at 90% C.L have been set for those bins in which no events are presents.

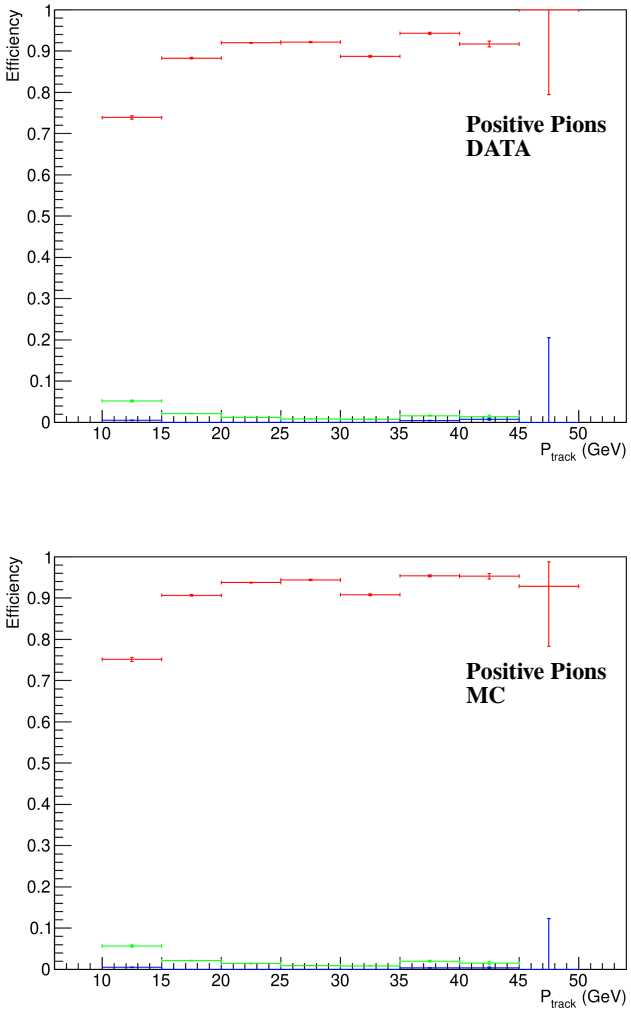

Figure 5.7: Positive pion identification efficiency as a function of the track momentum in bins of 5 GeV. In red is the probability to identify a pion-like track as a pion, in blue the probability to be identified as an electron and in green the probability to be identified as a muon. The top plot has been done with a data sample, while the bottom plot is obtained from a MC sample.

Momentum range (GeV)	π^+ (10^{-2})	μ^+ (10^{-2})	e^+ (10^{-2})
[10,15]	73.9±0.4	5.2±0.2	0.5±0.1
[15,20]	88.3±0.2	2.1±0.1	0.01±0.01
[20,25]	92.0±0.1	1.2±0.1	0.01±0.01
[25,30]	92.2±0.1	0.8±0.1	0.01±0.01
[30,35]	88.7±0.2	0.8±0.1	0.01±0.01
[35,40]	94.3±0.2	1.6±0.1	0.40±0.011
[40,45]	91.7±0.7	1.4±0.3	0.7±0.2

Table 5.7: Particle Identification probability for positive pions (DATA), selected from $K^+ \to \pi^+\pi^+\pi^-$ decays, to be identified as a pion, muon or positron, in each momentum bin.

Momentum range (GeV)	π^+ (10^{-2})	μ^+ (10^{-2})	e^+ (10^{-2})
[10,15]	75.1±0.5	5.7±0.3	0.5±0.1
[15,20]	90.7±0.1	2.1±0.1	0.01±0.01
[20,25]	93.8±0.1	1.4±0.1	0.003±0.006
[25,30]	94.4±0.1	1.0±0.1	0.007±0.009
[30,35]	90.8±0.2	0.9±0.1	0.01 ±0.01
[35,40]	95.4±0.2	2.0±0.2	0.4±0.1
[40,45]	95.3±0.6	1.4±0.4	0.4 ±0.2

Table 5.8: Particle Identification probability for positive pions (MC), selected from $K^+ \to \pi^+\pi^+\pi^-$ decays, to be identified as a pion, muon or positron, in each momentum bin.

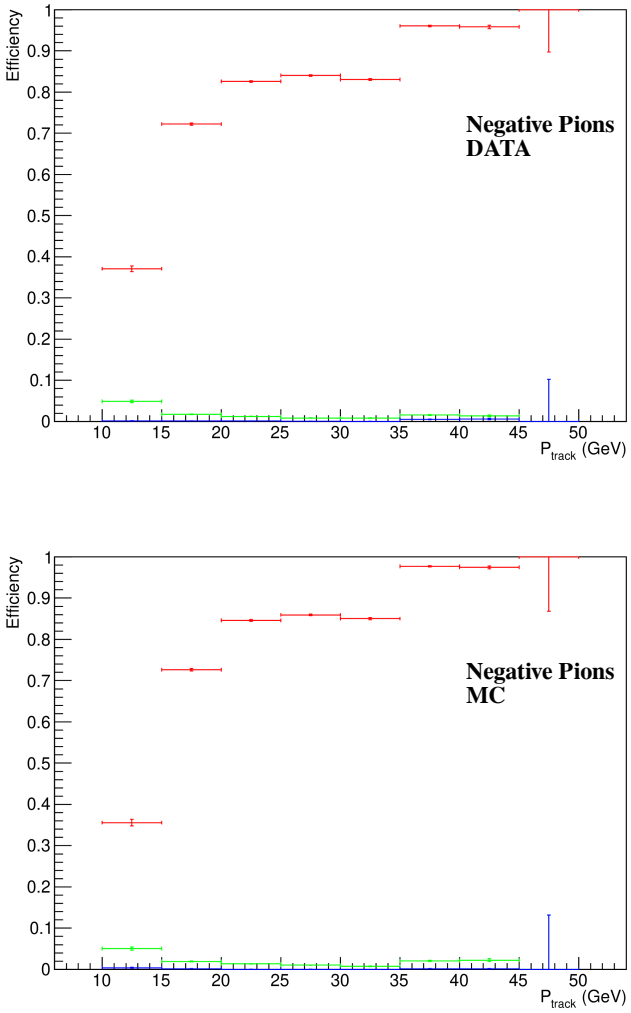

Figure 5.8: Negative pion identification efficiency as a function of the track momentum in bins of 5 GeV. In red is the probability to identify a pion-like track as a pion, in blue the probability to be identified as an electron and in green the probability to be identified as a muon. The top plot has been done with a data sample, while the bottom plot is obtained from a MC sample.

Momentum range (GeV)	π^- (10^{-2})	μ^- (10^{-2})	e^- (10^{-2})
[10,15]	37.1±0.7	4.8±0.3	0.20±0.08
[15,20]	72.2±0.3	1.7±0.1	0.10±0.02
[20,25]	82.6±0.2	1.2±0.1	0.10±0.02
[25,30]	84.0±0.2	0.8±0.1	0.04±0.01
[30,35]	83.1±0.2	0.8±0.1	0.02±0.01
[35,40]	96.1±0.2	1.5±0.1	0.50±0.07
[40,45]	95.8±0.4	1.3±0.3	0.6±0.2

Table 5.9: Particle Identification probability for negative pions (DATA), selected from $K^+ \to \pi^+\pi^+\pi^-$ decays, to be identified as a pion, muon or electron, in each momentum bin.

Momentum range (GeV)	π^- (10^{-2})	μ^- (10^{-2})	e^- (10^{-2})
[10,15]	35.6±0.8	5.0±0.4	0.4±0.1
[15,20]	72.6±0.3	1.9±0.1	0.20 ±0.03
[20,25]	84.6±0.2	1.3±0.1	0.02±0.01
[25,30]	85.9±0.2	1.0±0.1	0.02±0.01
[30,35]	85.0±0.2	0.8±0.1	0.01±0.01
[35,40]	97.7±0.1	2.0±0.1	0.20±0.5
[40,45]	97.5±0.3	2.2±0.3	0.10±0.1

Table 5.10: Particle Identification probability for negative pions (MC), selected from $K^+ \to \pi^+\pi^+\pi^-$ decays, to be identified as a pion, muon or electron, in each momentum bin.

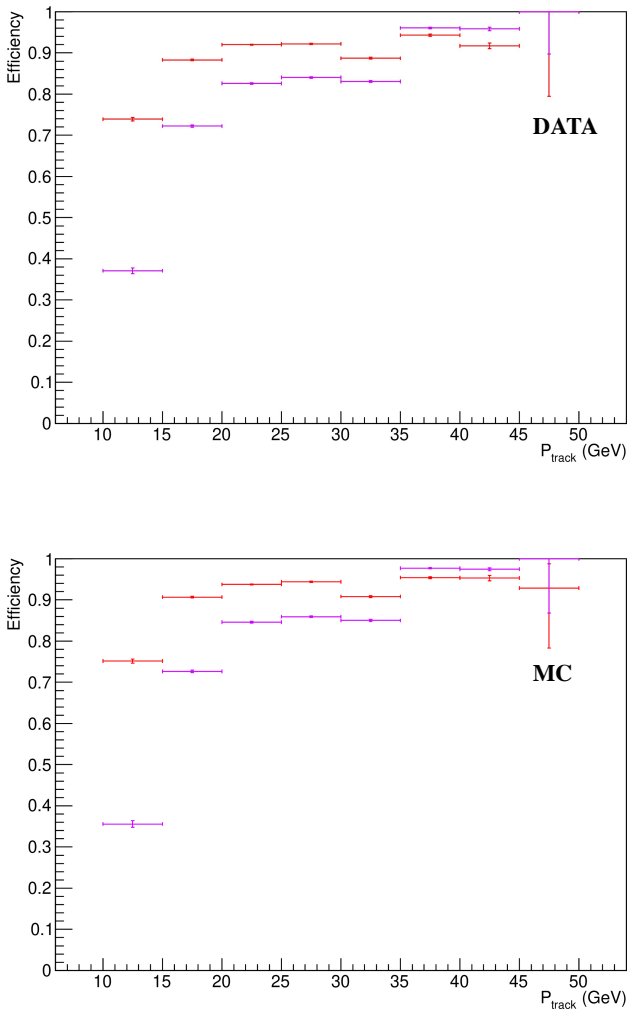

Figure 5.9: Negative and positive pion identification efficiency, for a data sample (top plot) and a MC sample (bottom plot) as a function of the track momentum in bins of 5 GeV. In red is the probability to identify a positive pion as a pion and in purple the probability to identify a negative pion as a pion.

Electron/Positron

The positron and electron PID efficiency in the case of multi-track events have been evaluated using a sample of K2π dalitz events. Due to the extremely low selection acceptance the available statistics is quite smaller than the other decays. The results are reported in Figure 5.10 and Table 5.11 for positrons and in Figure 5.11 and Table 5.13 for electrons. For completeness in Figure 5.12 and Table 5.15 are reported the results for positive pions selected with $K^+ \to \pi^+\pi^0$Dalitz.

As shown in Figure 5.14 the comparison between the positron efficiency obtained from MC sample for single track events and three tracks events pointed out a better performance of the PID procedure for single track events, as expected from the experiment design.

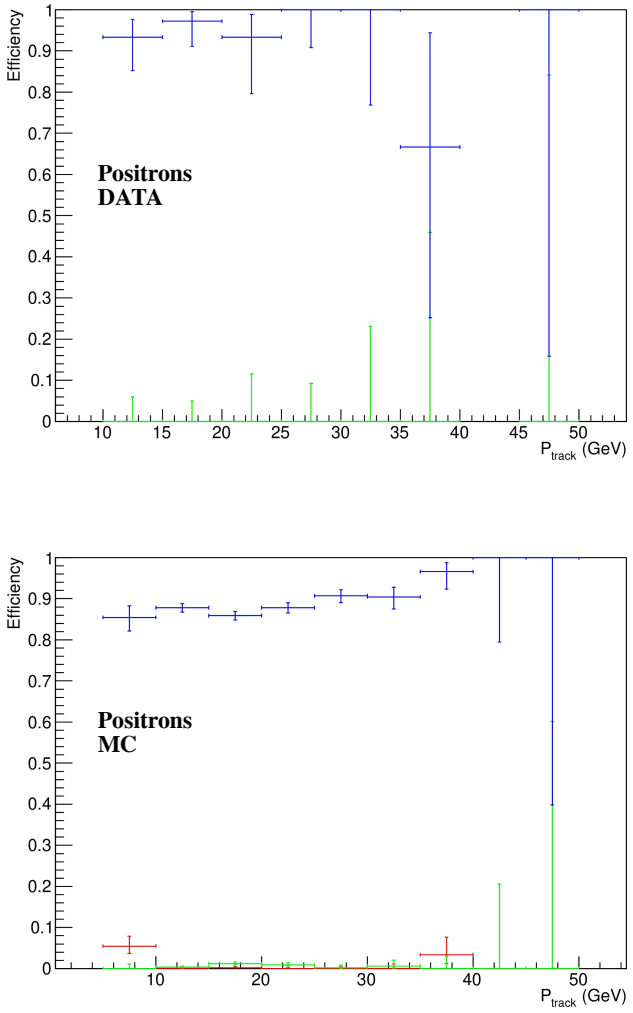

Figure 5.10: Positron identification efficiency as a function of the track momentum in bins of 5 GeV. In blue is the probability to identify a positron-like track as a positron, in red the probability to be identified as a pion and in green the probability to be identified as a muon. The top plot is done with a data sample, while the bottom plot is for a $K^+ \to \pi^+\pi^0$Dalitz MC sample

Momentum range (GeV)	e^+ (10^{-2})	π^+ (10^{-2})	μ^+ (10^{-2})
[10,15]	93.3±4.3	<7.7	<7.7
[15,20]	97.2±2.3	<6.4	<6.4
[20,25]	93.3±5.5	<15.3	<15.3
[25,30]	<98.8	<11.5	<11.5
[30,35]	<98.8	<32.8	<32.8
[35,40]	<79.6	<34.4	<34.4

Table 5.11: Particle Identification probability for positrons (DATA), selected from $K^+ \to \pi^+\pi^0$Dalitz decays, to be identified as a positron, pion or muon, in each momentum bin.

Momentum range (GeV)	e^+ (10^{-2})	π^+ (10^{-2})	μ^+ (10^{-2})
[10,15]	87.8±1.0	<0.3	<0.8
[15,20]	85.9±1.0	<0.6	1.2±0.4
[20,25]	87.8±1.2	<0.3	<1.6
[25,30]	90.7±1.3	<0.6	<1.0
[30,35]	90.4±2.4	<1.5	<2.5
[35,40]	96.6±2.1	<9.0	<3.9

Table 5.12: Particle Identification probability for positrons (MC), selected from $K^+ \to \pi^+\pi^0$Dalitz decays, to be identified as a positron, pion or muon, in each momentum bin.

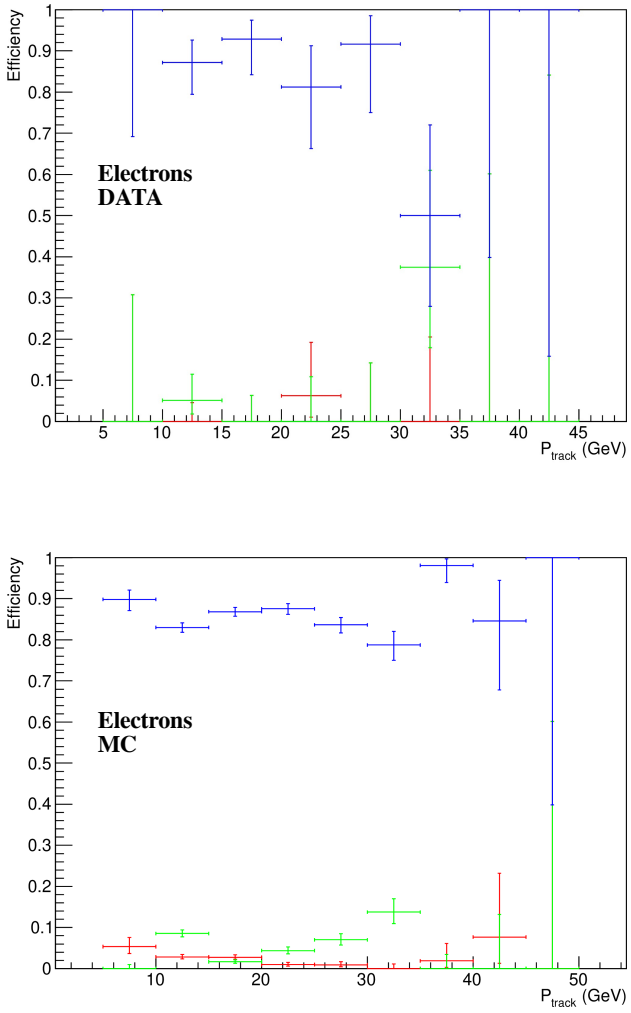

Figure 5.11: Electron identification efficiency as a function of the track momentum in bins of 5 GeV. In blue is the probability to identify an electron-like track as an electron, in red the probability to be identified as a pion and in green the probability to be identified as a muon. The top plot has been obtained with a data sample, while the bottom plot shows the efficiency evaluated with a MC sample.

Momentum range (GeV)	e^- (10^{-2})	π^- (10^{-2})	μ^- (10^{-2})
[10,15]	87.2±5.4	<5.9	<13.6
[15,20]	92.9±4.6	<8.2	<8.2
[20,25]	81.3±10.0	<24.4	<14.4
[25,30]	91.7±7.9	<19.2	<19.2
[30,35]	<61.5	<17.7	<51.4
[35,40]	<98.8	<43.3	<43.3

Table 5.13: Particle Identification probability for electrons (DATA), selected from $K^+ \to \pi^+\pi^0$Dalitz decays, to be identified as an electron, pion or muon, in each momentum bin.

Momentum range (GeV)	e^- (10^{-2})	π^- (10^{-2})	μ^- (10^{-2})
[10,15]	83.2±1.1	2.8±0.6	8.5±0.9
[15,20]	86.8±1.0	2.7±0.6	1.7±0.5
[20,25]	87.5±1.3	<1.7	4.4±0.9
[25,30]	83.6±1.8	<1.9	7.0 ±1.5
[30,35]	78.8±3.3	<1.5	13.8 ±3.3
[35,40]	98.1±1.6	<7.6	<4.3

Table 5.14: Particle Identification probability for electrons (MC), selected from $K^+ \to \pi^+\pi^0$Dalitz decays, to be identified as an electron, pion or muon, in each momentum bin.

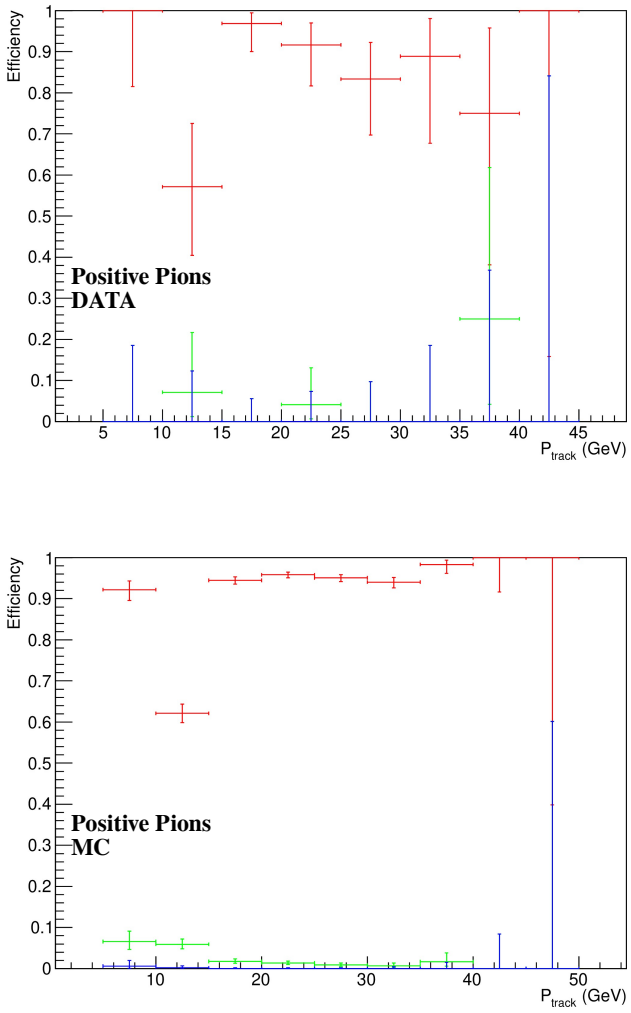

Figure 5.12: Pion identification efficiency as a function of the track momentum in bins of 5 GeV. In red is the probability to identify a pion-like track as a pion, in blue the probability to be identified as a positron and in green the probability to be identified as a muon. The top plot has been obtained with a data sample, while the bottom plot shows the efficiency evaluated with a MC sample.

Momentum range (GeV)	π^+ (10^{-2})	μ^+ (10^{-2})	e^+ (10^{-2})
[10,15]	<92.8	<27.8	<16.1
[15,20]	96.9±2.6	<7.1	<7.1
[20,25]	91.7±5.4	<16.2	<9.6
[25,30]	83.3±8.9	<12.8	<12.8
[30,35]	<88.8	<25.8	<25.8
[35,40]	<83.6	<48.8	<28.7

Table 5.15: Particle Identification probability for positive pions (DATA), selected from $K^+ \to \pi^+\pi^0$Dalitz decays, to be identified as a pion, muon or positron, in each momentum bin.

Momentum range (GeV)	π^+ (10^{-2})	μ^+ (10^{-2})	e^+ (10^{-2})
[10,15]	62.1±2.3	5.9±1.3	<0.5
[15,20]	94.5±0.8	1.7±0.6	<0.3
[20,25]	95.8±0.6	1.4±0.7	<0.2
[25,30]	95.1±0.8	<1.5	<0.3
[30,35]	94.0±1.1	<1.5	<0.5
[35,40]	98.3±1.1	<4.4	<1.9

Table 5.16: Particle Identification probability for positive pions (MC), selected from $K^+ \to \pi^+\pi^0$Dalitz decays, to be identified as a pion, muon or positron, in each momentum bin.

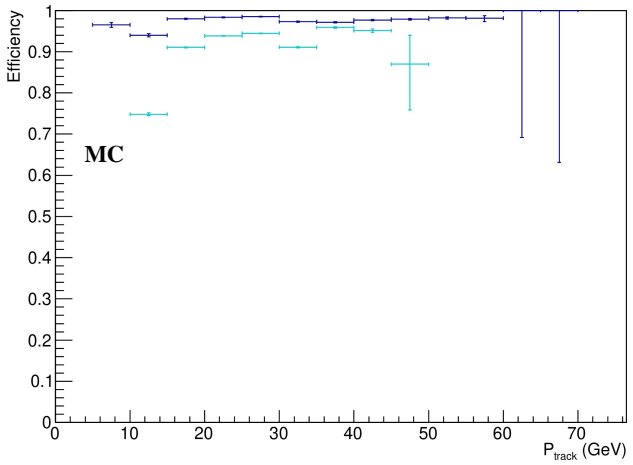

Figure 5.13: Pion identification efficiency as a function of the track momentum in bins of 5 GeV. In blue the pion efficiency for single track events from MC, in cyan the pion efficiency from three tracks events, specifically from K3π MC.

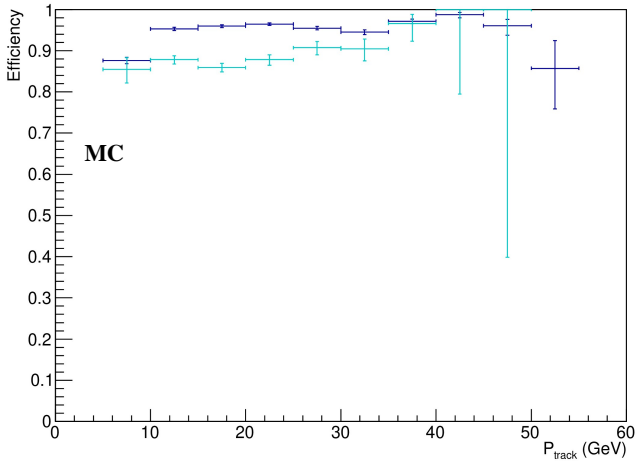

Figure 5.14: Positron identification efficiency as a function of the track momentum in bins of 5 GeV. In blue the positron efficiency for single track events from MC, in cyan the positron efficiency from three tracks events, specifically from K2π Dalitz MC.

5.7 Conclusions

In this chapter the study on the particle identification used in the analysis of $K \to \pi\mu e$ decays has been presented. The study was done both on single-track events, evaluating the PID efficiency for positive pions, muons and positron, and on three-track events in order to assess the PID efficiency for multi-track vertex.

The main purpose of the RICH, as proposed in the strategy for the $K^+ \to \pi^+\nu\bar{\nu}$ analysis is to increase the background rejection power of the NA62 detector, maintaining a good signal acceptance. The excellent performances of the RICH spill out from the results shown in this chapter. Even though the use of the RICH detector does not increase the PID efficiency, it has a fundamental role to heavily suppress the background in the [10,35] GeV momentum range, with respect to the momentum region where it is not used.

The results shown a good PID efficiency: for single track events the overall probability to identify a pion track as a pion is (96.2 $\pm$0.1)% while the probability to mis-identify that track as a muon is (1.8$\pm$0.1)% and as a positron (0.6$\pm$0.1)%. For a muon track the probability to be identified as a muon as been measured to be (94.20$\pm$0.05)% with a mis-identification probability as a pion equal to (3.50$\pm$0.03)% amd a positron mis-identification below 0.008% known at 90% CL. For positrons is not possible to take any conclusion since in the data sample the level of muons contamination from Kμ3 is at the level of 10%, assessed with a Kμ3 MC sample of 10^6 events.

The PID efficiency for multi-tracks events results lower than the single-track events: the decay kinematics and the hits multiplicity play a crucial role in the multi-tracks events in particular they affect the RICH performance. Differences have been spotted also between positive and negative tracks: the results show better performance in the case of positive tracks, as expected, as the full NA62 detector is optimized to detect positively charged particles and also in this case the RICH has a strong impact.

In particular the PID efficiency for positive and negative pions, selected from a sample of K3π events and for positrons and electrons, selected from a sample of K2π Dalitz decays have been presented. The results show a probability to identify a positive pion equal to (88.7$\pm$0.1)% with a mis-identification as a muon of (1.90$\pm$0.06)% and as a positron of (0.20$\pm$0.03)%. For negative pion the probability to be identified as a pion is (78.7$\pm$0.1)%, to be mis-identified as a muon is (1.70$\pm$0.07)% and to be mis-identified as an electron is (0.20$\pm$0.03)%. For positron and electron the results are less strong, due to the lack of statistics. However the results show a good positron/electron identification. The identification probability is of (95.0$\pm$8.0)% for positrons with a mis-identification as a pion/muon of 10.0% known at 90% CL. The

identification probability is of (88.0±15.0)% for electrons with a mis-identification as a pion/muon of 14.0% known at 90% CL.

As already mentioned the missing part of this study is the analysis of a sample of positive and negative muons from multi track events. The NA62 experiment collected the larger sample of $K^+ \to \pi^+\mu^+\mu^-$ in the world, made of few thousand events and the sample will increase with the 2018 data. This rare decay can be used to select a sample of positive and negative muons in order to asses the corresponding PID efficiency. At the moment this study is not included in the presented work and the it is assumed that the positive and negative muons PID efficiency is equal to the pion efficiency, assessed with K3π. As this is not the real case, an addittional contribution to the systematic error of the final result has to be take into account.

The analysis of $K \to \pi\mu e$ is performed using the same PID procedure presented in this section and the understanding of the particle mis-identification is extremely important for the background evaluation.

The results have been shown for both data and MC samples, proving that the agreement is not good enough to rely on MC sample, in order to understand and assess the PID system efficiency. On the other hand as the $K \to \pi\mu e$ signal selection acceptance is evaluated including the PID selection criteria and using the MC sample, it is foreseen to take into account of those discrepancies in the final results as a systematic uncertainty.

Chapter 6

The $K \to \pi\mu e$ analysis

As already mentioned in the introduction, the search for $K \to \pi\mu e$ decay presented in this work is based on two data samples: one collected in 2016 and the other in 2017. The data sample analyzed does not represent the full statistics collected in the two years, but for the time being only a fraction of the sample was fully processed.

A blind analysis has been performed in order to avoid any bias in the finalization of the event selection criteria. As it is explained in this chapter, due to the lack of statistics for some of the background kaon decays, the background estimation is not conclusive and it is quite rough. For this reason it is not possible to look inside the signal box. Nevertheless it is possible to give a first estimation of the branching ratios upper limit, taking into account the expected number of background events in the signal region, estimated with the available MC samples and assuming that the observed number of events is equal to zero or 1.

An upper limit(UL) on the three branching ratios $\mathcal{B}(K \to \pi\mu e\ )$ is set for 90% confidence level(CL) using the K3π decay as normalization channel; thanks to the similar kinematics between K3π and $K \to \pi\mu e$ most of the systematic effects, due to detector acceptance and trigger efficiencies, cancel, as shown in Section 3.

6.1 The sample

The data sample used for the analysis presented in this thesis is composed of two samples: one collected during the 2016 run at $\sim$30% of the design beam intensity, and the other during the 2017 run, taken with a beam intensity $\sim$60% of the design value.

As already mention in Section 3, the sample corresponds to the data collected with three trigger masks: the *Multi-Track*(MT) mask, which selects all multi-track events, the *Muon Multi-Track*(μMT) mask, which selects multi track events with at least one muon in the outer region of MUV3 and *Electron Multi-Track*(eMT) which selects multi track events with a energy deposition in the LKr E>20 GeV, then selects also events with electrons in the final state.

During the 2016 a set of filters has been developed within the NA62 framework in order to filter the data at the processing level according to the main analyses purpose. The used of filtered data helps each user to start with samples which are more clean and reduces the processing time of each analysis. For this analysis the data sets refer to the following sub-samples:

- *RestrictedThreeTrackVertex* sample: at least one 3-track vertex with χ^2 <40, Z_{Vtx} >102m, P_{track} <90 GeV/c, and all tracks reconstructed with 3/4 STRAW chambers and satisfying the standard STRAW acceptance conditions.
  This sample is used to select K3π events and compute the kaon flux.

- *MuEThreeTrackVertex* sample: filters out only control,MT, μMT, and eMT. For control and multi-track triggers, the conditions are identical to *RestrictedThree-TrackVertex*. For muon multi-track and electron multi-track triggers which are not control and not multi-track triggers, additionally one track of the vertex should have E/p>0.8 and one track should have MUV3 association. This sample is used for the $K \to \pi\mu e$ analysis.

The 2016 sample corresponds to 150 runs and 70k bursts, processed with the *v0.11.1* framework version, it is called 2016-A. While the 2017 sample is made of 74 runs and 74k bursts, processed with the *v0.11.2* framework version and it is called 2017-A. Even if the two samples have been processed with different versions of the framework, no major differences are present between the two.

At the processing level also a list of bad bursts for each detector, due to errors in data or inefficiencies is created, and at the analysis level those bursts can be skipped, in order to include in the analysis only good bursts.

The number of kaon decays analyzed in the two data samples are respectively:

$$N_K = (6.73 \pm 0.41) \times 10^{10} \quad \text{2016A}$$
$$N_K = (10.31 \pm 0.13) \times 10^{10} \quad \text{2017A}$$

More details on how the kaon flux is computed are presented in Section 6.3.

6.2 Three-track vertex

The selection strategy has been already presented in Chapter 3 but it is repeated in here. It is based on the reconstruction of a three-track vertex, which is common to the signal and the normalization channel selection. This preliminary selection aims to select good three-track events applying decisions on the tracks quality, acceptance, on the event timing and on the reconstructed vertex position.

A track is define as a *good track* if it satisfies the following conditions:

- it is within the four STRAW chambers acceptance;
- it is in the NA48-CHOD or CHOD acceptance;
- it is not in the LAVs acceptance;
- it is reconstructed using hits from at least three of the four STRAW chambers;
- the track reconstruction $\chi^2 < 30$;
- the reconstructed momentum is between 10 GeV and 65 GeV;
- it has a candidate associated in the NA48-CHOD or CHOD, which means spatially associated and within $\pm$ 10 ns (6 ns)with respect to the trigger time for 2016 (2017) data taking. If a candidate exists, its time is associated to the track.
- it has no other tracks reconstructed within a radius of 4 cm at the first STRAW chamber.

If the number of tracks passing the above requests is equal to three, further selection criteria at the event level are applied:

- At least one candidate in the KTAG, reconstructed with minimum 5 sectors and within $\pm$ 10 ns (6 ns)with respect to the trigger time for 2016 (2017) data taking, must exist;
- the three-track vertex, reconstructed with the LS method described in Section 4, has to be within the standard decay region [105,180] m [1];
- the total charge at the vertex is $Q = +1$;
- there is no LAV activity within $\pm$ 3 ns with respect to the trigger time.

All events passing the entire selection criteria are considered good three-track vertex and further requests can be applied on top of them to select any specific three-track kaon decay.

[1] Refer to the detector description in Section 2 for the NA62 reference frame

6.2.1 $K^+ \to \pi^+\pi^+\pi^-$ selection

To select K3π events from the data it is requested that each track has no MUV3 candidate associated, both spatially and in time within $\pm$ 1.5 ns (1.3 ns) with respect to the trigger time for 2016 (2017) sample. No other PID checks, using LKr or RICH, are applied, and $K^+ \to \pi^+\pi^+\pi^-$ events are selected with kinematics variables: the three-track total momentum ($\vec{P}_{3\pi}$) and the invariant mass ($M_{3\pi}$) (Figure 6.1) at the vertex:

$$\vec{P_{3\pi}} = \vec{P}_{\pi_1} + \vec{P}_{\pi_2} + \vec{P}_{\pi_3}, \quad M_{3\pi} = \sqrt{(P_{\pi_1} + P_{\pi_2} + P_{\pi_3})^2} \tag{6.1}$$

where P_{π_i} is the quadri-momentum of track *i* under the pion mass hypothesis.

In particular it is required that:

$$|\vec{P}_{3\pi}| = |\vec{P}_K| \pm 3\sigma_P, \tag{6.2}$$

$$M_{3\pi} = M_K \pm 3\sigma_M \tag{6.3}$$

where $\vec{P}_K$ is the kaon momentum, $M_K = 493.677$ MeV/c^2 is the kaon mass, $\sigma_P = 0.9$ GeV/c is the momentum resolution and $\sigma_M = 0.85$ MeV/c^2 is the invariant mass resolution. The effect of these two final cuts is visible in Figure 6.2. The top plot is the track angle versus momentum distribution for three-track vertex events before the kinematic cut on the total momentum and invariant mass. At this selection level there are still contamination from other kaon decays. Applying the cuts on $P_{3\pi}$ and $M_{3\pi}$ (bottom plot), the sample is cleaned up and the remaining events are only K3π. Applying the request on the total momentum the 8% of the events passing the three track event selection are rejected; then after the invariant mass cut a further 5% of the events are rejected. In Figure 6.3 is the total momentum versus invariant mass distribution for all events passing the three track vertex selection is shown, where the invariant mass is built under the K3π hypothesis. Events with wrong total momentum are mainly due to pion decays, $\pi \to \mu\nu$. In these events the neutrino carries part of the initial pion momentum, which is not taken into account in the final total momentum computation. Then the invariant mass reconstructed wrongly, as the mass hypothesis associated to the track is not correct.

A further check of the selection quality is the data-MC agreement. In Figure 6.4 the data-MC comparison is shown, looking at track momentum, track angle and vertex position.

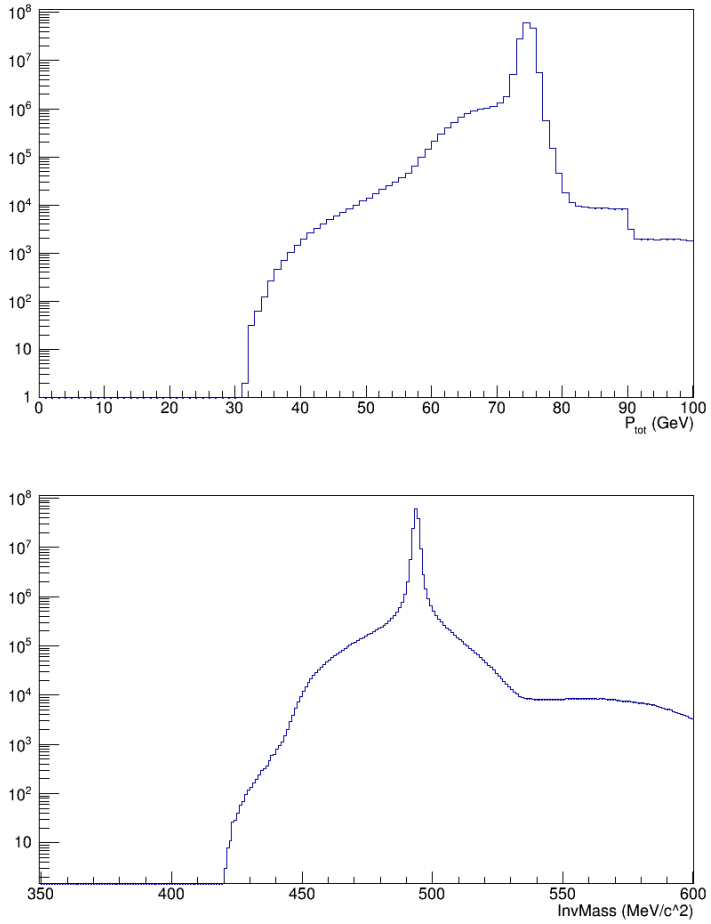

Figure 6.1: Three-track vertex reconstructed total momentum, $|\vec{P}_{3\pi}|$ (top plot) and invariant mass, $M_{3\pi}$ (bottom plot) from a data sample.

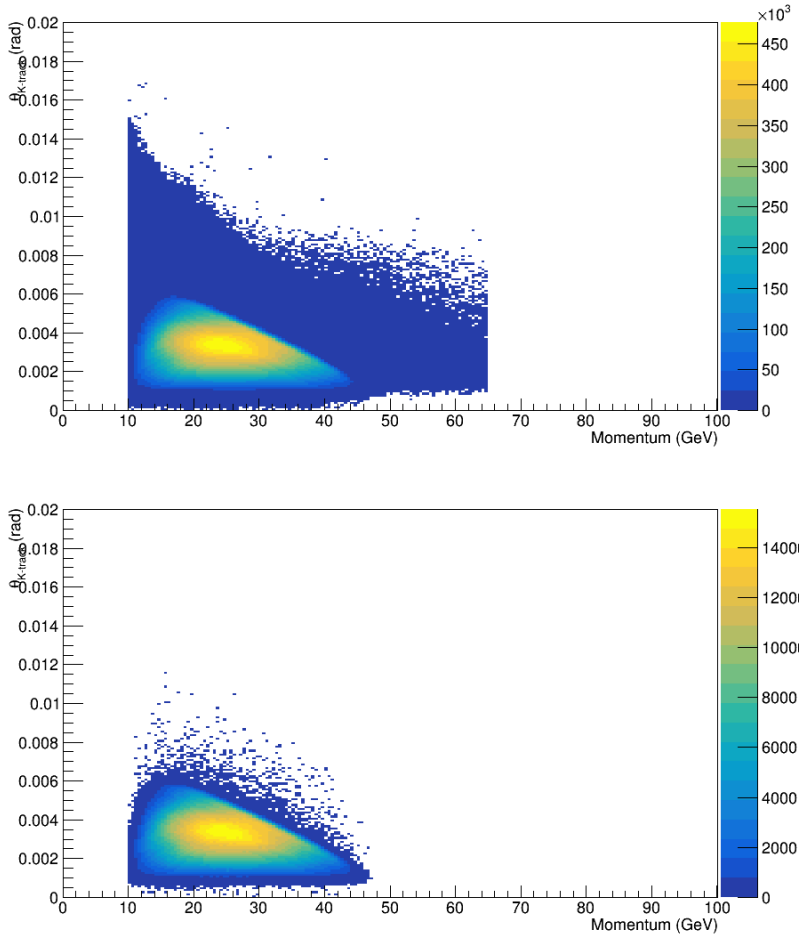

Figure 6.2: Top: Angle versus track momentum distribution for three-track vertex events from 2017 sample. Bottom: Angle versus track momentum distribution for three-track vertex events after cuts on the total momentum and invariant mass from 2017 sample.

The K3π final signal acceptance defined as:

$$A = \frac{n_{pass}}{N_{gen}} \tag{6.4}$$

where N_{gen} is the number of generated events and n_{pass} is the number of events passing the selection criteria, is computed using a MC sample.

It results being $(10.70 \pm 0.03)\%$.

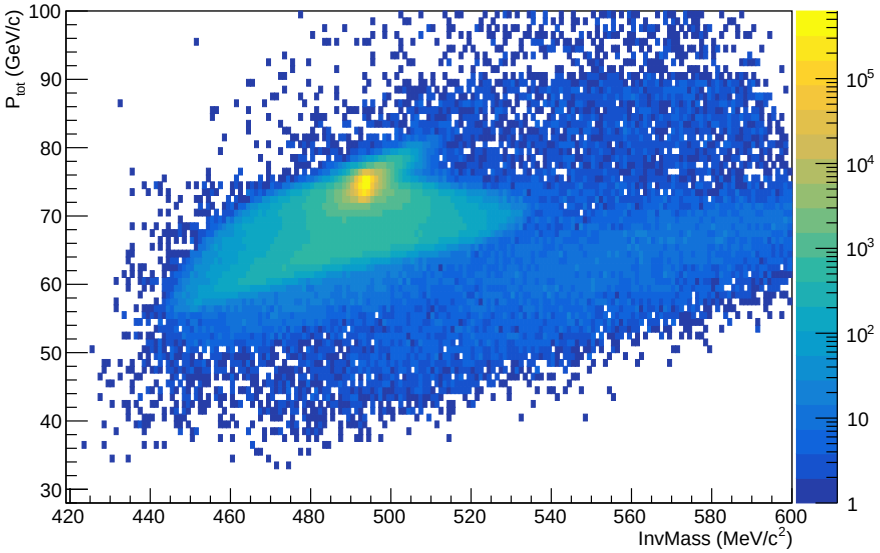

Figure 6.3: Distribution of three track vertex total momentum $|\vec{P}_{3\pi}|$ versus the invariant mass($M_{3\pi}$) under the K3π hypothesis obtained from data.

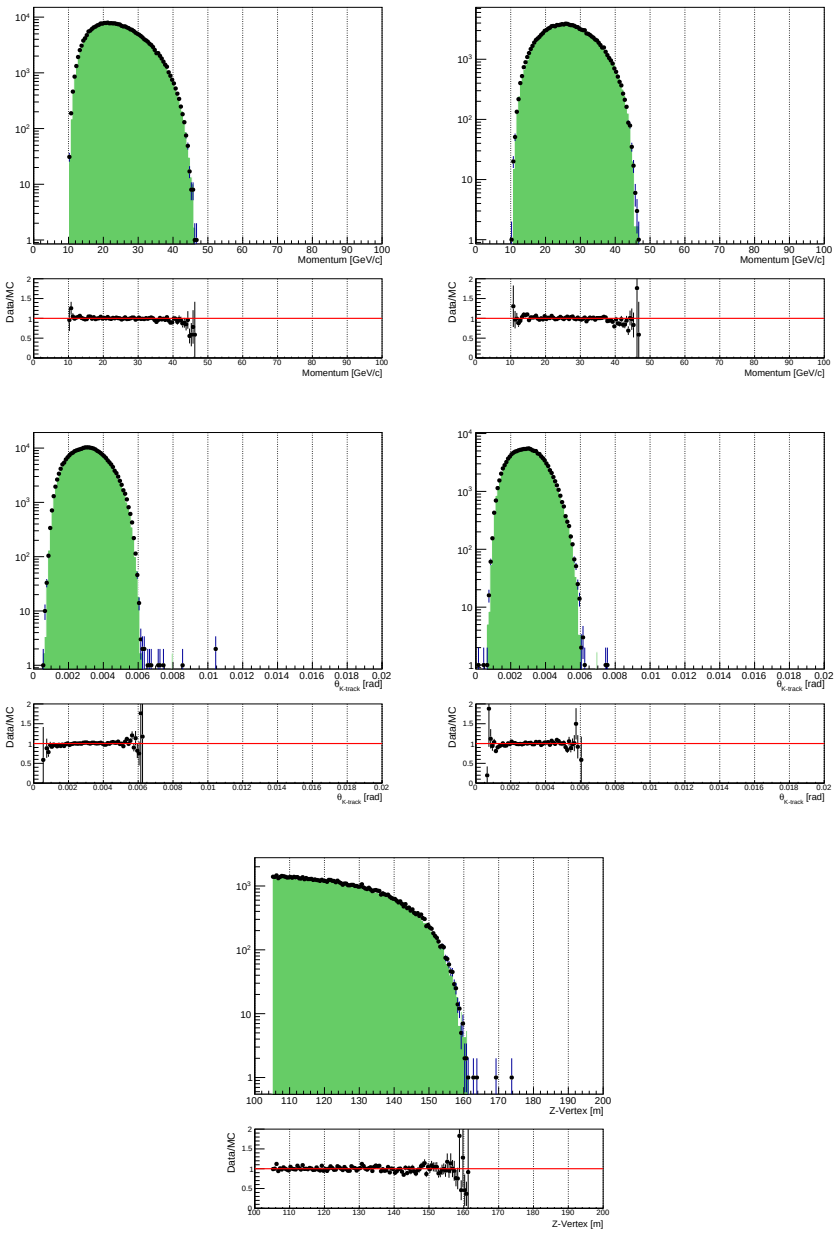

Figure 6.4: Data-MC comparison for K3π events: top row positive(left) and negative(right) track momentum, central row positive(left) and negative(right) track angle, bottom row Z-vertex position. The green histogram represents MC events while the black dots are data events.

6.2.2 $K \to \pi\mu e$ selection

The $K \to \pi\mu e$ selection is based on the three-track vertex selection, then the PID selection criteria, defined as described in Section 5, are applied in order to select events with exactly a pion-like, a muon-like and a electron-like particle, . Further conditions are checked after the PID to reduce the probability of wrong event association:

- the reconstructed total momentum must be between $\pm$2.5 GeV with respect to the beam momentum;
- the transverse total momentum with respect to the beam transverse momentum must be $<$35 MeV, in order to reject events in which one of the tracks is wrongly associated to the event e.g. it comes from on other kaon decay or beam pion decay.

Then the invariant mass is built and the region around the kaon mass is blinded.

The signal selection acceptance for the three decay channels has been evaluated with MC samples using the relation in (6.4). The values are reported in Table 6.1.

Decay mode	Acceptance
$K^+ \to \pi^+\mu^+e^-$	(5.60$\pm$0.02)%
$K^+ \to \pi^+\mu^-e^+$	(5.20$\pm$0.02)%
$K^+ \to \pi^-\mu^+e^+$	(5.20$\pm$0.02)%

Table 6.1: Signal selection acceptance

As one can notice the final signal acceptance of the $K \to \pi\mu e$ selection is lower than the one of the $K^+ \to \pi^+\pi^+\pi^-$ (it results approximately 1/2 of the K3π acceptance). The main reason is because in the $K \to \pi\mu e$ PID criteria are applied, while this is not the case for the $K^+ \to \pi^+\pi^+\pi^-$ selection.

6.3 Method

A blind analysis has been performed in order to avoid any bias in the finalization of the event selection criteria. The blind region corresponding to the signal region (SR) is defined using the invariant mass variable as the region covering the [480,505] MeV/c^2 range (about $\pm 10\sigma$ around the kaon mass). All the rest, the regions below 480 MeV/c^2 and above 505 MeV/c^2 define the so called control region (CR), where

the data-MC comparison of the background is performed in order to understand which are the sources of background for the analysis in each decay channel.

The background study has been performed using MC sample produced centrally within the *NA62 framework*. The main source of background comes from K3π decays for the three signal channels. For $K^+ \to \pi^+\mu^-e^+$ and $K^+ \to \pi^-\mu^+e^+$ also the Ke4 decay represents an important source of background. Other decays have been additionally considered and included in the expected background estimation.

The UL for the branching fractions $\mathcal{B}(K \to \pi\mu e$) have been estimated using the relation

$$\mathcal{B}(K^+ \to \pi\mu e) = \frac{N(K^+ \to \pi\mu e)}{N_K A_{\pi\mu e}} \tag{6.5}$$

where $A_{\pi\mu e}$ is the $K \to \pi\mu e$ selection acceptance, which has been evaluated using the MC sample for each of the three $K \to \pi\mu e$ decay (see Table 6.1).

The N_K number of kaons decaying in the fiducial volume has been computed using reconstructed $K^+ \to \pi^+\pi^+\pi^-$ decays, collected with a minimum bias trigger (CONTROL) and estimating the number expected from the masks used in the $K \to \pi\mu e$ analysis.
In general the N_K number of kaon decays evaluated with K3π events for a specific mask, called *X*, is computed as follows:

$$N_K = \frac{N_{K3\pi}}{\mathcal{B}(K3\pi)A_{K3\pi}} \frac{D_{MinBias}}{D_X \epsilon_{trig}} \tag{6.6}$$

where $\mathcal{B}(K3\pi)$ is the $K^+ \to \pi^+\pi^+\pi^-$ branching fraction; $A_{K3\pi}$ is the $K^+ \to \pi^+\pi^+\pi^-$ acceptance evaluated with a MC sample; $D_{MinBias}$ and D_x are the downscaling factors of the minimum bias trigger and mask *X* respectively and ϵ_{trig} is the trigger efficiency.

The $K \to \pi\mu e$ analysis has been performed using the data collected with three trigger masks, each with a different downscaling factor as shown in Table 3.5 and Table 3.6 for 2016 and 2017 respectively. In this case in the relation (6.6) D_x stands for the effective downscaling due to the three masks, which has been computed for each run according to a pure probabilistic relation:

$$D_{eff} = D_x = \frac{1}{1 - (1 - \frac{\epsilon_{MT}}{D_{MT}}) \cdot (1 - \frac{\epsilon_{\mu MU}}{D_{\mu MT}}) \cdot (1 - \frac{\epsilon_{eMT}}{D_{eMT}})} \tag{6.7}$$

where $\frac{\epsilon_i}{D_i}$ represents the probability to take the event using mask i, considering its trigger efficiency (ϵ_i) and its downscaling factor (D_i).

In Figure 6.5 and Figure 6.6 is the kaon flux for the 2016 and 2017 data taking, respectively. In each plot the kaon flux computed with the CONTROL triggers assuming a downscaling factor equal to one (black line), the kaon flux computed with the three masks used in this analysis assuming 100% trigger efficiency (blue line) and the kaon flux computed with the three masks used in this analysis taking into account the trigger efficiency measured as described in Section 3 for the normalization channel (red line) and the signal channel (green line) are shown.

As an example for Run-6677 of 2016 data taking the effective downscaling assuming 100% efficiency results 1.64 while including the trigger efficiency for each mask for the K3π decay it becomes 2.33, affecting the count of the kaon flux in the sample (red line in Figure 6.5 and Figure 6.6). In the case of $K \to \pi\mu e$, the final number of kaons (green line in Figure 6.5 and Figure 6.6) is larger than for the K3π , since the trigger masks work better for the signal than the normalization channel (specially the LKr conditions E20 and E10).

For 2016 run the total kaon flux for the $K \to \pi\mu e$ analysis results

$$N_K = (6.73 \pm 0.41) \times 10^{10} \tag{6.8}$$

For 2017 run the total kaon flux for the $K \to \pi\mu e$ analysis results

$$N_K = (10.31 \pm 0.13) \times 10^{10} \tag{6.9}$$

the quoted uncertainty is due to systematics[2] where the main contributions come from the limited precision on the K3π branching ratio and the trigger efficiency. On the other hand the statistical error results to be small compared to the systematic one, $\mathcal{O}(10^6)$ and is not reported.

[2]To compute the systematic error the error on the effective downscaling, the acceptance and the K3π branching ratio have been taken into account

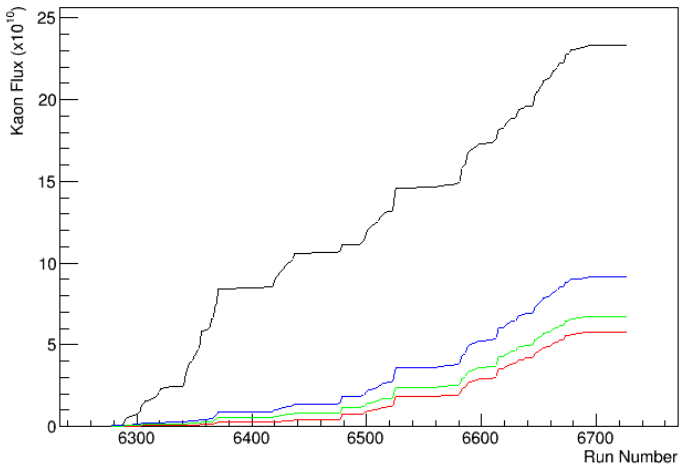

Figure 6.5: Kaon flux for the 2016 data sample from CONTROL trigger assuming a downscaling factor equal to one (black line); from the three masks used in the analysis assuming 100% trigger efficiency (blue line) and taking into account the trigger efficiency for the $K^+ \to \pi^+\pi^+\pi^-$ sample (red line) and the $K \to \pi\mu e$ sample (green line). The kaon flux is reported in units of 10^{10}.

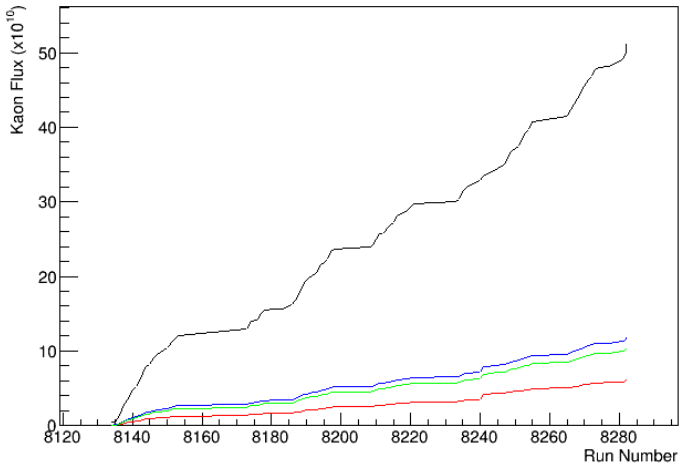

Figure 6.6: Kaon flux for the 2017 data sample from CONTROL trigger assuming a downscaling factor equal to one (black line); from the three masks used in the analysis assuming 100% trigger efficiency (blue line) and taking into account the trigger efficiency for the $K^+ \to \pi^+\pi^+\pi^-$ sample (red line) and for the $K \to \pi\mu e$ sample (green line). The kaon flux is reported in units of 10^{10}.

6.4 Background study

The study of background sources has been performed with MC sample. There are five categories of kaon decays which can be a background for the $K \to \pi\mu e$ analysis. The PDG branching ratios for each decay taken into account are listed in Table 6.2.

Type *A*

$\boldsymbol{K3\pi}$: is a three body decay as the $K \to \pi\mu e$, which can mimic the signal if the following situations occur:

- a pion decays in $\pi \to \mu\nu$ and an other pion is mis-identified as an electron/positron;
- a pion decays in $\pi \to \mu\nu$ and an other pion decays in $\pi \to e\nu$;
- a pion is mis-identified as a muon and on other decays in $\pi \to e\nu$;
- a pion is mis-identified as a muon and on other is mis-identified as an electron/positron

Type *B*

$\boldsymbol{K2\pi}$ Dalitz is a two body decay, kinematically different from the $K \to \pi\mu e$ but in which the following situations can occur:

- the charged pion can decay in $\pi \to \mu\nu$ or can be mis-identified as a muon, the π^0 decays in $\pi^0 \to e^+e^-\gamma$ and the electron or positron can be mis-identified as a pion; in those cases the K2π decay can be a source of background only for $K^+ \to \pi^+\mu^+e^-$ and $K^+ \to \pi^-\mu^+e^+$;
- the pion does not decay and the π^0 decays in $\pi^0 \to e^+e^-\gamma$ and e^+ or e^- can be mis-identified as a muon; in those cases the K2π decay can be a source of background only for all three $K \to \pi\mu e$ channels;

$\boldsymbol{Ke3}$ Dalitz is a not closed three body decay, due to the presence of a neutrino in the final state, then in general there will be a missing energy carried by the neutrino. However if the neutrino energy is extremely small or zero it can mimic the signal if:

- the π^0 decays in $\pi^0 \to e^+e^-\gamma$ and e^+/e^- are mis-identified as a pion or muon respectively; in those cases the Ke3 decay can be a source of background for $K^+ \to \pi^+\mu^-e^+$ and $K^+ \to \pi^-\mu^+e^+$ channels;

- the e^+ is mis-identified as a pion; the π^0 decays in $\pi^0 \to e^+e^-\gamma$ and the e^+ or e^- can be mis-identified as a muon; in those cases the Ke3 decay can be a source of background for $K^+ \to \pi^+\mu^+e^-$ and $K^+ \to \pi^+\mu^-e^+$ channels;

$\boldsymbol{K\mu 3}$ Dalitz is a not closed three body decay, due to the presence of neutrino in the final state, in which the following situations can occur:

- the muon can decay in $\mu \to e\nu$, the π^0 decays in $\pi^0 \to e^+e^-\gamma$ and e^+/e^- can be mis-identified as a pion/muon; in these cases the Kμ3 decay can be a source of background only for $K^+ \to \pi^+\mu^-e^+$ and $K^+ \to \pi^-\mu^+e^+$;
- the π^0 decays in $\pi^0 \to e^+e^-\gamma$ and one of e^+ or e^- can be mis-identified as a pion; in those cases the Kμ3 decay can be a source of background only for $K^+ \to \pi^+\mu^+e^-$ and $K^+ \to \pi^-\mu^+e^+$;
- the muon does not decay but is identify as a pion, the π^0 decays in $\pi^0 \to e^+e^-\gamma$ and one of e^+ or e^- can be mis-identified as a muon; in those cases the Kμ3 decay can be a source of background only for $K^+ \to \pi^+\mu^+e^-$ and $K^+ \to \pi^+\mu^-e^+$;

Type *C*

$\boldsymbol{Ke4}$ is a four-body decay in which the following situation can occur:

- one of the pion can decay $\pi \to \mu\nu$ or can be mis-identified as a muon; in those cases the Ke4 decay can be a source of background only for $K^+ \to \pi^+\mu^-e^+$ and $K^+ \to \pi^-\mu^+e^+$;

$\boldsymbol{K\mu 4}$ is a four-body decay in which the following situation can occur:

- pions do not decay but one of them can be mis-identified as a positron/electron; in those cases the Kμ4 decay can be a source of background only for $K^+ \to \pi^+\mu^+e^-$ and $K^+ \to \pi^-\mu^+e^+$;

Type *D*

$\boldsymbol{K^+ \to \pi^+\mu^+\mu^-}$ is a three-body decay in which the following situations can occur:

- the pion does not decay and the μ^+ or μ^- can decay in $\mu \to e\nu$; in those cases the $K^+ \to \pi^+\mu^+\mu^-$ decay can be a source of background only for $K^+ \to \pi^+\mu^+e^-$ and $K^+ \to \pi^+\mu^-e^+$ channels;

- the pion can be mis-identified as a positron, the μ^+ or μ^- can be mis-identified as a pion; in those cases the $K^+ \to \pi^+\mu^+\mu^-$ decay can be a source of background only for $K^+ \to \pi^+\mu^-e^+$ and $K^+ \to \pi^-\mu^+e^+$;

$\boldsymbol{K^+ \to \pi^+e^+e^-}$ is a three-body decay in which the following situation can occur:

- the pion decay in $\pi \to \mu\nu$ or is mid-identify as a muon and the e^+ or e^- can be mis-identified as a pion; in those cases the $K^+ \to \pi^+e^+e^-$ decay can be a source of background only for $K^+ \to \pi^+\mu^+e^-$ and $K^+ \to \pi^-\mu^+e^+$ channels;

Type *E*

$\boldsymbol{K^+ \to e^+\nu e^+e^-}$ is a four-body decay in which the following situation can occur:

- one electron/positron is mis-identified as a pion and one as a muon; in those cases the decay can be a source of background for all $K \to \pi\mu e$ channels;

$\boldsymbol{K^+ \to e^+\nu\mu^+\mu^-}$ is a four-body decay in which the following situation can occur:

- one muon is mis-identified as a pion; in those cases the decay can be a source of background for $K^+ \to \pi^+\mu^-e^+$ and $K^+ \to \pi^-\mu^+e^+$ channels;

$\boldsymbol{K^+ \to \mu^+\nu e^+e^-}$ is a four-body decay in which the following situation can occur:

- one electron/positron is mis-identified as a pion; in those cases the decay can be a source of background for $K^+ \to \pi^+\mu^+e^-$ and $K^+ \to \pi^-\mu^+e^+$ channels;

$\boldsymbol{K^+ \to \mu^+\nu\mu^+\mu^-}$ is a four-body decay in which the following situation can occur:

- one muon can decay in $\mu \to e\nu$ and on other is mis-identified as a pion; in those cases the decay can be a source of background for all $K \to \pi\mu e$ decay mode.

6.4.1 Expected number of background events

For each background channel *i* the number N^i_{exp} of expected events in the signal region (SR) and in the control region (CR) has been determined as

$$N^i_{exp} = \frac{N^i_{SR(CR)}}{\tau_i} \tag{6.10}$$

where N^i_{SR} and N^i_{CR} are the number of MC events observed in the SR and CR respectively, while τ_i is the size of the generated MC decaying in the fiducial volume in unit of data size

$$\tau_i = \frac{N^i_{gen}}{N_K \mathcal{B}^i} \tag{6.11}$$

where N^i_{gen} is the number of generated events decaying inside the fiducial volume, N_K is the number of kaon decays measured in Section 6.3 and $\mathcal{B}^i$ is the branching ratio of the background channel *i*.

In Table 6.3 the size of each MC sample and the corresponding expected number of events in the data are reported.

As can be seen the available MC samples for the K3π, Ke3 Dalitz, Kμ3 Dalitz, K2π Dalitz are not enough, thus the results shown in the following can not allow us to draw a strong conclusion. In order to solve this problem an alternative strategy to generate larger MC sample is under development, specially for the K3π channel. A qualitative approach to estimate the bakcground level will be also presented, in order to have an rough idea of the expected background level in the signal region, in particular from the K3π, Ke3 Dalitz, Kμ3 Dalitz, K2π Dalitz decays.

In the following tables, the expected number of background events in the SR and CR for each background channel, divided for each analysis, are reported together with the corresponding statistical and systematic error. When zero or few events(< 10 events) passing the selection has been observed, only an upper limit at 90% CL is reported[3].

As can be seen in the following plots the contribution to the background arises from different kaon decays, depending on the selected $K \to \pi\mu e$ channel.

[3]The 90% UL has been set using the standard Poisson single-side method

Type	Decay	Branching ratio
Type A	$K^+ \to \pi^+\pi^+\pi^-$	(5.583 $\pm$ 0.024)%
Type B	$K^+ \to \pi^+\pi^0_D$	(2.427 $\pm$ 0.081)$\cdot$ 10^{-3}
	$K^+ \to \pi^0_D e^+\nu$	(5.952 $\pm$ 0.224) $\cdot$ 10^{-4}
	$K^+ \to \pi^0_D \mu^+\nu$	(3.935 $\pm$ 0.156)$\cdot$ 10^{-4}
Type C	$K^+ \to \pi^+\pi^- e^+\nu$	(4.247 $\pm$ 0.024)$\cdot$ 10^{-5}
	$K^+ \to \pi^+\pi^- \mu^+\nu$	(1.4 $\pm$ 0.9)$\cdot$ 10^{-5}
Type D	$K^+ \to \pi^+\mu^+\mu^-$	(9.4 $\pm$ 0.6)$\cdot$ 10^{-8}
	$K^+ \to \pi^+ e^+ e^-$	(3.00 $\pm$ 0.09)$\cdot$ 10^{-7}
Type E	$K^+ \to e^+\nu e^+ e^-$	(2.48 $\pm$ 0.02)$\cdot$ 10^{-8}
	$K^+ \to e^+\nu\mu^+\mu^-$	(1.7 $\pm$ 0.5)$\cdot$ 10^{-8}
	$K^+ \to \mu^+\nu e^+ e^-$	(7.06 $\pm$ 0.31)$\cdot$ 10^{-8}
	$K^+ \to \mu^+\nu\mu^+\mu^-$	$<$4.1$\cdot$ 10^{-7}(90% CL)

Table 6.2: Summary of all the possible kaon decays source of background for the $K \to \pi\mu e$ analysis with the corresponding branching ratio.

Decay	N_{gen}(in FV)	N_{exp} (2016)	N_{exp} (2017)
$K^+ \to \pi^+\pi^+\pi^-$	45.8 $\times$ 10^6	5.1 $\times$ 10^9	6.5 $\times$ 10^9
$K^+ \to \pi^+\pi^+\pi^-$ + $\pi_e = 0.5$	45.8 $\times$ 10^6	0.6 $\times$ 10^6	0.8$\times$ 10^6
$K^+ \to \pi^+\pi^0_D$	45.0 $\times$ 10^6	2.2 $\times$ 10^8	2.8 $\times$ 10^8
$K^+ \to \pi^0_D e^+\nu$	4.8 $\times$ 10^6	5.4 $\times$ 10^7	6.9 $\times$ 10^7
$K^+ \to \pi^0_D \mu^+\nu$	22.8 $\times$ 10^6	3.6 $\times$ 10^7	4.6 $\times$ 10^7
$K^+ \to \pi^+\pi^- e^+\nu$	48.7 $\times$ 10^6	3.9 $\times$ 10^6	5.0 $\times$ 10^6
$K^+ \to \pi^+\pi^- \mu^+\nu$	74.1 $\times$ 10^6	1.3 $\times$ 10^6	1.6 $\times$ 10^9
$K^+ \to \pi^+\mu^+\mu^-$	9.8 $\times$ 10^6	8.6 $\times$ 10^3	10.9 $\times$ 10^3
$K^+ \to \pi^+ e^+ e^-$	8.7 $\times$ 10^6	2.8 $\times$ 10^4	3.5 $\times$ 10^4
$K^+ \to e^+\nu e^+ e^-$	0.96 $\times$ 10^6	2.3 $\times$ 10^3	2.9 $\times$ 10^3
$K^+ \to e^+\nu\mu^+\mu^-$	1.1 $\times$ 10^6	1.6 $\times$ 10^3	2.0 $\times$ 10^3
$K^+ \to \mu^+\nu e^+ e^-$	1.0 $\times$ 10^6	6.5 $\times$ 10^3	8.2 $\times$ 10^3
$K^+ \to \mu^+\nu\mu^+\mu^-$	10.2 $\times$ 10^6	3.8 $\times$ 10^4	4.8 $\times$ 10^4

Table 6.3: Summary of all the possible kaon decays source of background. In the table the size of each generated MC sample and the corresponding number of events expected in the 2016 data sample and 2017 data sample are reported.

$K^+ \to \pi^+\mu^+e^-$

2016 The number of data events selected in the CR is N^{CR}_{data}=5324, while the expected number of background events is N^{CR}_{BKG}=8572$\pm$813$_{stat}$ $\pm$583$_{syst}$ (Figure 6.7 and Table 6.4).

2017 The number of data events selected in the CR is N^{CR}_{data}=14913, while the expected number of background events is N^{CR}_{BKG}=13113$\pm$1244$_{stat}$ $\pm$409$_{syst}$ (Figure 6.8 and Table 6.5).

For the $K^+ \to \pi^+\mu^+e^-$ channel the statistical uncertanty is 9.6%.

$K^+ \to \pi^+\mu^-e^+$

2016 The number of data events selected in the CR is N^{CR}_{data}=2620, while the expected number of background events is N^{CR}_{BKG}=4729$\pm$591$_{stat}$ $\pm$322$_{syst}$ (Figure 6.9 and Table 6.6).

2017 The number of data events selected in the CR is N^{CR}_{data}=7337, while the expected number of background events is N^{CR}_{BKG}=7235$\pm$902$_{stat}$ $\pm$225$_{syst}$ (Figure 6.10 and Table 6.7).

For the $K^+ \to \pi^+\mu^-e^+$ channel the statistical uncertanty is 13.1%.

$K^+ \to \pi^-\mu^+e^+$

2016 The number of data events selected in the CR is N^{CR}_{data}=2576, while the expected number of background events is N^{CR}_{BKG}=4556$\pm$582$_{stat}$ $\pm$310$_{syst}$ (Figure 6.11 and Table 6.8).

2017 The number of data events selected in the CR is N^{CR}_{data}=7364, while the expected number of background events is N^{CR}_{BKG}=6970$\pm$891$_{stat}$ $\pm$217$_{syst}$ (Figure 6.12 and Table 6.9).

For the $K^+ \to \pi^-\mu^+e^+$ channel the statistical uncertanty is 13.4%.

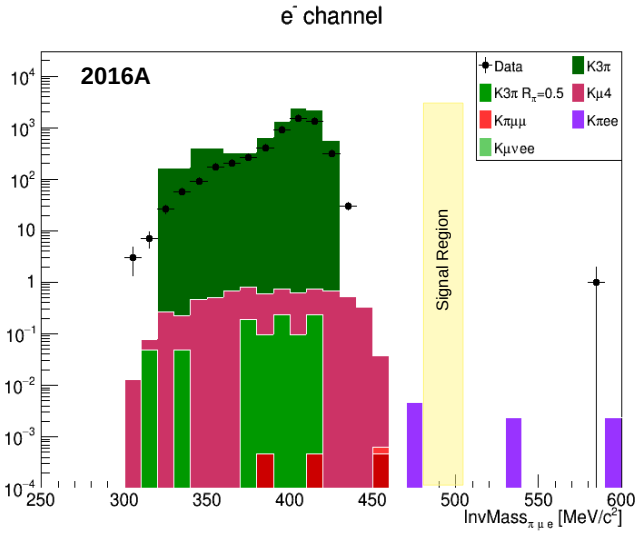

Figure 6.7: Reconstructed invariant mass $m_{\pi\mu e}$ in logarithmic scale at the end of the $K^+ \to \pi^+\mu^+e^-$ selection for data from 2016A (dots). The colored histograms refer to the background channels (Table 6.3) taken into account, using the available MC samples.

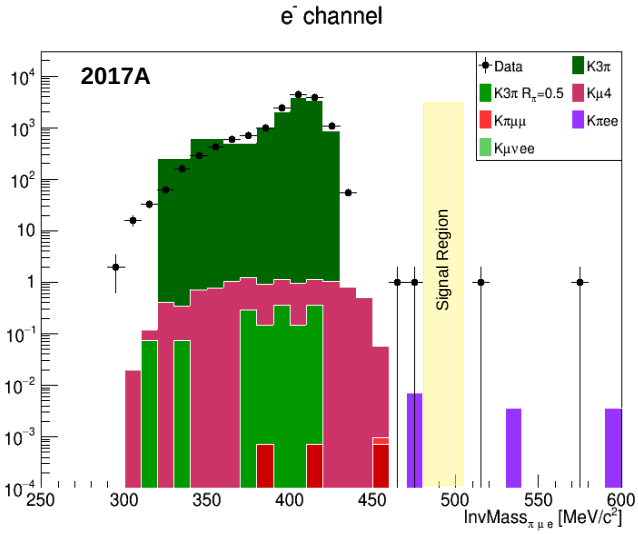

Figure 6.8: Reconstructed invariant mass $m_{\pi\mu e}$ in logarithmic scale at the end of the $K^+ \to \pi^+\mu^+e^-$ selection for data from 2017A (dots). The colored histograms refer to the background channels (Table 6.3) taken into account, using the available MC samples.

Decay	N_{exp}^{CR}	N_{exp}^{SR}
$K^+ \to \pi^+\pi^+\pi^-$	8534±813±580	<178.4
$K^+ \to \pi^+\pi^+\pi^-$ + $\pi_e = 0.5$	0.20±0.04±0.01	<0.02
$K^+ \to \pi^+\pi^0_D$	<8.4	<8.4
$K^+ \to \pi^0_D e^+\nu$	<19.2	<19.2
$K^+ \to \pi^0_D \mu^+\nu$	<2.7	<2.7
$K^+ \to \pi^+\pi^- e^+\nu$	<0.14	<0.14
$K^+ \to \pi^+\pi^- \mu^+\nu$	7.3±0.3±0.5	<0.03
$K^+ \to \pi^+\mu^+\mu^-$	<0.003	<0.002
$K^+ \to \pi^+ e^+ e^-$	<0.02	<0.005
$K^+ \to e^+\nu e^+ e^-$	<0.004	<0.004
$K^+ \to e^+\nu\mu^+\mu^-$	<0.003	<0.003
$K^+ \to \mu^+\nu e^+ e^-$	<0.03	<0.01
$K^+ \to \mu^+\nu\mu^+\mu^-$	<0.006	<0.006
Total	8572±813±583	<209

Table 6.4: Summary of all the possible kaon decays source of background for the $K^+ \to \pi^+\mu^+e^-$ channel for the 2016A sample: the number of expected background events evaluated with the available MC samples in the CR and SR are reported. In case of zero or few events observed an upper limit at 90% CL on the expected number of events has been computed.

Decay	N_{exp}^{CR}	N_{exp}^{SR}
$K^+ \to \pi^+\pi^+\pi^-$	13055±1244±407	<273
$K^+ \to \pi^+\pi^+\pi^-$ + $\pi_e = 0.5$	0.30±0.07±0.01	<0.03
$K^+ \to \pi^+\pi^0_D$	<12.8	<12.8
$K^+ \to \pi^0_D e^+\nu$	<29.4	<29.4
$K^+ \to \pi^0_D \mu^+\nu$	<4.1	<4.1
$K^+ \to \pi^+\pi^- e^+\nu$	<0.21	<0.21
$K^+ \to \pi^+\pi^- \mu^+\nu$	11.2±0.5±0.3	<0.04
$K^+ \to \pi^+\mu^+\mu^-$	<0.004	<0.002
$K^+ \to \pi^+ e^+ e^-$	<0.03	<0.008
$K^+ \to e^+\nu e^+ e^-$	<0.006	<0.006
$K^+ \to e^+\nu\mu^+\mu^-$	<0.004	<0.004
$K^+ \to \mu^+\nu e^+ e^-$	<0.05	<0.02
$K^+ \to \mu^+\nu\mu^+\mu^-$	<0.01	<0.01
Total	13114±1244±409	<320

Table 6.5: Summary of all the possible kaon decays source of background for the $K^+ \to \pi^+\mu^+e^-$ channel for the 2017A sample: the number of expected background events, evaluated with the available MC samples, in the CR and SR are reported. In case of zero or few events observed an upper limit at 90% CL on the expected number of events has been computed.

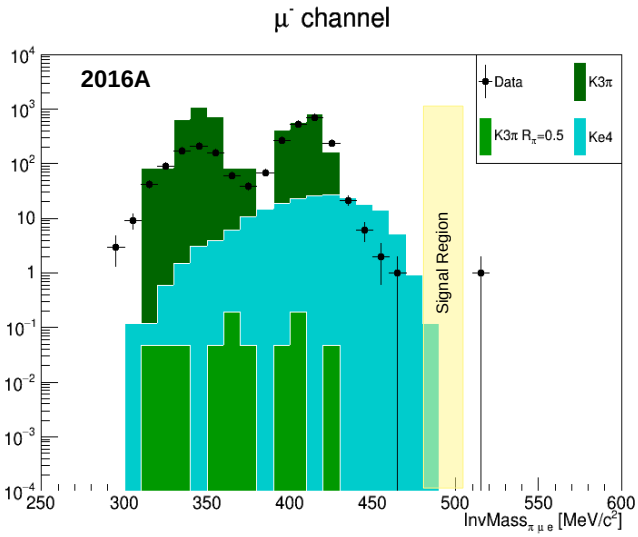

Figure 6.9: Reconstructed invariant mass $m_{\pi\mu e}$ in logarithmic scale at the end of the $K^+ \to \pi^+\mu^-e^+$ selection for data from 2016A (dots). The colored histograms refer to the background channels (Table 6.3) taken into account, using the available MC samples.

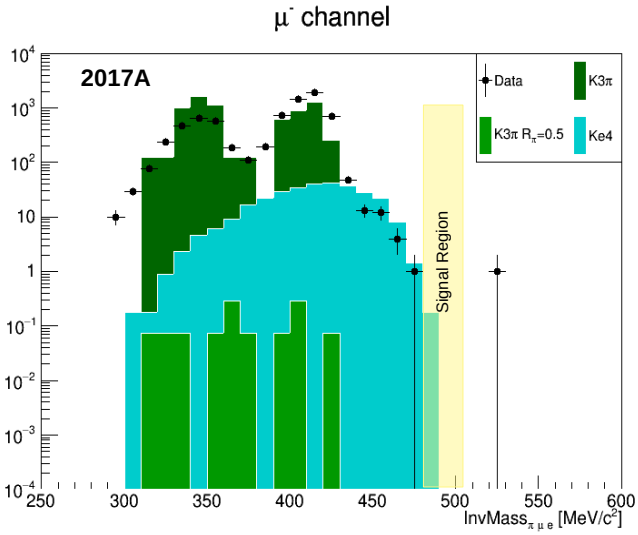

Figure 6.10: Reconstructed invariant mass $m_{\pi\mu e}$ in logarithmic scale at the end of the $K^+ \to \pi^+\mu^-e^+$ selection for data from 2017A (dots). The colored histograms refer to the background channels (Table 6.3) taken into account, using the available MC samples.

Decay	N_{exp}^{CR}	N_{exp}^{SR}
$K^+ \to \pi^+\pi^+\pi^-$	4500±590±306	<178.4
$K^+ \to \pi^+\pi^+\pi^-$ + $\pi_e = 0.5$	0.14±0.04±0.01	<0.02
$K^+ \to \pi^+\pi^0_D$	<8.4	<8.4
$K^+ \to \pi^0_D e^+\nu$	<19.2	<19.2
$K^+ \to \pi^0_D \mu^+\nu$	<2.7	<2.7
$K^+ \to \pi^+\pi^- e^+\nu$	198.6±3.4±13.5	<0.3
$K^+ \to \pi^+\pi^- \mu^+\nu$	<0.03	<0.03
$K^+ \to \pi^+\mu^+\mu^-$	<0.001	<0.001
$K^+ \to \pi^+ e^+ e^-$	<0.005	<0.005
$K^+ \to e^+\nu e^+ e^-$	<0.004	<0.004
$K^+ \to e^+\nu\mu^+\mu^-$	<0.002	<0.002
$K^+ \to \mu^+\nu e^+ e^-$	<0.01	<0.01
$K^+ \to \mu^+\nu\mu^+\mu^-$	<0.006	<0.006
Total	4729±591±322	<209

Table 6.6: Summary of all the possible kaon decays source of background for the $K^+ \to \pi^+\mu^- e^+$ channel for the 2016A sample: the number of expected background events, evaluated with the available MC samples, in the CR and SR are reported. In case of zero or few events observed an upper limit at 90% CL on the expected number of events has been computed.

Decay	N_{exp}^{CR}	N_{exp}^{SR}
$K^+ \to \pi^+\pi^+\pi^-$	6884±902±234	<273
$K^+ \to \pi^+\pi^+\pi^-$ + $\pi_e = 0.5$	0.2±0.05±0.01	<0.03
$K^+ \to \pi^+\pi^0_D$	<12.8	<12.8
$K^+ \to \pi^0_D e^+\nu$	<29.4	<29.4
$K^+ \to \pi^0_D \mu^+\nu$	<4.1	<4.1
$K^+ \to \pi^+\pi^- e^+\nu$	304±5.2±10.3	<0.5
$K^+ \to \pi^+\pi^- \mu^+\nu$	<0.04	<0.04
$K^+ \to \pi^+\mu^+\mu^-$	<0.002	<0.002
$K^+ \to \pi^+ e^+ e^-$	<0.008	<0.008
$K^+ \to e^+\nu e^+ e^-$	<0.006	<0.006
$K^+ \to e^+\nu\mu^+\mu^-$	<0.004	<0.004
$K^+ \to \mu^+\nu e^+ e^-$	<0.02	<0.002
$K^+ \to \mu^+\nu\mu^+\mu^-$	<0.01	<0.01
Total	7235±902±225	<320

Table 6.7: Summary of all the possible kaon decays source of background for the $K^+ \to \pi^+\mu^- e^+$ channel for the 2017A sample: the number of expected background events, evaluated with the available MC samples, in the CR and SR are reported. In case of zero or few events observed an upper limit at 90% CL on the expected number of events has been computed.

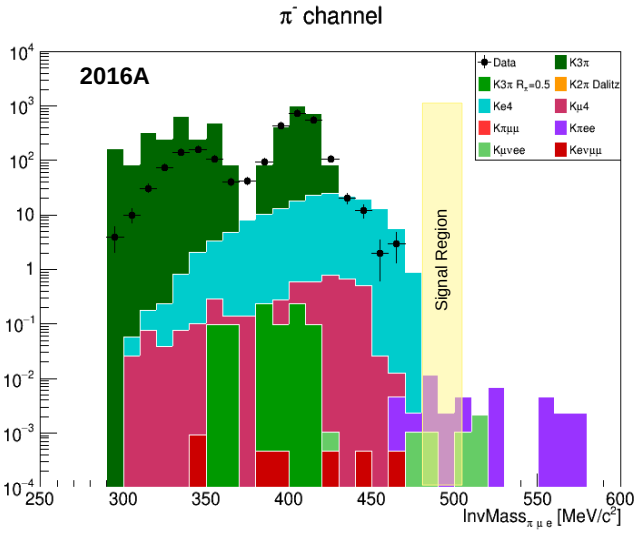

Figure 6.11: Reconstructed invariant mass $m_{\pi\mu e}$ in logarithmic scale at the end of the $K^+ \to \pi^-\mu^+e^+$ selection for data from 2016A (dots). The colored histograms refer to the background channels (Table 6.3) taken into account, using the available MC samples.

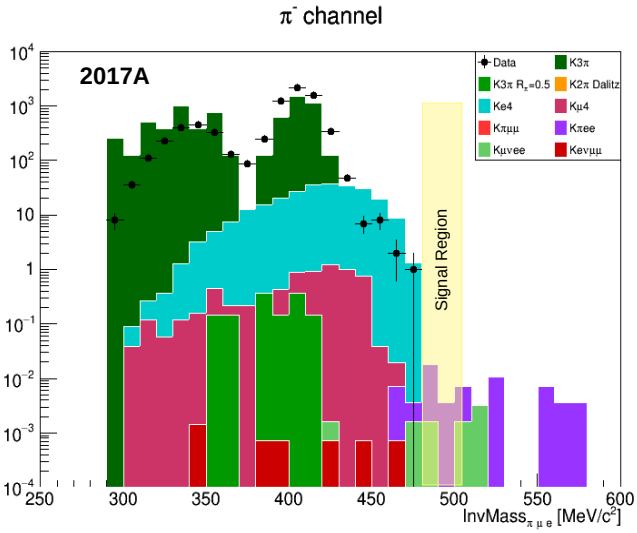

Figure 6.12: Reconstructed invariant mass $m_{\pi\mu e}$ in logarithmic scale at the end of the $K^+ \to \pi^-\mu^+e^+$ selection for data from 2017A (dots). The colored histograms refer to the background channels (Table 6.3) taken into account, using the available MC samples.

Decay	N_{exp}^{CR}	N_{exp}^{SR}
$K^+ \to \pi^+\pi^+\pi^-$	4344±582±295	<178.4
$K^+ \to \pi^+\pi^+\pi^-$ + $\pi_e = 0.5$	0.17±0.04±0.01	<0.02
$K^+ \to \pi^+\pi^0_D$	<14.2	<14.2
$K^+ \to \pi^0_D e^+\nu$	<19.2	<19.2
$K^+ \to \pi^0_D \mu^+\nu$	<2.7	<2.7
$K^+ \to \pi^+\pi^- e^+\nu$	170.6±3.2±11.6	<0.14
$K^+ \to \pi^+\pi^- \mu^+\nu$	4.5±0.2±0.3	<0.03
$K^+ \to \pi^+\mu^+\mu^-$	<0.003	<0.001
$K^+ \to \pi^+ e^+ e^-$	<0.04	<0.03
$K^+ \to e^+\nu e^+ e^-$	<0.004	<0.004
$K^+ \to e^+\nu\mu^+\mu^-$	<0.002	<0.002
$K^+ \to \mu^+\nu e^+ e^-$	<0.06	<0.01
$K^+ \to \mu^+\nu\mu^+\mu^-$	<0.02	<0.02
Total	4556±582±310	<209

Table 6.8: Summary of all the possible kaon decays source of background for the $K^+ \to \pi^-\mu^+e^+$ channel for the 2016A sample: the number of expected background events, evaluated with the available MC samples, in the CR and SR are reported. In case of zero or few events observed an upper limit at 90% CL on the expected number of events has been computed.

Decay	N_{exp}^{CR}	N_{exp}^{SR}
$K^+ \to \pi^+\pi^+\pi^-$	6647±891±207	<273
$K^+ \to \pi^+\pi^+\pi^-$ + $\pi_e = 0.5$	0.3±0.07±0.01	<0.03
$K^+ \to \pi^+\pi^0_D$	<21.7	<12.8
$K^+ \to \pi^0_D e^+\nu$	<29.4	<29.4
$K^+ \to \pi^0_D \mu^+\nu$	<4.1	<4.1
$K^+ \to \pi^+\pi^- e^+\nu$	261±4.0±8.1	<0.2
$K^+ \to \pi^+\pi^- \mu^+\nu$	6.9±0.4±0.2	<0.05
$K^+ \to \pi^+\mu^+\mu^-$	<0.004	<0.002
$K^+ \to \pi^+ e^+ e^-$	<0.05	<0.04
$K^+ \to e^+\nu e^+ e^-$	<0.006	<0.006
$K^+ \to e^+\nu\mu^+\mu^-$	<0.004	<0.004
$K^+ \to \mu^+\nu e^+ e^-$	<0.09	<0.02
$K^+ \to \mu^+\nu\mu^+\mu^-$	<0.03	<0.03
Total	6970±891±217	<320

Table 6.9: Summary of all the possible kaon decays source of background for the $K^+ \to \pi^-\mu^+e^+$ channel for the 2017A sample: the number of expected background events, evaluated with the available MC samples, in the CR and SR are reported. In case of zero or few events observed an upper limit at 90% CL on the expected number of events has been computed.

As already said the K3π represents the main source of background for all three signal channels; another significant contributions come from the Ke4 for the $K^+ \to \pi^+\mu^-e^+$ and $K^+ \to \pi^-\mu^+e^+$, while for $K^+ \to \pi^+\mu^+e^-$ and $K^+ \to \pi^-\mu^+e^+$ the Kμ4 is also important.

In all cases the number of expected background events in the control region is not well estimated due to the lack of statistics for the K3π, Ke3 Dalitz, Kμ3 Dalitz and K2π Dalitz channels and the same is for the expected number of background events in the signal region.

In the missing mass distribution a structure of two bumps below 450 MeV/c^2 can be recognized; It is more evident in the $K^+ \to \pi^+\mu^-e^+$ and $K^+ \to \pi^-\mu^+e^+$ channels. Even though the statistics of the K3π MC sample is not enough to well fit the data, it well reproduces the structure. In particular the two structure are associated to two different situations which can occur:

- a K3π event in which one pion is mis-identified as a muon and another as an electron/positron;
- a K3π event in which there is a real pion decay, $\pi \to \mu\nu$ and an other pion is mis-identified as an electron/positron.

In terms of background the $K^+ \to \pi^-\mu^+e^+$ results the only one in which, with the present MC statistics there are events ending up in the SR; this is mainly due to the lower power of the PID criteria to identify negative pion with respect to the positive one.

The errors quoted for the number of expected events, evaluated with MC samples, in the following tables are: the statistical error, $\delta N_{CR} = 1/\sqrt{N_{CR}}$, and the systematic error which main contribution comes from the MC PID efficiency, which differs from the one assessed with data of $\sim 3\%$. For the 2016 data an important contribution to the systematic error arises also from the trigger efficiency, due to dependencies which have not be taken into account in the evaluation of the trigger efficiency as discussed in Chapter 3.

The most dangerous cases for which a K3π event can be source of background are: when a pion decay in $\pi \to \mu\nu$ ($\sim 20\%$ probability to decay within the detector) and an other one is mis-identified as a positron/electron (P($\pi \to e$)=(0.20$\pm$0.03)%) or when a pion is mis-identified as a muon (P($\pi \to \mu$)=(1.90$\pm$0.06)%) and an other one as a positron/electron. Assuming that the selection acceptance without the PID efficiency selection for a K3π event to end up in the signal region is $< 8\times10^{-8}$ at 90% CL (computed with the available MC sample), the corresponding expected number of events for a sample of 10^{10} K3π simulated events is ~ 50 events. Then including the

PID pion identification efficiency and considering the most dangerous cases (one pion decaying in a muon and one pion mis-identified as a positron/electron), the effective expected number of events in the SR from K3pi would be $\sim$0.2. A similar approach can be used for the Ke3 Dalitz, Kμ3 Dalitz and K2π Dalitz and the obtained numbers of expected background events in the SR are shown in Table 6.10.

Decay	N_{exp}^{SR} at 90% CL
$K^+ \to \pi^+\pi^+\pi^-$	<0.2
$K^+ \to \pi^+\pi^0_D$	<0.1
$K^+ \to \pi^0_D e^+\nu$	<0.01
$K^+ \to \pi^0_D \mu^+\nu$	<0.01
Total	<0.3

Table 6.10: Qualitative study on the expected number of background events in the signal region in the case of MC samples of 10^{10} events

These qualitative results show that larger MC samples are mandatory to have a better estimation of the expected background events in the signal region. For this purpose a new method, called *Fast Simulation*, has been implemented within the NA62 framework. The idea behind is to generate events simulating only some of the detectors, in order to reduce the simulation time and the output file size. In the specific case the events information are available only up to the STRAW spectrometer. A first production of a K3π sample produced with such method was still ongoing at the moment of writing this work, so it was not possible to report the results with this sample.

6.5 Results

In this section, the chosen method for the statistical interpretation of the data is described. Finally, the obtained Single Event Sensitivity (SES) and the obtained UL for the branching fraction of each $K \to \pi\mu e$ channel are presented. The results presented here have been produced using the background estimation presented in the previous section.

6.5.1 Single event sensitivity

The single event sensitivity for the three $K \to \pi\mu e$ channels is defined as

$$SES = \frac{1}{N_K \times A_{\pi\mu e}} \tag{6.12}$$

where $A_{\pi\mu e}$ is the signal acceptance reported in Table 6.1. The SES are reported in Table 6.11, considering the statistics from 2016 and 2017 samples. For reference also the present limits are shown.

Decay mode	SES	Experimental Limits
$K^+ \to \pi^+\mu^+e^-$	(1.05±0.04)×10^{-10}	1.3 × 10^{-11}
$K^+ \to \pi^+\mu^-e^+$	(1.13±0.04)×10^{-10}	5.2 × 10^{-10}
$K^+ \to \pi^-\mu^+e^+$	(1.13±0.04)×10^{-10}	5.0 × 10^{-10}

Table 6.11: Single event sensitivity for each signal channel and the corresponding present limit.

6.5.2 The Rolke-Lopez statistical treatment

The ULs for the $K \to \pi\mu e$ branching ratios has been obtained using the Rolke-Lopez method. For this analysis the Rolke-Lopez method [93, 94] has been preferred to the Feldman-Cousins method [95], since the uncertainty on the background evaluation is not negligible, due to the limited size of some of the background sources, in particular of the $K^+ \to \pi^+\pi^+\pi^-$ decay, as discussed in the previous section.

The Rolke-Lopez method, as the Feldman-Cousins, uses a frequentistic approach to extract limits, following the "$\mathcal{L} + \frac{1}{2}$" method which is known in Statistics as the large-sample approximation to the likelihood ratio test statistic. This means that the Rolke-Lopez method performed for a small sample can provide limits that are not well computed as with the Feldman-Cousins, but on the other hand it has the advantage to handle background expectations or signal efficiencies which are known only with some limited accuracy. Also thanks to its simplicity with respect to the Feldman-Cousins method, it can be generalized to the case where there are many parameters of interest.

An application provided by Rolke and Lopez is the treatment of the problem of a Poisson process with mean μ in the presence of a Poissonian background with unknown mean b. In this treatment the only number of observed events in the SR, x, is not sufficient to set limits; it is needed to use the number of observed background events in the CR, y, obtained for example using Monte Carlo simulations together with the statistical significance of the control sample with respect to the signal one. This quantity is expressed as the size of the Monte Carlo sample relative to the size of the data sample, τ, previously defined in Eq. 6.11. Then the probability model for the data is give by:

$$X \sim Pois(\mu + b) \quad Y \sim Pois(\tau b) \tag{6.13}$$

and the probability to measure μ and b, given $X = x$ and $Y = y$, assuming that X and Y are independent is:

$$P_{\mu,b}(X = x, Y = y) = f(x, y|\mu, b) = \frac{(\mu + b)^x}{x!} e^{-(\mu+b)} \cdot \frac{(\tau b)^y}{y!} e^{-\tau b} \quad (6.14)$$

Then the likelihood function is given by $\mathcal{L}(\mu, b|x, y) = f(x, y|\mu, b)$ and the profile likelihood function is given by

$$\lambda(\mu|x, y) = \frac{\mathcal{L}(\mu, \hat{b}(\mu)|x, y)}{\mathcal{L}(\hat{\mu}, \hat{b}|x, y)} \quad (6.15)$$

where $\hat{\mu} = (0, x - y/\tau)$ and $\hat{b} = y/\tau$ are the allowed values maximizing $\mathcal{L}(\mu, b|x, y) = f(x, y|\mu, b)$ with respect to both μ and b. while $\hat{b}(\mu)$ is the value of b maximizing the likelihood function over b, fixing μ.

The main advantage in using the profile likelihood ratio is that the quantity $2log\lambda$ has an approximate χ^2 distribution with *d* degrees of freedom, where *d* is the number of parameters of the models minus the dimension of the subspace over which the numerator of the profile likelihood ratio λ has been maximized. In the considered case, d = 1, since the number of parameters is two (μ,b) and the numerator in Eq. 6.15 has been maximized over b only. Therefore, the confidence interval $[\mu_1, \mu_2]$ with CL α relative to the outcome (x_0, y_0) can be directly obtained by finding the values corresponding to an increase in the $2log\lambda$ function, with respect to the minimum value, equal to the α percentile of a χ^2 distribution with *d* degrees of freedom. For example, for *d*=1 the required increase to obtain a 90% confidence interval is of 2.706.

6.5.3 Upper limit for $K \to \pi\mu e$ branching ratios

As the analysis has not been unblinded, the only thing we can do is to put upper limits under the hypothesis that zero or one event has been observed in the signal region.

To summarize in Table 6.12 and Table 6.13 are reported the number of events expected and observed in the CR, the first evaluated using the available MC sample and the second obtained from data. In the tables also the expected number of events in the SR is reported but not the observed number as the analysis is still blind because of the poor background estimation.

Looking at the results for 2016A and 2017A data a better agreement between expected and observed events in the CR for the 2017A sample is obtained, as far as the central values are concerned. A possible indication of why this is the case can be traced in the trigger efficiency, which plays a crucial role in computing the kaon flux. Indeed

	Control Region		Signal Region
Decay	N_{exp}^{CR} at 90% CL	N_{obs}^{CR}	N_{exp}^{SR} at 90% CL
$K^+ \to \pi^+\mu^+e^-$	8572±813±583	5324	<209
$K^+ \to \pi^+\mu^-e^+$	4729±591±322	2620	<209
$K^+ \to \pi^-\mu^+e^+$	4556±582±310	2576	<209

Table 6.12: Number of expected and observed events in the CR and number of expected background events in the SR for the 2016A sample. The expected number of events is evaluated using MC samples.

	Control Region		Signal Region
Decay	N_{exp}^{CR} at 90% CL	N_{obs}^{CR}	N_{exp}^{SR} at 90% CL
$K^+ \to \pi^+\mu^+e^-$	13113±1244±409	14913	<320
$K^+ \to \pi^+\mu^-e^+$	7235±902±225	7337	<320
$K^+ \to \pi^-\mu^+e^+$	6970±891±217	7346	<320

Table 6.13: Number of expected and observed events in the CR and number of expected background events in the SR for the 2017A sample. The expected number of events is evaluated using MC samples.

the study on the trigger efficiency (see Chapter 3) shows better performance of the trigger in 2017 data than 2016 data, not only for what concern the efficiency level but especially for what concern the efficiency stability with respect to the observables taken into account. In 2016 data the efficiency of the Q_X primitive shows a trend as a function of the instantaneous rate, while the efficiency of the E20 primitive shows some features as a function of the total energy in the LKr. At the moment those dependencies are not taken into account and this means that the kaon flux is not well scaled with respect to the effective trigger efficiency.

The results shown here are obtained using the Rolke-Lopez method implemented in ROOT [96], considering two possible models:

- Gaussian uncertainty in the background estimate, assuming that the uncertainty on the number of events in the signal region is equal to the one estimated for the control region
- Poissonian uncertainty in the background estimate

In order to get the interval limits for the number of signal events for the three channels, assuming zero or one event observed in the signal region in Table 6.14, the number of expected events in the signal region, reported in Table 6.12 and Table 6.13, are

used. The final results reported in here are obtained considering the full statistics (2016A+2017A).

Limits	$K^+ \to \pi^+\mu^+e^-$	$K^+ \to \pi^+\mu^-e^+$	$K^+ \to \pi^-\mu^+e^+$
90% CL (Gauss)	[0,1.04]	[0,5.28]	[0,5.28]
90% CL (Poisson)	[0,1.90]	[0,1.90]	[0,1.90]

Table 6.14: Confidence intervals for the number of signal events.

Considering these results the limits on the branching ratio, computed using (6.5) are:

Decay mode	Upper limit 90% CL (Gauss)	Upper limit 90% CL (Poisson)	Experimental Limits (90% CL)
$K^+ \to \pi^+\mu^+e^-$	$1.09 < \times 10^{-10}$	$< 1.99 \times 10^{-10}$	1.3×10^{-11}
$K^+ \to \pi^+\mu^-e^+$	$< 5.97 \times 10^{-10}$	$< 2.14 \times 10^{-10}$	5.2×10^{-10}
$K^+ \to \pi^-\mu^+e^+$	$< 5.97 \times 10^{-10}$	$< 2.14 \times 10^{-10}$	5.0×10^{-10}

Table 6.15: Upper limits of the branching ratio at 90% CL obtained assuming a Gaussian or Poissonian uncertainty in the background estimate.

As already said the results have been obtained with a poor background estimation, due to the lack of statistics for some of the background channels and a more detailed study is needed in order to unblind the signal region and obtain a more reliable results.

The results in Table 6.15, assuming zero or one event observed in the signal region, show improvements with respect to the present experimental limit for the $K^+ \to \pi^+\mu^-e^+$ and $K^+ \to \pi^-\mu^+e^+$ channels but only if the limits are computed assuming a poissonian uncertainty of the background estimate. In the case of Gaussian uncertainty in the background estimate, the ULs do not improve with respect to the preset limits.

The results presented in this work prove the validity of the strategy developed for the $K \to \pi\mu e$ analysis, showing the capability of NA62 to set new limits for these kind of searches. In particular the analysis of the full statistics collected during the 2016-2018 data taking and larger MC samples will be mandatory to improve the actual limits.

Conclusion

The NA62 experiment, thanks to its high-intensity setup, trigger system flexibility, and detectors performance, is the perfect environment to search for beyond standard model physics from different scenarios.

The analysis presented in this thesis aims at contributing to new physics searches, looking at LN and LF violations in kaon decays. In particular it is focused on three channels: $K^+ \to \pi^+\mu^+e^-$, $K^+ \to \pi^+\mu^-e^+$, $K^+ \to \pi^-\mu^+e^+$, the first two violate only the lepton flavor, while the third violates both lepton number and flavor.

Contributions to LN and LF violations in kaon decays from beyond SM theories, as the Leptoquark and the $Z^{'}$ boson have been presented in this work, showing that, even though the expected branching ratios increase with respect to the SM ones, they are still far from the experimental reachable values in most of the New Physics models. Nevertheless there are some exceptions for specific values of the new particle mass and coupling, e.g. in the $Z^{'}$ boson scenario, for a $Z^{'}$ mass $\sim$200 GeV/c^2, and considering the $g_{Z'} \sim g_{W,Z}$, the branching ratios for the $K \to \pi\mu e$ channels are expected to be $\sim 10^{-13}$, value which is not too far from the present experimental sensistivities. Indeed, for the searches presented in this work the NA62 experiment is expected to reach sensitivities of $\sim 10^{-11}$ using the full statistics from the 2016-2018 data taking, giving a strong impact to set new limits in the phase space of the New Physics parameters.

In this work the strategy developed for the $K \to \pi\mu e$ selection and first preliminary results, using the data collected in 2016 and 2017, have been presented. The results have been derived with the signal region still blind, assuming that the number of observed events in the signal region is zero or one. This choice is due to the poor background estimation because of the small size of the available MC samples.

The two main steps for the signal selection are the three-track vertex reconstruction and the particle identification. For the first purpose a tool based on the Least Squared

method has been developed and implemented within the NA62 framework. It shows better performance in the three-track vertex reconstruction with respect to the standard Closest of Distance Approach method. It has been used in the current analysis and it is the official method at NA62 for multi-track vertex reconstruction.

The PID criteria make use of the information available from LKr (energy), MUV3 (signal) and RICH (ring radius). The study on PID efficiency presented in this work has been obtained both with data and MC and it shows good performance of the strategy adopted. In particular the overall PID efficiency, measured from data using multi-tracks events, to identify a positive pion as a pion results (88.7$\pm$0.1)% while the mis-identification as a muon is (1.90$\pm$0.06)% and as a positron is (0.20$\pm$0.03)%. For negative pion the probability to be identified as a pion is (78.7$\pm$0.1)% while to be mis-identified as a muon is (1.70$\pm$0.07)% and as an electron is (0.20$\pm$0.03)%. For positron and electron the results are less strong, due to the lack of statistics. However the results show a good positron/electron identification. The identification probability is of (95.0$\pm$8.0)% for positrons with a mis-identification as a pion/muon of 10.0% known at 90% CL. The identification probability is of (88.0$\pm$15.0)% for electrons with a mis-identification as a pion/muon of 14.0% known at 90% CL.

The results show better performance for positive than negative particles, as expected due to the RICH geometrical optimization to detect positive tracks. The study shows also that in the momentum range where the RICH is used, even though there is no gain in the particle identification efficiency, the probability to mis-identify a particle decreases, helping in background rejection. As already mentioned, in this work the muon (positive and negative) PID efficiency from multi-tracks events has not been presented and at the moment it is assumed to be as the pion PID efficiency. A more detailed study will be performed using the $K^+ \to \pi^+\mu^+\mu^-$ decay channel.

Furthermore the study done on the PID efficiency using the MC sample, showed some discrepancies with respect to the results obtained with data and since the signal acceptance used to provide the final results has been evaluated with MC samples,it is foreseen to take into account of those discrepancies as a systematic uncertainty.

The results shown in this work have been obtained analyzing the available data sample from the 2016 run and the 2017 run. The two sample corresponds to a kaon flux of

$$N_K = (6.73 \pm 0.41) \times 10^{10} \ \ (2016A)$$
$$N_K = (10.31 \pm 0.13) \times 10^{10} \ \ (2017A)$$

measured using the K3π decay, taking into account the trigger efficiency of the three trigger masks used in the analysis. A dedicated study presented in this thesis showed a trigger efficiency between 77%-60% in 2016 and around 90% in 2017, proving that the

actions taken to fix inefficiencies detected in 2016 improved the trigger efficiency. The trigger efficiency precision and the the K3π branching ratio precision represents the main contribution to the systematic error quoted in the kaon flux, while the statistical error results negligible with respect to the systematic one and it is not reported.

The analysis has been performed blinding the signal region, which is defined by the [480,505]MeV/c^2 region in the invariant mass spectrum.

A preliminary study on the main background sources for each decay channel has been presented. It is limited by the small size of the MC samples with respect to the data size for some of the background source: the K3π, Ke3 Dalitz, Kμ3 Dalitz and K2π Dalitz. For this reason the present background estimation is quite poor and it has been decided to keep the signal region still blind, until larger MC samples are available. Nevertheless preliminary results have been reported using the present background estimation.

Applying the selection criteria shown in the work, the SES for each $K \to \pi\mu e$ channel results:

Decay mode	SES	Experimental Limits
$K^+ \to \pi^+\mu^+e^-$	(1.05$\pm$0.04)$\times 10^{-10}$	1.3×10^{-11}
$K^+ \to \pi^+\mu^-e^+$	(1.13$\pm$0.04)$\times 10^{-10}$	5.2×10^{-10}
$K^+ \to \pi^-\mu^+e^+$	(1.13$\pm$0.04)$\times 10^{-10}$	5.0×10^{-10}

Table 6.16: Single event sensitivity for each signal channel and the corresponding present limit.

Taking into account the SES for the 2016 and partial 2017 data the NA62 experiment can reach sensitivity of $\sim 10^{-10}$, improving the current limits on the $K^+ \to \pi^+\mu^-e^+$ of a factor 4.6 and on the $K^+ \to \pi^-\mu^+e^+$ of a factor 4.4, while for the $K^+ \to \pi^+\mu^+e^-$ more data are needed due to a more stringent result from the previous experiment.

The ULs reported in Table 6.17 have been obtained using the Rolke-Lopez method assuming Gaussian or Poissonian distribution for the background uncertainty and assuming that the number of observed events in the signal region is equal to zero or one.

As already said, the results are made in a situation of poor knowledge of the background and cannot be consider final. For this reason an alternative strategy to generate larger MC sample is needed. In particular a fast simulation of the K3π is ongoing

Decay mode	Upper limit 90% CL (Gauss)	Upper limit 90% CL (Poisson)	Experimental Limits (90% CL)
$K^+ \to \pi^+\mu^+e^-$	$< 1.09 \times 10^{-10}$	$< 1.99 \times 10^{-10}$	1.3×10^{-11}
$K^+ \to \pi^+\mu^-e^+$	$< 5.97 \times 10^{-10}$	$< 2.14 \times 10^{-10}$	5.2×10^{-10}
$K^+ \to \pi^-\mu^+e^+$	$< 5.97 \times 10^{-10}$	$< 2.14 \times 10^{-10}$	5.0×10^{-10}

Table 6.17: Upper limits of the branching ratio at 90% CL obtained assuming a Gaussian or Poissonian uncertainty in the background estimate.

within the NA62 framework: it omits most of the detectors simulation allowing to generate larger samples in a feasible amount of time and with feasible file size. In particular to get reasonable results on the background estimation, at least $\sim 10^{10}$ K3π and $\sim 10^8$ Ke3 and Kμ3 events are needed, in order to have the same statistics as the 2016 and 2017 samples. On the other hand, to reduce the statistical and systematic errors a factor 10 more would be necessary. A MC K3π sample with 10×10^{10} events, produced with the fast simulation, will be available by the end of 2018 and by that time a better background estimation will be possible.

Even if the results are not conclusive, they show improvements with respect to the present experimental limits for the $K^+ \to \pi^+\mu^-e^+$ and $K^+ \to \pi^-\mu^+e^+$ channels but only if the limits are computed assuming a Poissonian uncertainty of the background estimate.

The results presented in this work prove the validity of the strategy developed for the $K \to \pi\mu e$ analysis, showing the capability of NA62 to set new limits for these kind of searches. In particular the analysis of the full statistics collected during the 2016-2018 data taking and larger MC samples will be mandatory to improve the actual limits. For what concern the 2017 data, the processing of the full statistics would be available by the end of 2018, while for the 2018 data the full processing would be probably available by the end of 2019. For this reason first resulsts, from 2016 and 2017 data could be ready for the 2019 winter conferences, while the results using also the 2018 data set will be presented in winter 2020.

In conclusion considering the full data collected between the 2016 and 2018 the kaon flux is expected to be of the order of $6 - 7 \times 10^{11}$ (taking into account the trigger efficiency) and thanks to the availability of larger MC samples, leading to a better background estimation, larger improvements on the present experimental limits are expected. In Table 6.18 a SES estimation considering the full statistics is presented, showing improvements of a factor ~ 16 for the $K^+ \to \pi^+\mu^-e^+$ and $K^+ \to \pi^-\mu^+e^+$ channels, while to improve on the present $K^+ \to \pi^+\mu^+e^-$ limit more statistics is needed.

Decay mode	SES	Experimental Limits
$K^+ \to \pi^+\mu^+e^-$	3.0×10^{-11}	1.3×10^{-11}
$K^+ \to \pi^+\mu^-e^+$	3.2×10^{-11}	5.2×10^{-10}
$K^+ \to \pi^-\mu^+e^+$	3.2×10^{-11}	5.0×10^{-10}

Table 6.18: Expected single event sensitivity for each signal channel considering the full statistics collected between 2016 and 2018 and the corresponding present limit.

Appendix A

Least squares fit of vertex parameters

The track parametrization in NA62 at reference plane $Z = const$ is:

$$\theta_{X,i}, \theta_{Y,i} \qquad \mathrm{d}x/\mathrm{d}z \text{ and } \mathrm{d}y/\mathrm{d}z \text{ slopes}, \tag{A.1}$$

$$X_i, Y_i \tag{A.2}$$

$$P_i, \tag{A.3}$$

These previously fitted (in the STRAW and GTK reconstructions) track parameters are viewed as *'virtual measurements'* within the vertex LSF formalism which aims to find the best estimate of the vertex position $\vec{x}$ and the three-dimensional new track parameters $\vec{q}_i$ at the vertex.

$$\vec{x}(x, y, z) \qquad \text{vertex coordinates}, \tag{A.4}$$

$$\vec{q}_i(\theta_{x,i}, \theta_{y,i}, P_i) \qquad \text{slopes and momentum of track } i, \tag{A.5}$$

$$\vec{m}_i(\theta_{X,i}, \theta_{Y,i}, X_i, Y_i, P_i) \qquad \text{parametrisation of the } \textit{measured} \text{ track } i \tag{A.6}$$

The following notation will be used to describe the LSF method in a general way:

$$\vec{q} = \begin{pmatrix} \vec{x} \\ \vec{q}_1 \\ \vdots \\ \vec{q}_n \end{pmatrix} \qquad \text{vector of vertex parameters,} \tag{A.7}$$

$$\vec{m} = \begin{pmatrix} \vec{m}_1 \\ \vec{m}_2 \\ \vdots \\ \vec{m}_n \end{pmatrix} \qquad \text{vector of track measurements,} \tag{A.8}$$

$$V = \begin{pmatrix} V_1 & 0 & \dots & 0 \\ 0 & V_2 & \dots & 0 \\ \vdots & \vdots & \ddots & \vdots \\ 0 & 0 & 0 & V_n \end{pmatrix} \qquad \text{cov. matrix of all measurements,} \tag{A.9}$$

$$W = \begin{pmatrix} W_1 & 0 & \dots & 0 \\ 0 & W_2 & \dots & 0 \\ \vdots & \vdots & \ddots & \vdots \\ 0 & 0 & 0 & W_n \end{pmatrix} \qquad \text{weight matrix, where } W_n = V_n^{-1} \tag{A.10}$$

If the true vertex position and momentum $(\vec{x}^t, \vec{q}_i^t)$ of track i are known then $\vec{m}_i$ can be expressed as:

$$\vec{m}_i = h(\vec{x}^t, \vec{q}_i^t) + \vec{v}_i \tag{A.11}$$

where h is a function which maps the vector of parameters $\vec{q}$ into the vector of measurements $\vec{m}$ and $\vec{v}_i$ is the measurement noise. The solution of the vertex fit is the set of parameters $\vec{q}$ that minimise the χ^2 function:

$$\chi^2 = (\vec{m} - h(\vec{q}))^T W (\vec{m} - h(\vec{q})) \tag{A.12}$$

In the LSF the measurement model h must be linear in the unknown parameters $\vec{q}$. If that is not the case, and indeed for the NA62 parametrisation it is not, the model has to be linearised. Expanding around the current (or initial and best known) estimate of the vertex parameters $(\vec{x}^{(0)}, \vec{q}_i^{(0)})$, h becomes:

$$h(\vec{x}, \vec{q}_i) = h(\vec{x}^{(0)}, \vec{q}_i^{(0)}) + A(\vec{x} - \vec{x}^{(0)}) + B(\vec{q}_i - \vec{q}_i^{(0)}), \tag{A.13}$$

$$A = \left.\frac{\partial h(\vec{x}, \vec{q}_i)}{\partial \vec{x}^t}\right|_{(\vec{x}^{(0)}, \vec{q}_i^{(0)})} \qquad B = \left.\frac{\partial h(\vec{x}, \vec{q}_i)}{\partial \vec{q}_i^t}\right|_{(\vec{x}^{(0)}, \vec{q}_i^{(0)})} \tag{A.14}$$

The vector of vertex parameters $\vec{q}$ should minimise the χ^2 function.

$$\frac{\partial \chi^2}{\partial \vec{q}} = -2G^T W(\vec{m} - h(\vec{q}^{(0)}) - G(\vec{q} - \vec{q}^{(0)})) = 0 \tag{A.15}$$

where G is:

$$G = \begin{pmatrix} A_1 & B_1 & 0 & 0 & \dots & 0 \\ A_2 & 0 & B_2 & 0 & \dots & 0 \\ A_3 & 0 & 0 & B_3 & & \vdots \\ \vdots & \vdots & \vdots & & \ddots & 0 \\ A_n & 0 & 0 & \dots & 0 & B_n \end{pmatrix} \tag{A.16}$$

$$G^T W G(\vec{q} - \vec{q}^{(0)}) = G^T W(\vec{m} - h(\vec{q}^{(0)})) \tag{A.17}$$

By simplifying a bit Eq. 17 the change in the initial vector of vertex parameters $\Delta\vec{q} = \vec{q} - \vec{q}^{(0)}$ becomes:

$$\Delta\vec{q} = M^{-1} N \, \Delta\vec{m} \, , \tag{A.18}$$

where $\Delta\vec{m} = \vec{m} - h(\vec{q}^{(0)})$ and the matrices M and N are defined as:

$$M = G^T W G = \begin{pmatrix} D_0 & D_1 & D_2 & \dots & D_n \\ D_1^T & E_1 & 0 & \dots & 0 \\ D_2^T & 0 & E_2 & & \vdots \\ \vdots & \vdots & & \ddots & 0 \\ D_n^T & 0 & 0 & \dots & E_n \end{pmatrix} \tag{A.19}$$

$$N = G^T W = \begin{pmatrix} A_1^T W_1 & A_2^T W_2 & \dots & A_n^T W_n \\ B_1^T W_1 & 0 & \dots & 0 \\ 0 & B_2^T W_1 & & \vdots \\ \vdots & & \ddots & 0 \\ 0 & \dots & 0 & B_n^T W_n \end{pmatrix} \tag{A.20}$$

$$D_0 = \sum_{i=1}^{n} A_i^T W_i A_i \, , \quad D_i = A_i^T W_i B_i \, , \quad E_i = B_i^T W_i B_i \tag{A.21}$$

The inverse matrix M^{-1} is:

$$M^{-1} = \begin{pmatrix} C_{00} & C_{01} & \dots & C_{0n} \\ C_{10} & C_{11} & \dots & C_{1n} \\ \vdots & \vdots & \ddots & \vdots \\ C_{n0} & C_{n2} & \dots & C_{nn} \end{pmatrix} \quad C_{ij} = C_{ji}^T \tag{A.22}$$

The C_{ij} submatrices are the covariance matrices of the fitted vertex coordinates and track parameters. They can be computed explicitly by considering that the product of M with its inverse M^{-1} should be a unitary matrix I.

$$C_{00} = (D_0 - \sum_{i=1}^{n} D_i E_i D_i^T)^{-1} \ , \tag{A.23}$$

$$C_{0i} = C_{i0}^T = -C_{00} D_i E_i^{-1} \ , \tag{A.24}$$

$$C_{ij} = \delta_{ij} E_j^{-1} - E_i^{-1} D_i^T C_{0j} \ , \tag{A.25}$$

and finally

$$\Delta\vec{x} = C_{00} \sum_{i=0}^{n} G_i^T W_i (I - B_i E_i^{-1} B_i^T W_i) \Delta\vec{m}_i \ , \tag{A.26}$$

$$\Delta\vec{q}_i = E_i^{-1} B_i^T W_i (-A_i \Delta\vec{x} + \Delta\vec{m}_i). \tag{A.27}$$

The measurement model, h, maps the vertex parameters to the measured track parameters by assuming that the particle trajectories are linear.

$$h(\vec{x}, \vec{q}_i) = \begin{pmatrix} \theta_{x,i} \\ \theta_{y,i} \\ x + (Z_i - z)\theta_{x,i} \\ y + (Z_i - z)\theta_{y,i} \\ P_i \end{pmatrix} \quad A = \begin{pmatrix} 0 & 0 & 0 \\ 0 & 0 & 0 \\ 1 & 0 & -\theta_{x,i} \\ 0 & 1 & -\theta_{y,i} \\ 0 & 0 & 0 \end{pmatrix} \quad B = \begin{pmatrix} 1 & 0 & 0 \\ 0 & 1 & 0 \\ Z - z & 0 & 0 \\ 0 & Z - z & 0 \\ 0 & 0 & 1 \end{pmatrix} \tag{A.28}$$

This assumption holds in the case of no magnetic field or matter between the reference plane and the vertex. And in a more realistic scenario, where there is some inhomogenious magnetic field present in the fiducial decay region, the Z coordinate of the reference plane has to be 'chosen' sufficienctly close to the z coordinate of the vertex.

Momentum and Mass constraints

The momentum of the kaon (GTK) track can be used in the fit to constrain the sum of the momentas of the daughter (STRAW) tracks. The total three-momentum of all

STRAW tracks assigned to the fit and its covariance matrix are given by:

$$P_{\rm tot} = \sum_i \vec{p}_i(p_x, p_y, p_z) \quad \text{and} \quad R = \text{Cov}(P_{\rm tot}) = \sum_{i,j} K_i D_{i,j} K_j^T \ , \tag{A.29}$$

where

$$\vec{p}_i = \begin{pmatrix} \theta_{x,i} P_i/n_i \\ \theta_{y,i} P_i/n_i \\ P_i/n_i \end{pmatrix} \tag{A.30}$$

$$K_i = \begin{pmatrix} (1+\theta_{y,i}^2)P_i/n_i^3 & -\theta_{x,i}\theta_{y,i}P_i/n_i^3 & \theta_{x,i}/n_i \\ -\theta_{x,i}\theta_{y,i}P_i/n_i^3 & (1+\theta_{x,i}^2)P_i/n_i^3 & \theta_{y,i}/n_i \\ -\theta_{x,i}P_i/n_i^3 & -\theta_{y,i}P_i/n_i^3 & 1/n_i \end{pmatrix} \tag{A.31}$$

$$n_i = \sqrt{1+\theta_{x,i}^2+\theta_{y,i}^2} \tag{A.32}$$

Using the reconstructed momentum $\vec{P}_{tot}$ and the momentum $\vec{P}_K$ measured by the GTK we form a residual for the mass constraint: $\vec{r} = \vec{P}_K - \vec{P}_{tot}$. The constrained vertex position and track parameters are calculated as follows:

$$\vec{x} = \vec{x}_0 - \sum_i C_{0i}^T K_i^T R^{-1} r \quad \text{and} \quad \vec{q}_i = \vec{q}_{i,0} - \sum_j C_{i,j}^T K_j^T R^{-1} r \tag{A.33}$$

Magnetic field in the decay volume

The residual magnetic field in the decay region, which is due to the geomagnetic field and the magnetization of the decay tank. The magnetic field components have been measured in 39 z planes in the range from $z_0 = 105.795$ m to 177.845 m. The field is not homogeneous and the track propagation is done in steps. The dependence of the momentum kick in x and y on the field components B_x, B_y and B_z is parametrised with low-order polynomials which are recalculated at each z plane. For what concers the covariance matrix of track parameters, it is corrected by a Jacobian matrix, F, which is derived from the aforementioned parametrisation and updated at each step: $V_i = FV_{i-1}F^T$. The initial covariance matrix, V_0 , is the one provided by the STRAW fit. The elements of the Jacobian matrix are defined as $F(i,j) = \partial m_i^{new}/\partial m_j$. At

each step the new parameters $\vec{m}^{new}$ are:

$$\theta_x^{new} = \theta_x + A(1 + \alpha_y x + \beta_y y + \epsilon_y xy), \tag{A.34}$$

$$\theta_y^{new} = \theta_y + A(1 + \alpha_x x + \beta_x y + \epsilon_x xy + \gamma_x x^2 + \lambda_x y^2), \tag{A.35}$$

$$x^{new} = x - \Delta z(\theta_x + \theta_x^{new})/2, \tag{A.36}$$

$$y^{new} = y - \Delta z(\theta_y + \theta_y^{new})/2, \tag{A.37}$$

$$P^{new} = P_z\sqrt{(\theta_x^{new})^2 + (\theta_y^{new})^2 + 1} \sim P. \tag{A.38}$$

$$\tag{A.39}$$

where $A = q/P_z$, Δz is the step length, and $\alpha_x, \alpha_y, \beta_x, \beta_y, \epsilon_x, \epsilon_y, \gamma_x, \lambda_x$ are parameters which have been pre-computed for each step of the magnetic field propagation. The corresponding Jacobian matrix is then:

$$F = \begin{pmatrix} 1 & 0 & A(\alpha_y + \epsilon_y y) & A(\beta_y + \epsilon_y x) & 0 \\ 0 & 1 & A(\alpha_x + \epsilon_x y + 2\gamma_x x) & A(\beta_x + \epsilon_x x + 2\lambda_x y) & 0 \\ -\Delta z & 0 & 1 - A(\alpha_y + \epsilon_y y)\Delta z/2 & -A(\beta_y + \epsilon_y x)\Delta z/2 & 0 \\ 0 & -\Delta z & -A(\alpha_x + \epsilon_x y + 2\gamma_x x)\Delta z/2 & 1 - A(\beta_x + \epsilon_x x + 2\lambda_x y)\Delta z/2 & 0 \\ 0 & 0 & 0 & 0 & 1 \end{pmatrix} \tag{A.40}$$

Bibliography

[1] *A. D. Sakharov* Violation of CP invariance, C asymmetry, and baryon asymmetry of the universe, Pisma Zh. Eksp. Teor. Fiz.5(1967) 32, [JETP Lett.5(1967) 24]

[2] *R.Aaij et al.*[LHCb Collaboration] Phys. Rev. Lett. 119, 181807 (2017)

[3] *D.Griffiths* Introduction to Elementary Particles

[4] *F.Haltzen and A.D Martin* Quarks and Leptons: An Introductory Course in Modern Particle Physics

[5] *G. t Hooft*, Phys. Rev. D 14 (1976) 3432 [Phys. Rev. D 18(1978) 2199]

[6] *R. Aaij et al.* [LHCb], Phys.Rev.Lett. 113, 151601 (2014)

[7] *W. Altmannshofer and D. M. Straub* (2015), 1503.06199

[8] *S. Descotes-Genon, L. Hofer, J. Matias, and J. Virto*(2015), 1510.04239

[9] *M. Huschle et al.* [Belle Collaboration] Phys. Rev. D 92, 072014 (2015)

[10] *Y. Sato et al.* [Belle Collaboration] Phys. Rev. D 94, 072007 (2016)

[11] *S. Hirose et al.* [Belle Collaboration] Phys. Rev. Lett. 118, 211801 (2017)

[12] *J. P. Lees et al.*[BaBar Collaboration] Phys. Rev. Lett. 109, 101802 (2012)

[13] *R. Aaij et al.* [LHCb Collaboration] Phys. Rev. Lett. 115, 111803 (2015)

[14] *R. Aaij et al.* [LHCb Collaboration] JHEP 08 (2017) 055

[15] *J. Woithe et al.* Phys.Educ. 52 (2017) 034001

[16] *Greiner, Muller*, Gauge theory of weak interactions (Third edition), Springer

[17] *A. Buras*,JHEP 11 (2015) 033

[18] *A. Buras*, JHEP 11 (2015) 166

[19] *N. Cabibbo*, Phys. Rev. Lett., 10, 531 (1963)

[20] *S. L. Glashow, J. Iliopoulos, L. Maiani*, Phys. Rev. D2 (1970) 1285

[21] *J.J Aubert et al.* Phys. Rev. Lett. 33, 1404 (1974)

[22] *J.E. Augustin et al.* Phys. Rev. Lett. 33, 1406 (1974)

[23] *M Kobayashi, T Maskawa*, Progress of Theoretical Physics, 49, 2 (1973)

[24] Particle Data Group Collaboration, M. Tanabashi et al.,Phys. Rev. D 98, 030001 (2018). http://pdg.lbl.gov

[25] *L. Wolfenstein*, Phys. Rev. Lett. 51, 1945 (1983)

[26] *J.H. Christenson et al.*, Phys. Rev. Lett. 13, 138 (1964)

[27] *A.Angelopoulos et al.*[CPLEAR Coll.], Physics Letters B 458 (1999)

[28] *S. Bertolini, M. Fabbrichesi, and J. O. Eeg*. Rev. Mod. Phys. 72, 1 (2000)

[29] *J. Batley et al.* [NA48 Collaboration],Phys. Lett. B544(2002) 97112

[30] *A. Alavi-Harati et al.* [KTeV Collaboration],Phys. Rev.D67(2003) 012005

[31] *E. Worcester* [KTeV Collaboration],arXiv:0909.2555

[32] *G.Barr et al.* (NA31),Phys.Lett.B 317, 233 (1993)

[33] *J.R. Batley et al.* [NA48 Collaboration], Phys.Lett.B 544, (2002) 97

[34] *A.Alavi-Harati et al.* [KTeV Collaboration], Phys.Rev.D 67 (2003) 012005

[35] *A. J. Buras, M. Gorbahn, S. Jger, and M. Jamin*, JHEP 11 (2015) 202

[36] *A. J. Buras and J.-M. Gerard*, JHEP 12 (2015) 008; *A. J. Buras and J.-M. Gerard* Eur.Phys.J. C77 (2017) 10

[37] *Z. Bai, T. Blum, P. Boyle, N. Christ, J. Frison, et al.*, Phys.Rev.Lett. 115, 212001 (2015)

[38] *J. Aebischer, A.J. Buras, J.M Gerard* arXiv:1807.01709

[39] *S.Fukuda et al.*, (Super-Kamiokande Collab.), Phys. Rev. Lett. 86, 5651 (2001); *Q.R.Ahmad et al.*, (SNO Collab.) Phys. Rev. Lett. 87, 071301 (2001); 89, 011302 (2002); *R.Davis* (Homestake Collab.), Rev. Mod. Phys. 75, 985 (2003)

[40] *M.N.Ahn et al.*, (K2K Collab.), Phys. Rev. Lett. 90, 041801 (2003)

[41] *K.Eguchi et al.*, (KamLAND Collab.), Phys. Rev. Lett. 90, 021802

[42] *S.Fukuda et al.*, (Super-Kamiokande Collab.), Phys. Rev. Lett. 81, 1562 (1998); 82, 2644 (1999); 85, 3999 (2000)

[43] *B.Pontecorvo*, JETF, 33, 549 (1957); 34, 247 (1957)

[44] *Z.Maki, M.Nakagawa and S.Sakata*, Prog. Theor. Phys. 28, 870 (1962)

[45] *S.M. Bilenky, and S. T. Petcov*,Rev. Mod. Phys.59 (1987) 671

[46] *S.M. Bilenky, C. Giunti, W. Grimus* Prog.Part.Nucl.Phys.43:1-86,1999

[47] *S. Petcov*, Adv.High Energy Phys. 2013, 852987 (2013), 1303.5819

[48] *P. Minkowski*, Phys.Lett. B67, 421 (1977)

[49] *A.V. Borisov* [arXiv:1112.3269]

[50] *L. S. Littenberg and R. Shrock*, Phys.Lett. B491, 285 (2000), Phys.Lett. B491 (2000) 285-290

[51] *A. Ali, A. Borisov, and N. Zamorin*,Eur.Phys.J. C21, 123 (2001), Eur.Phys.J.C21:123-132,2001

[52] *A.Abada et al.* J. High Energ. Phys. (2018) 2018: 169

[53] *P. Langacker*, Rev. Mod.Phys. 81 3 (2009)

[54] .*L.Ritchie and S.Wojcicki*, Reviews of Mod. Phys., 65, 1149 (1993)

[55] *T.G.Rizzo*, hep-ph/9809526

[56] *L.G. Landsberg* Phys.Atom.Nucl.68:1190-1210,2005

[57] *J.C. Pati,A.Salam*, Phys.Rev.D 10, 27 (1974)

[58] *M.Bordone, C. Cornella, J. Fuentes-Martin, G.Isidori* Phys.Lett. B779 (2018) 317-323

[59] *M.Bordone, C. Cornella, J. Fuentes-Martin, G.Isidori* arXiv:1805.09328

[60] *J.R. Batley et al.* [NA48/2 Collaboration] Phys.Lett.B 769 (2017)

[61] *A.Sher et al.* Phys.Rev.D72 (2005) 012005

[62] *R.Appel et al.* Phys.Rev.Lett 85 (2000) 2877

[63] *R.Appel et al.* Nucl.Instr.and Meth. A479 (2002) 349

[64] *S.M. Bilenky, S.T. Petcov and B. Pontecorvo*, Phys. Lett. B 67 (1977) 309

[65] *E. Farhi and L. Susskind*, Phys. Rep. 74, 277 (1981)

[66] *H. E. Haber and G. L. Kane*, Phys. Rep. 117, 75 (1985)

[67] *T. Han, H. E. Logan, B. Mukhopadhyaya and R. Srikanth*, Phys. Rev.D 72 (2005) 053007

[68] *A. Goyal* AIP Conf.Proc. 805 (2006) 302-305

[69] *R. D. Peccei and Helen R. Quinn* Phys. Rev. D 16, 1791 (1977)

[70] *W.J. Marciano, A. Masiero, P. Paradisi, M. Passera* Phys. Rev. D 94, 115033 (2016

[71] *M.Borsato et al.* arXiv:1808.02006

[72] *A. V. Artamonov et al. Phys. Rev. Lett.* Phys. Rev. Lett. 101, 191802 (2008)

[73] J.R. Batley *et al.* [NA48/2 Collaboration], *Eur. Phys. J.* C **52**, 875 (2007)

[74] V. Fanti *et al.* [NA48/2 Collaboration], *Nucl. Instrum. Methods* A **574** 433 (2007)

[75] Technical design of the NA62 experiment *na62.web.cern.ch/na62/Documents/TechnicalDesign.html*

[76] E. Cortina Gil *et al.* [NA62 Collaboration] The beam and detector of the NA62 experiment at CERN. *Journal of Instrumentation* **12** (2017)

[77] Anelli *et al.* Optimum Segmentation and Thickness of Silicon Pixel Detectors for Signal to Noise Ratio and Timing Resolution. Nuclear Science Symposium Conference Record IEEE, Vol 2, 2006, 671-680

[78] G. Nuessle. Development of a novel micro channel cooling system for the NA62 GTK detector. PhD thesis. Univ. cath. Louvain, 2015. url: http://hdl.handle.net/2078.1/171150

[79] B. Velghe. Development and Commissioning of the Silicon Pixel GigaTracker for the NA62 Experiment at CERN. PhD thesis. Univ. cath. Louvain, 2016. url: http://cp3.irmp.ucl.ac.be/upload/theses/phd/velghe.pdf

[80] G. Aglieri Rinella *et al.* The NA62 GigaTracker. Nucl.Instrum.Meth. A845 (2017) 147-149

[81] G. Ruggiero. Straw Spectrometer Reconstruction. Internal note: NA62-12-01, 2012

[82] V. Fanti *et al.*, Nucl. Instrum. Methods A574, (2007) 433

[83] G. Barr *et al.* Performance of an electromagnetic liquid krypton calorimeter based on a ribbon electrode tower structure. In: Nucl. Instrum. Methods Phys. Res., Sect. A 370.2 3 (1996), pp. 413424. doi: 10.1016/0168-9002(95)00800-4

[84] A. Ceccucci *et al.* The NA62 Liquid Krypton calorimeter readout module. In: J. Instrum. 6.12 (2011), p. C12017. doi: 10.1088/1748-0221/6/12/C12017

[85] *R.Fruhwirth, M. Regler, R.K. Bock, H. Grote, D. Notz* Data Analysis technique for high energy physics, Second Edition, Cambridge

[86] *V. Lendermann et al.* Nucl.Instrum.Meth.A 604 (2009)

[87] *M.Sozzi A concept for the NA62 Trigger and Data Acquisition. Internal Note NA62-07-03*

[88] *D.Soldi, S.Chiozzi* arXiv:1802.06548

[89] E.Minucci, P.Petrov Method for vertex fit in NA62. Internal Note NA62-16-05

[90] P.Billoir, R.Fruhwirth, M.Regler, Nucl. Instr. Meth. A 241 (1985) 115

[91] J. Fry and M. Nelson, note NA62-14-05 (May 2014) https://na62.web.cern.ch/NA62/restricted/NotesDoc/NA62-14-05.pdf

[92] F. Hahn, J. Fry and M. Nelson, Magnetic Field Measurements for NA62 (September 2013). https://edms.cern.ch/document/1286277/3

[93] W. A. Rolke and A. M. Lopez, Nucl.Instrum.Meth. A458, 745 (2001)

[94] W. A. Rolke, A. M. Lopez, and J. Conrad, Nucl.Instrum.Meth. A551, 493 (2005)

[95] G. J. Feldman and R. D. Cousins, Phys.Rev. D57, 3873 (1998)

[96] https://root.cern/doc/v610/Rolke$_8C.html$